Platinum-nickel nanowires and nanotubes arrays as carbon-free cathodes for the PEM fuel cell

Othman Lagrichi

THÈSE

Pour obtenir le grade de

DOCTEUR DE L'UNIVERSITE GRENOBLE ALPES

Spécialité : **Nanophysique**

Arrêté ministériel : 25 mai 2016

Présentée par

Othman LAGRICHI

Thèse dirigée par **Denis BUTTARD, Professeur, Université Grenoble-Alpes**, et

codirigée par **Arnaud MORIN, Chargé de Recherche, Laboratoire d'innovation pour les technologies des énergies nouvelles et les nanomatériaux (LITEN), CEA-Grenoble**

Préparée au sein du **Laboratoire des Composants pour Pile à Combustible (LCP)** et du **Laboratoire Photonique Electronique et Ingénierie Quantiques (IRIG-PHELIQS), CEA-Grenoble**
dans **l'École Doctorale de Physique**

Platinum-Nickel Nanowires and Nanotubes Arrays as Carbon-free Cathodes for the PEM Fuel Cell

Thèse soutenue publiquement le **« Jeudi 29 Avril 2021 »**
devant le jury composé de :

Pr. Elena R. SAVINOVA
Professeur, Université de Strasbourg, Rapporteur
Dr. Vincent VIVIER
Directeur de Recherche du CNRS, Sorbonne Universités, Rapporteur
Pr. Christophe COUTANCEAU
Professeur, Université de Poitiers, Examinateur
Dr. Eric CHAÎNET
Directeur de Recherche, Université Grenoble-Alpes (LEPMI), Examinateur
Dr. Bryan PIVOVAR
Senior Research Fellow, US National Renewable Energy Laboratory, Invité
Pr. Marian CHATENET
Professeur, Université Grenoble-Alpes (INP/LEPMI), Président de Jury
Pr. Denis BUTTARD
Professeur, Université Grenoble-Alpes, Directeur de Thèse
Dr. Arnaud MORIN
Chargé de Recherche, CEA/Liten/LCP, Co-Directeur de Thèse

إلى أمي...

To my Mother...

وَأَلْقَيْتُ عَلَيْكَ مَحَبَّةً مِنِّي وَلِتُصْنَعَ عَلَىٰ عَيْنِي

"And I showered you with lovability from Me, and I had you made before My Watchful Eye"

“Et J'ai répandu sur toi une affection de Ma part, afin que tu sois élevé sous Mon œil”

Quran - Chapter 20 (Ta’ha) – 39

دَواؤُكَ فيكَ وَما تُبصِرُ

وَدَاؤُكَ مِنكَ وَما تَشعُرُ

و تحسب أَنَّكَ جِرم صَغير

وَ فيكَ اِنطَوى العالَمُ الأَكبَرُ

*

Your sickness is from you but you don't perceive it

Your remedy is within you but you don't sense it

You presume you are a speck

But within you is enfolded the entire Universe

*

Ta maladie provient de toi mais tu ne la perçois pas

Ton remède est en toi mais tu ne le sens pas

Tu présumes que tu n’es qu’un grain

Mais en toi est enveloppé l’Univers entier

الإمام علي بن أبي طالب - Imam Ali Ibn Abi Taleb

After almost two years, this image was exactly like the wonderfully refreshing breeze that you feel after a painfully hard climb.

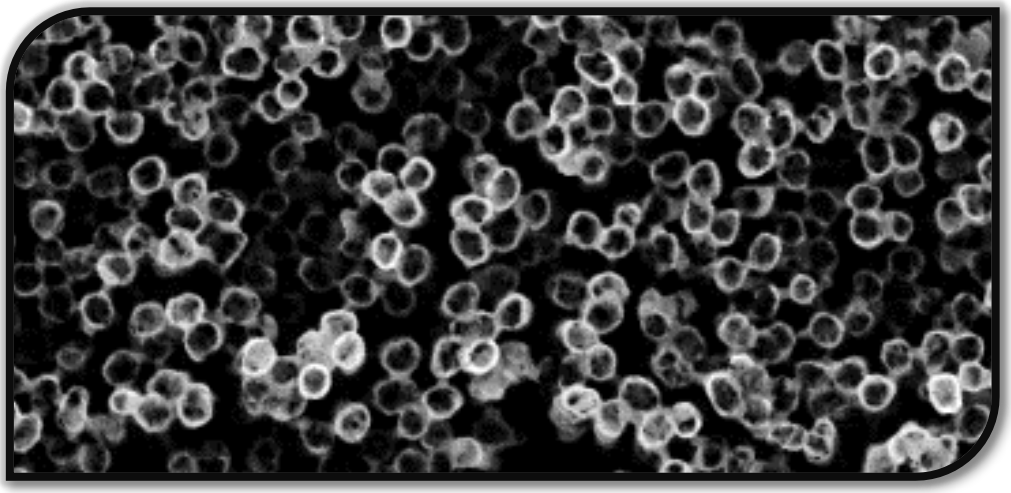

The Heart Nebula, IC 1805, Sharpless 2-190, lies some 7500 light years away from Earth (macrocosm) and its nanometric Platinum doppelganger (microcosm). From a size of $1{,}5.10^{15} km$ *to* $2.10^{-11} km$.

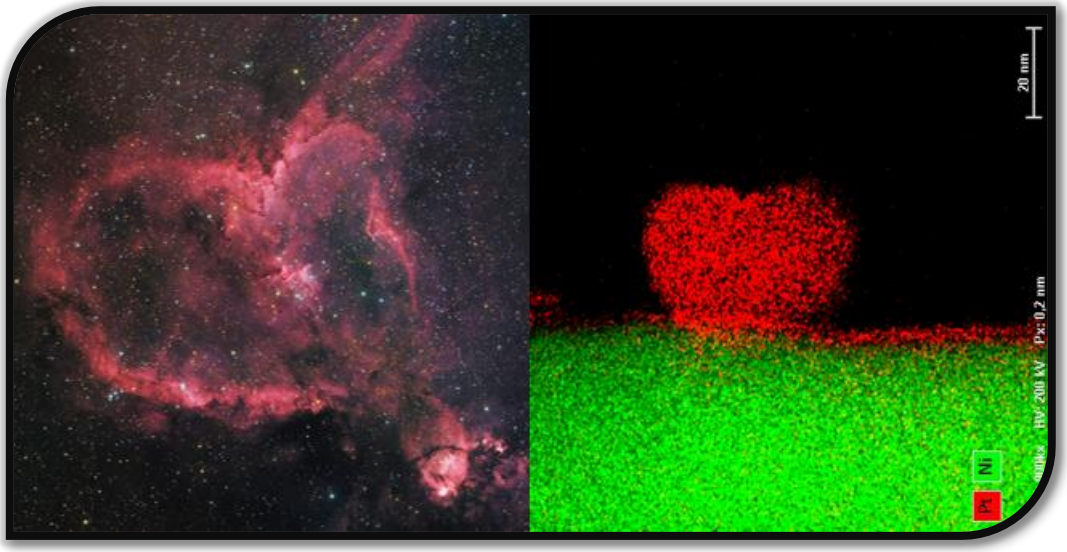

As above, so below. As the universe, so the soul. As without, so within.

Throughout my spiritual journey, an individual and personal quest to consciously deepen my insight about life and reconnect with life's purpose, I have crossed surprisingly enjoyable stages that led me to where I am standing now. Turning Inwards for Your Truth and inner guidance is a key to understanding your surroundings and charting your path. A return to the « self » starts by setting your code of living and ethical guidelines that couldn't be flouted.

Professionally

In a world of higher changing rates, flexibility is mandatory to cope up with evolution. Attaining a higher level of flexibility and creativity is fourfold: Unlearn. Neutralize to emotionlessness. Drop your ego-hood. Learn again. That's the surest way to move things forward. Remember: the only constant thing in life is Change. The firing and wiring in your brain only increase when you go through new and untried paths.

Spiritually

All in scales and in fractal structure, from the subatomic quantum levels to the multiverses, in toroidal flow and ascending spirals of evolution, in a one divine single thought. Outside the physical world, time doesn't exist. Time exists only when there is motion. According to Einstein, "the dividing line between past, present, and future is an illusion". Your only precious asset is ***the here and now****, the precious moving* ***eternal now****. Your life lies on limited heartbeats. Don't waste them on fighting for illusions or vagaries of perception.*

Acknowledgements

This journey would not have been possible without the dedicated support, motivation, presence, insights, wisdom, and help of many individuals.

This part of the manuscript expresses my sincere gratitude and thanks to the fantastic people I have crossed paths with during this journey. Now that my Ph.D. has “Phinishe.D”, I would extend my heartfelt thanks to:

My supervisor, Professor Denis Buttard, thank you for your presence and support, for all the attention you gave to this work. It was a great privilege and honor to work under your guidance.

My co-supervisor, Doctor Arnaud Morin, for your daily support and presence: thank you for your efforts in supervising this work, correcting my slides, and the dozens of my manuscript’s versions. Thanks for the investment of your precious time to make my fuzzy ideas more straightforward. You made me see the Fuel Cell through your eyes. Your motto, « Rien n’est facile dans la pile à combustible » and your professionalism in explaining, helped me gain precious insights into the PEMFC.

Philippe Clément, head of the LCP lab: Thank you for your engaging conversations, good cheer, and vital encouragement.

Sébastien Benoit, head of the STP: Thank you for your kind support.

Without your supervision, I would not have completed this challenging project.

I’d like to show my great thanks to Pr. Marian Chatenet, Dr. Eric Chaînet, Dr. Vincent Vivier, Pr. Elena Savinova, and Pr. Christophe Coutanceau for kindly accepting, examining, and reviewing this manuscript. My thanks also go to Dr. Bryan Pivovar for accepting my invitation as a guest.

My most authentic love to my family for believing in me and believing in my choices for many years. I am, and I will always be grateful for your presence, your unconditional love and every precious moment we spent together. Please excuse my mood shifts. I cannot begin to give you the thanks that you deserve.

To my colleagues: I am very grateful for your important inputs during the past 3.3 years. I am profoundly thankful to have met and worked with all of you. Thanks ever such a lot to:

The clarinetist Jongmin Lee, for our humorous conversations and all your exciting advice.

Pierre Toudret, for every tip you shared with me, from data treatment to CV hacks.

Denis and Thomas, for your morning enthusiasm and the famous “Ooooothmaaan!”. Bon vent! Keep up the “afternoon running” ritual.

Samira for spreading joy all over the lab.

Dominique, for your time, your empathy, your presence, and your detailed answers to all my questions. Thank you for the UV-vis and Fluorescence analysis results, which are parts of this manuscript.

Laure Guetaz, for your keen interest and the beautiful TEM-EDX captures.

Olivier Sicardy, for the insights about XRD measurements.

Eric Delamadeleine, for your help and assistance on the other side of CEA, “IRIG/SiNaPS”.

Florian Chabot, for your daily humor and your endless funny jokes. I would also like to thank you for your assistance in making the home-made Pt/C catalysts.

Florent Vandenberghe, Camille Roiron, Clémence Lafforgue, Clémence Marty, Thi Bich Hue Tran, Lucas, Vlad, Oumaima, Younes, for the great talks and amazing conversations we have shared.

Frédéric Fouda-Onana, for your assistance, your advices, and your help with checking reference electrodes.

Last but definitely not least, I would like to express my special gratitude to my ~~friends~~ lifelong second family, genuine humans, people who do share the state of mind like mine. From the bottom of my heart, I would like to say big thank you to all of you for existing in this “lifetime”: the Artist Khaoula Chatt, Hassan Abbad, Ilias Elalaoui Elbalghiti, Rabie Moubarek Gargaà, Mohamed Ait El Guerrag, Rita Benkirane, Mohamed Bounnit, Houda Jaouzi, Dr. Amal Jaouzi, Marouane Mbarki, Haitam El Khassal, Badr Boutgayout, The singer Chaimae Zehrouni, Dr. Mostafa Oulfarsi, Dr. Younes El Manzani, Dr. Mohamed Darari, Dr. Mohamed Kbibou, Abdellah Aguerzame, Dr. Mohamed Seqqat Dakhma, Dr. Anas Zeroual, Chaïmae Yousfi and Mr. Samir Sebai.

I dedicate this manuscript to all of you, my Dear Ones

- **Latin abbreviations:**

AAO	Anodic Aluminum Oxide
AL	Acid Leaching
AST	Accelerated Stress Test
at. %	Atomic Fraction
CCM	Catalyst-Coated Membrane
Co	Cobalt
Cu	Copper
CV	Cyclic Voltammetry
DBL	Barrier Layer thickness
D_{int}	Interpore Distance
D_p	Pore Diameter
e	Thickness of the alumina membrane
E°	Standard Potential
e^-	Electron
ECSA	Electrochemical Surface Area
EDX	Energy Dispersive X-ray Spectroscopy
EIS	Electrochemical Impedance Spectroscopy
F	Faraday's Constant (96485.33 C/mol)
FC	Fuel Cell
GD	Galvanic Displacement
GDE	Gas Diffusion Electrode
GDL	Gas Diffusion Layer
H_2	Dihydrogen Gas
HAADF	High-Angle Annular Dark-Field imaging
HF	Hydrofluoric Acid
HOR	Hydrogen Oxidation Reaction
H_{UPD}	Hydrogen Underpotential Deposition
Hz	Hertz
i	Electric Current (A)
iR-Free	Ohmic Drop Corrected
J	Current Density A/cm²
J^0	Exchange Current
MA	Mass Activity (A/g_{Pt})
N_2	Nitrogen gas
Ni	Nickel
NIL	Nanoimprint Lithography

NiNWs	Nickel Nanowires
NSTF	Nanostructured Thin Film
NTs	Nanotubes
NWs	Nanowires
O_2	Dioxygen Gas
OCV	Open-Circuit Voltage
ORR	Oxygen Reduction Reaction
P(%)	Porosity
PED	Pulsed Electrodeposition
PEIS	Potentio-Electrochemical Impedance Spectroscopy
PEMFC	Proton Exchange Membrane Fuel Cell
Pt	Platinum
PtNiNTs	Platinum-Nickel Nanotubes
PtNiNWs	Platinum-Nickel Nanowires
Q	Quantity of electric charge in Coulomb (C)
R	Universal Gas Constant (8.314 $J \cdot K^{-1} \cdot mol^{-1}$)
RDE	Rotating Disk Electrode
RH	Relative Humidity
RHE	Reversible Hydrogen Electrode
R_{ohm}	Ohmic Resistance
SA	Specific Activity (A/cm^2_{Pt})
SEM	Scanning Electron Microscopy
Si	Silicon
S_{Pt}	Platinum Surface
TEM	Transmission Electron Microscopy
U	Applied potential (V)
UV-Vis	Ultraviolet-Visible Spectroscopy
wt. %	Weight Fraction
XRD	X-Ray Diffraction Analysis
XRF	X-Ray Fluorescence Spectrometry

- **<u>Greek abbreviations:</u>**

$\boldsymbol{\rho}$	Density (mass per unit of volume)
$\boldsymbol{\eta_{ORR}}$	Cathode kinetic overpotential
$\boldsymbol{\eta_{HOR}}$	Anodic kinetic overpotential
$\boldsymbol{\alpha}$	Charge Transfer Coefficient
$\Delta \boldsymbol{E}$	Electrode overpotential (compared to the OCV)
$\boldsymbol{\Omega}$	Ohm
$\boldsymbol{\omega}$	Sinusoidal Frequency Perturbation

General Introduction

Nowadays, climate change is a bunch of consequences of human mismanagement. Today, as usual, businesses alter our environment and make our planet in severe drought, ice caps, crucial ice sheets have continued to melt, and coral reefs are threatened by human activity due to combined land and ocean temperature increase by greenhouse gas emissions[1]. It is a common question we have to ask frequently: *What role can we play in the climate fight?* We should strive to evolve and give more energy for a sustainable future world, livable and healthier.

Our need for energy goes back centuries ago, or more! Some even attributed the first batteries to more than 2000 years ago, known as *Baghdad* or *Parthian* battery[2], found in Iraq in 1934. Three artifacts were found together: a ceramic pot, a copper tube, and a rod of iron. When combined with a liquid acid, they could have been used to create chemical reactions that produce an electrical charge.

Humans have always wanted to vault ahead of all fossils due to their horrific effects on us. The current energy transition of production plants requiring fewer fossil fuels is driving technological research focused on renewable energies but mainly intermittent energy sources, such as PVs, wind power energy, to name a few. To alleviate the intermittency, we tend to store the surplus energy, whether in batteries or chemical bonds (*e.g.*, hydrogen, hydrocarbons, etc.). While most branches of renewable and decarbonized energies have ascended in this era, the hydrogen vector persistently rises to the top.

In response to the climate challenges, there is a growing interest in hydrogen vector that uses the H_2 gas as an alternative to fossil fuel: producing hydrogen using either natural gas reformation or water electrolysis.

[1] Climate Change: Global Temperature | NOAA Climate.gov https://www.climate.gov/news-features/understanding-climate/climate-change-global-temperature (accessed February 14, 2021).

[2] F. Joseph, Ancient High Tech: The Astonishing Scientific Achievements of Early Civilizations, Simon and Schuster, 2020.

Recent advancements on hydrogen carrier hold the potential to make far-reaching positive impacts on decarbonized energy vectors (depending on how it is produced) to planetary well-being and achieve social betterment for all living systems, enabling human beings, technology, and nature to progress sustainably. One of the key roles of hydrogen as an alternative fuel lies in the use of fuel cells as an electrochemical device for converting chemical reactions into electricity (HOR: Hydrogen Oxidation Reaction at the anode, and ORR: Oxygen –pure or from Air- Reduction Reaction at the cathode), with solely water and heat as safe byproducts. The flow of electrons is carried through an external circuit which allows the production of electrical energy.

Aim of the Ph.D.

In this Ph.D., we aim at developing and controlling a well-ordered Pt-Based tubular nanostructure of the cathode made only with catalyst without carbon support and ionomer. The tubular structure's choice is to expect a decrease of the Pt agglomeration and to enhance stability thanks to a bulkier structure. Also, the tubes' orientation could make the transport of reactants and products easier [1]. Among the various transition metals, alloying platinum with nickel has shown exceptional oxygen reduction reaction (ORR) mass activities and promising durability in rotating disk electrode (RDE) studies [2][3][4][5]. Previous studies have shed light on the dealloyed PtNi core-shell nanoparticles and hollow Pt-alloy nanoparticles and have shown interesting electrocatalytic properties for the ORR.

Accordingly, combining the tubular structure and the higher activity of PtNi catalyst has the potential for overcoming the limitations of conventional Pt/C electrodes. Some research groups [2] dedicated their studies to the synthesis of disoriented PtNi nanotubes by galvanic displacement process [8] and have tested their electrochemical performances using rotating disk electrode (RDE). Only *C. Fan* and co-workers [8] have synthesized and tested PtNi nanotubes' activity in a complete MEA in a direct-methanol fuel cell (DMFC).

During this thesis work, the PtNi nanowires and nanotubes, templated from nickel nanowires grown inside a sacrificial mold of porous anodic aluminum template, are synthesized by the galvanic displacement process; an electrochemical process that involves the oxidation of the transition metal (nickel) by the ions of a platinum salt (hexachloroplatinate acid H_2PtCl_6, potassium hexachloroplatinate K_2PtCl_6 or potassium tetrachloroplatinate K_2PtCl_4) at different concentrations of the Hydrochloric acid (HCl).

Later, using the hot-pressing process of Nafion® membrane on the synthesized nanotubes led to their integration in a complete Membrane Electrode Assembly in order to understand transport limitations in the Catalyst Layer as shown in *figure I-1* below.

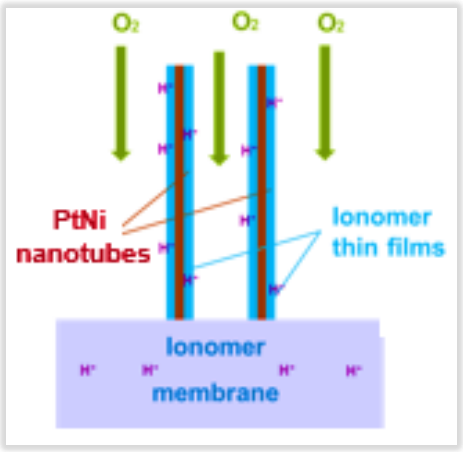

Figure I-1: Scheme of the cross-section of an oriented carbon-free PtNi nanotube transferred onto the Nafion® membrane.

The fabrication process of PtNi nanotubes is held by a succession of four steps, as displayed in *figure I-2* below: **i/** the first step consists of elaborating the porous anodic aluminum template (PAAT) as a sacrificial mold; **ii/** The second step includes the confined growth of nickel nanowires inside the AAO template by the pulsed electrodeposition (PED) process; **iii/** This step is followed by the galvanic displacement mechanism; **vi/** Finally, the last step will lead to transferring PtNi nanotubes/nanowires to a Nafion® membrane by a hot-pressing process to test the electrochemical performance in a complete MEA.

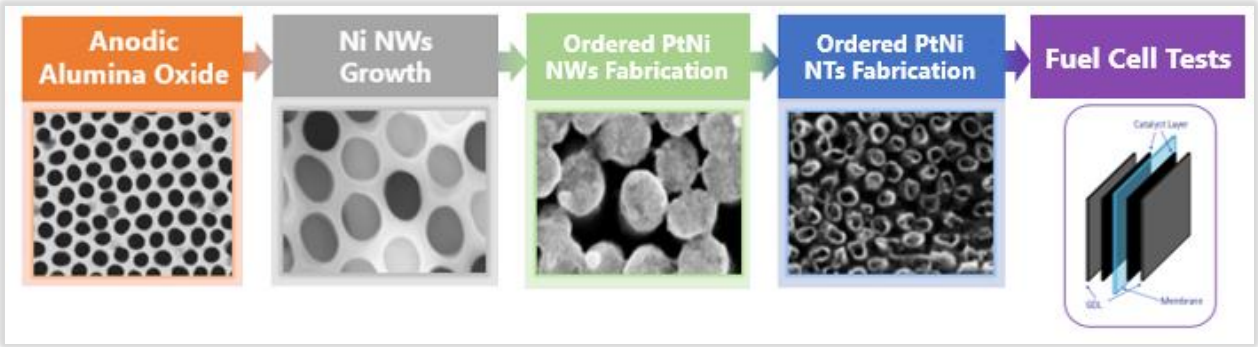

Figure I-2: Methodology of the elaboration process of PtNi nanotubes.

It should be noted that the aim of the thesis is not to reduce the total cost of the complex and expensive process but to demonstrate if the aligned PtNi nanotubes concept would allow the improvement of the performance and durability of the catalyst layer, also to improve the understanding of transport limitations. Consequently, the goal consists of

elaborating and engineering a new carbon-free structure of electrodes based on PtNi active electrocatalysts.

We target in this thesis to control and rationally design architecture of a carbon-free cathode for the PEMFC in order to improve the ORR and reduce Pt loading. Also, to increase durability of the cathode and understanding the transport limitations in the catalyst

The **first chapter** of the manuscript heeds to today's challenges related to renewable energies and hydrogen as a key to a clean, economical, and sustainable energy system. We will shed light upon the PEMFC technology as a viable, clean energy converter and revealing its main limitations.

In the **second chapter**, we will advocate a general overview of the theory behind porous anodic aluminum oxide (AAO) formation. Then, we will shed light on the fabrication process and the usefulness of the AAO template as a flexible sacrificial template for the growth of nickel nanowires.

The **third chapter** addresses a general description of the electrodeposition process followed by an experimental section of the nickel nanowires' growth inside a nanoporous alumina template, aiming to understand the growth phenomena related to it. The third part is dedicated to a non-exhaustive state-of-the-art on PtNi electrocatalysts. It will thenceforth underline the processes involved in the fabrication of PtNiNWs and PtNiNTs via the galvanic displacement process. A detailed fabrication process was held to gain insights into the effect of hydrochloric acid addition, thermal treatment, and acid leaching in order to elaborate reproducible PtNi nanowires and PtNi nanotubes.

The **fourth and last chapter** will first highlight the experimental protocol used to test a conventional Pt/C electrode at low Pt-loading. Secondly, it will hover over the transfer of the as-made nanowires and nanotubes by hot-pressing into a Nafion® membrane and their functioning in a real cell made of a conventional Pt/C anode the carbon-free PtNiNWs/PtNiNTs at the cathode side.

Chapter 1

Hydrogen and Fuel Cells: A Reliable, Safe and Clean Energy Alternative

"The energy of the mind is the essence of life."

-Aristotle

Table of Content

Energy has always been the fulcrum of civilizations and their undeniable pillar of development. A wide range of energy sources are already known and have been used until today, such as fossil fuels, natural gas, to name a few. One of the primary sources of energies discovered by the modern human was coal (*ca.* 3500 years ago) until 1712 when *Tomas Newcoman* had found an alternative of the use of coal to power steam engines. This discovery was the tide of a new industrial era. In 2018, coal power generation was still dominant by far, reaching 38 percent of global electricity generated[3].

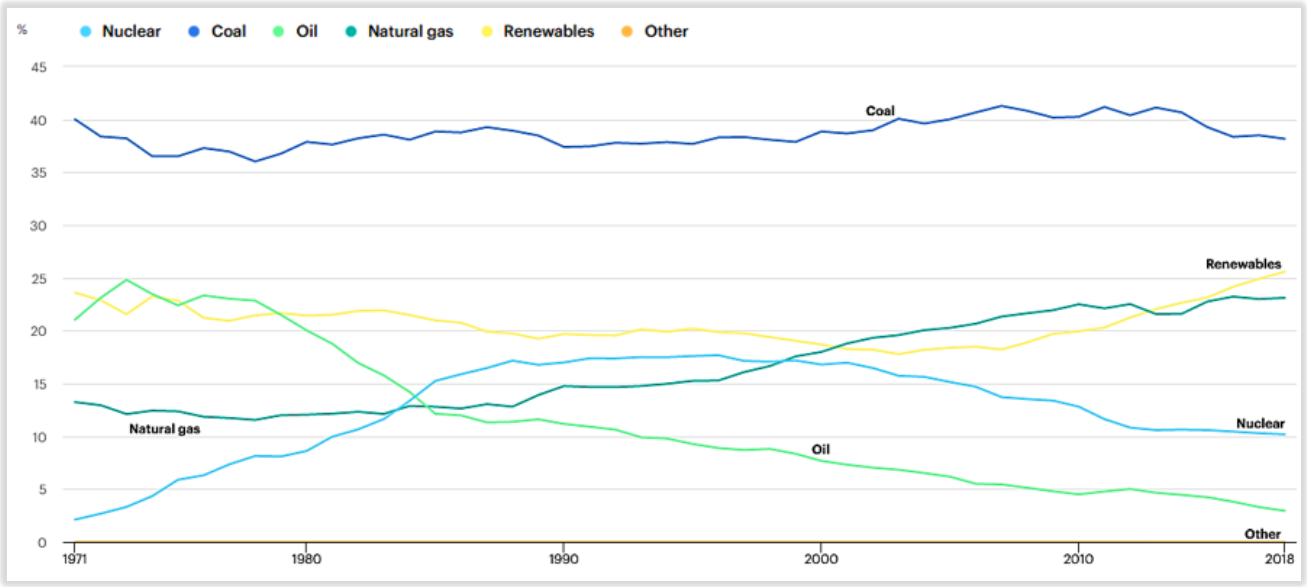

Figure I-3: World electricity generation mix by fuel from 1971 to 2018. Reprinted from IEA World Energy Balances.

For over 300 years, the significant increase in population led to a sharp increase in energy consumption, mainly from carbonized fossil sources.

In order to build a sustainable future society, we have to make great efforts to build sustainable, decarbonized, and renewable sources of energy. A systematic framework depicted in *figure I-4* below shows possible sustainable pathways for the production of highly demanded fuels and chemicals, including hydrogen, hydrocarbons, oxygenates, and ammonia, by either replacing or working in concert with conventional energy production [9].

[3] World Energy Balances – Analysis, IEA., https://www.iea.org/reports/world-energy-balances-overview (accessed February 16, 2021).

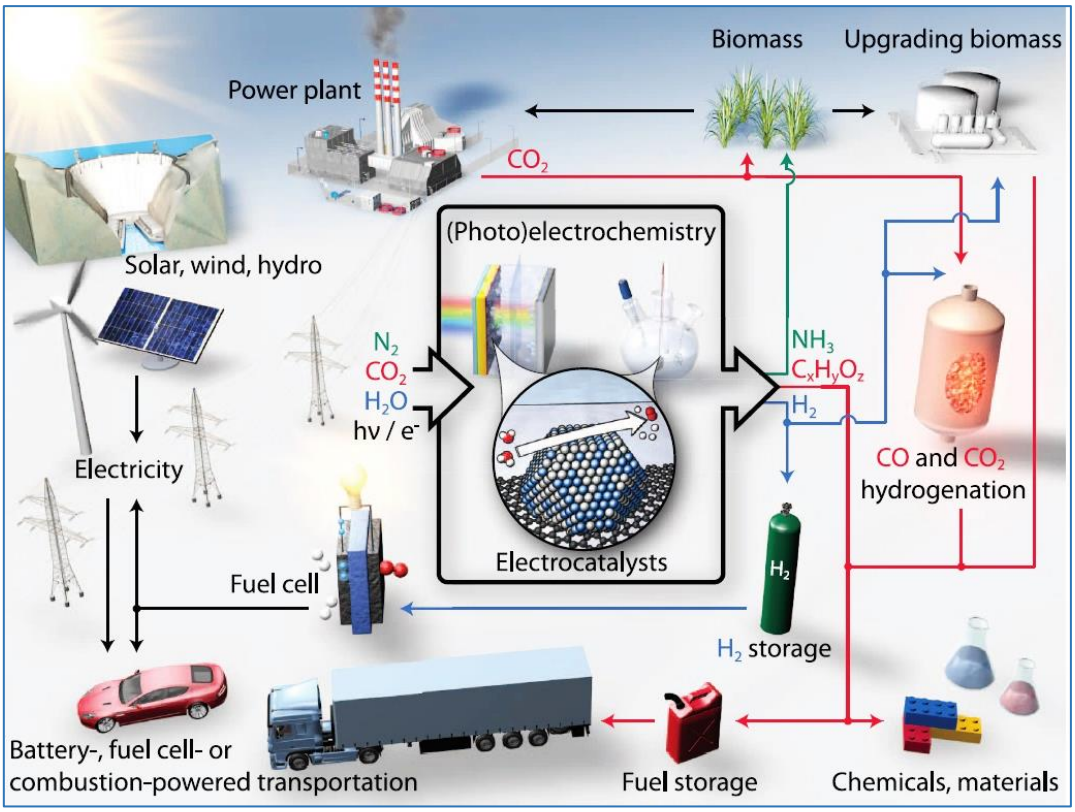

Figure I-4: Schematic of a sustainable energy landscape based on electrocatalysis. Reprinted from reference [9].

I. Nowadays position in the "Energy Challenge"

Energy is the lifeblood of many aspects of our world: transportation, food, and heating. Relying mainly on earth's resources continuously and relentlessly, our excessive consumption of these resources has generated deleterious and irreversible consequences against humans, flora, and fauna. The latest International Energy Outlook 2020 (IEO2020) [6] by the U.S. Energy Information Administration projects world energy consumption to grow by 28% between 2015 and 2040. Most of this growth is expected to come from countries that are not part of the Organization for Economic Cooperation and Development (OECD) and, particularly, from countries where strong economic growth is driving demand, especially in Asia.

More than 60% of the world's total increase in energy consumption from 2015 to 2040 is accounted for by non-OECD Asia (including China and India).

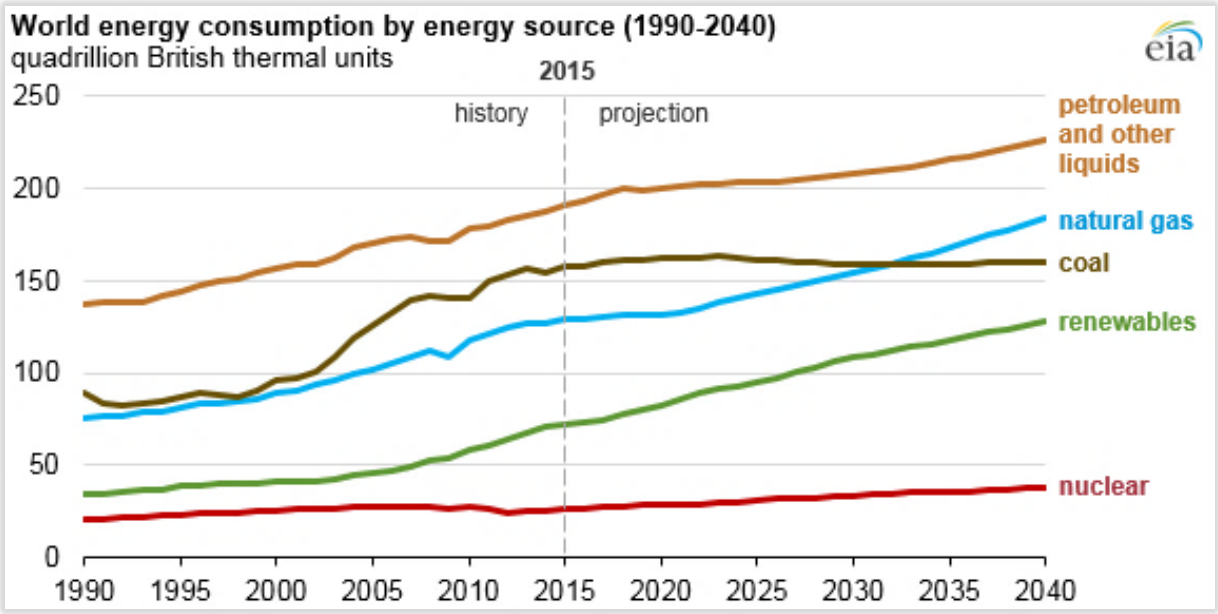

Figure I-5: World energy consumption by source. It is projected to rise to 736 quadrillion BTU (quads) in 2040 from 575 quads in 2015, an increase of 28%, according to the latest International Energy Outlook 2017 (IEO2017) from the US Energy Information Administration.

This unsustainable energy productions lead to critical challenges: climate change and global warming caused by anthropogenic greenhouse gases emission. The combustion of fossil fuels contributes around two-thirds of global greenhouse gas (GHG) emissions and the bulk of CO_2 emissions (see *figure I-6*), so the energy sector must be at the front line of efforts to tackle climate change. Much to our interest, last year, carbon emissions dropped a record 7% as COVID19 pandemic lockdowns halted whole sectors and towns [7].

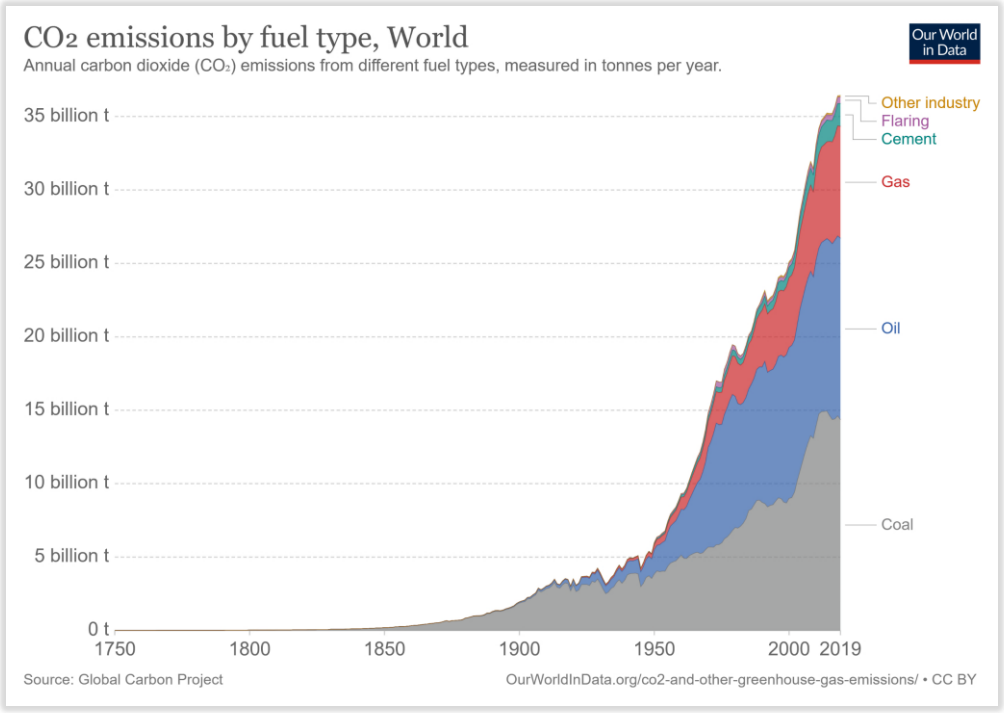

Figure I-6: The amount of CO_2 emitted each year from various fuel sources, measured in tonnes per year. Emissions from fossil fuels continue to increase as we burn more each year for energy[4].

Moreover, instead of CO_2, the primary greenhouse gases emitted by human activities on a global scale are depicted in *figure I-7* below:

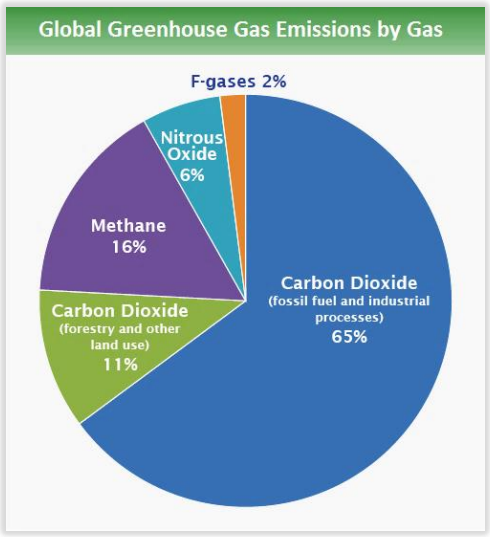

Figure I-7: Chart showing the Global Emissions by Gas. F-gases refers to Fluorinated gases: Industrial processes, refrigeration, and the use of a variety of consumer products contribute to emissions of F-gases, which include hydrofluorocarbons (HFCs), perfluorocarbons (PFCs), and sulphur hexafluoride (SF_6)[5].

[4] H. Ritchie, M. Roser, Energy, Our World in Data. (2014). https://ourworldindata.org/energy (accessed February 16, 2021).

[5] O. US EPA, Global Greenhouse Gas Emissions Data, US EPA. (2016). https://www.epa.gov/ghgemissions/global-greenhouse-gas-emissions-data (accessed February 16, 2021).

II.1. Energy supply: A concoction of diverse sources

In 2018, according to the IEA's annual statistical report (see *figure I-8*), the global total energy supply was approximately 14.282 Mtoe (megatonnes of oil equivalent), of which only 13.5% was derived from renewable energy sources, including hydro, biofuels, renewable municipal waste, solar PV, the solar thermal, wind, and geothermal.

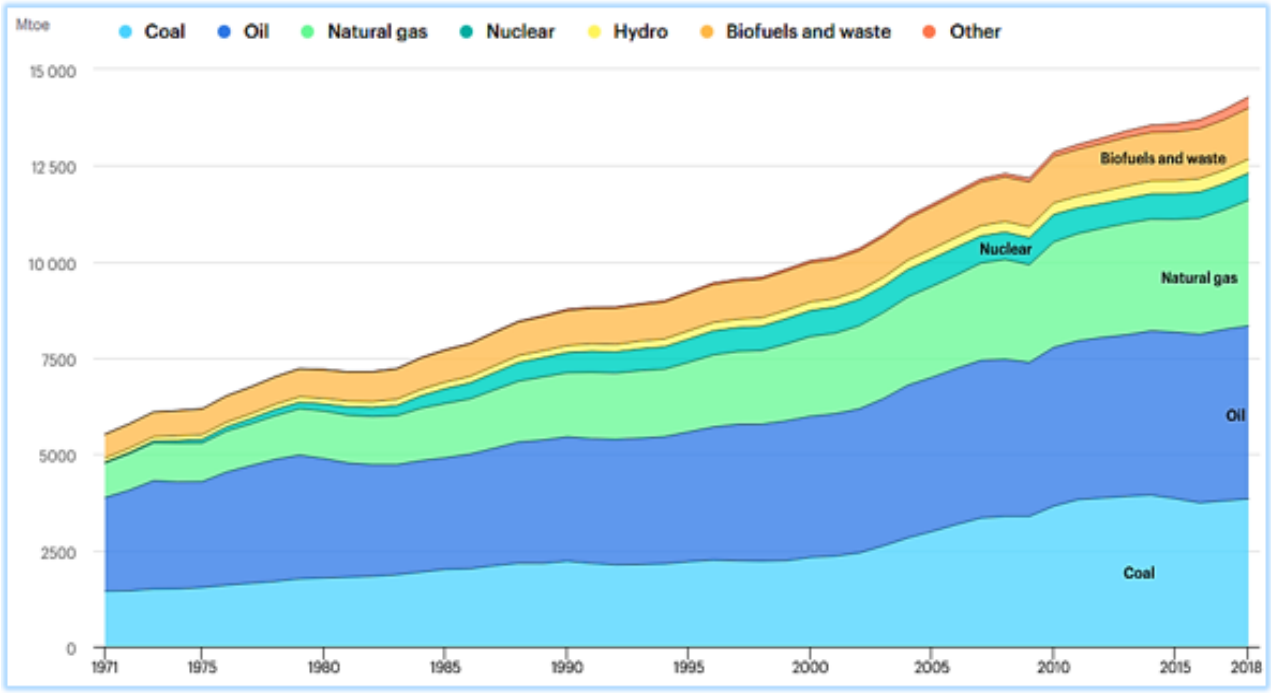

Figure I-8: World total energy supply by source from 1971 to 2018 in Mtoe. All Rights Reserved to IEA.

Due to its widespread use in developing countries for heating and cooking, solid biofuels/ charcoal is the largest renewable energy source by far, and the second largest source is hydro. Liquid biofuels, wind, geothermal, solar, biogases, renewable municipal waste, and tidal make up the rest of the renewable energy supply. It was mentioned that since 1990, renewable energy sources have grown at an average annual rate of 2.0%, which is slightly higher than the growth rate of the world's total energy supply of almost 1.8%. For solar PV and wind power, which developed at average annual rates of 36.5% and 23%, respectively, growth was remarkably high. On the flip side, biogases had the third highest growth rate at 11.5%, followed by solar thermal (10.9%) and liquid biofuels (9.7%), as depicted in *figure I-9* below [10].

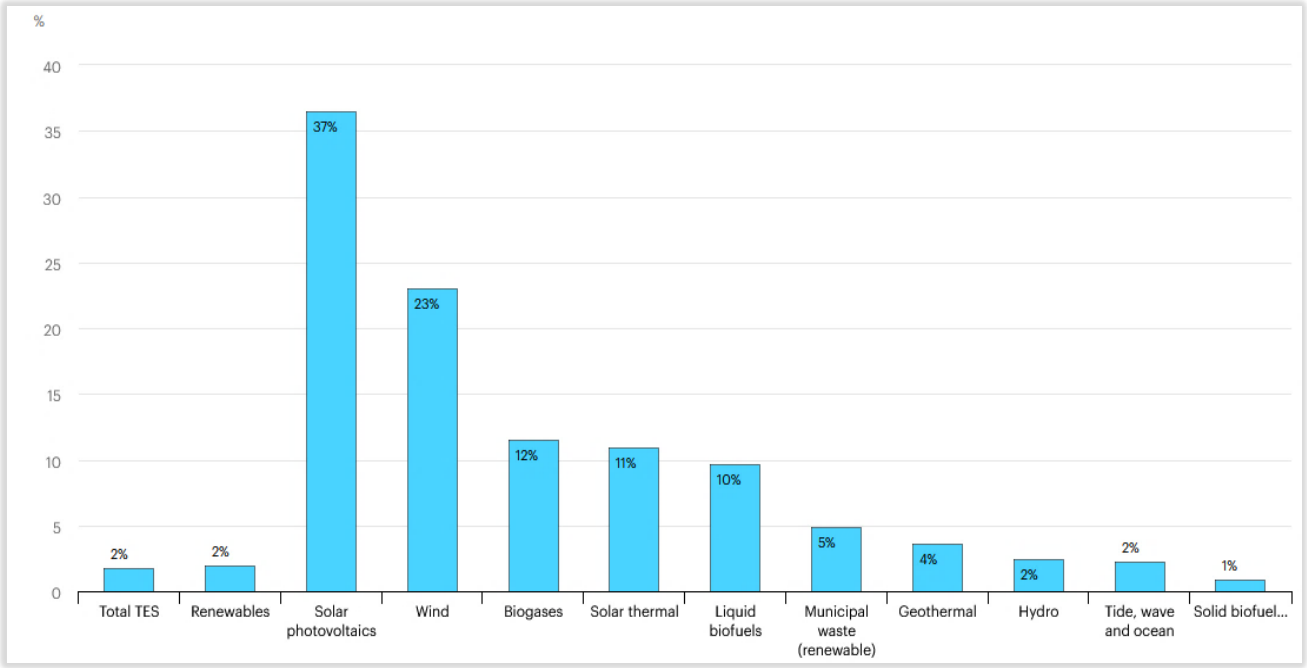

Figure I-9: Average annual growth rates of world renewables supply from 1990 to 2018 as cited in the IEA annual report.

II.2. Humankind's life: Is it really at stake?

A recent new study published in *Environment Research* journal has reported that fossil fuel pollution caused one in five deaths globally (more than eight million premature deaths in 2018) [12]. Lately, another research from the European Society of Cardiology assessed the impact of air pollution on life expectancy, enhancing the risk of cardiovascular and respiratory diseases [13].

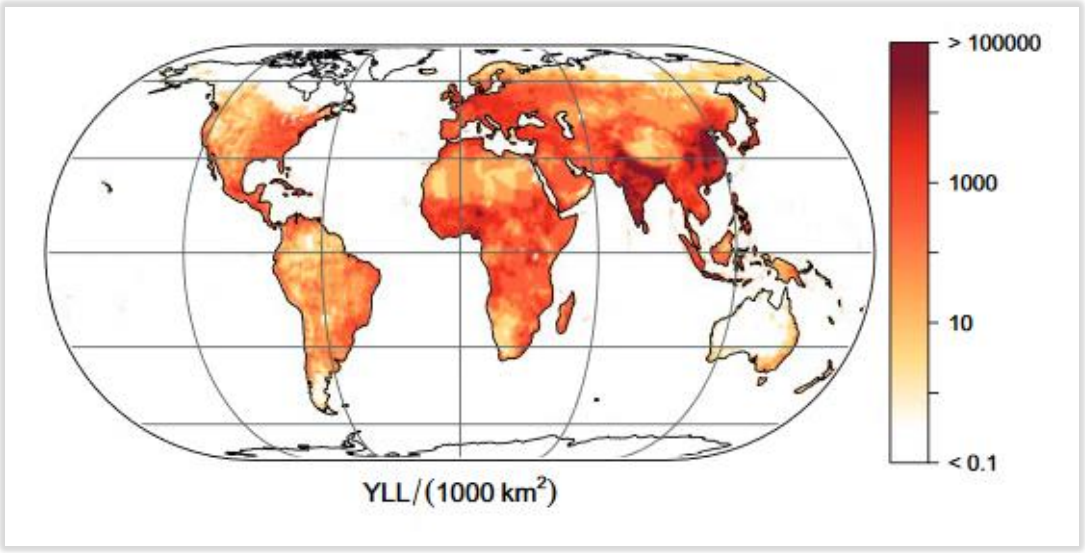

Figure I-10: Annual years of life lost from air pollution (units per 1000 km^2). The global total is 233 (221–250) million per year. YLL refers to years of life lost.

II.3. Limiting global warming to 1.5˚C: The Bold Challenge

Since the Industrial Revolution, most human activities have had a high impact on CO_2 drastic increase in the atmosphere. International decisions and policymakers urged to gather alongside scientists to leverage the effect of greenhouse gases emission on climate change, for instance, the Intergovernmental Panel on Climate Change (IPCC), the International Energy Agency (IEA), the International Renewable Energy Agency (IRENA) and Conference of the Parties (COP) experts.

As stated by the recent NASA's GISTEMP[6] (Goddard Institute Surface Temperature) analysis, the earth's global average surface temperature in 2020 tied with 2016 as the warmest year on record. As long as the long-term warming trend of the planet continues due to terrific GHG emissions, the average temperature of the Earth has increased more than 1.2°C since the 1880s.

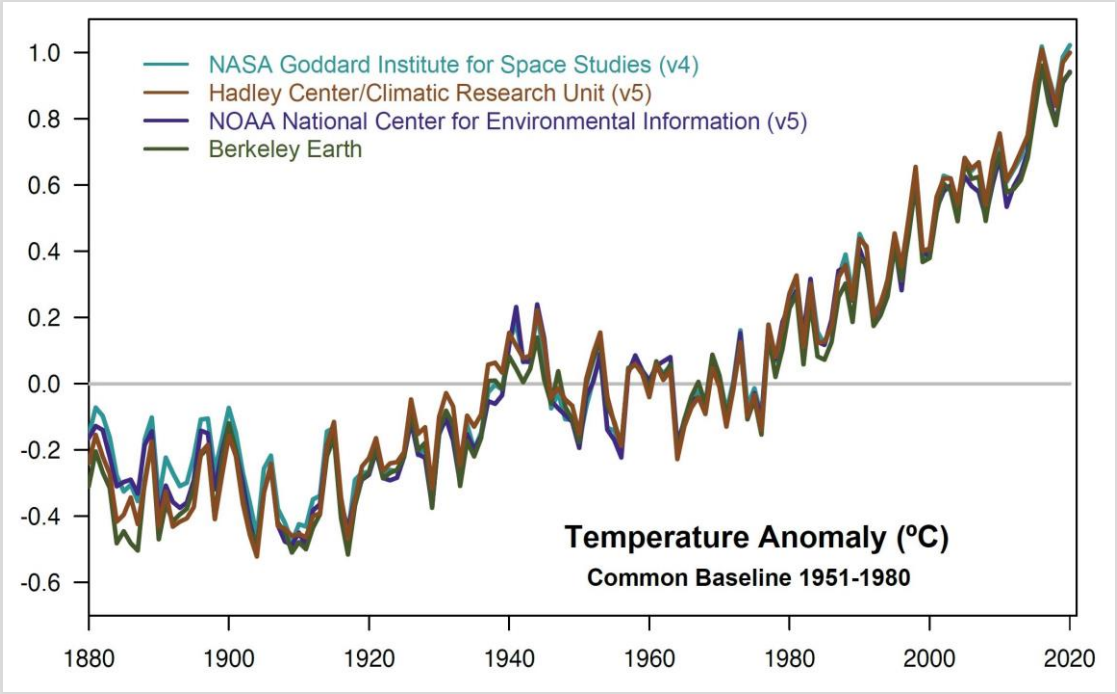

Figure I-11: Schematic plot showing yearly temperature anomalies from 1880 to 2019, with respect to the 1951-1980 mean, as recorded by NASA, NOAA, the Berkeley Earth research group, and the Met Office Hadley Centre (UK). Though there are minor variations from year to year, all five temperature records show peaks and valleys in sync with each other. All show rapid warming in the past few decades, and all show the past decade has been the warmest. (Credits: NASA GISS/Gavin Schmidt).

[6] NASA GISS: NASA News & Feature Releases: 2020 Tied for Warmest Year on Record, NASA Analysis Shows. https://www.giss.nasa.gov/research/news/20210114/ (accessed February 13, 2021). doi:10.1093/cvr/cvaa025

What does the most recent climate change science tell us, according to the annual report from IPCC (2018)?

> "In late 2018, the Intergovernmental Panel on Climate Change (IPCC) published a special report on the impacts of global warming of 1.5 °C above preindustrial levels compared with an increase of 2°C, based on the assessment of the latest available scientific, technical and socio-economic literature (IPCC, 2018). The report finds, with a high degree of confidence, that human activity has already caused 0.8 to 1.2°C of warming, and that global warming is likely to reach 1.5°C between 2030 and 2052 if it continues to increase at the current rate. It warns that many of the physical impacts of climate change may escalate in a non-linear fashion as the global temperature rises: in other words, the effects of 2°C of warming are likely to be far worse than those of 1.5°C. It also underlines the urgency of the need for action: combined national efforts to reduce emissions so far fall far short "of what is needed to be on track to limit global warming to 2°C, let alone 1.5°C."

Henceforth, the undesired rising temperature in the earth's atmosphere is causing a combination of eerie and hellish phenomena such as longer periods of drought in some regions, increase in the intensity of tropical storms/hurricanes, shrinking glaciers, sea-level rise, more intense heat waves, shifts in plant and animal habitats, more acidic oceans, changes and unstable precipitation patterns, higher wildlife extinction rates, farming and fishing communities are at socio-economical dangers and coral reef ecosystems threats.

Figure I-12: The Great Barrier Reef has suffered damage from both nature and humanity (Image extracted from www.marinescoop.com).

Midst all the climate change chaos, there is still a natural hope: *Phytoplankton* [7]. Most of the earth's oxygen comes from tiny ocean plants called phytoplankton, which, like land plants, have *chlorophyll* to capture sunlight. They use photosynthesis to turn it into chemical energy. They consume carbon dioxide and release oxygen. All phytoplankton photosynthesize, but some get additional energy by consuming other organisms.

Figure I-13: Phytoplankton – the foundation of the oceanic food chain. Scientists estimate that phytoplankton contributes between 50 to 85 percent of the oxygen in Earth's atmosphere. (Collage adapted from drawings and micrographs by Sally Bensusen, NASA EOS Project Science Office).

II.4. Energy transition: Toward a Clean & Green sustainable future

Sifting through the global warming issue to build up insofar a sustainable future, societies are veering toward new energy sources (decarbonized and/or renewable) for the sake of cutting carbon emissions as much as possible. For such a purpose, many international initiatives were held three decades ago: The United Nations Framework Convention on Climate Change (UNFCCC) in 1992, followed by the Kyoto Protocol in 1997, and then COP21 held in Paris 2015, in which 195 Parties agreed upon the increase in using renewable energy sources and limiting the global warming to less than 2°C by 2100. Nevertheless, most energy source alternatives depend mainly on metrological shifts (wind, sun, hydropower et cetera). Such intermittent sources need to be coupled with energy-storage devices/systems in order to save the harnessed energy (whether in chemical covalent bonds, lithium-ion batteries, supercapacitors, to name a few) depending on the application field (*i.e.*, short/long-term storage, high/low-power densities).

[7] What are Phytoplankton?, (2010). https://earthobservatory.nasa.gov/features/Phytoplankton (accessed February 13, 2021).

II. Dihydrogen: Viable alternative toward an affordable, sustainable and reliable energy supply

Pollution from fossil fuels remains the crux of concerns of humans recently. Energy accounts for two-thirds of total greenhouse gas, so efforts to reduce emissions and mitigate climate change must include the energy sector [14]. Aiming to reduce greenhouse gases, renewable and decarbonized energies maintain strong evolution momentum, including the Hydrogen vector. Hydrogen, however, is an attractive energy carrier that can produce clean electricity via fuel cells, where the hydrogen oxidation and oxygen reduction reactions convert chemical energy into electrical energy.

It is a versatile energy vector that can help address a variety of critical energy challenges. Hydrogen can be produced from almost all energy resources. However, the current use of hydrogen in oil refining and chemical production is mainly covered by hydrogen from fossil fuels, with significant CO_2 emissions associated.

II.1 Hydrogen Utility

Hydrogen, derived from the Greek *hydro* and *genes*, means water forming[8]. It is known as the lightest element of the Mendeleev table. One of its significant properties is its calorific value (*i.e.*, the heat produced by the complete combustion of a specified quantity of fuel) that reads 120-140 MJ/kg. As a matter of comparison, the table below expresses various widely used fuels and their corresponding heat value[9].

Fuels	Heat value (MJ/kg)
Methane (CH_4)	50-55 MJ/kg
Petrol / Gasoline	44-46 MJ/kg
Diesel fuel	42-46 MJ/kg
Natural gas	42-55 MJ/kg

Table I-1: A variety of widely used fuels and their related heat in MJ/kg.

[8] Hydrogen - Element information, properties and uses | Periodic Table. https://www.rsc.org/periodic-table/element/1/hydrogen (accessed February 11, 2021).

[9] World Nuclear Association - World Nuclear Association. https://www.world-nuclear.org/ (accessed February 11, 2021).

Hydrogen has the ability to serve as a clean energy intermediate, as illustrated in *figure I-14* below. Its production, however, usually involves fossil fuels. It could be produced from diverse sources, including natural gas, coal, water, and electricity (electrolysis). Such properties lead to the use of hydrogen as a promising energy carrier. Other approaches include hydrogen production via photoelectrochemical cells or solar thermochemical systems. Today, hydrogen's primary demand is as a chemical feedstock in petroleum refining and ammonia production [16].

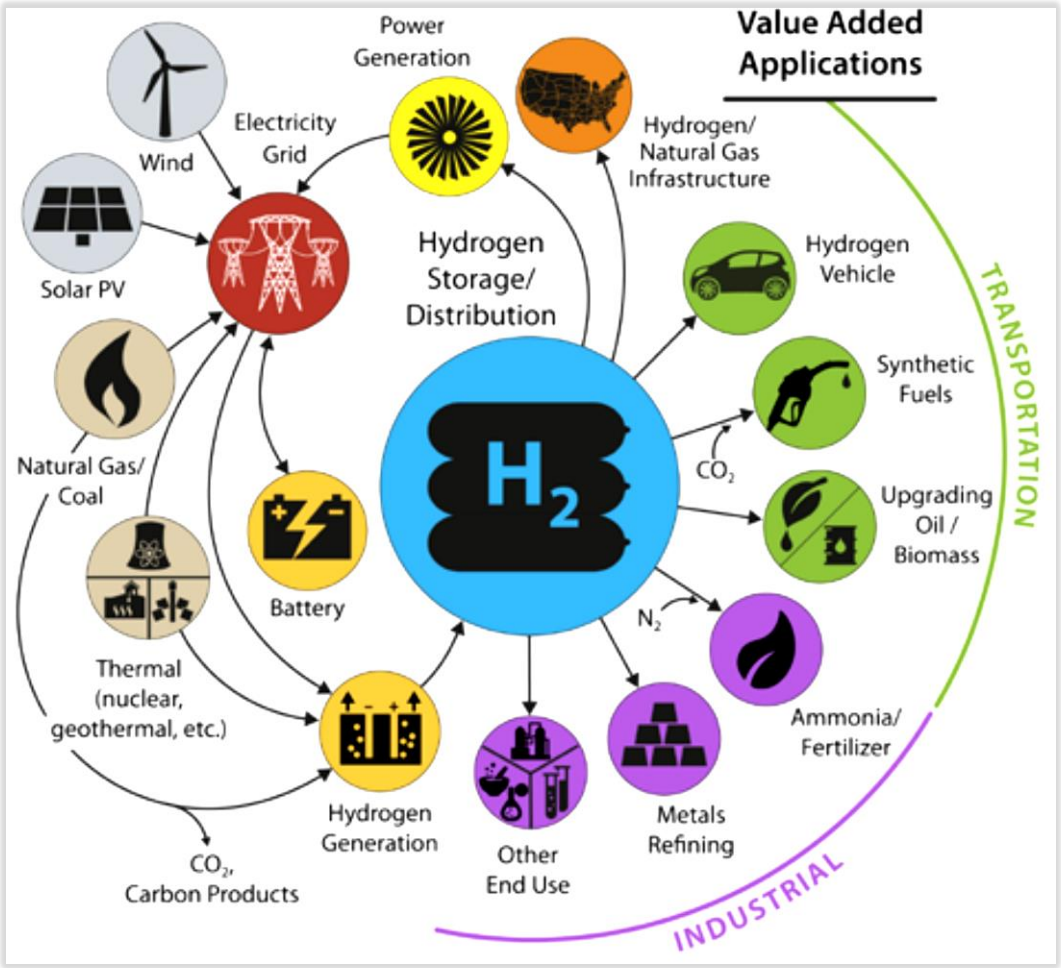

Figure I-14: Illustrative schematic of H_2@Scale energy system. Reprinted from reference [16].

II.2 Hydrogen production and major application areas

Although the expansion of the FC electric vehicles market (mostly in the USA, China, Japan, and Korea), and the increase in electrolysis capacity of H_2 production, low-carbon production capacity remained relatively constant. As evidenced in the IEA's annual report of hydrogen, more efforts are needed to **i/** scale-up to reduce costs; **ii/** replace

high-carbon with low-carbon hydrogen in current applications; **iii/** and expand hydrogen use to new applications.

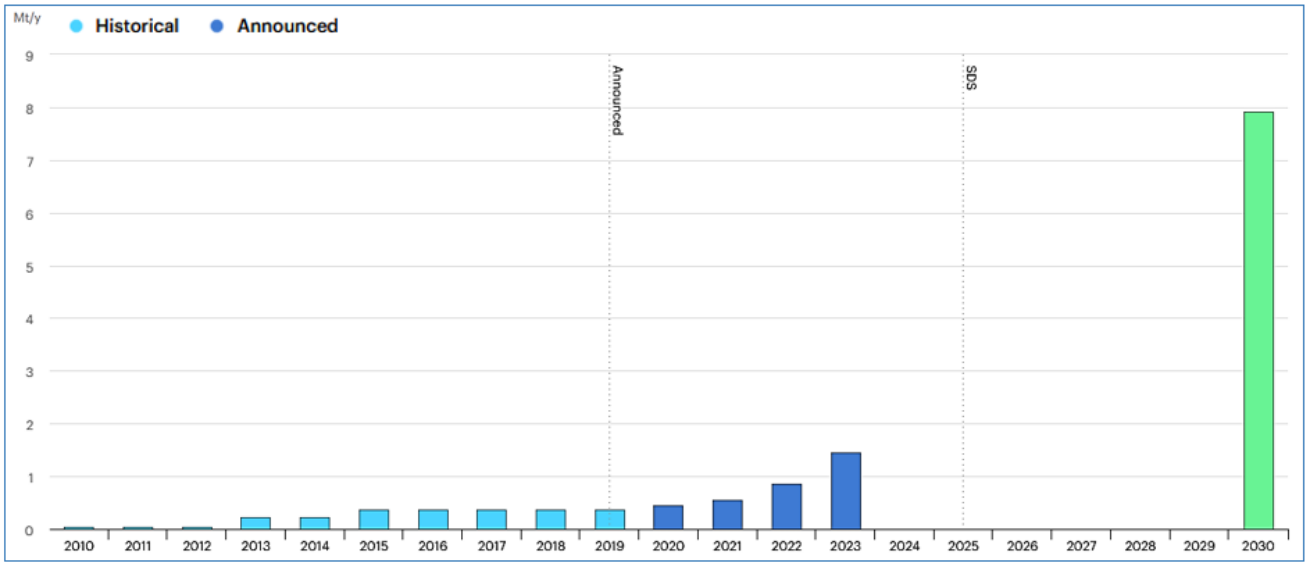

Figure I-15: Low-carbon hydrogen production, 2010-2030, historical, announced, and in the Sustainable Development Scenario (SDC), 2030. Extracted from reference [15].

However, the global demand for pure hydrogen has increased sharply in the past four decades. An estimation of the yearly demand for pure hydrogen is around 70 Mt, mainly for oil refining and chemical production. This hydrogen currently is produced from natural gas and coal, and associated CO_2 emissions are significant [15].

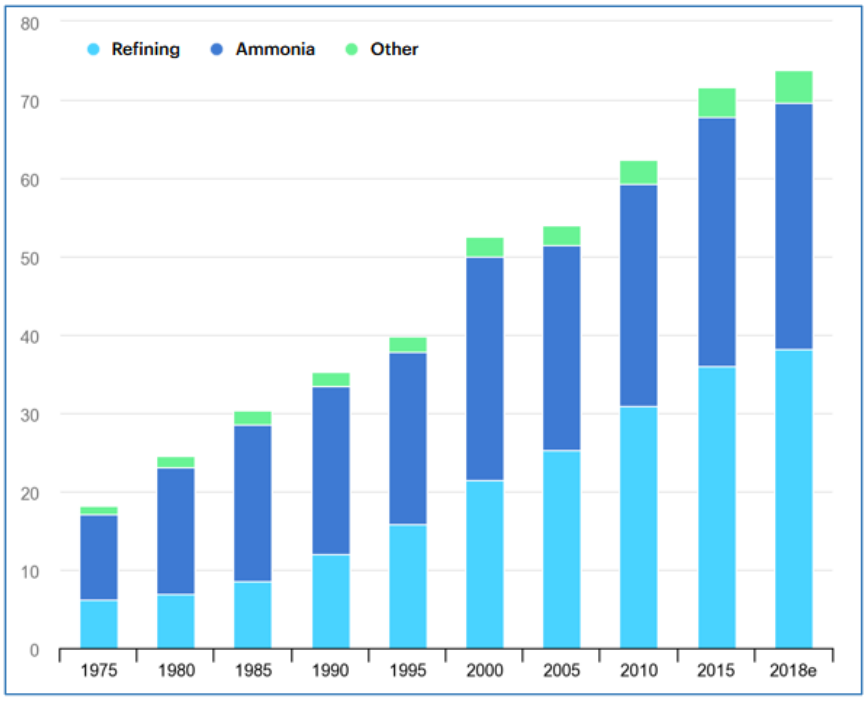

Figure I-16: Global demand for pure hydrogen from 1975 to 2018 as reprinted from IEA annual report.

Thus, developing low-carbon hydrogen production routes is critical for hydrogen to aid in clean energy transitions. The three main low-carbon production routes involve:

- Coupling conventional technologies with the Carbon Capture, Utilization, and Storage (CCUS) emissions reduction technologies.
- The solar-powered thermochemical water splitting using water and solar thermal energy as the only feedstock by concentrating solar radiations on a metallic salt (Cadmium oxide, for instance). In general, a simple two-step thermochemical water-splitting reaction to produce hydrogen requires very high-temperature heat to release oxygen for endothermic metal oxide reduction and a lower temperature exothermic reaction of water with the metal, increasing the metal's oxidation state and releasing hydrogen [17].
- Electrolyzers enable clean hydrogen production from low-carbon electricity and water (*i.e.*, the water-splitting reaction, which consists of the hydrogen and oxygen evolution half-reactions). Only 4% of the global hydrogen production, labeled the "green hydrogen", is produced by the water electrolysis process, making it possible to transform electricity without any CO_2 emission into high purity hydrogen (and oxygen). In recent years, the number of projects and installed electrolyzer capacity have expanded considerably, from less than 1 MW in 2010 to more than 25 MW in 2019.

Additionally, on top of using hydrogen in the transportation and ammonia industry, domestic and industrial heating are sectors that could raise low-carbon hydrogen demand for decarbonization purposes by injecting hydrogen into the gas grid. For instance, the GRHYD project in France, which began blending 6% hydrogen into the natural gas grid in 2018, already reached 20% on a volumetric basis in 2019, demonstrating the technical feasibility of this approach for domestic use [15].

On the other hand, hydrogen and fuel cell technologies have great potential to provide low-carbon electricity generation electrochemically. Nowadays, attention was drawn to using fuel cells in transportation (both light-duty and heavy-duty sectors). The fuel cell electric vehicle market is expected to be worth $42 billion by 2026, with major players

including Toyota, Hyundai, Honda, Audi, Daimler, Volvo, BMW, General Motors, and MAN[10].

Finally, fuel cells have been a current research subject for applications for EVs. They work similarly to batteries but do not have to be recharged. They will run indefinitely (until they die because of degradation) as long as they are supplied by hydrogen (the fuel) and oxygen (the oxidizer): this is the following paragraph's subject. This Ph.D. thesis aims to address some issues related to this system.

II.3 Hydrogen storage and distribution

A major benefit of hydrogen is that it can be generated from (surplus) renewable energy, and it can also be stored for long periods in large quantities, unlike electricity. Physical storage techniques based on either compression or cooling or a combination of the two are the most important hydrogen storage methods that have been tried and tested over long periods of time (hybrid storage). In addition, a significant range of other emerging technologies is being explored or investigated for hydrogen storage[11].

[10] A.M. Research, Hydrogen Fuel Cell Vehicle Market To Garner $42.03 Billion by 2026: AMR, GlobeNewswire News Room. (2020). http://www.globenewswire.com/news-release/2020/02/21/1988377/0/en/Hydrogen-Fuel-Cell-Vehicle-Market-To-Garner-42-03-Billion-by-2026-AMR.html (accessed February 11, 2021).

[11] Hydrogen Storage | Hydrogen, (n.d.). https://hydrogeneurope.eu/hydrogen-storage (accessed February 16, 2021).

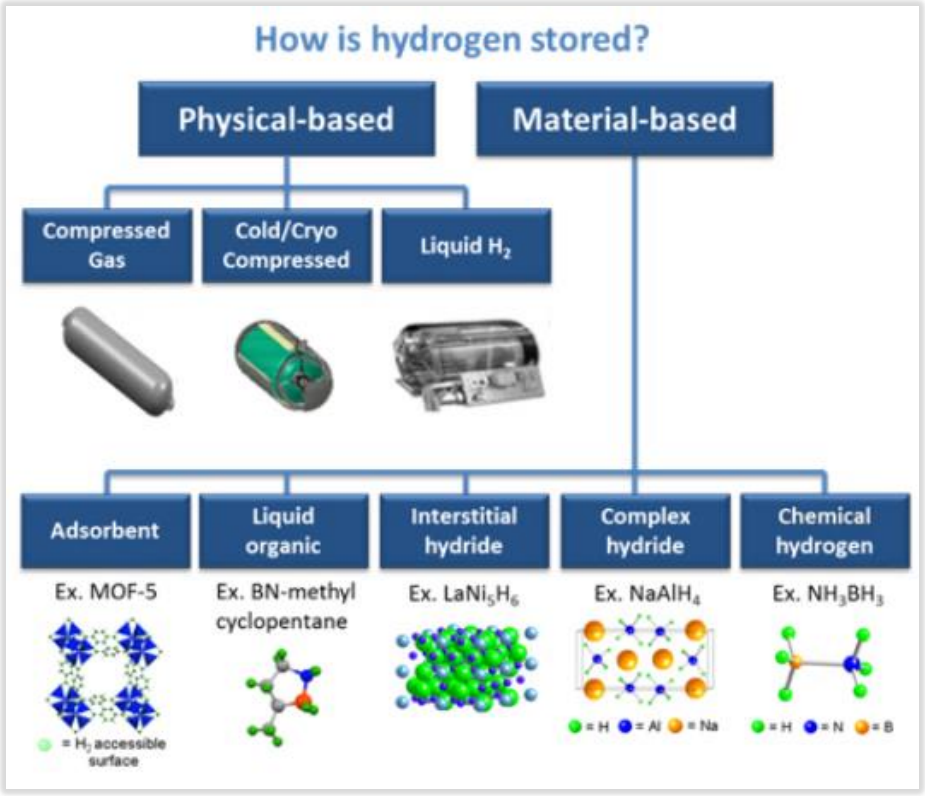

Figure I-17: Schematic chart of the common techniques of Hydrogen storage. Copyright Hydrogen Europe[12].

Contrastingly, hydrogen can be transported in various formats and is easy to transport over long distances. The most popular means of hydrogen transport, covering the needs of the various hydrogen markets, are **i/** Compressed gas cylinders or cryogenic liquid tankers; **ii/** Pipelines; and **iii/** Blending it into natural gas pipeline networks[13]. There is currently more than 4,500 km of hydrogen pipelines worldwide (2016), the vast majority of which are owned by hydrogen producers in general. The longest pipelines are in service in the USA, followed by Belgium and Germany.

[12] Hydrogen Storage | Hydrogen, (n.d.). https://hydrogeneurope.eu/hydrogen-storage (accessed March 7, 2021).
[13] Hydrogen Transport & Distribution | Hydrogen, (n.d.). https://hydrogeneurope.eu/hydrogen-transport-distribution (accessed February 16, 2021).

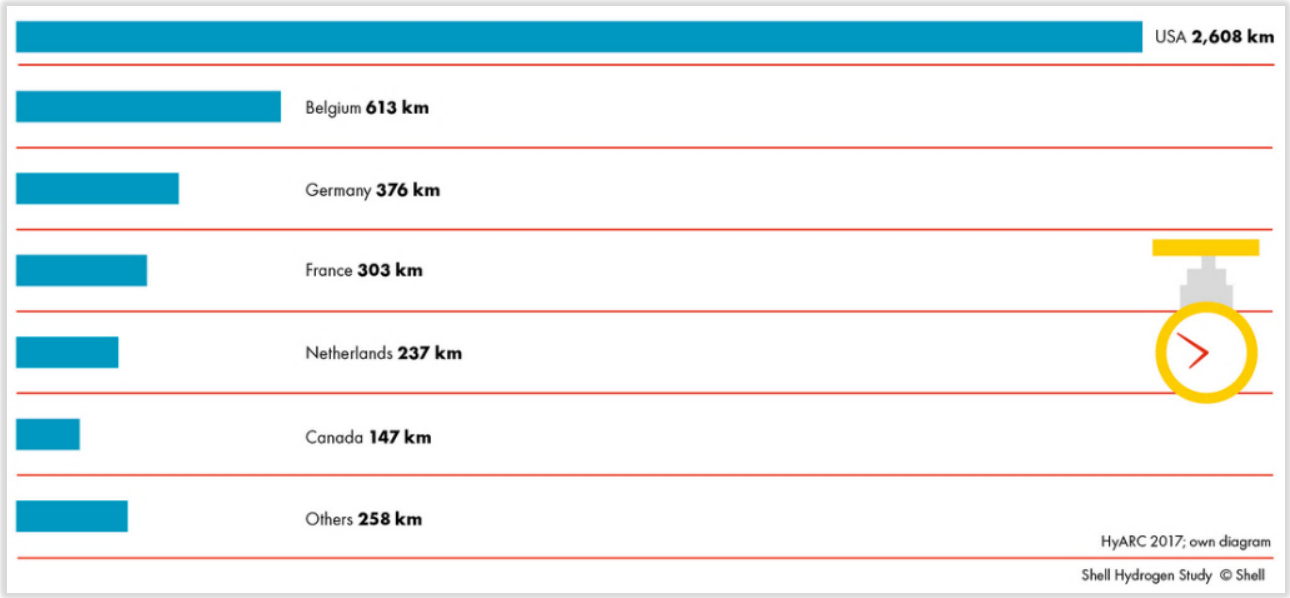

Figure I-18: Length of hydrogen transmission pipelines for various countries. Transporting gaseous hydrogen via existing pipelines is a low-cost option for delivering large volumes of hydrogen[14].

III. The Proton Exchange Membrane Fuel Cell (PEMFC) technology

For more than a century and a half, Sir William Robert Grove (1811 -1896) had exposed his first works about the realization of the first fuel cell system and its components since 1839. This included the mechanism of a single cell, consisting of hydrogen and oxygen, in contact with two platinized platinum electrodes [18].

[14] Hydrogen Pipelines, Energy.Gov. (n.d.). https://www.energy.gov/eere/fuelcells/hydrogen-pipelines (accessed February 16, 2021).

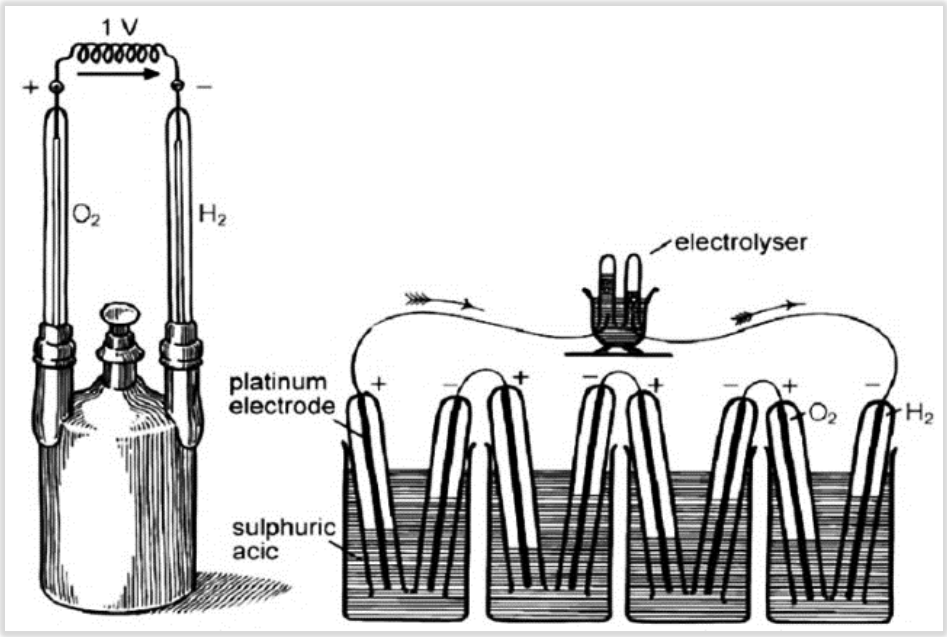

Figure I-19: On the left, Grove's gas battery' produced a voltage of about 1 volt, and on the right, Grove's gas chain powering an electrolyser. Reprinted from reference [11].

The fuel cell (*figure I-20*) is an electrochemical device that converts chemical energy into electrical energy as long as it is supplied with hydrogen (fuel) and oxygen (pure oxygen or from the air, as an oxidizer) with water and heat as byproducts. Such conversion is achieved by electrochemical reactions: oxidation of the hydrogen (at the anode) and reduction of the oxygen (at the cathode). The controlled electrochemical combustion of dihydrogen and dioxygen thus produces water and heat according to the following reactions:

Anode (H_2 Oxidation Reaction HOR):

$$\mathbf{2H_2 \leftrightarrows 4H^+ + 4e^-} \quad (E_0(H^+/H_2) = 0\ V_{RHE})$$

Cathode (O_2 Reduction Reaction ORR in acidic electrolyte):

$$\mathbf{O_2 + 4H^+ + 4e^- \leftrightarrows 2H_2O} \quad (E_0(O_2/H_2O) = 1.23\ V_{RHE})$$

Overall reaction:

$$\mathbf{O_2 + 2H_2 \leftrightarrows 2H_2O + Heat + Electricity}\ (\Delta E = 1.23\ V_{RHE}, \text{ at standard conditions})$$

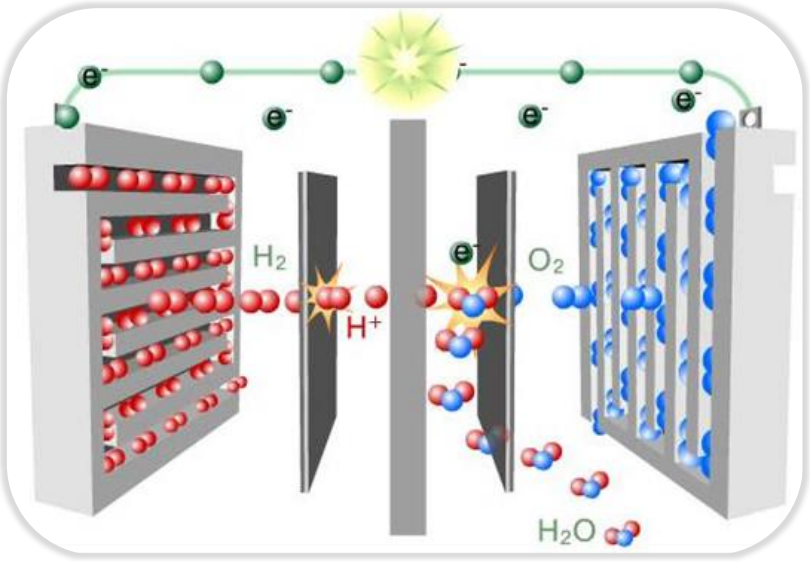

Figure I-20: Simplified scheme of the operating principle of a proton exchange membrane fuel cell (PEMFC).

For the PEMFC functioning, hydrogen is the basic fuel, but fuel cells also require pure oxygen or air. Hydrogen oxidation and oxygen reduction reactions are performed at the electrolyte/electrode interface in the presence of a catalyst, which fastens the electrochemical reactions that are sluggish when done at low temperatures (<100°C). At the anode, protons pass through the membrane joining the cathode, while the electrons flow to the cathode via an external electrical circuit. The adhesion of the membrane to the electrodes using the ionomer must be ensured.

III.1 PEMFC performance: Polarization curve and the oxygen Reduction Reaction mechanisms

Several phenomena limit the performance of PEMFC. As evidenced in *figure I-21* below, a polarization curve corresponds to a conventional PEMFC under real operating conditions with the contributions of the major losses. The main losses are due to the cathode side because of the coupling between a sluggish ORR and H^+ and O_2 transport losses issues.

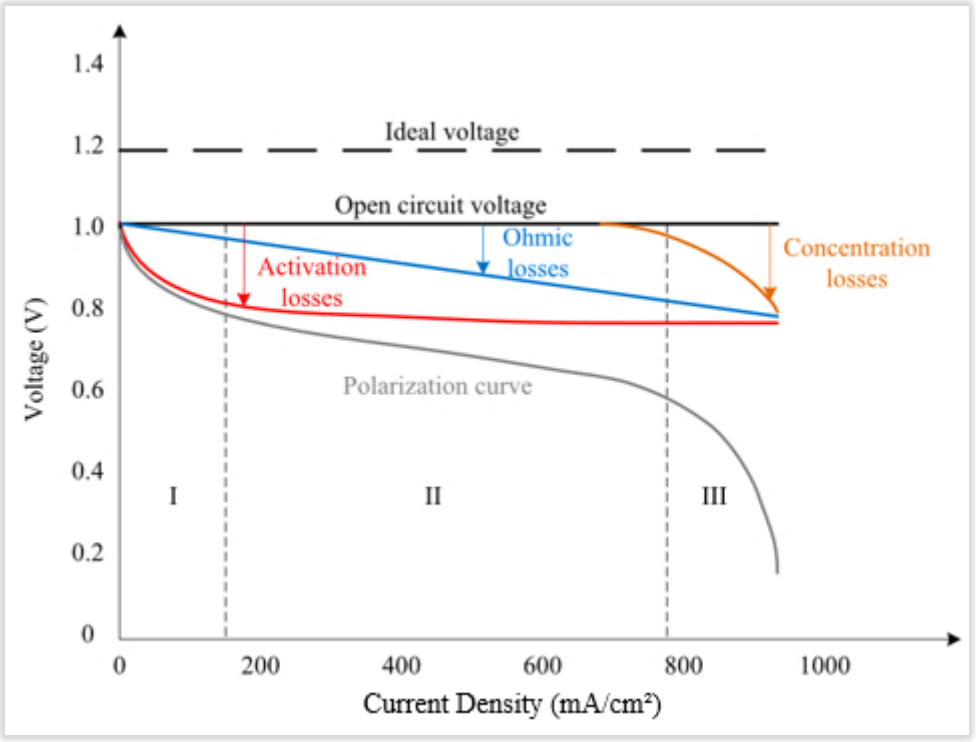

Figure I-21: Various voltage losses and polarization curve of an operating PEMFC [20].

From a thermodynamical viewpoint, the measured potential is not equal to the theoretical potential (1.23 V_{RHE}) due to the losses that are present for all current densities, where **i/** Zone I: electrochemical reactions (activation losses); **ii/** Zone II: ohmic losses; and **iii/** Zone III: concentration or reactants transport losses. These various factors can induce cell voltage drops. Technically, it is not really possible to separate transport from kinetic losses.

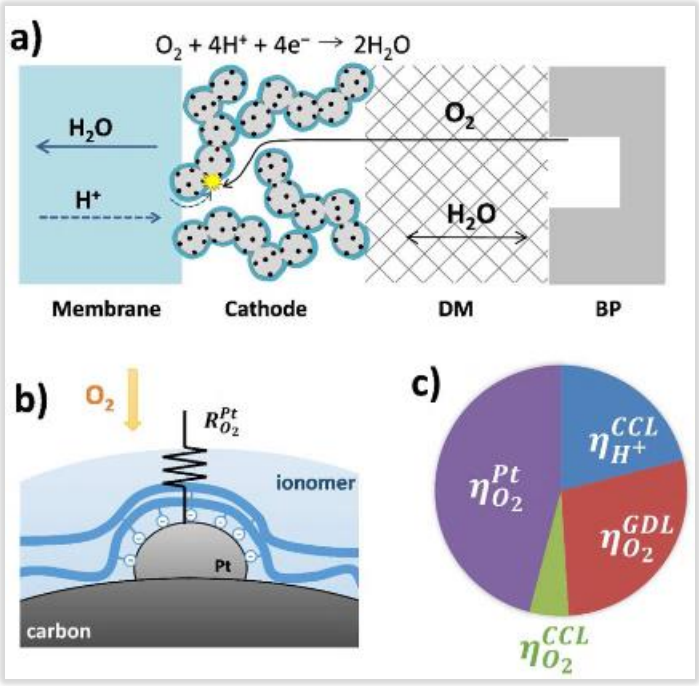

Figure I-22: a) Schematic of the membrane, cathode, diffusion medium (DM), and bipolar plate (BP) and the transport therein. b) Close-up view of the local O_2 transport to a Pt nanoparticle through the ionomer film. c) Simulated mass-transport voltage losses at 1.75 A/cm^2 for a cathode with 0.10 mg_{Pt}/cm^2 loading with operating conditions in the order of anode/cathode: H_2/Air, 94°C, 65/65% RH, 250/250 $kPa_{abs,outlet}$, stoichiometries of 1.5/2. Single-cell: 50 cm^2 active area [21].

Taking into account the aforementioned factors, the observed cell voltage of a PEMFC E_{cell} may be described as follows:

$$\mathbf{E_{cell} = E_{rev} - i \cdot R_{\Omega} - \eta_{HOR} - i \cdot R^{effective}_{H^+,anode} - \eta_{ORR} - i \cdot R^{effective}_{H^+,cathode}}$$

Where:

- $\mathbf{E_{rev}}$ is the thermodynamic equilibrium potential as a function of temperature and gas partial pressure;
- **i** is the applied current density;
- $\mathbf{R_{\Omega}}$ is the relative humidity (RH) dependent cell resistance (the sum of the RH-dependent membrane proton resistance, $R_{membrane}$, and the RH-independent contact and bulk electronic resistances R_{e-});
- $\boldsymbol{\eta_{ORR}}$ and $\boldsymbol{\eta_{HOR}}$ are the anode and cathode kinetic overpotentials;
- $\mathbf{R^{effective}_{H^+,\ anode}}$ and $\mathbf{R^{effective}_{H^+,\ cathode}}$ are the RH-dependent effective proton resistances in the anode and cathode catalyst layers, respectively,

At the cathode, the ORR is relatively complex, sluggish, and presents various mechanisms compared to the HOR. Many studies suggested possible occurring mechanisms. The results obtained from these studies of oxygen reduction on platinum and platinum-based alloy electrodes have been used to support a parallel reaction mechanism with a predominantly direct four-electron reduction to water [21].

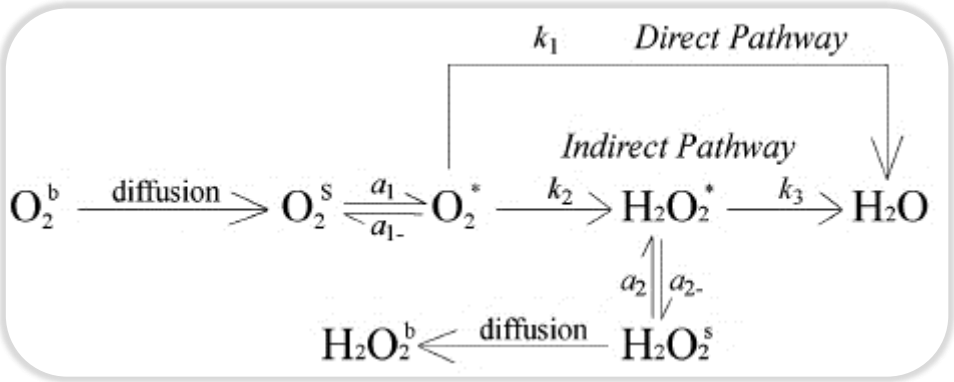

Figure I- 23: Wroblowa scheme for the pathways of the oxygen reduction reaction as extracted from reference [21].

Other studies have been conducted on the same subject, analyzing the kinetics of electrochemical O_2 reduction on Pt, assuming that the reaction occurs via the dissociative or associative mechanism with participation of adsorbed atomic oxygen [21][23][24][25]. *Nørskov* and co-workers have investigated the reaction free energy (ΔG) of various reaction intermediates during the electrochemical processes of ORR based on electronic structure calculations by employing density functional theory (DFT), and reported that the direct pathway (an associative mechanism) on Pt is itself divided into elementary steps:

$$O_2(g) + * \rightarrow O_2^*$$

$$O_2^* + H^+ + e^- \rightarrow HOO^*$$

$$HOO^* + H^+ + e^- \rightarrow O^* + H_2O(l)$$

$$O^* + H^+ + e^- \rightarrow HO^*$$

$$HO^* + H^+ + e^- \rightarrow H_2O(l) + *$$

where * stands for an active site on the surface of electrocatalyst, (l) and (g), refer to liquid and gas phases, respectively, and O_2*, O*, OH*, and HOO* are the adsorbed intermediates.

III.2 Main components of the PEMFC

A PEM fuel cell consists of one or more cells, two current collectors, and two clamping plates (or terminal plates). We talk about a fuel cell stack if the fuel cell contains several cells in series. Each cell comprises several basic components that make up the fuel cell and each of them must have specific properties to maximize the fuel cell's efficiency and reduce its cost. Some of these components include:

- **Bipolar plates**: Plates used as the boundary between two cells containing channels (ranging from several hundreds of µm to mm) that supply reactive gases, collect and conduct the electric current, evacuate heat, water, and unreacted gases. They are mostly made of metal, carbon, or composites. Moreover, for circulating a liquid coolant, additional channels can be added within each plate.
- **Electrodes**: Active layers on both sides of the membrane are mostly composed of catalyst and its support, usually Pt (or Pt-M: M refers to a transition metal) nanometer-sized particles (3-5 nm) deposited on a high surface carbon support (higher electrical conductivity and low-cost). They are mixed with an ion-conducting polymer (ionomer) in order to elaborate a CCM (Catalyst Coated Membrane) or a GDE (Gas Diffusion Electrode).

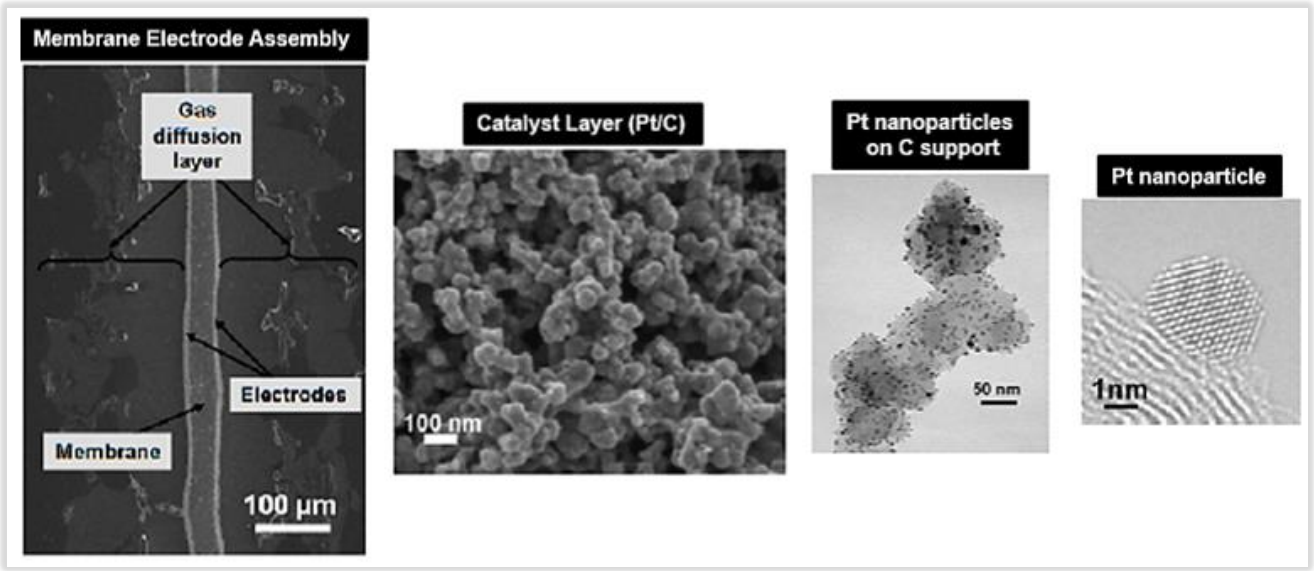

Figure I-24: Scanning electron image of a) Membrane Electrode Assembly (*i.e.*, Membrane, GDL, and electrodes), b) a top close scanning image of the catalyst layer containing Pt nanoparticles on a carbon support, ionomer binder. Transmission Electron Microscopy micrographs of: c) Pt NPs on C support, d) Pt nanoparticle. The figure is reprinted from reference [29].

The commercial Vulcan XC72 carbon black is the most frequently used C-support in the preparation of commercial electrocatalysts. It provides excellent conductivity and high surface area.

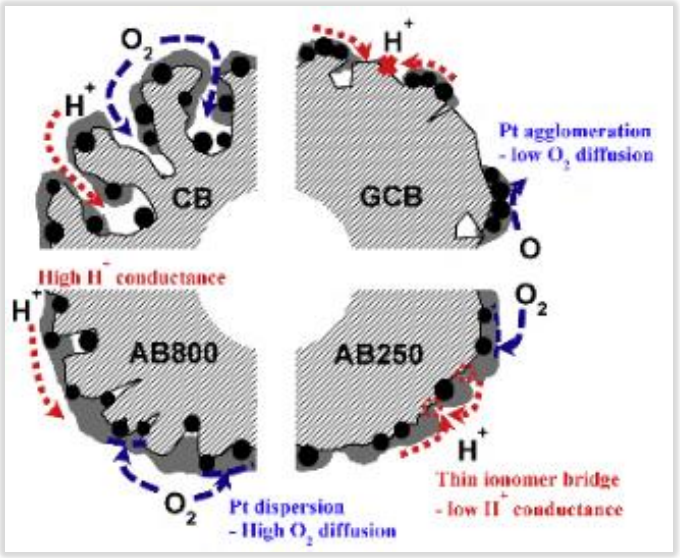

Figure I-25: Schematic ORR models of different carbon-supported Pt catalysts, CB: Carbon Black, GCB: Graphitized Carbon Black, AB250: Acetylene Black 250 and 800. 250 and 800 refer to the specific surface area of AB800 and AB250 (779 m^2/g and 219 m^2/g). Reprinted from reference [27].

- **Proton Exchange Membrane**: Thermally and chemically stable perfluorosulfonated (PFSA) acidic polymer material and mechanically stabilized by the PTFE host membrane. The ion exchange capacity stems from the perfluorinated side chain with the terminal sulfonic acid groups.

  When sufficiently hydrated, it ensures protonic conduction (H^+ ions) and prevents electrons flow. Its quasi-impermeability to reactive gases avoids the mixing between hydrogen and oxygen (cross-over phenomenon). In the case of cross-over, O_2 at the cathode passes through the membrane to the anode, while hydrogen crosses from the anode to the cathode. This recombination of O_2 and H_2 leads to a voltage loss along with the possible formation of radical species that can degrade the membrane. Also, the solubility of O_2 in H_2O decreases when temperature decreases. The conventional PEM commonly used in PEMFC is the Nafion® by DuPont de Nemours company and the Aquivion® from Solvay company.

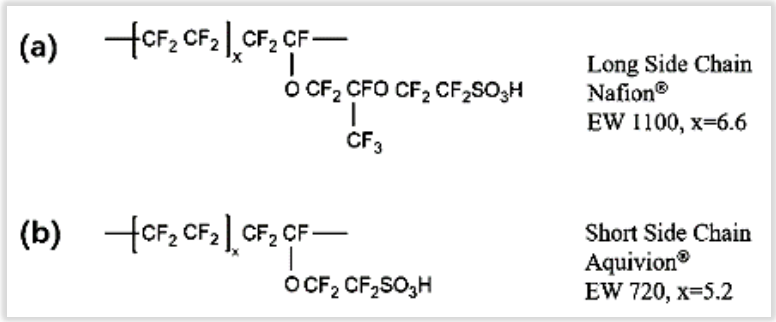

Figure I-26: Nafion® and Aquivion® perfluorinated sulfonic acid ionomer structures.

- **Gas Diffusion Layer** (GDL, *i.e.,* macroporous/microporous carbon layer): Carbonaceous material offering better gas dispersion, a good electronic and thermal conductor allowing the evacuation of water produced and ensures the supply of hydrated gases to the active zone. Between two bipolar plates, polymer gaskets must be added in-between, covering the edges of the MEA to ensure gas-tight sealing. Usually, each GDL consists of a carbon paper sheet in which the carbon fibers are partially coated with polytetrafluoroethylene (PTFE). In the GDL, gases disperse easily through the pores. The hydrophobic PTFE, which prevents excessive water buildup, holds these pores open [28].

Figure I-27 below displays the main components of a PEMFC.

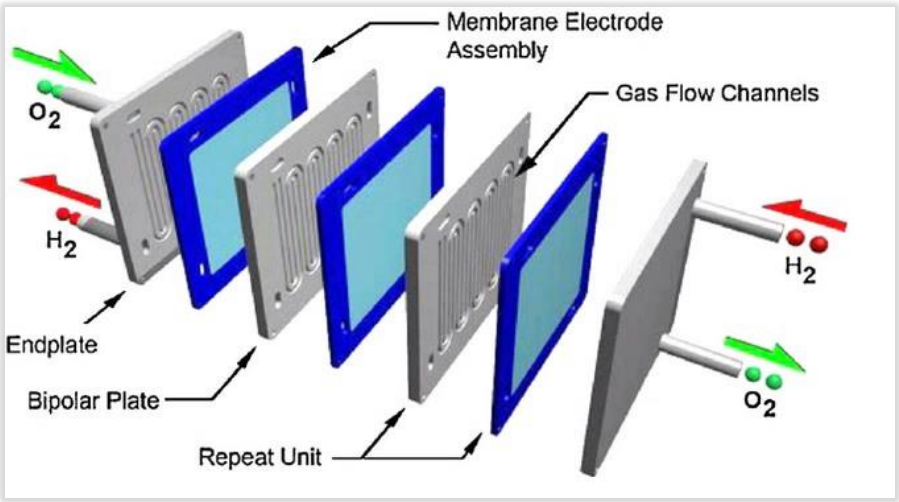

Figure I-27: Schematic representation of the Components of a PEMFC single cell.

According to the type of electrolyte of fuel cells, they can be divided into polymer electrolyte membrane fuel cells (PEMFCs), solid oxide fuel cells (SOFCs) and alkaline membrane fuel cells (AMFCs), and so on, as summarized in *table I-2* below:

Fuel Cell	Electrolyte	Operating Temperature	Electrical Efficiency	Fuel 'Mixture'
Alkaline Fuel Cell (AFC)	Potassium hydroxide (KOH) solution	Room temperature to 90°C	60-70%	H_2 - O_2
Proton Exchange Membrane Fuel Cell (PEMFC)	Proton exchange membrane	Room temperature to 80°C	40-60%	H_2 - O_2 or Air
Direct Methanol Fuel Cell (DMFC)	Proton exchange membrane	Room temperature to 130°C	20-30%	CH_2OH - O_2 or Air
Phosphoric Acid Fuel Cell (PAFC)	Phosphoric acid	160-220°C	55%	Natural Gas, Biogas, H_2 - O_2 or Air
Molten Carbonate Fuel Cell (MCFC)	Molten mixture of alkali metal carbonates	620-660°C	65%	Natural Gas, Biogas, Coalgas, H_2 - O_2 or Air
Solid Oxide Fuel Cell (SOFC)	Oxide ion conducting ceramic	800-1000°C	60-65%	Natural Gas, Biogas, Coalgas, H_2 - O_2 or Air

Table I-2: Characteristics of Various Types of Fuel Cells as described in reference [11].

III.3 Pt/C as a conventional electrocatalyst to PEMFC: Types and degradation mechanisms

The commercialization of the PEMFCs is limited primarily by catalyst cost. The conventional Pt nanoparticles supported on carbon are the highly used nanostructure as a catalyst for the PEMFC [30]. *Figure I-28* below outlines the different types of Pt-based catalysts.

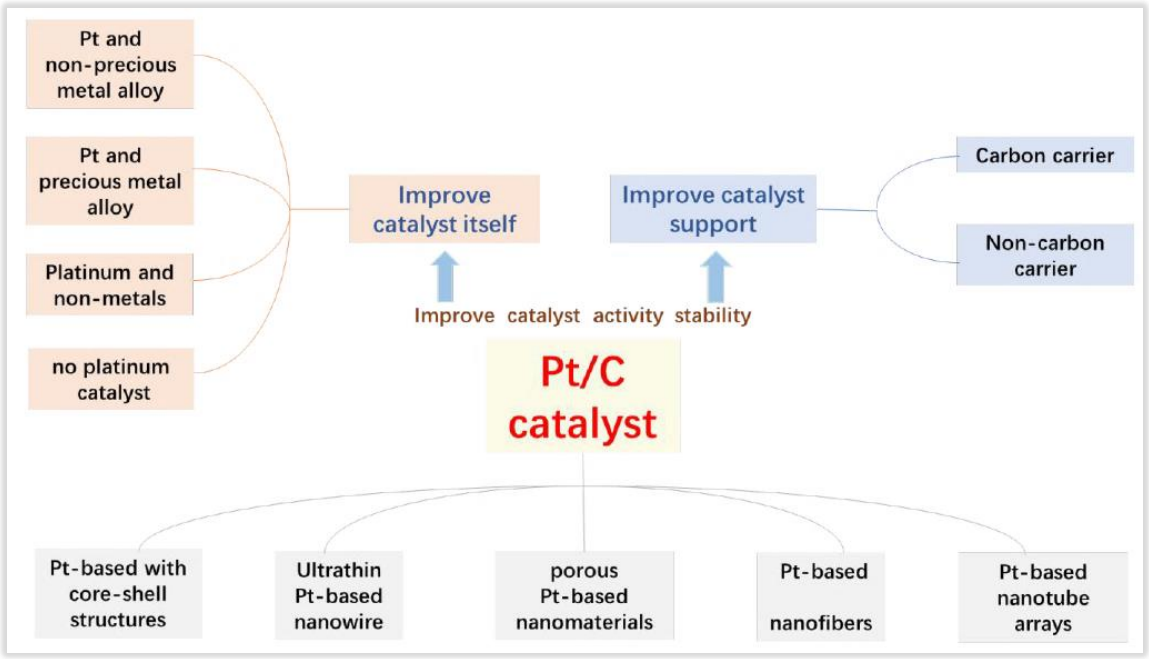

Figure I-28: Schematic illustration of the Approaches for the performance improvement of Pt/C and Pt-free catalysts. Reprinted from reference [31].

So far, the Pt/C catalyst is limited by corrosion of the C and Pt dissolution and/or agglomeration through electrochemical Ostwald ripening mechanism, which is reflected by a fast and significant loss of electrochemical surface area (ECSA) over time during fuel cell operation [30][32].

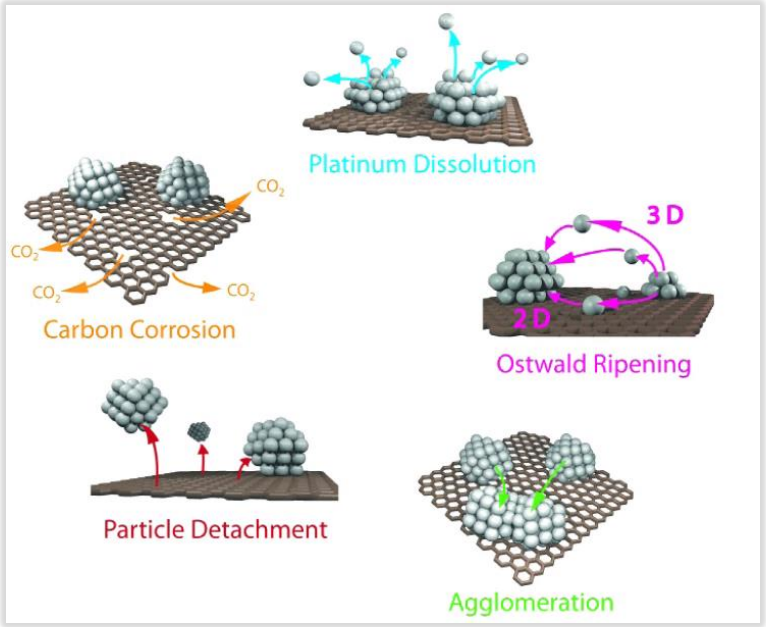

Figure I-29: Schematic representation of suggested primary and secondary degradation mechanisms for carbon-supported platinum catalyst particles in fuel cells. Reprinted from reference [30].

This architecture can hardly be more optimized; for this reason, many researches have been led to design new carbon-free architectures of electrodes.

III.4 PEMFC: Development challenges

Since the discovery of the PEMFC technology, durability and cost remain the key barriers to the commercialization of fuel cells and must be faced simultaneously.

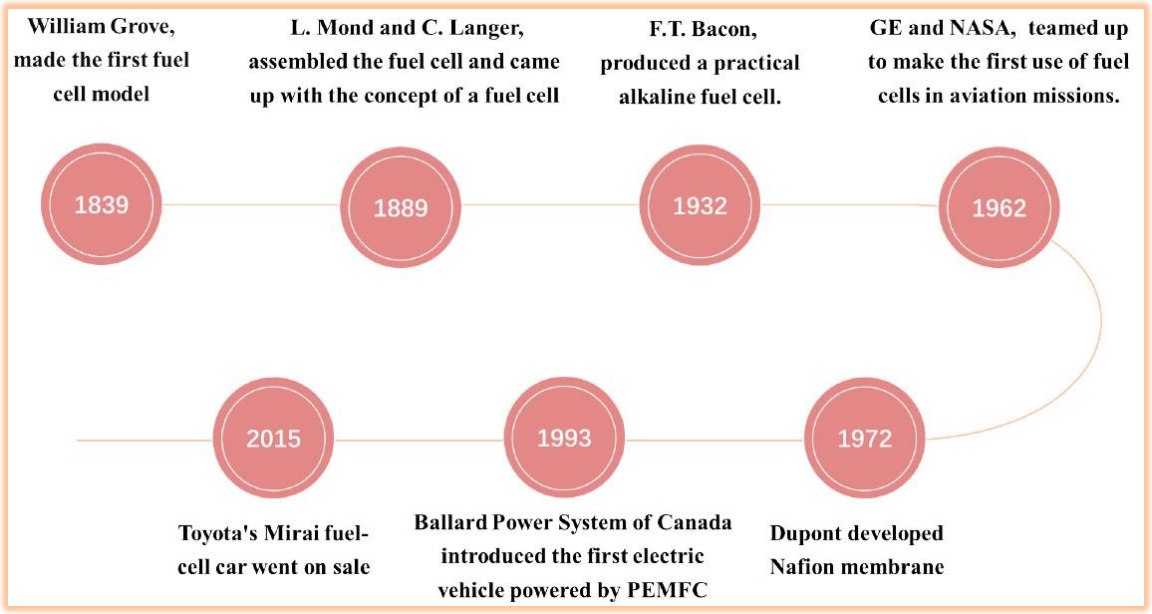

Figure I-30: Timeline of fuel cell research progress from 1839 to now. Reprinted from reference [31].

Even though their cost has decreased and their performance and durability have met significant progress over the past several decades, they have not yet achieved the objectives required in various applications, particularly in the automotive and stationary sectors. Thus, Multi-component improvements are needed to meet the targets outlined by the *Department of Energy* (DOE) [33]. In addition, the FC cost dropped by about 67% since 2006 due to optimizing stack components.

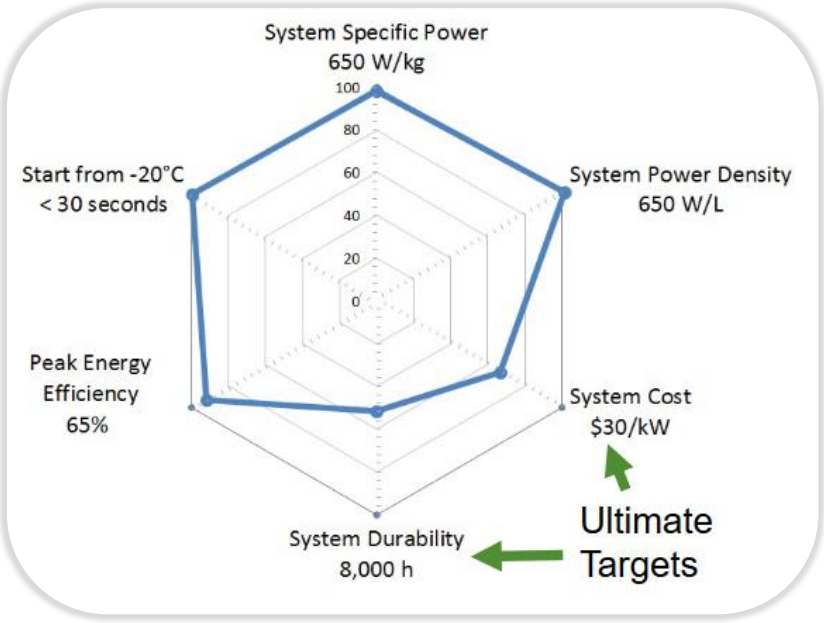

Figure I-31: Schematic diagram depicting the PEMFC properties and their corresponding industrialization targets. The blue line indicates the current status as a fraction of the target value [33].

It was indicated by Strategic Analysis, Inc. analysis that the fuel cell stack would account for 66% and 43% of the total system cost at 1,000 and 500,000 systems per year, respectively. In *figure I-32*, a breakdown of stack component costs is shown. Among the various components, catalyst and bipolar plates are dominated by commodity materials costs (platinum and stainless steel, respectively), which are relatively insensitive to manufacturing volume [34].

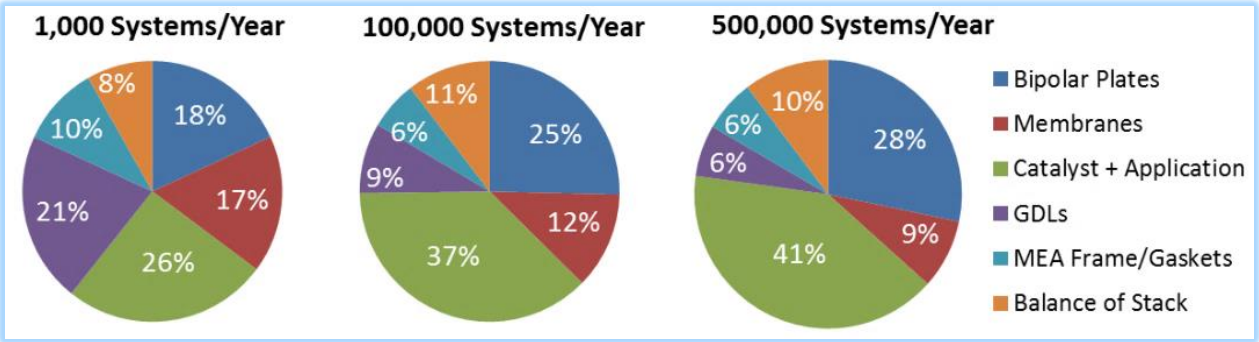

Figure I-32: Breakdown of the 2017 projected fuel cell stack cost at 1,000, 100,000, and 500,000 systems per year [34].

Nowadays, high-performance PEM fuel cells, as electrical power sources, are reaching steady improvements in order to alleviate major issues associated with the production and consumption of energy. Nevertheless, two major problems present barriers to

maximize the performance: durability and cost. As previously depicted, the catalyst layer reveals both durability and cost drawbacks (expensive Pt-based catalyst, expensive membrane, and moderate lifetime). For this purpose, this Ph.D. work was dedicated to elaborating a new architecture of the cathode to tackle the aforementioned barriers, as it will be presented in the following chapters.

List of figures and tables

References

[1]. Z. Chen, M. Waje, W. Li, Y. Yan, Supportless Pt and PtPd Nanotubes as Electrocatalysts for Oxygen-Reduction Reactions, Angewandte Chemie International Edition. 46 (2007) 4060–4063.

[2]. S.M. Alia, C. Ngo, S. Shulda, M.-A. Ha, A.A. Dameron, J.N. Weker, K.C. Neyerlin, S.S. Kocha, S. Pylypenko, B.S. Pivovar, Exceptional Oxygen Reduction Reaction Activity and Durability of Platinum–Nickel Nanowires through Synthesis and Post-Treatment Optimization, ACS Omega. 2 (2017) 1408–1418.

[3]. L. Gan, M. Heggen, C. Cui, P. Strasser, Thermal Facet Healing of Concave Octahedral Pt–Ni Nanoparticles Imaged in Situ at the Atomic Scale: Implications for the Rational Synthesis of Durable High-Performance ORR Electrocatalysts, ACS Catal. 6 (2016) 692–695.

[4]. B. Han, C. E. Carlton, A. Kongkanand, R. S. Kukreja, B. R. Theobald, L. Gan, R. O'Malley, P. Strasser, F. T. Wagner, Y. Shao-Horn, Record activity and stability of dealloyed bimetallic catalysts for proton exchange membrane fuel cells, Energy & Environmental Science. 8 (2015) 258–266.

[5]. L. Dubau, T. Asset, R. Chattot, C. Bonnaud, V. Vanpeene, J. Nelayah, F. Maillard, Tuning the Performance and the Stability of Porous Hollow PtNi/C Nanostructures for the Oxygen Reduction Reaction, ACS Catal. 5 (2015) 5333–5341.

[6]. L. Capuano, U.S. Energy Information Administration's International Energy Outlook 2020 (IEO2020), (2019) 7.

[7]. C. Le Quéré, R.B. Jackson, M.W. Jones, A.J.P. Smith, S. Abernethy, R.M. Andrew, A.J. De-Gol, D.R. Willis, Y. Shan, J.G. Canadell, P. Friedlingstein, F. Creutzig, G.P. Peters, Temporary reduction in daily global CO2 emissions during the COVID-19 forced confinement, Nature Climate Change. 10 (2020) 647–653.

[8]. C. Fan, G. Wang, L. Zou, J. Fang, Z. Zou, H. Yang, Composition- and shape-controlled synthesis of the PtNi alloy nanotubes with enhanced activity and durability toward oxygen reduction reaction, Journal of Power Sources. 429 (2019) 1–8.

[9]. Z.W. Seh, J. Kibsgaard, C.F. Dickens, I. Chorkendorff, J.K. Nørskov, T.F. Jaramillo, Combining theory and experiment in electrocatalysis: Insights into materials design, Science. 355 (2017) eaad4998.

[10]. IEA (2020), Renewables Information: Overview, IEA, Paris. https://www.iea.org/reports/renewables-information-overview. Accessed on February, 13th 2021.

[11]. G. P. Panayiotou, S. A. Kalogirou, S. A. Tassou, PEM Fuel Cells for Energy Production in Solar Hydrogen Systems, Recent Patents on Mechanical Engineering (2010), 3, 226-235.

[12]. K. Vohra, A. Vodonos, J. Schwartz, E.A. Marais, M.P. Sulprizio, L.J. Mickley, Global mortality from outdoor fine particle pollution generated by fossil fuel combustion: Results from GEOS-Chem, Environmental Research. (2021) 110754.

[13]. J. Lelieveld, A. Pozzer, U. Pöschl, M.Fnais, A. Haines, T. Münzel, Loss of life expectancy from air pollution compared to other risk factors: a worldwide perspective, Cardiovascular Research (2020)116, 1910–1917.

[14]. Climate change – Topics - IEA, (n.d.). https://www.iea.org/topics/climate-change (accessed February 11, 2021).

[15]. IEA – International Energy Agency, IEA. (n.d.). https://www.iea.org (accessed February 11, 2021).

[16]. B. Pivovar, N. Rustagi, S. Satyapal, Hydrogen at Scale (H 2 @Scale): Key to a Clean, Economic, and Sustainable Energy System, Electrochem. Soc. Interface. 27 (2018) 47–52.

[17]. R. Perret, Solar Thermochemical Hydrogen Production Research (STCH), Sandia Report, 2011.

[18]. A.J. Appleby, From Sir William Grove to today: fuel cells and the future, Journal of Power Sources. 29 (1990) 3–11.

[19]. D.V. Dao, G. Adilbish, T.D. Le, I.-H. Lee, Y.-T. Yu, Triple phase boundary and power density enhancement in PEMFCs of a Pt/C electrode with double catalyst layers, RSC Adv. 9 (2019) 15635–15641.

[20]. Z. Li, Z. Zheng, L. Xu, X. Lu, A review of the applications of fuel cells in microgrids: opportunities and challenges, BMC Energy (2019) 1:8.

[21]. A. Kongkanand, M.F. Mathias, The Priority and Challenge of High-Power Performance of Low-Platinum Proton-Exchange Membrane Fuel Cells, The Journal of Physical Chemistry Letters (2016), 7 (7), 1127-1137.

[22]. S. Chen, A. Kucernak, Electrocatalysis under Conditions of High Mass Transport Rate: Oxygen Reduction on Single Submicrometer-Sized Pt Particles Supported on Carbon, J. Phys. Chem. B. 108 (2004) 3262–3276.

[23]. R. Ma, G. Lin, Y. Zhou, Q. Liu, T. Zhang, G. Shan, M. Yang, J. Wang, A review of oxygen reduction mechanisms for metal-free carbon-based electrocatalysts, Npj Computational Materials. 5 (2019) 1–15.

[24]. J. K. Nørskov, J. Rossmeisl, A. Logadottir, and L. Lindqvist, Origin of the Overpotential for Oxygen Reduction at a Fuel-Cell Cathode, J. Phys. Chem. B (2004), 108, 17886-17892.

[25]. V. P. Zhdanov, B. Kasemo, Kinetics of electrochemical O2 reduction on Pt, Electrochemistry Communications 8 (2006) 1132–1136.

[26]. K.C. Neyerlin, W. Gu, J. Jorne, A. Clark, H.A. Gasteiger, Cathode Catalyst Utilization for the ORR in a PEMFC, J. Electrochem. Soc. 154 (2007) B279.

[27]. Y-C. Park, H. Tokiwa, K. Kakinuma, M. Watanabe, M. Uchida, Effects of carbon supports on Pt distribution, ionomer coverage and cathode performance for polymer electrolyte fuel cells, Journal of Power Sources 315 (2016) 179e191.

[28]. DOE, Parts of a Fuel Cell, Energy.Gov., https://www.energy.gov/eere/fuelcells/parts-fuel-cell (accessed February 16, 2021).

[29]. L. Guetaz, M. Lopez-Haro, S. Escribano, A. Morin, G. Gebel, D.A. Cullen, K.L. More, R.L. Borup, Catalyst-Layer Ionomer Imaging of Fuel Cells, ECS Trans. 69 (2015) 455.

[30]. S. Cherevko, N. Kulyk, K.J.J. Mayrhofer, Durability of platinum-based fuel cell electrocatalysts: Dissolution of bulk and nanoscale platinum, Nano Energy. 29 (2016) 275–298.

[31]. X. Ren, Y. Wang, A. Liu, Z. Zhang, Q. Lv, B. Liu, Current progress and performance improvement of Pt/C catalysts for fuel cells, J. Mater. Chem. A. 8 (2020) 24284–24306.

[32]. Z.-B. Wang, P.-J. Zuo, Y.-Y. Chu, Y.-Y. Shao, G.-P. Yin, Durability studies on performance degradation of Pt/C catalysts of proton exchange membrane fuel cell, International Journal of Hydrogen Energy. 34 (2009) 4387–4394.

[33]. D. Papageorgopoulos, Fuel Cell R&D Overview – Fuel Cell Technologies Office, 2019 Annual Merit Review and Peer Evaluation Meeting, April 29, 2019.

[34]. A. Wilson, G. Kleen, and D. Papageorgopoulos, DOE Hydrogen and Fuel Cells Program Record, Fuel Cell System Cost - 2017, Record #:17007

Chapter 2

Anodic Aluminum Oxide as a Template for the Nickel Nanowires Growth

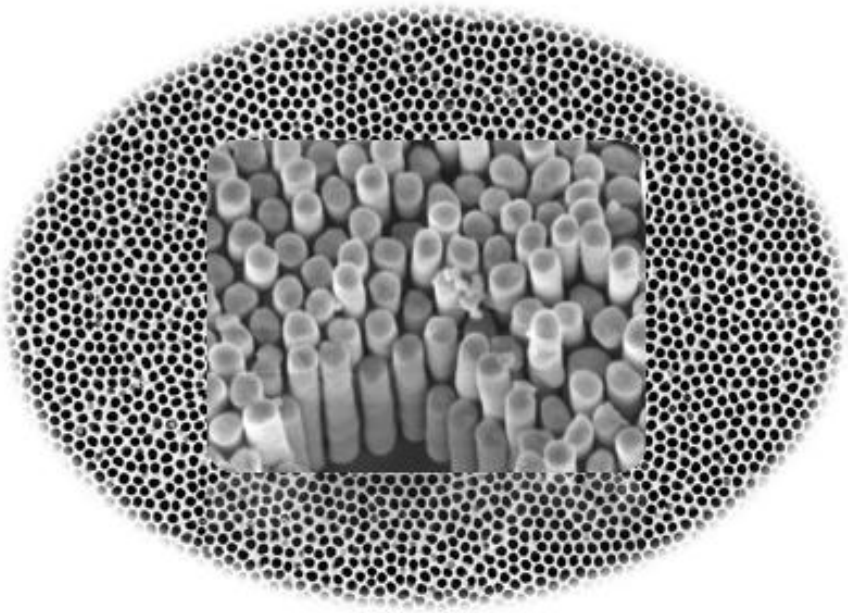

"If you want to find the secrets of the universe, think in terms of energy, frequency, and vibration."

-Nikola Tesla

Table of Content

Since we aim to elaborate the architecture of electrodes of straight aligned and organized Pt-Ni nanotubes and nanowires for the PEM fuel cell and reduce transport limitations in the electrodes, we leaned out to use tuned mold-based templates made of aluminum oxide. To that end, several steps are required to obtain the desired structure of the anodic alumina. The first step will consist of the manufacturing of the nanoporous alumina template with vertically oriented organized pores. Its design will govern the final organization of the electrode. Tuning the parameters of anodization, the achieved template will be used as a mold for the growth of the nickel nanowires, which are considered precursors for the PtNi nanotubes.

This chapter will draw attention to the total steps required to elaborate anodic aluminum oxide as a template for nickel nanowires' growth. To ensure this, we have first anodized an aluminum surface sputtered on p-type silicon leading to the formation of a porous template (*i.e.,* we can use a pure Al foil as well). The latter offers a cylindrical and vertically aligned nanoporous structure with a regular pore distribution and a small diameter dispersion.

As will be covered in the following paragraphs, the study will be held according to the main key points:

Part I: Overview: Elaboration and characterization of nanoporous alumina membrane;

Part II: Anodic Aluminum Oxide: Introduction to double-step anodization and kinetics of self-organization;

Part III: Elaboration of anodic aluminum oxide (AAO) by a two-steps anodization process.

I. Overview: Elaboration and characterization of nanoporous alumina membrane

For the last few decades, nanoporous alumina production by electrochemical route (*i.e.,* anodization process) on aluminum foils became common. It is now possible to obtain nanoporous alumina substrates on a laboratory scale or an industrial scale (*SPI Supplies*

company[15], *Smart Membranes company*[16]). They are used in a wide range of specialized applications, mainly as a functional material and growth of metallic nanowires.

Aluminum oxide or "Alumina" (sometimes called Aloxide) is formed over the aluminum surface due to its natural oxidation with atmospheric oxygen according to the equation:

$$4Al + 3O_2 \rightarrow 2Al_2O_3$$ Reaction II-1

The peculiarity of aluminum oxide is to be impervious to oxygen that cannot penetrate through the alumina layer and make it grow. *Buff* [1] was the first to find that aluminum can be electrochemically oxidized. To thicken the native oxide layer on Al (~2-3 nm thick oxide layer), an "anodization process" in an electrolytic solution is performed, which renders it denser, thus providing further aluminum surface protection. Concomitantly, this process in an aqueous electrolyte solution promotes the formation of two distinct morphologies: **i/** The nonporous (barrier-type) thick oxide film; and **ii/** the porous oxide film on the surface as depicted in *figure II-1*, depending mainly on the nature of the electrolytes (*i.e.,* acidic or alkaline media) [2][3][4].

The compact nonporous AAO films can be formed under potentiostatic conditions (*i.e.,* U = constant) in neutral electrolytes (pH 5−7), such as borate, oxalate, or citrate solutions, in which the anodic oxide is practically insoluble [5] while the porous AAO films are formed in acidic electrolytes (pH 1−4), such as sulfuric, oxalic, or phosphoric in which anodic oxide is slightly soluble (see *figure II-1*) [6][7].

[15] SPI Supplies, https://www.2spi.com/ (accessed March 2, 2021).
[16] Smartmembranes - Home, http://www.smartmembranes.de/en/ (accessed March 2, 2021).

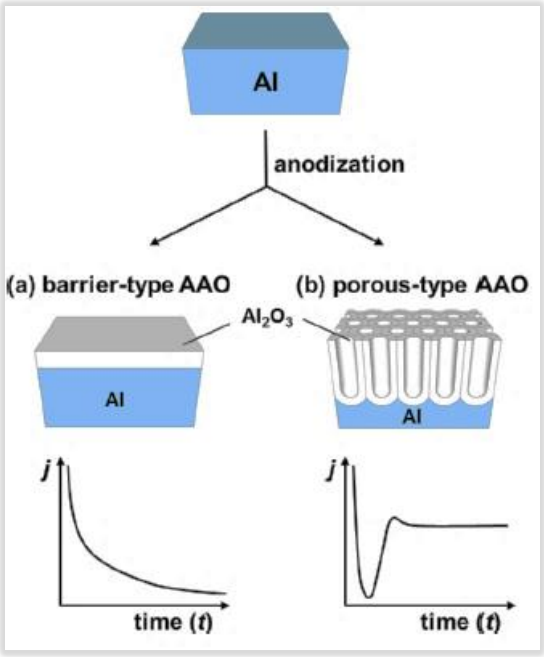

Figure II-1: Two different types of anodic aluminum oxide (AAO) formed by a) barrier-type and b) porous-type anodization, along with the respective current (j) *vs.* time (t) transients under potentiostatic conditions, as extracted from reference [8].

Further details will be explained in *paragraphs III* about the evolution of current density *vs.* anodizing time. Throughout this Ph.D. work, we will be interested only in the porous-type structure, which exhibits many practical properties such as corrosion resistance, hardness, and geometry tuning [9]. For this purpose, AAO templates were fabricated from a thin aluminum layer deposited on silicon substrates. Lastly, the anodization process follows a multi-step procedure to obtain the desired geometry of nanoporous AAO templates:

i. Formation of massive alumina layer at the beginning of the process;

ii. Nanopores initiation and growth of parallel nanochannels;

iii. Wet etching process in an acidic solution, which leads to the formation of hollow and ordered nanocells.

I.1 Growth of nanoporous anodic aluminum oxide

Porous anodic aluminum oxide, as mentioned above, is formed in acidic electrolytes in which the oxide layer is soluble, leading to the formation of a porous structure while applying a constant voltage between the anode (aluminum) and the cathode (Pt-Ir counter-electrode). Anodizing parameters play a key role, enabling us to ensure high

quality and self-organized porous structure (*e.g.,* voltage, temperature, concentration and pH of acidic electrolyte, and the quality of aluminum). It is worth noting that the fabrication of AAO could be either under the potentiostatic regime (*i.e.,* U = constant) or the galvanostatic regime (*i.e.,* J = constant), as shown in *figure II-2* below. This figure depicts the different steps undertaken during which the aluminum oxide layer's morphology evolves to end up with the nanoporous structure of aluminum oxide.

The following are the four steps of growth in galvanostatic (a) and potentiostatic (b) regimes, together with stages of porous oxide development: **i/** formation of the barrier layer (resistance increases); **ii/** initiation of nanoholes from initial aluminum surface defects; **iii/** pores growth (resistance decreases); **iv/** growth of cylindrical nanopores arrays via oxidation/dissolution of aluminum oxide. As an adjunct to this, and to enlarge the diameter of the pores and remove the barrier from the nanochannels' bottom, the samples are dipped into an acidic solution heated to an appropriate temperature. We will shed light on further details in the next paragraph of this chapter (see *paragraphs II.2.4* and *III.2*).

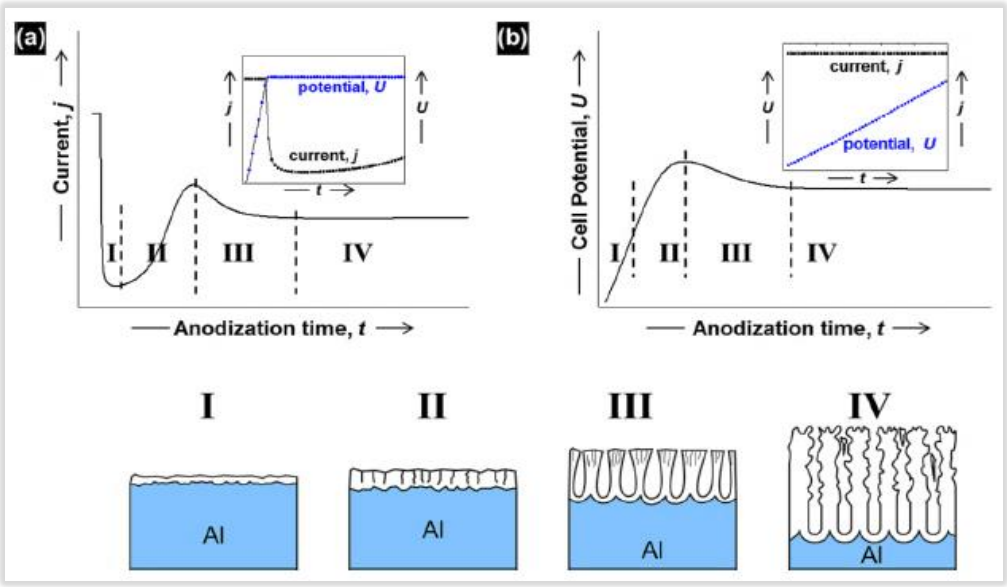

Figure II-2: Schematic diagram of the kinetics of porous AAO growth from an aluminum foil in a) potentiostatic (*i.e.*, U = constant) and b) galvanostatic (*i.e.*, j = constant) conditions. I/ formation of the barrier layer (resistance increases), II/ initiation of nanoholes from initial aluminum surface defects, III/ pores growth (resistance decreases), IV/ growth of cylindrical nanopores arrays via oxidation/dissolution of aluminum oxide. Reprinted from reference [8].

Typically, it is best to perform the process under a potentiostatic regime because of the proportional relationship between the applied voltage and the structural properties (interpore distance, pores' diameter, thickness) of the mold, as we shall see later [8].

I.2 Principle: Anodization of aluminum thin films

Porous anodic alumina membranes with self-organized structures are grown by electrochemical oxidation from pure aluminum foils or thin aluminum layers deposited on silicon wafers. When an aluminum sample is placed at the anode of an electrochemical system, and a voltage is applied through the circuit, the electric field generated causes the aluminum's ionization at the Al/Oxide interface. However, by controlling anodization parameters, we can tune the geometry of the pores. The effect of each parameter will be described further in *paragraph II.2*.

The anodizing voltage defines the interpore distance (D_{int}) and the pore diameter (D_p) of the AAO, while anodizing time determines the final thickness of the formed alumina template. *Figure II-3* below the general structure of AAO.

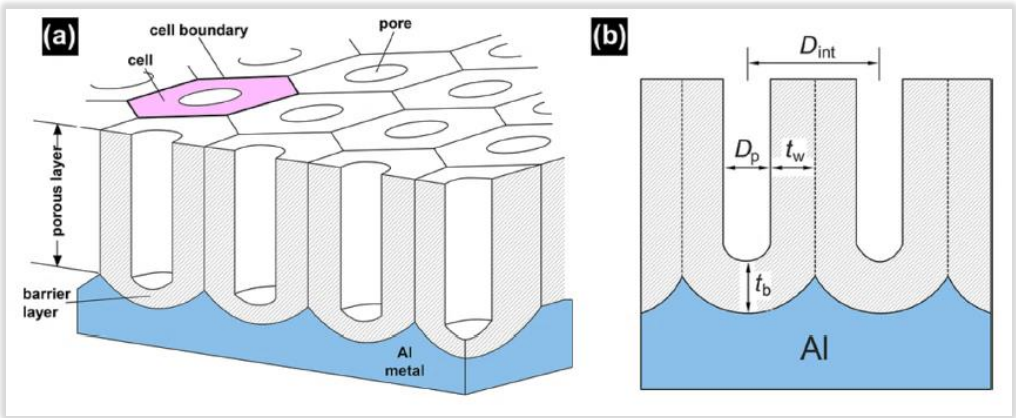

Figure II-3: Schematic structure of a) porous anodic aluminum oxide (AAO) structure and b) the cross-sectional view of nanopores. Extracted from reference [8].

Several methods for the fabrication of highly-ordered AAO have been discussed in the literature. Studies on alumina anodization expounded two distinct regimes:

- Mild anodization (**MA**): used for highly ordered and homogeneous templates at a slow rate growth of nanochannels. It exhibits low current density at a fixed voltage (*i.e.,* low anodizing potential) and a low concentration of acidic solution [4].

- Hard anodization (**HA**): for fast fabrication and high growth rate of AAO mold by applying a high and fixed voltage (*i.e.,* high current density) for a relatively controlled short time in a highly concentrated acidic electrolyte [10][11].

Moreover, it would be preferable to quote the different anodization types that lead to the ordering phenomena.

I.2.1 One-step Anodization process

It consists of a single-step process to obtain a nanoporous oxide layer that has non-uniform pores and interpore distance but high porosity [12]. It is mainly carried out in sulfuric, oxalic, and orthophosphoric acid under constant voltage.

The pores' initiation stage relies mainly on mechanical (*i.e.,* surface stress and surface local defects) and electrochemical (*i.e.,* anodization parameters) effects. *O'Sullivan's* group [13] believed that the current flows within initial defects of the Al surface from which the porous structure begins. On the other hand, *Thompson* [5] suggested that pores' initiation occurs from initial surface defects of the native oxide layer due to concentrated mechanical stress, as shown in *figure II-4* below.

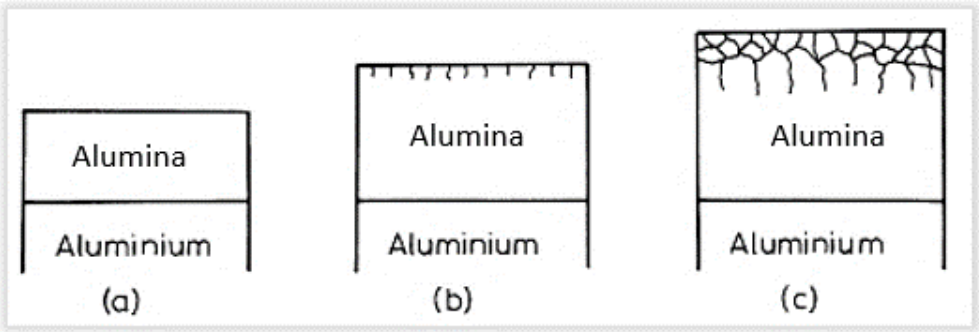

Figure II-4: Schematic diagram illustrating the development of penetration paths, from the precursors (surface defects) to pores, during anodizing in chromic acid. Reprinted from reference [5].

Further details about pore formation, barrier layer, interpore distance, pore diameter will be held and depicted in detail in *paragraph II.2*.

Given that the single-step anodization provides a poor organization of pores, and since the aim is to control the pores' structure with better organization precisely, an alternative

solution to alleviate this downside is using whether pre-patterned anodization to initiate ordered surface defects or the double anodization method.

I.2.2 Pre-patterned Anodization

During the formation of porous AAO, pores are distributed along the surface in a poly-domain structure, where each domain contains quasi-hexagonally ordered nanopores exhibiting akin orientation and separated by boundaries [8]. Geared toward a quasi-ideal AAO structure and highly homogeneous pore size, Nanoimprint Lithography (NIL) seemed to be a practical alternative. In 1995, *Stephen Y. Chou et al.* [14] have demonstrated a nanoimprinting technology that can imprint sub-25 nm vias in a PMMA film (AAO supporting polymer membrane) with a SiO_2 mold. The process consists of hot pressing a pre-patterned mold with the desired geometry (with the opposite of the desired patterns on the surface of the substrate) onto the substrate surface by mechanical pressure.

Two years later, *Masuda et al.* reported the fabrication of ideally ordered porous AAOs with a single-domain configuration over a few mm^2 areas using the NIL process followed by anodization in 3%wt oxalic acid. The process involved a SiC mold with a hexagonally ordered array of convexes for aluminum texturing. His experiment showed that NIL was suitable for mass production of restrictedly ordered nanochannel array architectures with a high aspect ratio, as evidenced in *figure II-5* below [15].

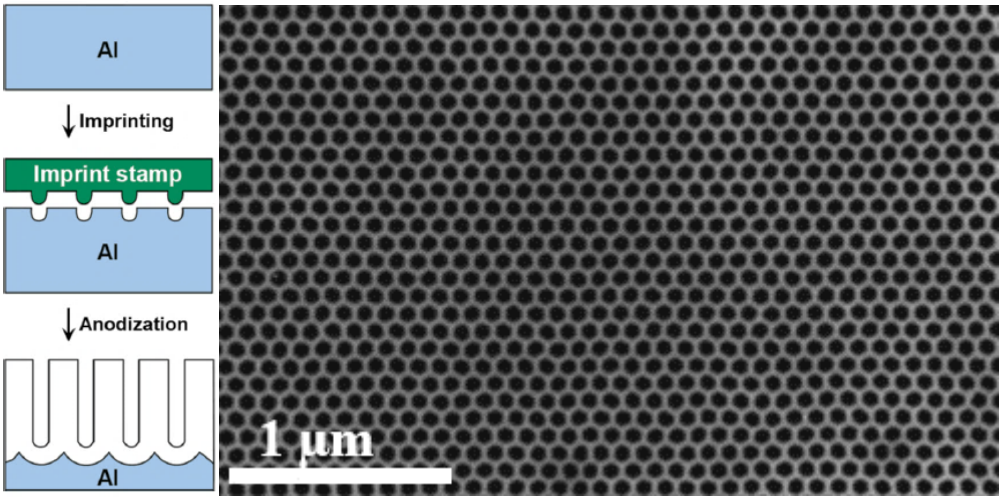

Figure II-5: Illustration showing the NIL process on the aluminum surface, and SEM micrograph of porous AAO formed by nanoimprint lithography NIL process followed by anodization, with 100 nm pore diameter conducted in 0.3 M oxalic acid at 17 °C [15].

In 2001, the same research group showed the possibility to obtain nanochannel arrays with an ideally ordered hole configuration with a 63 nm hole periodicity and 15–40 nm hole diameter sing anodization of the pre-textured Al in sulfuric acid solution [16]. To improve and control AAO formation, *T. Gorisse et al.* [17] have used nanoimprint lithography combined with standard anodization etching to elaborate perfectly organized triangular arrays of vertical cylindrical alumina nanopores onto silicon wafers (*figure II-6*). Both the pore diameter and the period of the porous alumina array are well controlled and can be tuned: the periods vary from 80 to 460 nm, and the diameters range from 15 nm to any required diameter.

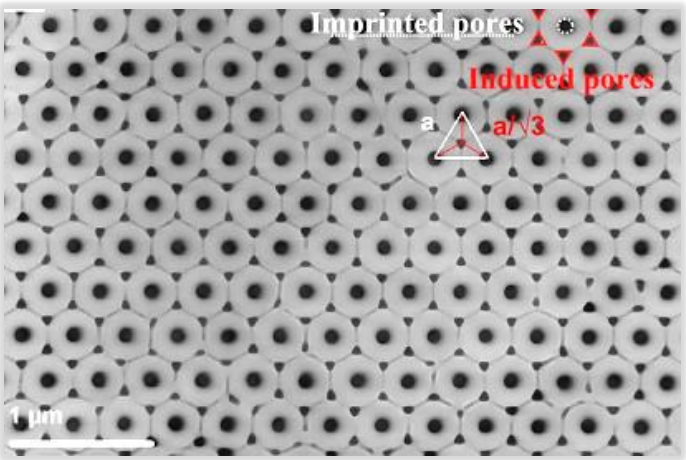

Figure II-6: Scanning electron micrographs of porous aluminum oxide obtained by nanoimprint lithography NIL process follow by one-step anodization in oxalic acid. This image shows an example of a pore array obtained when only one-third of the pores are localized using nanoimprint lithography [17].

Anodization of pre-patterned aluminum is indeed an effective way of obtaining ideally ordered porous AAO. However, the process has some limitations: **i/** the NIL requires a cleanroom elaboration; **ii/** any change in the desired geometry of pores, it is mandatory to fabricate new mold with new architecture; **iii/** for anodization of aluminum of a given pattern interval, one should adequately select anodizing parameters (*e.g.,* potential and electrolyte) to fulfill the self-ordering requirement of pores [8].

Unlike the double-anodization process that we will use in this work, the pre-patterned anodization technique appears complex and costly.

I.2.3 Double anodization process:

Since its beginning almost a century ago, aluminum anodization has shown many advancements and has been drawing attention to nanotechnology. Until 1996, *Masuda* and his co-workers [4] demonstrated the feasibility of highly ordered hexagonal arrays in anodic alumina by two-step anodization of a pure aluminum sheet. The structure exhibited parallel nanopores extending from the barrier oxide layer to the aluminum film surface.

The first-step of anodization is carried out and promotes the growth of nanopores on the aluminum surface. This step takes a long time until the nanochannels reach highly arranged in-depth throughout aluminum (sacrificial aluminum). Subsequently, a first wet isotropic etching process is applied by dipping the sample in an acidic solution (*e.g.,* heated solution of 5%wt orthophosphoric acid) to remove the first anodized alumina layer with disordered pores in its top part. In contrast, the dissolution should be selective, leaving aluminum nanobowls-like patterns at the remaining alumina surface formed during the first step (see *figure II-7*). Dimensions of the remaining spherical structures depend mainly on the first anodization conditions.

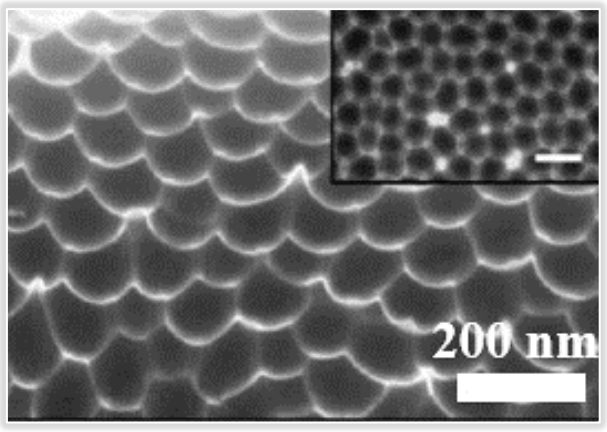

Figure II-7: Micrograph of tilted-view scanning electron microscope image of an Al foil with nanobowl surface patterns after the first etching process, reprinted from reference [18].

The second step is performed on the as-prepared sample. The remaining aluminum nanocells are thus self-organized into a hexagonal close-packed arrangement. It allows pores to nucleate in this area, forming a honeycomb-like structure [4][19]. The last step consists of a second wet isotropic etching to remove the barrier oxide layer at the bottom of pores and enlarge pores at the same time according to the desired dimensions (pores diameter, depth of nanochannels, and inter-pore distance). *Figure II-8* illustrates the main steps of the double anodization process briefly.

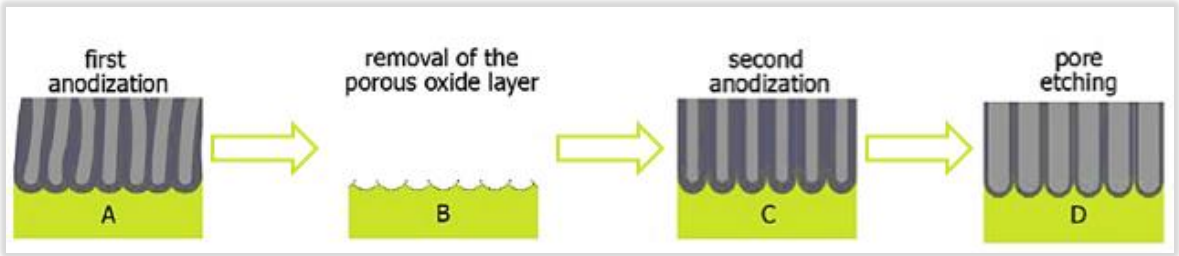

Figure II-8: Schematic representation of template-based nanoporous aluminum oxide templates. Reprinted and edited from reference.

II. Anodic Aluminum Oxide: Kinetics of Self-Organization

All over this part of the chapter, we will investigate the theoretical aspects of nanoporous AAO formation, the parameters influencing relatively its geometry, and models describing steady-state pore. This paragraph will also provide fundamental electrochemical processes associated with the anodic oxidation of aluminum.

II.1 Nanochannels formation: Kinetics and self-organization of pores

Highly ordered AAO exhibits many advantages, including the mechanical strength, chemical resistance, and high aspect ratio of the porous anodic structure. Such benefits make it highly desired for nanotechnology fabrication and functional nanodevices. By adequately choosing anodization conditions, mostly inter-dependent, the formed AAO could be tuned to ensure: **i/** formation of a honeycomb-like structure (hexagonal cell alignment); **ii/** variety of pores diameter D_p and interpore distance (D_{int}) and density and wall thickness.

II.1.1 Growth mechanisms of nanoporous aluminum oxide

This paragraph describes the growth mechanisms of nanoporous alumina on silicon. The origin of chemical reactions involved in the alumina elaboration process comes from three main phenomena: electrochemical reactions, alumina dissolution by the acidic electrolyte, and acid-basic reactions. It will be recalled that the spontaneous reaction leading to the formation of aluminum oxide in the air can be ascribed to the significant negative Gibb's free energy changes [20]:

$$2Al_{(s)} + \frac{3}{2}O_{2(g)} \rightarrow \alpha Al_2O_{3(s)} \qquad \Delta G° = -1582\ kJ/mol \qquad \text{Reaction II-2}$$

$$2Al_{(s)} + 3H_2O_{(l)} \rightarrow \alpha Al_2O_{3(s)} + 3H_{2(g)} \qquad \Delta G° = -871\ kJ/mol \qquad \text{Reaction II-3}$$

Two reactions are likely to occur:

Al Oxidation: $2Al_{(s)} \rightarrow 2Al^{3+} + 6e^-$ Reaction II-4

H_2O Reduction: $6H_2O_{(l)} + 6e^- \rightarrow 3H_{2(g)} + 6OH^-$ Reaction II-5

Overall reaction: $2Al_{(s)} + 6H_2O_{(l)} \rightarrow 3H_{2(g)} + 6OH^- + 2Al^{3+}$ Reaction II-6

Or: $2Al_{(s)} + 6H_2O_{(l)} \rightarrow 3H_{2(g)} + Al_2O_{3(s)} + 3H_2O_{(l)}$ Reaction II-7

II.1.1.1 Processes involved in the formation of anodic aluminum oxide

Electrochemical reactions:

At the anode side: where aluminum is oxidized at the Al/Oxide interface according to the following reaction:

$$\mathbf{Al_{(s)} \rightleftharpoons Al^{3+} + 3e^-}$$ Reaction II-8

Aluminum metal forms Al^{3+} cations that will either react with reactive oxygen species (*i.e.,* O^{2-} or OH^-, see *reaction II-5* and *reaction II-6*) leading to the formation of aluminum oxide or emerging in the electrolyte solution after migration through the oxide layer [21].

$$\mathbf{2Al^{3+} + 3O^{2-} \rightleftharpoons Al_2O_{3_{(s)}}}$$ Reaction II-9

$$\mathbf{2Al^{3+} + 6OH^- \rightleftharpoons Al_2O_{3_{(s)}} + 3H_2O_{(l)}}$$ Reaction II-10

Also, these reactions may occur at two different interfaces: either at the Metal/Oxide interface or the Oxide/Electrolyte interface. *Thompson et al.* [5] study revealed the usefulness of inert Xenon ions as marker and tracer to prove the simultaneous occurrence of both reactions.

When aluminum is electrochemically anodized, the growth of aluminum oxide occurs at the anode according to the reaction:

$$\mathbf{2Al_{(s)} + 3H_2O_{(l)} \rightleftharpoons Al_2O_{3_{(s)}} + 6H^+ + 6e^-}$$ Reaction II-11

Simultaneously, dihydrogen evolves at the cathode according to the reaction II-8:

$$\mathbf{6H^+ + 6e^- \rightleftharpoons 3H_{2(g)}}$$ Reaction II-12

Assuming there are no complex anions, the Nernst equation reads:

$$\mathbf{E = E^\circ - \frac{RT}{zF} ln. \frac{[Red]}{[Ox]}}$$ Equation II-1

where: R is the universal gas constant; T is the absolute temperature in Kelvin; z is the number of electron moles exchanged for the electrode reaction, and F is the Faraday constant (96.500 C/mol). The electrode potential E at the anode (*reaction II-8*) can be written at 25°C as:

$$\mathbf{E = -1,55 - (0,00591.pH)}$$ Equation II-2

This explains that the reaction at the anode electrode (Al) thermodynamically depends on the pH value, which is determined by electrolyte and temperature.

At the cathode side: where hydronium ions H_3O^+ are reduced at the counter-electrode surface according to *reaction II-9* below:

$$2H_3O^+ + 2e^- \rightleftharpoons H_{2(g)} + 2H_2O$$ Reaction II-13

This reaction leads to a release of dihydrogen, which creates bubbles at the Pt-Ir electrode.

Alumina dissolution reaction:

At the oxide/electrolyte interface occurs the dissolution of alumina depending on the pH through:

$$6H_3O^+ + Al_2O_{3_{(s)}} \rightleftharpoons 2Al^{3+} + 9H_2O$$ Reaction II-14

Acid-base reactions:

Chemical reactions that crop up between acidic solution and pure water. We can identify three main types of acid-base reactions of the widely used acids in anodization: sulfuric (di-acid), oxalic (di-acid), and phosphoric acid (tri-acid). The anodizing of aluminum usually only occurs in acid electrolytes containing divalent or trivalent anions [13].

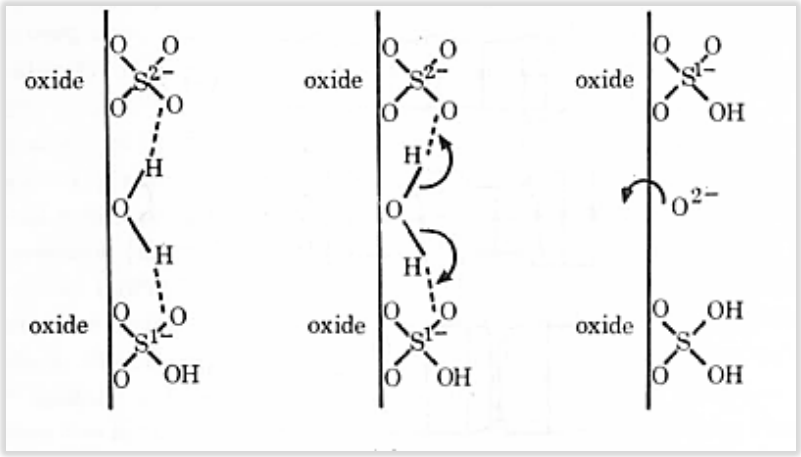

Figure II-9: Schematic representation of the production of O^{2-} or OH^- ions at the surface of a barrier layer during growth. Reprinted from reference [13].

- The dissolution reaction is activated by the acidity levels of electrolytes associated with their pKa (*i.e.,* pH). The dissociation of orthophosphoric acid is given as follow:

$$H_3PO_4 + H_2O \rightleftharpoons H_2PO_4^- + H_3O^+ \quad pKa_1=2,12 \quad \text{Reaction II-15}$$

$$H_2PO_4^- + H_2O \rightleftharpoons HPO_4^{2-} + H_3O^+ \quad pKa_2=7.21 \quad \text{Reaction II-16}$$

$$HPO_4^{2-} + H_2O \rightleftharpoons PO_4^{3-} + H_3O^+ \quad pKa_3=12.67 \quad \text{Reaction II-17}$$

For oxalic acid:

$$H_2C_2O_4 + H_2O \rightleftharpoons HC_2O_4^- + H_3O^+ \quad pKa_1=1.2 \quad \text{Reaction II-18}$$

$$HC_2O_4^- + +H_2O \rightleftharpoons HC_2O_4^{2-} + H_3O^+ \quad pKa_2=4.3 \quad \text{Reaction II-19}$$

For sulfuric acid:

$$H_2SO_4 + H_2O \rightleftharpoons HSO_4^- + H_3O^+ \quad pKa_1=3 \quad \text{Reaction II-20}$$

$$HSO_4^- + H_2O \rightleftharpoons SO_4^{2-} + 2H_3O^+ \quad pKa_2=1.9 \quad \text{Reaction II-21}$$

- Water autoprotolysis (*i.e.,* water self-ionization) where H^+ proton is transferred between two identical molecules (usually a solvent) of H_2O, one acting as a Brønsted acid and the other as a Brønsted base [22]:

$$2H_2O \rightleftharpoons H_3O^+ + OH^- \quad \text{Reaction II-22}$$

  In this case, the reaction allows the creation of oxygen ions that can either directly react with Al^{3+} ions to form aluminum oxide or migrate through the oxide at the Metal/Oxide interface and then react thus form the oxide at this interface.

- Lastly, possible recombination of OH^- in O^{2-} anion and H_2, before or during its migration within the oxide layer, takes place following the reaction:

$$OH^- + H_2O \rightleftharpoons O^{2-} + H_3O^+ \quad \text{Reaction II-23}$$

Normally, O^{2-} has no real existence in H_2O but only in solid oxides.

II.1.1.2 Ionic migration mechanisms

This paragraph will provide global considerations to gain insight into the ionic transport phenomena (*i.e.,* ions migration) in amorphous alumina.

Ions migration in the electrolyte:

The electrical potential difference (*i.e.,* voltage) between the counter-electrode (Pt-Ir gauze) and the aluminum sample leads to ions displacements and is forced through the field-assisted mechanism. In a concentrated electrolyte, the main phenomenon in transport is diffusion. Moreover, hydronium cations (H_3O^+) resulted from acid-base reactions are transported to the cathode, releasing dihydrogen bubbles. On the other hand, as introduced in *figure II-10* below, anions resulted from water self-ionization (O^{2-} and OH) and those resulted from acidic solutions (orthophosphoric, oxalic, and sulfuric acids) will be transported to the Oxide/Metal interface.

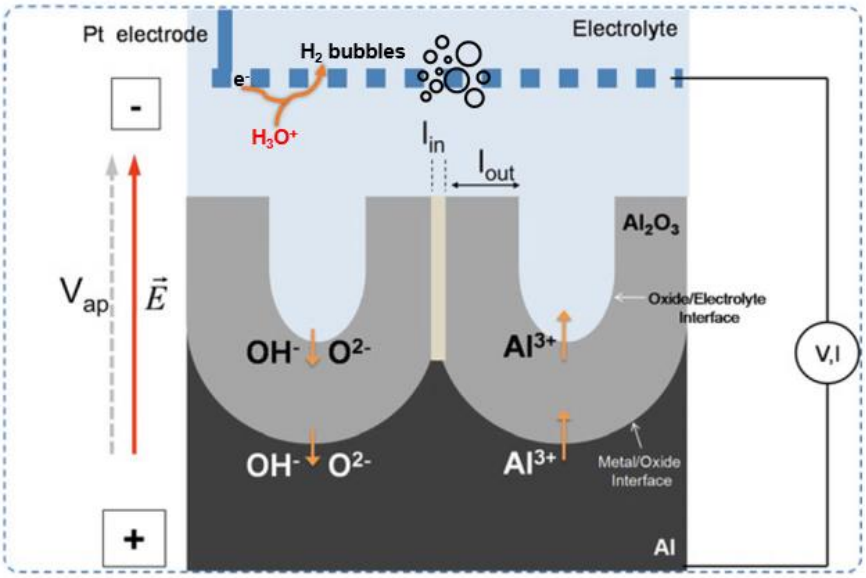

Figure II-10: Schematic illustration of the electrochemical processes at the anode: at the oxide/electrolyte interface, the Al^{3+} ions are incorporated into the solution, while at the metal/oxide interface, the oxide layer grows. Reprinted from reference [23].

Ions migration into the alumina layer:

During the growth phase of AAO templates, a balance between electrical-field-driven oxide formation at the Metal/Oxide interface and oxide dissolution at the Electrolyte/Oxide interface occurs [24].

- At the Oxide/Electrolyte interface: Al^{3+} cations migrate from the Oxide/Metal region to the Oxide/Electrolyte interface and react with the oxygen anions existing in the solution.

- At the Oxide/Metal interface: Migration of oxygen ions (OH^- or O^{2-}) through alumina's width and react with Al^{3+} ions formed in this region.

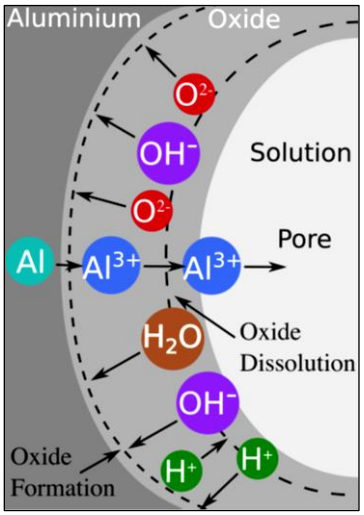

Figure II-11: Schematic illustration of the movement of charges during anodization in acid solution.

Clearly, we can claim that incorporating oxygen atoms deep into the alumina in an acidic electrolyte and the ejections of Al^{3+} cations are a key process to the formation of porous aluminum oxide. As evidenced by *Thomson et al.* [5], porous structures are formed when anodization conditions (pH<<7, current density which varies according to electrolyte type) tend not to form an oxide layer during Al^{3+} cation migration at the surface.

Besides, *Hoar* and *Mott* [24] suggested that at the base of the pores, the thickness of the barrier oxide layer is maintained by the dynamic rate balance between the following two processes occurring at the Oxide/Electrolyte interface: **i/** A high field pulling the anions toward oxide helping the transfer of oxygen through it, **ii/** The presence of hydrogen ions in the acid, which may lead to the production at the barrier-layer of a hydroxyl ion instead of an oxide ion, and **iii/** the oxide dissolution, which occurs at a greater rate compared to oxide formation at the Metal/Oxide interface since the oxide ions from the Oxide/Electrolyte interface are spread over a larger area at the Metal/Oxide interface.

Meanwhile, O^{2-} ions in contact with acid electrolyte become OH^- and move through the oxide to form a new oxide at the Metal/Oxide interface. The proton H^+ released by the oxide formation reaction would then diffuse back to the electrolyte by proton transfer between the lattice O^{2-} ions.

Impurities migration:

For porous anodic alumina, it is possible to detect the presence of ionic impurities from the electrolyte according to some analytical techniques such as Auger Electron Spectroscopy or Secondary Ion Mass Spectrometry. Taking the example of an orthophosphoric solution where phosphate ions (PO_4^{3-}) are predominantly present depending on the pH (above pH=13 in this case, anions migrating to the Al surface during anodization), it is, therefore, possible to make a profile scanning showing the presence (*i.e.,* migration) of these electrolytic species in the alumina layer due to the applied electrical field [25]. However, migrations in the oxide layer are more complex than in the electrolyte and generally depend on the electrolyte and anodizing conditions.

II.1.1.3 Mechanisms leading to pores initiation

Among various theories cited by many research groups specialized in alumina membranes, the pores' growth might result from the transport of fostered ions along the intense electric current lines and the local increase of temperature at the pores' bottom. Moreover, the electric field-assisted dissolution theory is often mentioned.

From the earliest moment of the anodization process, preexisting surface defects (*i.e.,* impurities on aluminum, grain boundaries, or pretreatment defects such as polishing, etc..) will entail non-homogeneous electrical current densities on the surface of the sample, resulting in variation in the electrical field. A scheme relating to vertically aligned electrical lines is displayed in *figure II-12* below. They are distributed over the spherical cap of oxide present at the bottom of the pore. The dissolution will take place preferentially in this area of AAO, where ions migrate more quickly.

However, the oxide layer beneath this area will be automatically compensated, and a localized dissolution should necessarily occur all over again, continuously, until a dissolution/growth equilibrium of the oxide is established.

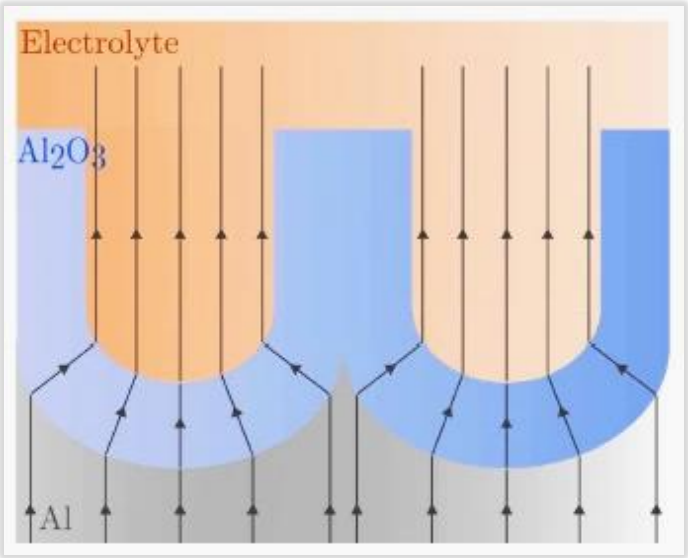

Figure II-12: Illustration of field lines distribution in porous aluminum oxide. Reprinted from reference [12].

Dissolution might also be attributed to the incorporation of impurities owing to field-effect as evidenced by *Murphy* and *Michaelson* [26]: variations in electrical fields generate a migration flux of hydrated impurities that penetrate throughout areas (*i.e.,* pores' bottom) subjected to these fluxes. Porous alumina would then be a hydrated compound, easier to dissolve than pure alumina. Therefore, flux and species migration under the effect of the electrical field would facilitate localized dissolution.

This mechanism leads to the appearance of penetration paths through which a higher rate of ions migration is favored: the electric field lines directed towards the defects seem to be more intense than elsewhere. There is a consequent increase in local field strength for the more advanced penetration paths, enhancing their development through field-assisted dissolution, which effectively polarizes the Al–O bonds, allowing more ready Al^{3+} dissolution than in the absence of the field [5].

Additionally, the localized increase in the electrolyte temperature could explain the number of chemical reactions involved at the bottom of the pores. Current density is dense at the bottom of the pores, leading to local heating by the joule heating effect. The localized temperature phenomenon can bring on autocatalysis of reactions in these areas [27].

Another hypothesis by *O'Sullivan et al.* detailed a physical [13] mechanism for field-assisted chemical dissolution of anodic oxide and qualitatively explained the dependence of the porous morphology on anodizing conditions. They suggested that the dissolution might arise from the Al-O bonds polarization due to the electrical field's increase at the bottom of the pores. Briefly, the electrostriction effect[17] would cause the polarization of the Al-O bonds close to the electrolyte/alumina interface. Thus, the oxygen atom would be attracted to the oxide layer and the Al atom to the electrolyte. Given the fact that the Al-O bond is strongly polarized, the binding energy of the two atoms would be reduced, which would favor its rupture, therefore its dissolution [13][28].The flow mechanism of steady-state pore generation has been supported by the theoretical modeling of *Houser* and *Hebert* [29], which highlighted not only the ionic migration under the gradients of mechanical stress and electric potential but also its implication on the Newtonian viscoelastic flow of oxide materials from the pore base toward the pore bottoms and further into the cell walls.

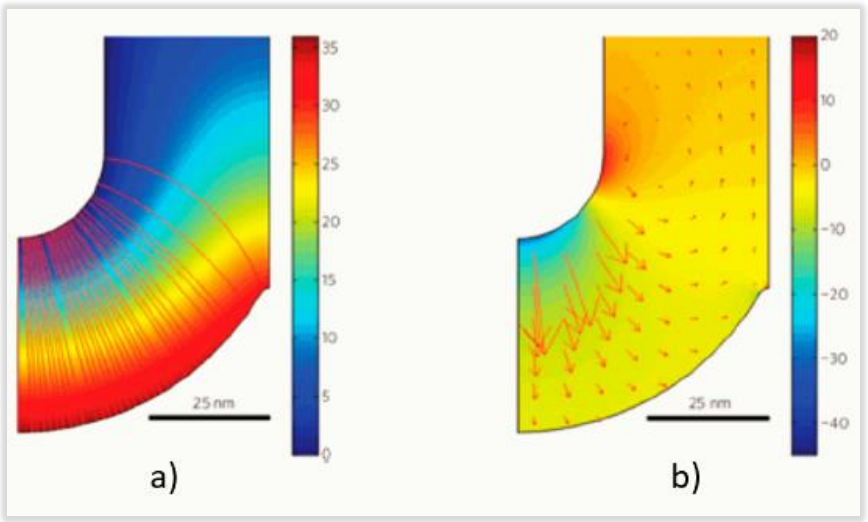

Figure II-13: a) Simulated current lines and potential distribution for porous AAO growth in oxalic acid at 36 V (color scale represents the potential in volts). b) Simulated flow velocity vectors and mean stress (color scale represents dimensionless stress).

[17] Electrostriction: property of all electrical nonconductors, or dielectrics, that manifests itself as a relatively slight change of shape, or mechanical deformation, under the application of an electric field.

Further investigations on the mechanisms of pores' organization were held to shed light on the role of non-linear dynamics in the formation of self-assembled nanostructures. *L. G. Stanton et al.* [30] developed a mathematical model which incorporates the electrochemical transport of oxygen ions within the oxide layer and the chemical reactions at the metal-oxide and oxide-electrolyte interfaces. On the other hand, *Fábio D. A. et al.* [31] suggested mathematical modeling (a scaling approach) to explain pattern nucleation in an oxide layer.

II.2 General Structure of nanoporous anodic aluminum oxide (AAO)

The well-ordered nanoporous aluminum oxide is distinguished by its geometrical parameters such as the pore's diameter, the distance between two adjacent pores, the thickness, and the barrier layer. These parameters could be tuned and controlled according to anodization interdependent parameters, namely the applied voltage, the electrolyte type, concentration, temperature, and exposure time. In the following paragraphs, a detailed bibliographic review was carried out, offering a theoretical and experimental background of the geometry tuning of the AAO.

II.2.1 Pore diameter (D_p)

Anodizing voltage seems to be the most critical factor affecting the final geometry of the nanoporous alumina matrix. A microscopical analysis was performed by *O'Sullivan* and *Wood* of AAO [13], formed at a potentiostatic regime in orthophosphoric acid (H_3PO_4) electrolyte. Their study revealed that the pore diameter (D_p) was directly proportional to the applied voltage (U), according to the following equation:

$$\mathbf{D_p = 1.29 \times U} \qquad \text{Equation II-3}$$

where: D_p is the pore diameter in nm; U is the applied voltage for anodization in V and 1.29 a constant in $nm.V^{-1}$ referring to the pore increasing rate.

Their work drew attention to the effect of electrolyte concentrations, which did not significantly influence the pore diameter under low voltage. In high concentrated electrolytes (decreasing electrolyte pH), larger pores could be formed due to the highly

chemical dissolution of oxide [32]. Moreover, the study carried out by *Sulka* and *Parkoła* indicated that the pore diameter decreases with decreasing temperature [7].

K. Nielsch and his co-workers underlined that the smallest pores could be obtained in the lowest pH value, *i.e.*, in the strongest acid [33]. According to their best self-ordering AAO condition, they obtained a perfect hexagonal pores' arrangement in their study. Their diameter can be calculated according to the following equation:

$$\mathbf{D_p} = \sqrt{\frac{\%\mathbf{P}\times\sqrt{\mathbf{3}}}{\boldsymbol{\pi}}} \times \mathbf{U} \times \mathbf{k} \qquad \text{Equation II 4}$$

where: %P is the porosity (in this case 10%), k is the proportionally constant (the definition is given in *paragraph II.2.6*).

II.2.2 Electrolyte type

The electrolyte choice (*i.e.,* type, pH, and concentration) used for anodizing depends on the voltage range applied. It widely affects the final and desired template structure. Some researchers pointed out the effect of the acidic electrolyte (pH < 4) on the quality of the self-organization of pores. Among these acids, we can quote sulphuric, oxalic, orthophosphoric acids that are more commonly used than citric, maleic, malonic, tartaric acids due to the better-obtained self-organization of the pores through the redistribution of stress within the oxide (*i.e.*, by adjusting the mechanical stress between the metal/oxide interface according to the size of the anions). Furthermore, each acid has its conductivity (*i.e.,* ion migration) and dissolution rate. It is the balance of these factors that will influence the current of the steady-state regime (*Cf., Figure II-2*).

As the increase in applied voltage during anodizing implies an increase in current density, this leads to the consequence that each acid will be used preferentially in a voltage range adapted to its properties. Therefore, acids with lower current density at high voltages and acids with a high current density at low voltages must be used: Sulphuric acid has a higher current density than oxalic acid and orthophosphoric acid.

Taking the example of sulphuric acid, having the strongest acid dissociation constant pKa=-3, which has a very high current density, will be used preferentially for low voltages

between 7 and 70 V (with optimum self-organization at 25 V that allows obtaining the best organization of the pores). On the other hand, oxalic acid (with a first acid dissociation constant pKa=1.2) has a high current density as well, is used for voltages between 40 V and 160 V (with an optimum at 40 V) [28][34][35]. Lastly, orthophosphoric acid with average current densities and acid dissociation constant of pKa=2.12 is used between 60 and 235 V with an optimum at 170 V. Whereas for even higher voltages, the use of tartaric, malic, or citric acid is suggested, and their acid dissociation constants are also higher.

The self-ordering voltages reported until now and the corresponding cell diameters are summarized in *figure II-14* below as summarized by *Sachiko Ono et al.* [6].

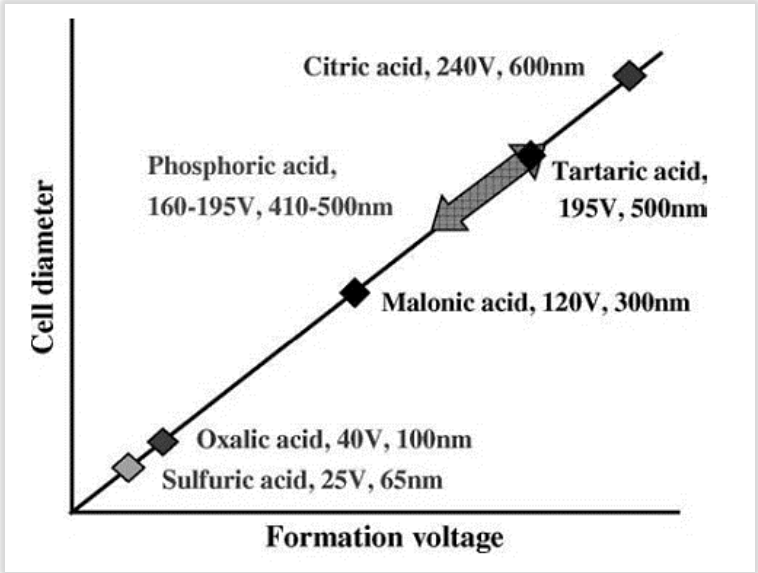

Figure II-14: Result view of self-ordering voltages and corresponding cell diameters reported in reference [6].

The ranges of voltages cited above are not constant. However, it is possible to use the acidic electrolytes above (or below) these ranges by decreasing (or increasing) the electrical density either by using lower acid concentration or by lowering the electrolyte's temperature.

Electrolytes	Potentials (V)	Formula	Concentrations	Temperatures (K)
Sulfuric acid	8 – 70	H_2SO_4	5 – 10 vol%	273 – 288
Oxalic acid	40 – 160	$(COOH)_2$	0.25 – 3wt%	274 – 288
Phosphoric acid	60 – 235	H_3PO_4	1 – 10 vol%	273 – 277
Glycolic acid	60 – 150	$HOCH_2COOH$	1 – 10 vol%	283 – 293
Tartaric acid	235 – 240	$(CHOH)_2(COOH)_2$	2 – 4 wt%	278
Malic acid	220 – 450	$C_2H_2OH(COOH)_2$	2 – 4 wt%	283 – 293
Citric acid	270 – 370	$C_3H_4OH(COOH)_3$	2 – 4 wt%	293

Table II-1: Solution and conditions for aluminum anodization in acid-based electrolytes used for the formation of porous alumina, their range of concentration, with the tension of better self-organization. Reprinted from reference [35].

Acids also influence the diameter and shape of pores. For instance, sulphuric acid will form smaller diameters and more cylindrical-shaped pores than oxalic acid or phosphoric acid. Thus, anodization in sulphuric acid leads to obtaining diameters around 10-15 nanometers (before the pore widening process), in oxalic acid around 20-30 nm, and in phosphoric acid *ca.* one hundred nanometers [33]. Later on, it is well understood in literature how to adapt diameters after anodization by an anisotropic acid etching (mainly in orthophosphoric acid).

Subsequently, the temperature is also an essential factor affecting anodization kinetics. An increase in the electrolyte temperature will accelerate ions migrations (*i.e.,* the flow of current) and thus accelerating chemical reactions. Lowering the temperature is meant to limit the reaction rate when large voltages are needed (*e.g.*, anodization at 170 V at a very low temperature, close to 0°C, would be better) [36]. It also affects the hexagonal self-organization of the pores. Most research groups agreed on an optimum of around 15°C

to 17°C for oxalic acid 3wt% at 40 V would lead to the best pore organization. Also, the higher the temperature, the greater the porosity.

However, it remains unclear to what extent such factor may affect pore diameter and the barrier layer's thickness. Predictions made by *Keller et al.* revealed the independence of temperature from pore diameter and the barrier layer [37]. *Hunter et al.* [38] and *O'Sullivan et al.* [13] have seen the temperature's effect differently; that is, temperature could decrease the ratio of the thickness of the barrier layer in accordance with the voltage, thus the cell size. However, *O'Sullivan*'s experiments have shown that the pores' diameter does not seem to change with the temperature.

To sum up, the influence of temperature on the formation of AAO, namely, on the porous structure, remains relatively low compared to the effect of the voltage or the electrolyte type and concentration. Its main impact on the current density at constant voltage and, therefore, on the speed of anodization was noticed.

Furthermore, as for the temperature, the increase in the concentration of the acidic electrolyte (pH lower than 2.4 to form a porous layer) implies an increase in reactivity (*i.e.,* dissolution of aluminum) and migrations, thus the speed rate of anodization [39].

II.2.3 Interpore Distance (D_{int})

As ascribed by *Nielsch* et *al.* [33], interpore spacing (D_{int}) between two adjacent nanocells at the steady-state growth regime is linearly proportional to the anodizing voltage with a constant value of approximately 2.5 nm^{-1} in an acidic solution according to the *equation II*-5 (see *figure II-15* below):

$$\mathbf{D_{int} = 2,5 \times U} \qquad \text{Equation II-5}$$

However, this empirical formula is not valid for hard anodization (HA) under conditions in which a high electric field (E) is exerted across the barrier layer due to high current density (j) during anodization [40].

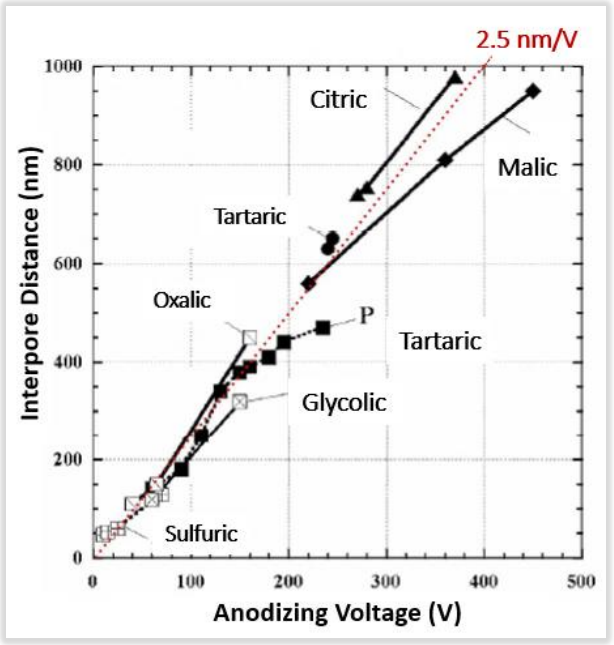

Figure II-15: Evolution of the interpore distance (in nm) of nanoporous alumina as a function of anodizing voltage (in V) in various acidic solutions [2].

It is believed that *equation II-5* is only valid for specific operating methods. *O'Sullivan* and *Wood* [13] have conclusively claimed that acid electrolyte concentration is inversely proportional to the interpore distance. On the other hand, *Hwang et al.* [41], *A.P. Li et al.* [42], and *Ebihara et al.* [43] conducted an in-depth study on this subject; their empirical expressions on the relationship between the interpore distance (D_{int}) and anodizing potential (U) for each acidic electrolyte is described in *table II-2* below. Performing anodization in oxalic acid was assessed by *Hwang* and his co-workers, as the interpore distance is independent of the temperature of the acid solution at the constant anodizing potential regime.

Acid electrolytes	Interpore Distance (D_{int})	Anodizing potential range (U)
Sulfuric acid	$\mathbf{D_{int} = 12.1 + 1.99.U}$	U = 3 - 18 V
Oxalic Acid	$\mathbf{D_{int} = 14.5 + 2.00.U}$ $\mathbf{D_{int} = -1.70 + 2.81.U}$	U ≤ 20 V U ≥ 20 V
Oxalic Acid	$\mathbf{D_{int} = -5.2 + 2.75.U}$	U = 20 - 60 V

Table II-2: Empirical expressions on the relationship between the interpore distance (D_{int}) and anodizing potential (U). Reprinted from the references [41][42][43].

A different study conducted by *Sulka et al.* [7] aimed to understand the influence of temperature on the nanopores arrangement in 20%wt sulphuric acid. As their results have shown, there is a dependence between interpore distance and anodizing temperature at a potentiostatic regime. At a given anodizing potential, the pore diameter increases with the increasing temperature of anodization, as displayed in *figure II-16* below.

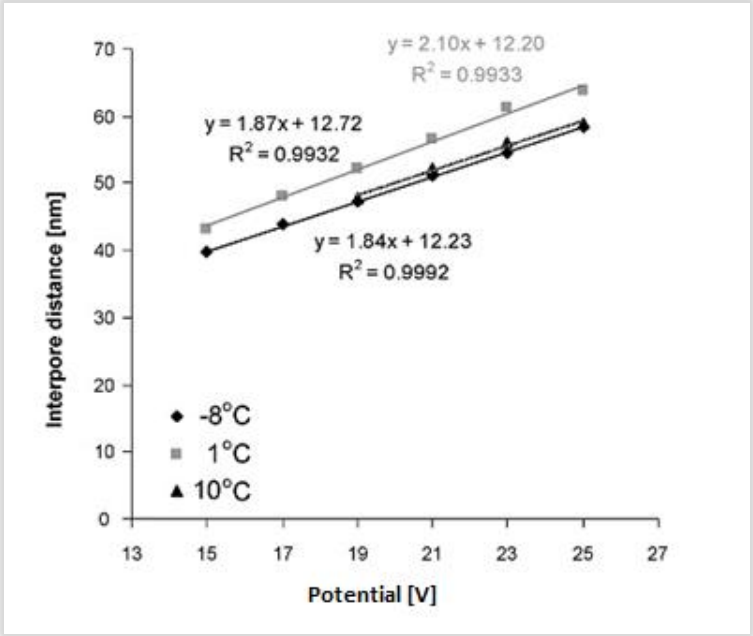

Figure II-16: Average interpore distance in nm (D_{int}) as a function of anodizing potential in V at various temperatures [7].

II.2.4 Pore Wall (D_W) thickness and Barrier Layer (D_{BL})

Pore wall (*i.e.,* the oxide sidewall) is mainly formed due to diffusion of OH^- and O^{2-} acid anions, driven by the electrical field slowly through inward migration due to their relatively large size [44][45]. Subsequently, the wall exhibits a duplex structure in terms of chemical composition, with an acid anion contaminated outer oxide layer and a relatively pure inner oxide layer adjacent to the metal/oxide interface as evidenced in *figure II-17* below.

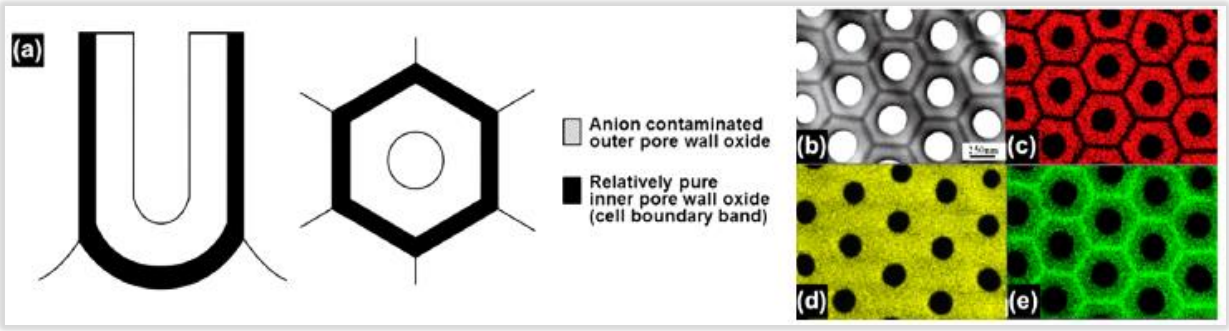

Figure II-17: a) Schematics illustrating the duplex structure of pore walls of porous AAO: vertical (left) and transverse (right) cross-sections. TEM plane view b) of H_3PO_4-AAO and the corresponding X-ray diffraction maps of the elements: c) phosphorus, d) oxygen, and e) aluminum [46].

Starting with the knowledge that the thickness ratio of the inner to outer pore wall oxide layer increases in the order: *sulfuric acid < oxalic acid < phosphoric acid < chromic acid*, they depicted the same order of thickness ratio for the barrier oxide at the bottom of pores and correlated it to the rates of oxide formation at the same anodizing potential (U). *Thompson* and *Wood* [45] proposed an AAO structure formed in major acids (*figure II-17-a*) with an inner pure alumina layer (away from the pore center, schematized in black) and an outer anion-contaminated layer (near the pore center: external part of the alumina wall, schematized in grey).

Eventually, the ideal structure consists of a densely packed hexagonal array of ordered pores of uniform size, as shown in *figure II-17-b.*

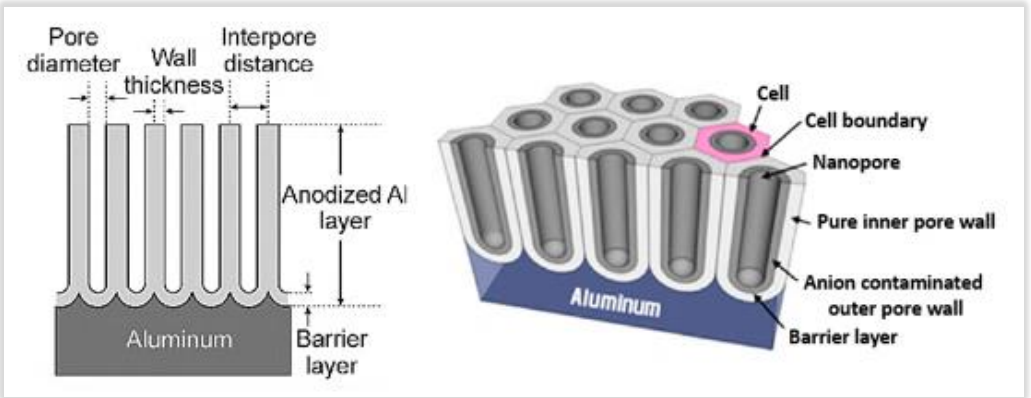

Figure II-18: Idealized structure of anodic porous alumina and a cross-sectional view of the anodized layer. Reprinted from references [47][48].

On the other hand, while AAO nanochannels grow in-depth, a dense oxide layer at the bottom of pores is formed during the process of anodization, allowing current to flow

through the layer's defects. Its dielectric aspect inhibits metals' growth inside the AAO, which requires a well-controlled wet etching process to remove it. Some studies have demonstrated that the type and concentration of acid electrolytes and anodizing potential have direct relevance to the barrier layer thickness [13][37][49][50].

Additionally, initial studies suggested that the barrier layer thickness depends on the anodizing voltage with a proportionality constant of 1.2 $nm.V^{-1}$ for porous structures [13][37]. Concisely, since anodizing potential has a proportional influence on the thickness of the barrier layer of AAO, *figure II-19* below summarizes the effect of anodizing potential on the thickness of barrier layers for the porous anodic films formed in different solutions [35].

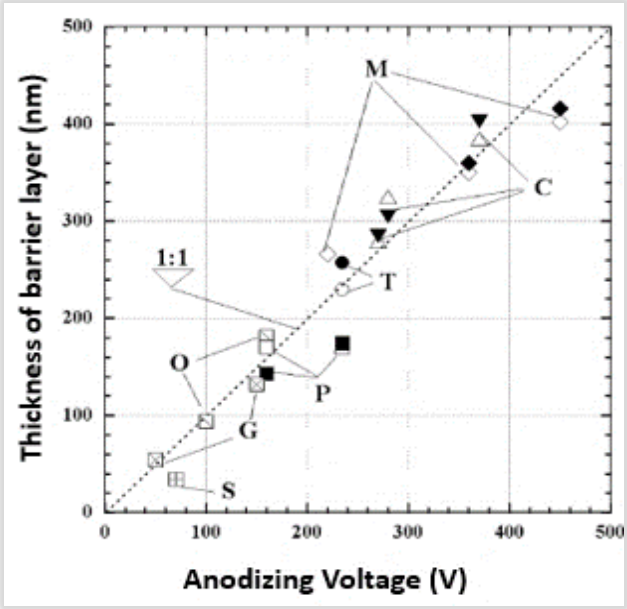

Figure II-19: Effect of anodizing potential on the thickness of barrier layers for the porous anodic films formed in different solutions. Solid marks: measured values; blank marks: calculated values from the half-thickness of the pore walls ($D_{BL} \approx D_{int}/2$). Reproduced from reference [35].

II.2.5 Pores' widening: Wet-etching process

The advantage of wet and isotropic etching is the complete control over pores size. This process, performed mostly in orthophosphoric acid at different temperatures and concentrations, is extensively used as the most attractive feature of porous AAO for template-based nanofabrication.

To adjust the diameter (*i.e.,* pore widening process) of the nanopores after the second anodization, 5%wt orthophosphoric acid is widely used as an alumina etching solution during this thesis. Also, alongside voltage, which is the main parameter responsible for initial pores diameter, the pores diameter distribution depends on the pores widening duration and temperature. It is employed for tuning the diameter and reducing the distribution.

It should be noted that, before the etching process, the thickness of a cell wall is thinner than the thickness of the barrier layer at the bottom of the pore (see *figure II-19* above).

II.2.6 Surface porosity and Pore Density

Given the fact that pores have periodic internal pore structures and hexagonally organization in the plane, it is possible to define easily macroscopic parameters such as surface porosity and pore density.

The relation that relates the porosity P to the surface occupied by the pores and the total surface, therefore to the interpore distance (D_{int}) and the pore diameter D_p, is given as follow:

$$\mathbf{P}(\%) = \frac{\pi}{2\sqrt{3}} . \left(\frac{\mathbf{D_p}}{\mathbf{D_{int}}}\right)^2 \qquad \text{Equation II-6}$$

Furthermore, porosity depends on the ratio of oxide growth and its chemical dissolution in acidic solution. Hence, pH is the main parameter influencing porosity at the wet-etching step.

On the other hand, pore density ρ (pores number/cm²) sheds light on the total number of pores occupying the surface area of 1cm². For ideally ordered porous AAO, it is defined as follows:

$$\boldsymbol{\rho(cm^2)} = \left(\frac{2}{\sqrt{3} . \mathbf{D_{int}^2(nm^2)}}\right) \times \mathbf{10^{14}} \qquad \text{Equation II-7}$$

This parameter is tunable in wide ranges by properly choosing anodization parameters and wet-etching conditions. Besides, its exploitation is extended for synthesizing a diverse range of nanostructured materials in the forms of nanodots, nanowires, and nanotubes and for developing functional nanodevices.

II.2.7 Volume expansion of anodic aluminum oxide

After anodization is performed in an acidic medium relying on parameters as previously evidenced, an increase in the thickness of AAO was observed. During the oxide growth at the Metal/Oxide interface, a volume expansion occurs due to the lower atomic density of aluminum in Al_2O_3 compared to metallic aluminum. During the oxide growth, the significant volume expansion $\zeta = \frac{V(Al_2O_3)}{V(Al)}$ [18] gives rise to mechanical stress in the barrier layer, forcing pore walls to grow only in the upright direction [33]. The incorporation of electrolyte-derived anionic species (O^{2-} and OH^-) within the anodic oxide near the oxide/electrolyte interface was also associated with volume expansion.

However, not all oxidized Al gives rise to aluminum oxide, and thus the real volume expansion was found to depend on the applied voltage and electrolyte composition [23].

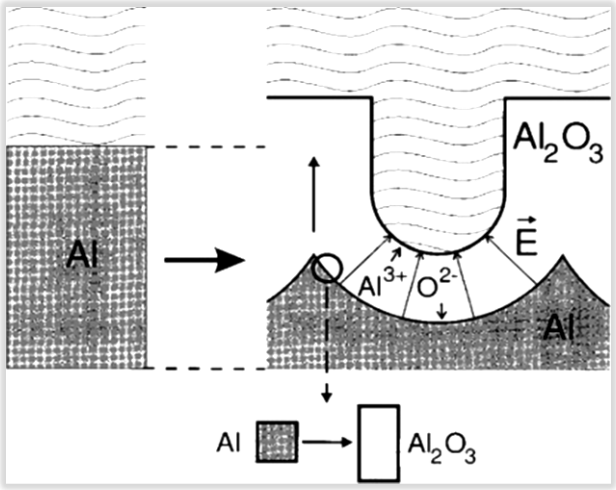

Figure II-20: Expansion of Al during anodic oxidation, depicting on the left level of the unoxidized metal surface. Reprinted from reference [34].

Moreover, the volume expansion factors were found to vary between 1.25 and 1.9 depending on the anodizing parameters. The variation is explained in connection with the electric field, ion transport number, temperature effect, concentration, and acids' activity [51].

[18] The volume expansion factor is the ratio of the volume of the AAO formed to the volume of Al consumed, and simplified to the thickness ratio of AAO formed to Al consumed.

II.2.8 Post-treatment of the AAO: Annealing and HF Deoxidization

After the double anodization and the pore widening process, the nanoporous alumina is ready to be used as a guidance matrix for the confined growth of nickel nanowires. However, a pretreatment process is required. Post-thermal treatment of AAO aims to get rid of, if they exist, organic impurities and possible adsorbed H_2O molecules. For this reason, the range of temperature is chosen to be below the phase-changing temperature (~1050 °C) to avoid change in the amorphous structure of alumina and to obtain a dried α-phase of nanoporous alumina.

For depositions inside nanoporous alumina made directly on silicon, electrical contact at the bottom of the pores is not ensured homogeneously due to the electrochemical oxidation of silicon formed at the end of the anodizing process and the wet-etching process.

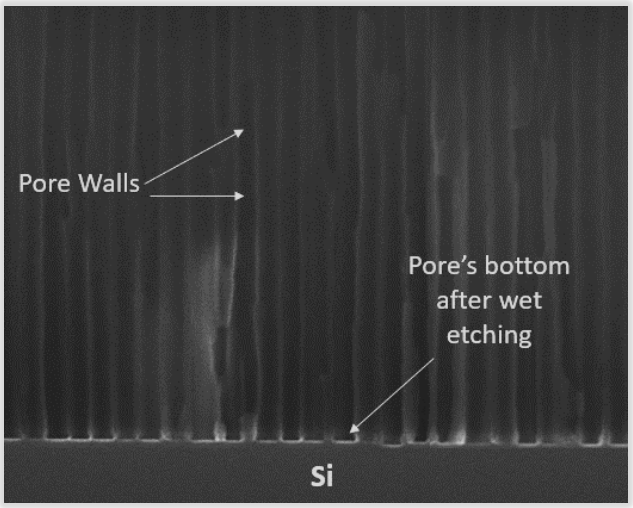

Figure II-21: SEM cross-sectional image of porous anodic aluminum oxide after the wet-etching process. The barrier layer was removed from the pores' bottom, reaching the silicon substrate.

To overcome this inhomogeneity, silicon oxide is deoxidized with Hydrofluoric vapor acid (HF). The latter being volatile, exposing the sample to such vapors allows silicon deoxidation without etching nanoporous alumina, thus allowing a better growth of embedded nickel nanowires inside it. Without a prior post-heating treatment of the sample, H_2O molecules are still embedded inside the alumina pores; the HF vapors will solubilize and etch the alumina, leading to an increase in pores' diameter.

II.3 Conclusion:

The fabrication of anodic aluminum oxide can be carried out using a double anodization process. Special attention was paid to the effect of experimental conditions on the AAO structure to obtain a homogeneous and ordered porous layer. Also, anodic alumina is considered a versatile mold: the interpore distance can vary from 20 nm to more than 900 nm, pores diameter from ten nanometers or so to over 500 nm. The novel and tunable structural features of porous AAOs have been intensively exploited for synthesizing a diverse range of nanostructured materials in the forms of nanodots, nanowires, and nanotubes [8].

The following paragraph of this part is devoted to dissecting the experimental processes of the double anodization technique. It will provide a framework onto which we can fabricate a suitable porous anodic alumina for the confined growth of nickel nanowires later on.

III. Experimental Section: Elaboration of Anodic Aluminum Oxide

As previously reported, the development of the nanostructures (*i.e.,* nanowires growth) requires good control of the porosity of the AAO. By tuning the anodization parameters, which directly impact the kinetics of the pores' formation, we tend to control the thickness of AAO, which would be the final length and diameter of the nanowires when grown unto the matrix. The first anodization has two main interests: **i/** removing a controlled thickness of aluminum and **ii/** obtaining a pre-patterned aluminum surface after the wet etching. The latter, performed in the right conditions, would predict the final pores' size (*i.e.,* porosity and density).

Strikingly in a way that attracts attention, we suggested during this thesis two AAO geometries to maximize specific platinum surfaces. Both types of alumina used are elaborated with a double anodizing process at 38 V and 54 V with enlargement times 9 min and 12 min, leading to respective nanopore diameters of 50-55 nm and 100-110 nm.

In a nutshell, the preparation of alumina membranes is a flexible process to control and vary the architecture and requires a multi-step process:

- **First step**: The samples are cleaned in Acetone then isopropanol to remove microparticles and organic contaminations.
- **Second step**: First anodization in an acidic electrolyte in accordance with the applied voltage, temperature, concentration, and duration. Such parameters have a direct effect on the pore size, interpore distance, thickness of the barrier layer, and the length of pores (*i.e.,* thickness).
- **Third step**: The wet and isotropic etching by dipping the sample in an appropriate acidic solution to remove the first inhomogeneous anodized layer.
- **Fourth step**: Second anodization in the same solution mentioned in the second step, keeping the same parameters.
- **Fifth step**: Second wet and isotropic etching to enlarge pores and remove the barrier layer at the pores' bottom until reaching the Silicon substrate.
- **Sixth step**: Thermal treatment followed by an HF deoxidation.

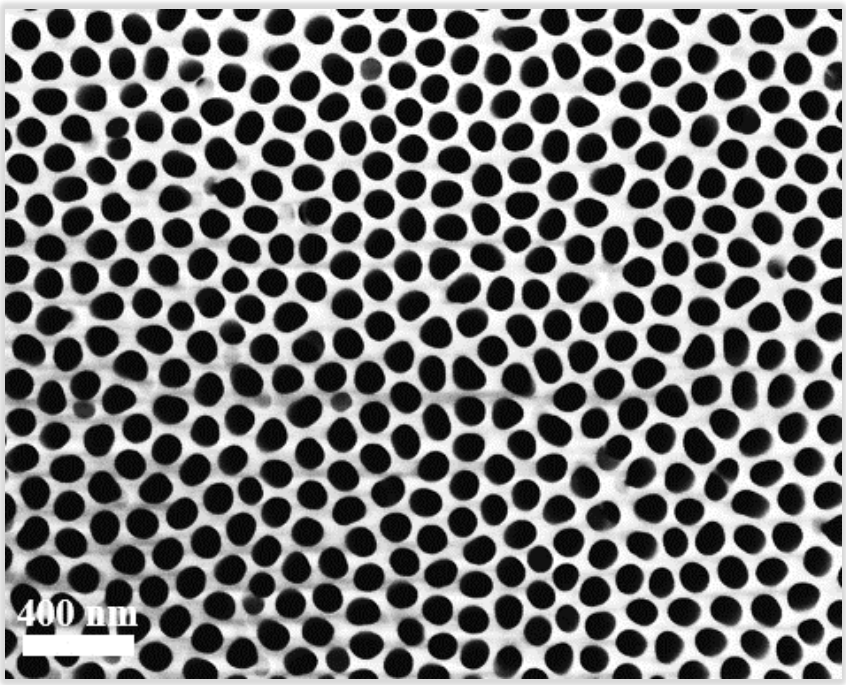

Figure II-22: A scanning electron microscope (SEM) image of the nanoporous anodic aluminum oxide fabricated during this work through the double-step anodization process in 3%wt oxalic acid, under potentiostatic regime, with an applied voltage of 54 V at 23°C.

The next paragraphs will entail experimental protocols aiming at the realization of nanoporous alumina membranes. They also describe the electrochemical processes involved in the realization of these structures and tuning their geometry.

III.1 Experimental setup

The template used throughout this Ph.D. thesis was made on a highly doped p-type silicon wafer (very low resistivity ρ (ρ < 0.01 Ω.cm) by electrochemical oxidation of a 1 µm and 5µm aluminum thin layer deposited through physical vapor deposition PVD sputtering in an evaporation set-up under a vacuum of approximately 10^{-7} mbar. The mirror-like aluminum surface indicates the surface's low roughness. Also, post-deposition annealing was performed at 300°C would improve the adhesion between the aluminum film and silicon substrate and increase the Al grain size [21][52].

Aluminum anodization was carried out in a PVC (Polyvinyl Chloride) electrochemical cell, chemically resistant to the acidic electrolyte, developed in the *IRIG/SiNaPS* laboratory and manufactured for this thesis, as shown in an apparatus in *figure II-23*.

The system consists of: **i/** the cell with a mechanical holder for the sample, **ii/** a circular Platinum-Iridium gauze acting as counter-electrode, **iii/** a stirrer to assure solution homogeneity which guarantees stable conditions during anodization and to remove hydrogen bubbles effectively, and **iv/** a computer-controlled *Keithley™ 2612A* Source meter combined with *TSP® Express* software. All components were mounted in a closed metal box for safety issues.

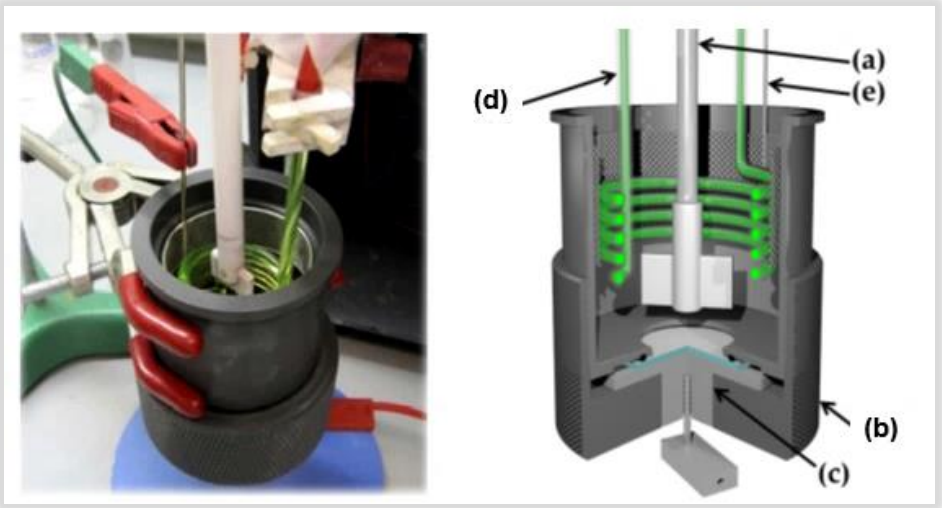

Figure II-23: Electrochemical cell setup used for anodizing aluminum on p-type silicon substrate: a) Stirrer, b) 3D model of the PVC cell, c) Metal cap that ensures electrical contact and mechanical cohesion between the cell and the sample (electrode), d) Flowing cooling Liquid system to adjust the temperature of the electrolyte, e) Cylindrical platinum gauze as counter-electrode.

The sample (Al/Si substrate) is placed on the backside of the PVC cell and electrically contacted by a stainless-steel piece whose role is to press the front side of the substrate, while the front side (where the aluminum layer has been deposited) is in contact with the acidic solution. The Platinum-Iridium cylindrical gauze's relevance (*i.e.,* counter electrode) is to facilitate the escape of hydrogen bubbles and removes local heat on the surface, and allows a homogenous diffusion of anions into pore channels. It is placed into the electrolyte, far from the sample, to ensure parallel electric field lines on the entire surface of the Al surface. Finally, a cap is screwed under the cell to assure its mechanical cohesion. To have more precise control of the anodization process in this work, the voltage was applied by *Agilent N8741A DC* power supply. The electric current was monitored and recorded using *Agilent Truevolt 34461A* digital multimeter. The apparatus was controlled by a home-built computer script. The control of the experimental conditions is critical to maintaining a stable and homogeneous medium during anodization.

III.2 Fabrication of AAO membranes

In this study, I took advantage of the existing data in the literature and previous laboratory works. I then redefined these parameters and adapted them to the fabrication process: temperature, voltage, anodizing time, and the wet-etching duration.

As previously evidenced, surface defects promote the growth of nanopores on the surface of aluminum. A large number of small pores are initiated from these concavities. When the anodizing setup is mounted, anodization was carried out in 3%wt oxalic acid at 34 V at room temperature (23°C). The voltage, temperature, and acid concentration have been adapted to the final pore's size.

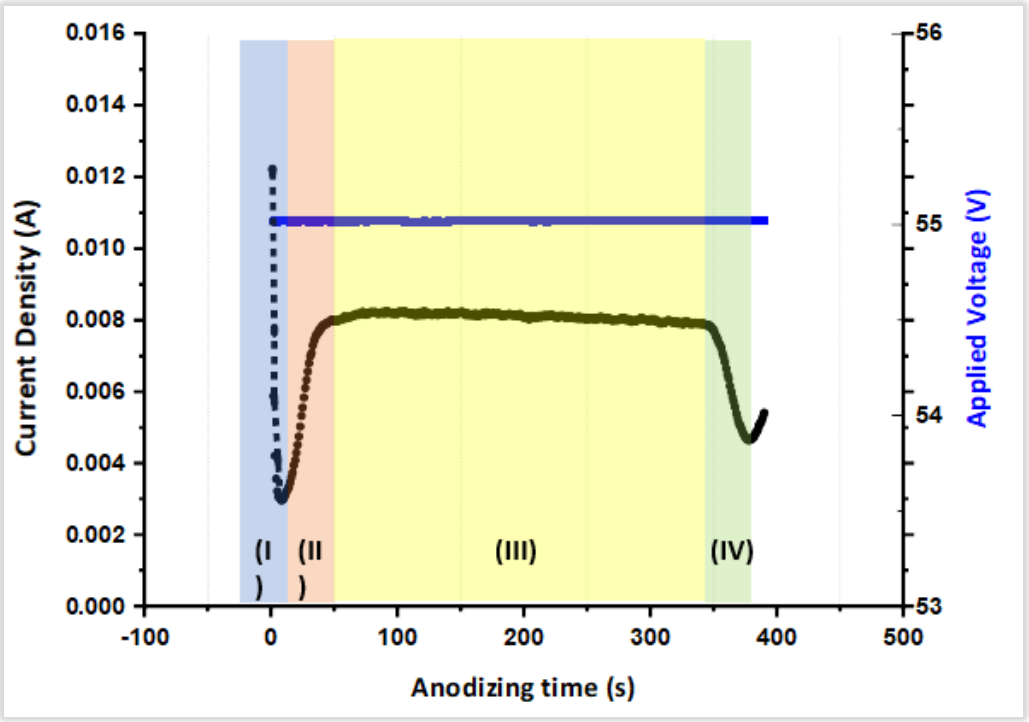

Figure II-24: Schematic diagram of the evolution of current (j) *vs.* time (t) curve for one-step anodization in potentiostatic regime, for an aluminum/silicon (1 µm) sample anodized at 54 V in 3w% Oxalic acid at 23°C. The blue plot refers to the applied constant voltage of 54 V; the black plot refers to the evolution of the current density over time.

From the plot displayed above, we can depict four different regimes during the anodization process [53]:

- **Stage I**: the growth of a non-porous oxide on the surface of aluminum in addition to its native oxide naturally present on the surface. The total resistance of the system increases, whereas the current decreases.
- **Stage II:** The beginning of aluminum oxide dissolution. The pores grow preferentially over the surface defects that locally (*i.e.*, where the electric field concentrates), allowing the diffusion of Al^{3+} and O^{2-} ions through the compact oxide layer, thus increasing the oxidation current.
- **Stage III:** A permanent anodizing regime marks this phase. The aluminum oxidation current and the total ohmic resistance of the system remain constant because of the steady-state between the dissolution of alumina and aluminum's oxidation.

- **Stage IV:** Characterized by a drop of the current: the end of the anodization process (total oxidation of aluminum) alongside the silicon oxidation, an increase of the total resistance of the system.

Applying merely a one-step anodization process in 3%wt oxalic acid at 35 V followed by a pore widening process in 5%wt orthophosphoric acid at 35°C, *figure II-25* displays an image of the resulting nanoporous structure, which lacks pores' homogeneity. Also, the morphology of the aluminum surface (*figure II-25-a)* after one-step anodization shows a random dispersion of small pores occurs. *Figure II-25-b* illustrates the final state of the porous template after pores enlargement in 5%wt orthophosphoric acid (H_3PO_4) at 35°C. After this process (one-step anodization), the quality of AAO is not as good as AAO obtained by double-anodization in *figure II-22* earlier.

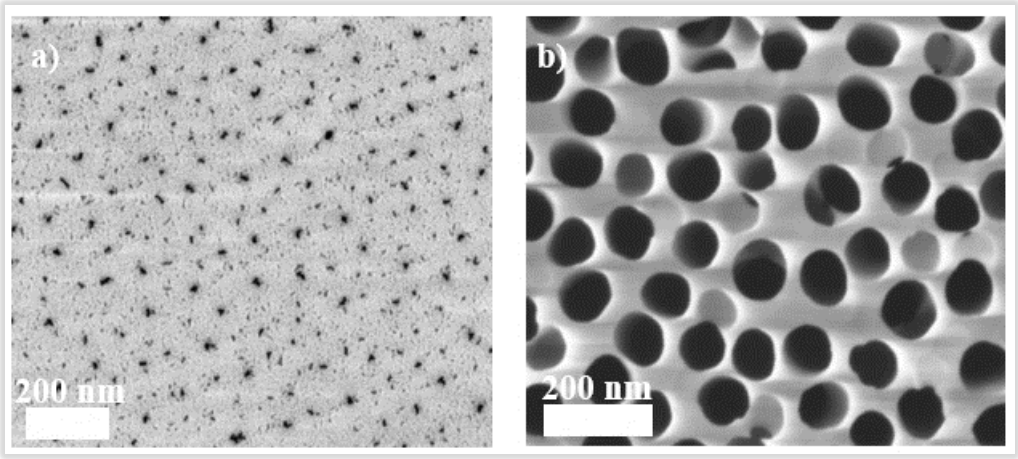

Figure II- 25: SEM micrographs of a) One-step anodization of thin aluminum layer deposited on p-type silicon formed in 3%wt. Oxalic acid at 34 V, b) Result of the wet isotropic etching performed in a 5%wt orthophosphoric acidic solution at 35°C.

The one-step anodization has shown badly ordered nanopores. In order to establish hexagonally ordered pores, the double-anodization process will be applied, following the steps below:

III.2.1 First anodization:

First and foremost, one-step anodization must adapt the quantity of remaining aluminum needed for the second anodization. Real-time oxidization current measurement enables accurate control of anodizing evolution and calibration of oxidization speeds, as illustrated in *figure II-26* below. Accordingly, for an initial aluminum thickness of 1µm,

the first anodization was performed for about 90 seconds. By controlling anodization time, we controlled the length of the initial nanopores. The anodization should be interrupted in the third phase (*stage III, figure II-24)*, known as the steady-state growth of AAO (*see figure II-24* above).

We have followed the variation in initial pores diameter throughout many experiments held in 3%wt oxalic acid solution at different anodization voltages (24 V, 34 V, 54 V, and 64 V); we have followed the variation in initial pores diameter according to voltage dependence. According to the graph represented in *figure II-26* below, it can be shown that the relation between the mean pore diameter and the anodizing voltage is linear, as previously cited in *II.2.1* following the equation:

$$\mathbf{D_p = 1,13 + 0,47.U}$$ Equation II-8

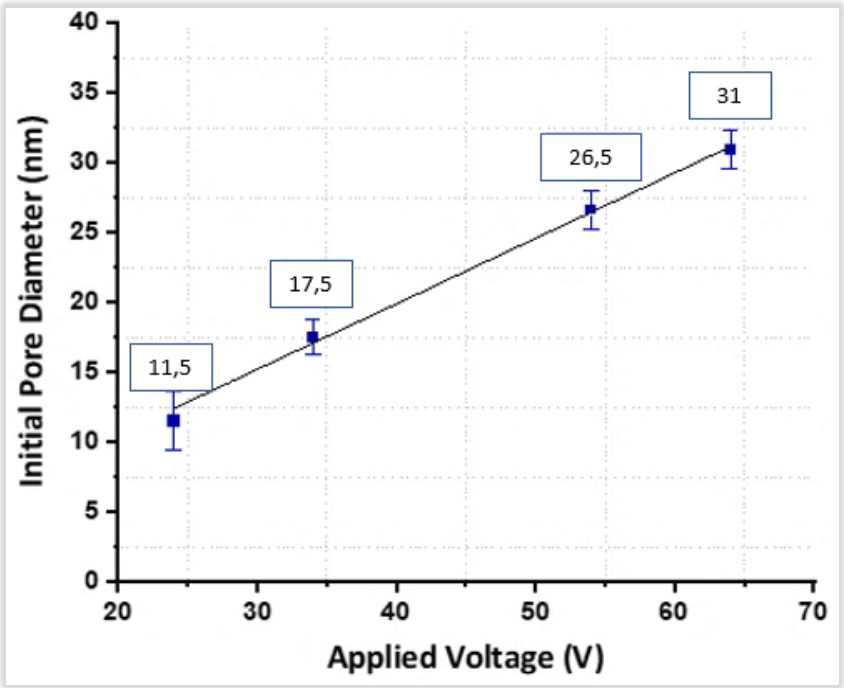

Figure II-26: The evolution of mean initial pores diameter (D_p) as a function of the anodizing voltage of porous anodic aluminum oxide formed in 3%wt Oxalic acid at 24 V, 34 V, 54 V et 64 V at 23°C during the first anodization.

As shown in *figure II-27* below, pseudo-hexagonal and less-ordered pore arrays are formed. We can notice a gradual increase in alumina thickness after anodizing an aluminum surface (1 µm in thickness) in 3%wt oxalic acid at 34 V. *O. Jessensky et al.* [34] suggested that this volumetric expansion is due to mechanical stress associated with the expansion of the aluminum during oxide formation in the alumina/nanoporous alumina

interface. At this stage, the anodizing time must be well-controlled in order to calculate the desired thickness of the alumina template accurately.

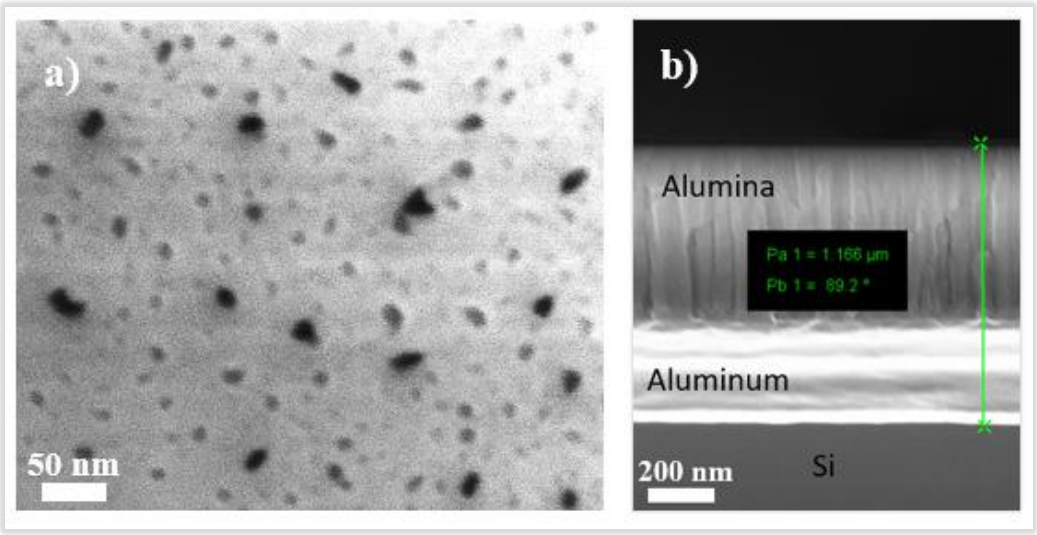

Figure II-27: Scanning electron microscope (SEM) image of a) top view b) and a cross-section view of the formed pore arrays after the first anodization at 34 V in 3%wt oxalic at 23°C.

III.2.2 Wet-etching process:

The next step consists of wet and isotropic etching in 5%wt orthophosphoric solution at 35°C to achieve complete removal of the anodized alumina with irregular pores arrays, leaving pore imprints on the surface of residual aluminum as illustrated in *figure II-28* below. Such nanobowls are used as a precursor during the second anodization for the growth of more regular pores arrays hexagonally ordered.

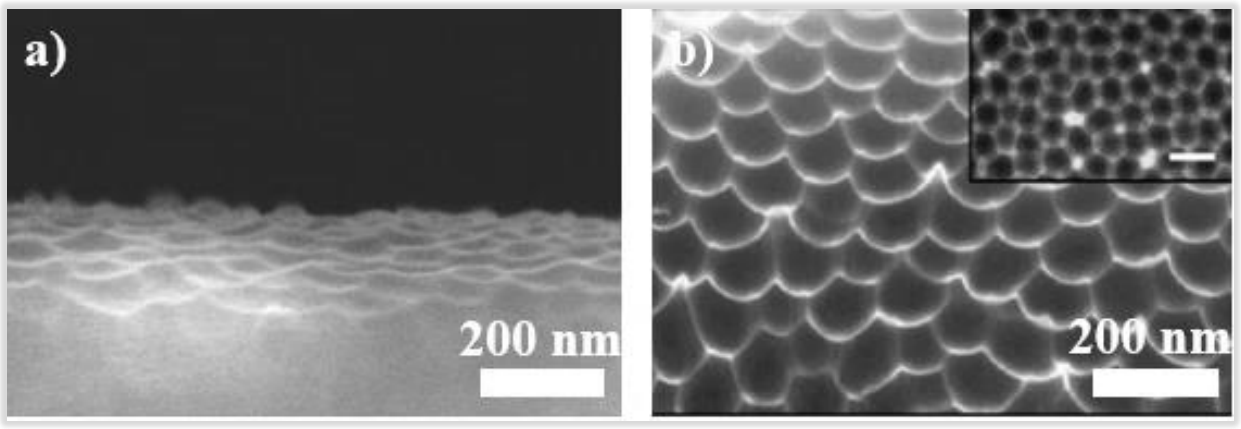

Figure II-28: Scanning electron microscopy micrographs of a) aluminum nanobowls-like surface after i/ first step anodization of aluminum thin film (1 µm) on a silicon substrate, and ii/ first etching in 5%wt Orthophosphoric acid at 35°C; b) tilted-view scanning electron microscopy image of an Al foil with nanobowl surface patterns. Reprinted from reference [18].

III.2.3 Second anodization:

The second anodization was carried out at the same conditions during which the electrical field is concentrated on the remaining footprints, and thus improving the surface organization of nanopores. After the double anodization, the pores' organization depends mainly on the first anodization's duration, where the hexagonal arrays are well defined, offering better control of the structure. If the second anodization is not interrupted in time (as illustrated above on *stage IV*, *figure II-24*), we observe a total peel-off (detachment) of the alumina membrane layer from the silicon substrate and the oxidation of the latter.

III.2.4 Wet-etching process: Pores' widening

The final step requires a second wet isotropic etching at the same conditions cited previously, for 8 minutes (adapted time to reach a pore's diameter of *ca.* 50-55 nm), which markedly lead to pore widening as well as the opening of the bottom barrier oxide layer (*see figure II-29*) until reaching silicon substrate. The latter could undergo local oxidation first due to an extended period of anodization and second due to contact with acidic electrolytes.

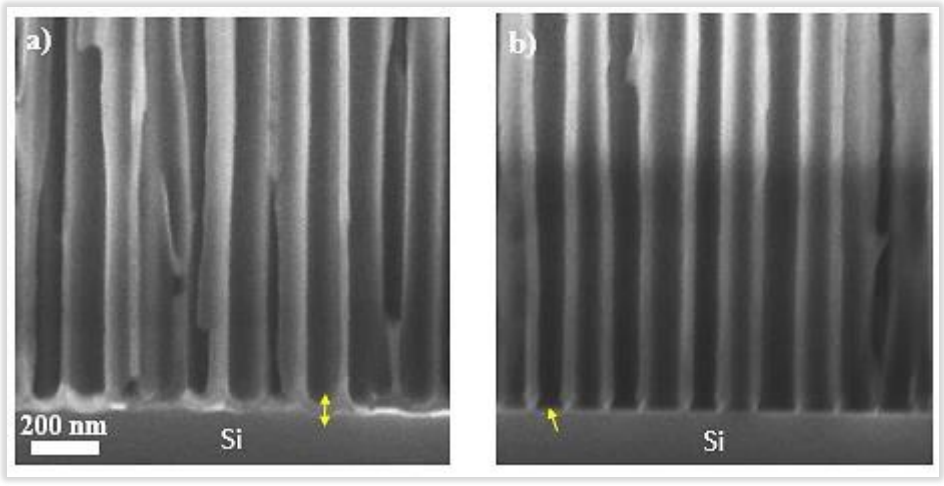

Figure II-29: Cross-section scanning electron microscopy micrographs of porous aluminum oxide formed in 3%wt oxalic acid at 38 V a) before etching the barrier layer and b) after etching the barrier layer in 5%wt orthophosphoric acid at 35°C.

As evidenced in the literature, the etching rate is dependent on the chemical composition of the pore wall oxide of AAO [54]. *Figure II-30* below shows the evolution of pore diameter (D_p) as a function of pore wall etching time for porous AAO formed in 3%wt

Oxalic acid ($H_2C_2O_4$). The plot is characterized by an inflection point, at which the slope of the curve changes. Pore wall oxide in the early stage is etched at a slightly higher rate than in the later stage. The retarded rate of etching in the later stage can be attributed to the relatively pure nature of the inner pore wall oxide compared to the less dense outer pore wall oxide due to the incorporation of anionic species [8].

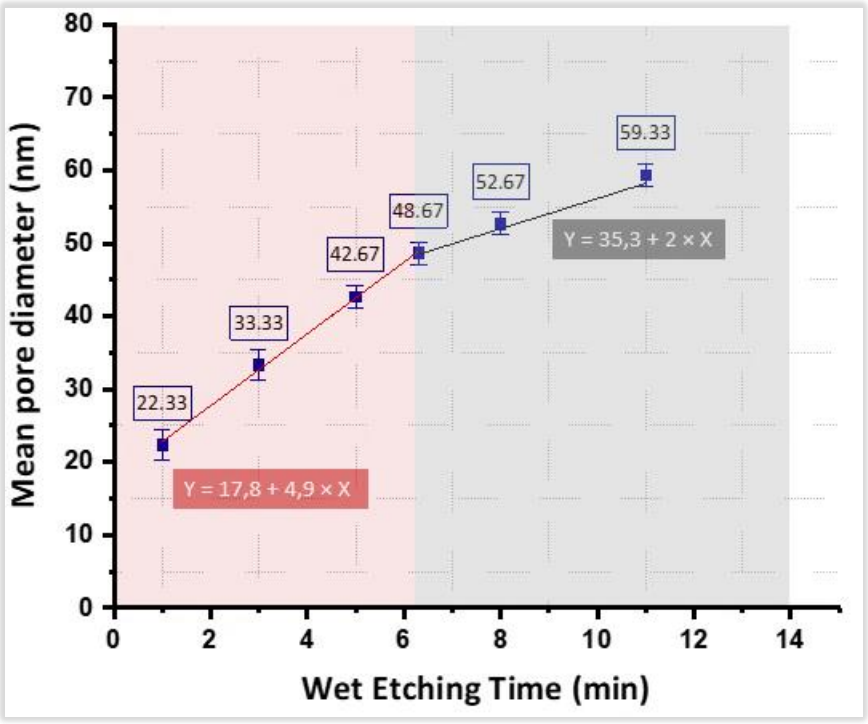

Figure II-30: Evolution of mean pore diameter size (D_p) as a function of wet chemical etching time of porous anodic aluminum oxide formed in 3%wt oxalic acid at 34 V. Wet etching was performed in 5%wt orthophosphoric acid at 35°C.

The ability to precisely control the pore diameter by the pore widening process is one of the most attractive features of porous AAO for template-based nanofabrication.

It should be noted that pores have the particularity of self-organizing in organizational areas (of some µm² in surface), naturally, throughout the elaboration as reflected in *figure II-31*.

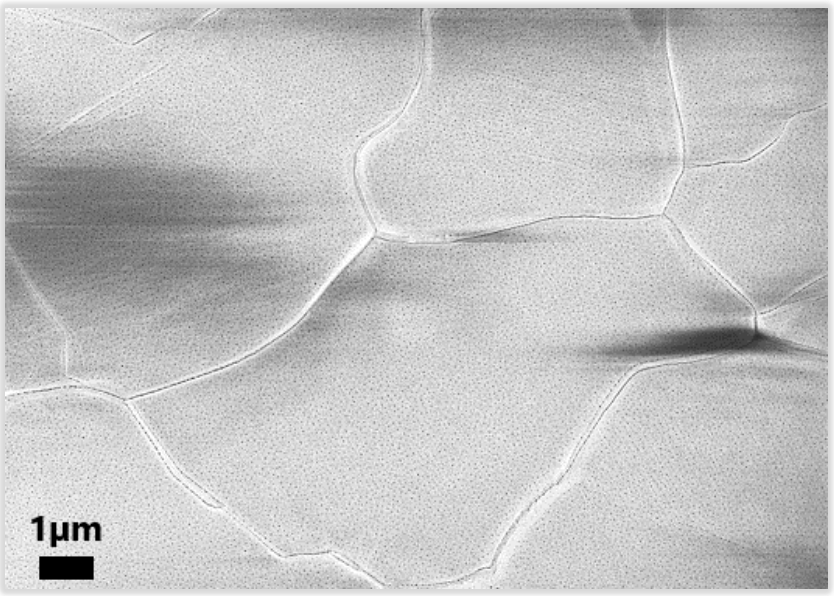

Figure II-31: Top-view scanning electron microscopy micrograph of porous anodic aluminum oxide made after the first anodization of aluminum (1 µm thickness) on silicon in 3%wt oxalic acid at 34 V. The appearing lines illustrate boundaries separating small areas of the anodic aluminum oxide.

Another AAO type with a larger pore's size *ca.* 100-110 nm and a thickness of *ca.* 800 nm was fabricated during this thesis following the same experimental process of elaboration cited in the previous paragraphs. Accordingly, anodization was carried out in a 3%wt oxalic acid solution through the double anodization method at a constant voltage at 54 V. the pore widening step was employed to enlarge pores in a 5%wt orthophosphoric acid solution at 35°C for 12 minutes. *Figure II-32* below exhibits the two suggested geometries with almost uniform pores' size throughout this thesis. The choice of the two distinct geometries of AAO was based on the theoretical calculation of Pt loading (~0,1 - 0,15 mg_{Pt}/cm^2), assuming that the final PtNi nanotubes are regular and exhibit a PtNi Pt wall thickness of *ca.* 5 nm.

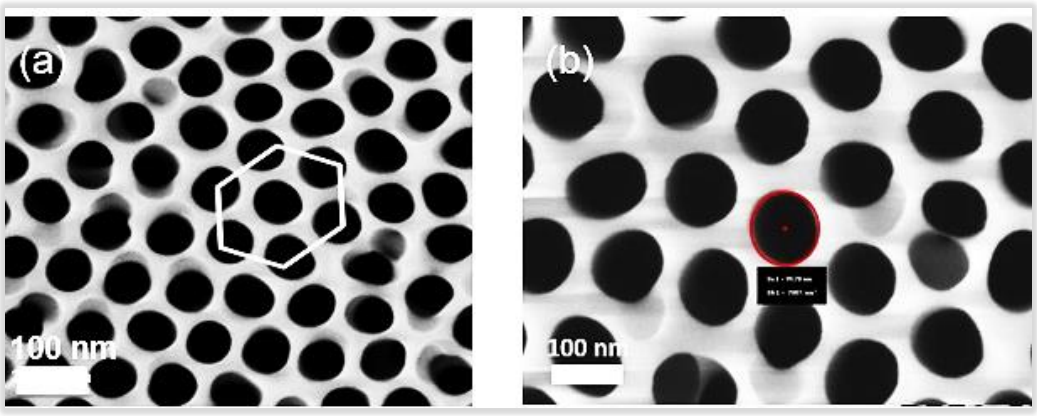

Pores' diameter = **55-55 nm** Porosity = **37%** Thickness = **400 nm**	Pores' diameter = **100-110 nm** Porosity = **40%** Thickness = **800 nm**

Figure II-32: Top-view scanning electron microscopy micrographs of the two suggested pores' size of porous anodic alumina template, a) narrow pores of 50-55 nm in diameter and 400 nm in thickness, b) wide pores of 100-110 nm in diameter and 800 nm in thickness.

The choice of the geometry of the pores (diameter, interpore distance, and thickness) was chosen in such a way that the platinum loading is identical, then to study the influence of these structures on the fuel cell performance.

III.3 Thermal treatment and HF deoxidation

After the fabrication of anodic aluminum oxide by a double-step anodization process, it is, therefore, ready to be used as a guidance matrix for confined nanowires growth. However, a final step is required before embarking on the next process. Thermal treatment of AAO samples has been carried out inside a resistance furnace (*i.e.,* by Joule effect) with a homogenous and controlled circulation of gaseous Nitrogen at 100 mbar to get rid of all possible generated gases.

As we have reported earlier in *paragraph II.2.8,* the annealing temperature should remain below ~1050°C to avoid alumina phase transformation (*i.e.,* crystallization) to γ-alumina, which is resistant to chemical etching [55]. Also, since we are using an Al/Si substrate, annealing temperature should not reach the aluminum melting point (~650°C) to create AlSi alloy during thermal treatment. For such conditions, the annealing temperature is

therefore chosen to be 450°C. This step is mandatory and provides a framework onto which we can not only reduce organic contaminants and anions from the electrolyte (oxalate and phosphate anions) incorporated in nanoporous alumina [33] but also to get rid of water molecules which can, thereafter, react with vapor HF during deoxidation step.

Concomitantly, the electrical contact at the bottom of the pores is not homogeneously ensured due to the silicon electrochemical oxide formed at the end of anodization. A silicon deoxidization step by vapor HF was added to the process to overcome this issue. This single process was held into a *Primaxx Monarch 3 Module* that performs a vapor phase, selective, isotropic etch on the native silicon oxide. A constant flux of HF/N_2 (500 sccm/1200sccm) along with alcohol flow at a maintained pressure of 75 torr is used to etch SiO_2, whose calibrated speed of etching is 11 nm/min.

Figure II-33: HF Vapor Release Etch from Primaxx® Monarch 3 with an integrated Panel PC in PTA-Grenoble cleanroom.

IV. Conclusion

Based on the two-step anodization process, we could vary and tune the geometry of nanoporous anodic aluminum oxide. The aspects listed in this chapter provided a method that would eventually bring us to ensure the desired cell size (D_{p1}=50-55 nm and a thickness of 400 nm; D_{p2}=100-110 nm and a thickness of 800 nm).

Combining alumina templates and electrodeposition methods, one can obtain ordered arrays of magnetic nanowires or nanotubes, to name a few. The tuning of the geometrical characteristics of the arrays (diameter, interpore distance, length, and nanotube wall thickness).

List of figures and tables

References

[1]. Buff, H. Liebigs Ann. Chem., (1857), 3, 265

[2]. G. Hass, On the Preparation of Hard Oxide Films with Precisely Controlled Thickness on Evaporated Aluminum Mirrors, J. Opt. Soc. Am. 39, (1949) 532-540.

[3]. A.R. Despić, A note on the effect of the electrolyte on the type of growth of anodic oxide on aluminium, Journal of Electroanalytical Chemistry and Interfacial Electrochemistry. 191 (1985) 417–423.

[4]. H. Masuda, M. Satoh, Fabrication of Gold Nanodot Array Using Anodic Porous Alumina as an Evaporation Mask, Jpn. J. Appl. Phys. 35 (1996) L126.

[5]. G. E. Thompson, "Porous anodic alumina: fabrication, characterization and applications," Thin solid film, 297 (1997), 192.

[6]. S. Ono, M. Saito, H. Asoh, Self-ordering of anodic porous alumina formed in organic acid electrolytes, Electrochimica Acta. 51 (2005) 827–833

[7]. G.D. Sulka, K.G. Parkoła, Temperature influence on well-ordered nanopore structures grown by anodization of aluminium in sulphuric acid, Electrochimica Acta. 52 (2007) 1880–1888.

[8]. Woo Lee and Sang-Joon Park, Porous Anodic Aluminum Oxide: Anodization and Templated Synthesis of Functional Nanostructures, Chem. Rev. (2014), 114, 7487−7556.

[9]. Sheasby, P.G., Wernick, S., and Pinner, R. Surface treatment and finishing of aluminum and its alloys. Volumes 1 and 2 (5th revised and enlarged edition). United States: N. p., 1987. Web. https://www.osti.gov/biblio/6801805 (accessed May 7, 2020).

[10]. S.-Z. Chu, K. Wada, S. Inoue, M. Isogai, A. Yasumori, Fabrication of Ideally Ordered Nanoporous Alumina Films and Integrated Alumina Nanotubule Arrays by High-Field Anodization, Advanced Materials. 17 (2005) 2115–2119.

[11]. M. Almasi Kashi, A. Ramazani, Ordered Nanoporous Alumina Membranes Formed in Oxalic/Phosphoric Acid Using Hard Anodization, International Journal of Nanoscience and Nanotechnology. 6 (2010) 78–87.

[12]. A.P. Li, F. Müller, A. Birner, K. Nielsch, U. Gösele, Hexagonal pore arrays with a 50–420 nm interpore distance formed by self-organization in anodic alumina, Journal of Applied Physics, 84 (1998) 6023–6026.

[13]. J.P. O'Sullivan, G.C. Wood, N.F. Mott, The morphology and mechanism of formation of porous anodic films on aluminium, Proceedings of the Royal Society of London. A. Mathematical and Physical Sciences. 317 (1970) 511–543.

[14]. S.Y. Chou, P.R. Krauss, P.J. Renstrom, Imprint of sub-25 nm vias and trenches in polymers, Appl. Phys. Lett. 67 (1995) 3114–3116.

[15]. H. Masuda, H. Yamada, M. Satoh, H. Asoh, M. Nakao, T. Tamamura, Highly ordered nanochannel-array architecture in anodic alumina, Appl. Phys. Lett. 71 (1997) 2770–2772.

[16]. H. Asoh, K. Nishio, M. Nakao, T. Tamamura, H. Masuda, Conditions for Fabrication of Ideally Ordered Anodic Porous Alumina Using Pretextured Al, J. Electrochem. Soc. 148 (2001) B152.

[17]. T. Gorisse, L. Dupré, P. Gentile, M. Martin, M. Zelsmann, D. Buttard, Highly organised and dense vertical silicon nanowire arrays grown in porous alumina template on <100> silicon wafers, Nanoscale Res Lett. 8 (2013) 287.

[18]. M.H. Lee, N. Lim, D.J. Ruebusch, A. Jamshidi, R. Kapadia, R. Lee, T.J. Seok, K. Takei, K.Y. Cho, Z. Fan, H. Jang, M. Wu, G. Cho, A. Javey, Roll-to-Roll Anodization and Etching of Aluminum Foils for High-Throughput Surface Nanotexturing, Nano Lett. 11 (2011) 3425–3430.

[19]. Masuda, H., Fukuda, K., Ordered Metal Nanohole Arrays Made by a Two-Step Replication of Honeycomb Structures of Anodic Alumina, Science, (1995), 268, 1466.

[20]. Aluminum anodization, (2004). https://www.semanticscholar.org/paper/1.-Aluminum-anodization/661bd436edc6a73c407d1deda40dcd37431367f5 (accessed March 7, 2021).

[21]. A. Lahmar, G.H. Lee, M. Cailler, C. Constantinescu, Adhesion studies of magnetron sputtered copper films on steel substrates: Effects of heat treatments, Thin Solid Films. 198 (1991) 115–137.

[22]. P. Muller, Glossary of terms used in physical organic chemistry (IUPAC Recommendations 1994), Pure and Applied Chemistry. 66 (1994) 1077–1184.

[23]. C.T. Sousa, D.C. Leitao, M.P. Proenca, J. Ventura, A.M. Pereira, J.P. Araujo, Nanoporous alumina as templates for multifunctional applications, Applied Physics Reviews. 1 (2014) 031102.

[24]. T.P. Hoar, N.F. Mott, A mechanism for the formation of porous anodic oxide films on aluminium, Journal of Physics and Chemistry of Solids. 9 (1959) 97–99.

[25]. G.E. Thompson, Y. Xu, P. Skeldon, K. Shimizu, S.H. Han, G.C. Wood, Anodic oxidation of aluminium, Philosophical Magazine B. 55 (1987) 651–667.

[26]. J. F. Murphy and C. E. Michaelson, Proceedings Conference on Anodizing, University of Notthingham, UK, (1962), 83.

[27]. J.S.L. Leach, P. Neufeld, Pore structure in anodic Al2O3 films, Corrosion Science. 9 (1969) 413-IN6.

[28]. Y. Xu, G.E. Thompson, G.C. Wood, Mechanism of anodic film growth on aluminium, Transactions of the IMF. 63 (1985) 98–103.

[29]. J.E. Houser, K.R. Hebert, The role of viscous flow of oxide in the growth of self-ordered porous anodic alumina films, Nature Mater. 8 (2009) 415–420.

[30]. L.G. Stanton, A.A. Golovin, Effect of ion migration on the self-assembly of porous nanostructures in anodic oxides, Phys. Rev. B. 79 (2009) 035414.

[31]. F.D.A.A. Reis, J.P. Badiali, D. di Caprio, Modeling Growth of Organized Nanoporous Structures by Anodic Oxidation, Langmuir. 28 (2012) 13034–13041.

[32]. G.E. Thompson and G.C. Wood, in Corrosion: Aqueous processes on passive films, (1983), Vol.23 of Treatise on Materials Science and Technology, J.C. Scully, Editor, p.205, Academic Press, New York.

[33]. K. Nielsch, J. Choi, K. Schwirn, R.B. Wehrspohn, U. Gösele, Self-ordering Regimes of Porous Alumina: The 10 Porosity Rule, Nano Lett. 2 (2002) 677–680.

[34]. O. Jessensky, F. Müller, U. Gösele, Self-organized formation of hexagonal pore arrays in anodic alumina, Appl. Phys. Lett. 72 (1998), 1173–1175.

[35]. S.Z. Chu, K. Wada, S. Inoue, M. Isogai, Y. Katsuta, A. Yasumori, Large-Scale Fabrication of Ordered Nanoporous Alumina Films with Arbitrary Pore Intervals by Critical-Potential Anodization, J. Electrochem. Soc. 153 (2006) B384.

[36]. D. Singhal, J. Paterson, M. Ben-Khedim, D. Tainoff, L. Cagnon, J. Richard, E. Chavez-Angel, J.J. Fernandez, C.M. Sotomayor-Torres, D. Lacroix, D. Bourgault, D. Buttard, O. Bourgeois, Nanowire forest of pnictogen–chalcogenide alloys for thermoelectricity, Nanoscale. 11 (2019) 13423–13430.

[37]. F. Keller, M.S. Hunter, D.L. Robinson, Structural Features of Oxide Coatings on Aluminum, J. Electrochem. Soc. 100 (1953) 411.

[38]. M. S. Hunter and P. Fowle, Factors affecting the formation of anodic oxide coatings, J. Electrochem. Soc., 101 (1954), 514.

[39]. H. Takahashi, K. Fujimoto, and M. Nagayama, Effect of pH on the distribution of anions in anodic oxide films formed on aluminum in phosphate solutions, J. Electrochem. Soc., 135 (1988), 1349.

[40]. W. Lee, K. Nielsch, U. Gösele, Self-ordering behavior of nanoporous anodic aluminum oxide (AAO) in malonic acid anodization, Nanotechnology 18 (2007), 475713.

[41]. S.-K. Hwang, S.-H. Jeong, H.-Y. Hwang, O.-J. Lee, K.-H. Lee, Fabrication of highly ordered pore array in anodic aluminum oxide, Korean J. Chem. Eng. 19 (2002) 467–473.

[42]. A.P. Li, F. Müller, A. Birner, K. Nielsch, U. Gösele, Hexagonal pore arrays with a 50–420 nm interpore distance formed by self-organization in anodic alumina, Journal of Applied Physics. 84 (1998) 6023–6026.

[43]. K. Ebihara, Takahashi, H. and and M. Nagayama, "J. Met. Finish. Soc. Japan," Kinzoku Hyomen Gijutsu, vol. 34, pp. 548-553, 1983.

[44]. G.E.J. Poinern, N. Ali, D. Fawcett, Progress in Nano-Engineered Anodic Aluminum Oxide Membrane Development, Material, 4 (2011) 487–526.

[45]. G.E. Thompson, G.C. Wood, Porous anodic film formation on aluminium, Nature. 290 (1981) 230–232.

[46]. F. Le Coz, L. Arurault, L. Datas, Chemical analysis of a single basic cell of porous anodic aluminium oxide templates, Materials Characterization. 61 (2010) 283–288.

[47]. G.D. Sulka, Highly Ordered Anodic Porous Alumina Formation by Self-Organized Anodizing, in: Nanostructured Materials in Electrochemistry, John Wiley & Sons, Ltd, 2008: pp. 1–116.

[48]. H. Han, S.-J. Park, J.S. Jang, H. Ryu, K.J. Kim, S. Baik, W. Lee, In Situ Determination of the Pore Opening Point during Wet-Chemical Etching of the Barrier Layer of Porous Anodic Aluminum Oxide: Nonuniform Impurity Distribution in Anodic Oxide, ACS Appl. Mater. Interfaces. 5 (2013) 3441–3448.

[49]. I. Vrublevsky, V. Parkoun, V. Sokol, J. Schreckenbach, Study of chemical dissolution of the barrier oxide layer of porous alumina films formed in oxalic acid using a re-anodizing technique, Applied Surface Science. 236 (2004) 270–277.

[50]. K. Schwirn, W. Lee, R. Hillebrand, M. Steinhart, K. Nielsch, U. Gösele, Self-Ordered Anodic Aluminum Oxide Formed by H2SO4 Hard Anodization, ACS Nano. 2 (2008) 302–310.

[51]. T.-T. Kao, Y.-C. Chang, Influence of anodization parameters on the volume expansion of anodic aluminum oxide formed in mixed solution of phosphoric and oxalic acids, Applied Surface Science, 288 (2014), 654–659.

[52]. D.M. Mattox, Thin film metallization of oxides in microelectronics, Thin Solid Films. 18 (1973) 173–186.

[53]. G. Patermarakis, The origin of nucleation and development of porous nanostructure of anodic alumina films, Journal of Electroanalytical Chemistry. 635 (2009) 39–50.

[54]. H. Han, S.-J. Park, J.S. Jang, H. Ryu, K.J. Kim, S. Baik, W. Lee, In Situ Determination of the Pore Opening Point during Wet-Chemical Etching of the Barrier Layer of Porous Anodic Aluminum Oxide: Nonuniform Impurity Distribution in Anodic Oxide, ACS Appl. Mater. Interfaces. 5 (2013) 3441–3448.

[55]. L.F. Marsal, L. Vojkuvka, P. Formentin, J. Pallarés and J. Ferré-Borrull, "Fabrication and optical characterization of nanoporous alumina films annealed at different temperatures", Optical Materials 31 (2009), 860–864

Chapter 3

Confined Growth of Nickel Nanowires and Platinum Galvanic Displacement as a Chemical Route to PtNi Nanowires and Nanotubes Fabrication

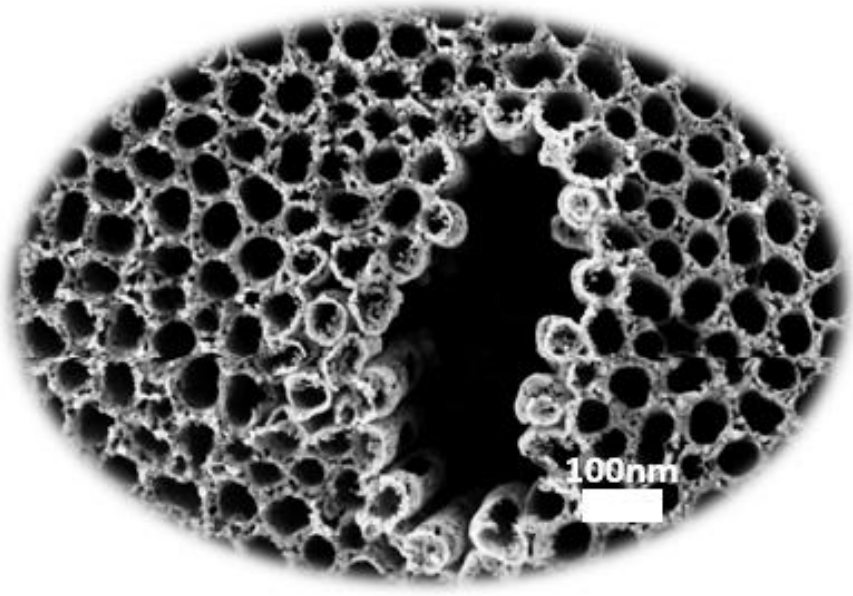

"Science is not only compatible with spirituality; it is a profound source of spirituality."

-Carl Sagan

Table of Content

Nanoporous aluminum oxide was found to be ideal for the growth of dense nanowire arrays, providing ordered, parallel, and uniform pore channels with a high aspect ratio and mechanical support to fragile nanowires [1][2].

Among the aspects studied in this chapter, well-ordered and perpendicularly aligned nickel nanowires grown onto the AAO template will be used as sacrificial nanomaterials for the PtNi nanotubes elaboration by galvanic displacement process.

This chapter will discuss the background of the study and the methodologies applied. It can be formulated as follows:

- **Section I:** Aims to present a bibliographic overview about the electrodeposition process as a route to growing nanowires;
- **Section II:** Experimental results for the nickel nanowires growth inside nanoporous aluminum oxide;
- **Section III:** Oriented to an in-depth bibliographic synthesis of the PtNi nanostructures as electrocatalysts for the PEMFC;
- **Section IV:** Experimental results of the elaborated PtNi nanowires and nanotubes via galvanic displacement process.

I. Bibliographic Synthesis: Electrodeposition as an electrochemical route to the growth of nanowires

Nanowire structure is a polycrystalline pillar ranging from 1-100 nanometers in diameter and hundreds of micrometers in length. They are made of metals, insulators, semiconductors, or organic compounds. Due to their one-dimensional morphology-related novel electronic, electrochemical, thermal, and mechanical properties, semiconductor nanowires hold great promise in energy harvesting from light irradiation, temperature gradient, and mechanical deformation [3].

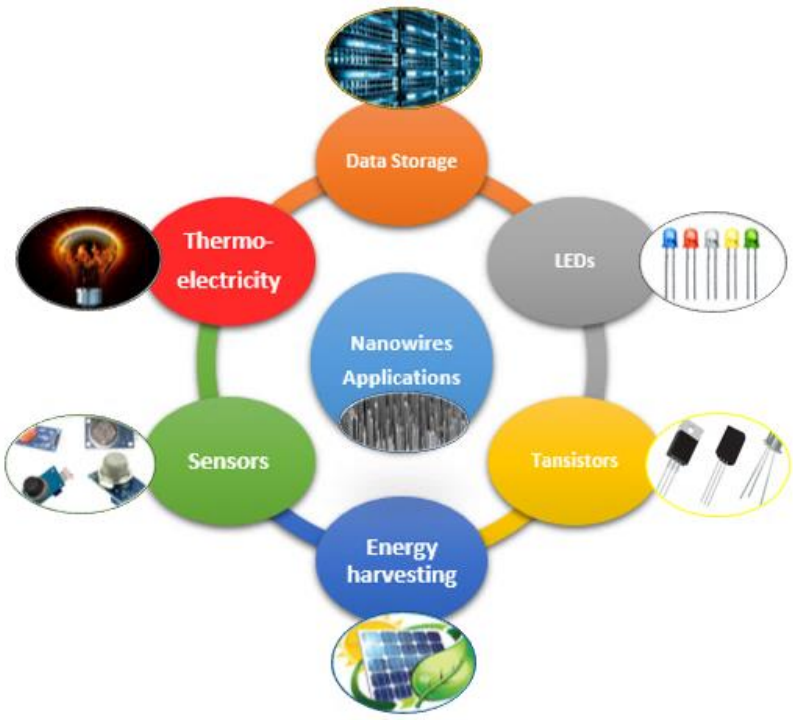

Figure III-1: Schematic diagram of Nanowires' applications.

As commonly known, nanowires are grown whether by direct synthesis (*i.e.,* bottom-up synthesis such as Vapor-Liquid-Solid (VLS) method, electrodeposition, etc...), which exhibits gradual metal assembly by periodic blocks, or a conventional lithography patterning (*i.e.,* top-down synthesis) combined with etching processes.

I.1 Overview: The electrodeposition process

Electrodeposition is an electrochemical process that involves imposing a potentiostat-controlled potential to transform metal ions, molecules, or complexes in an aqueous solution at the cathode/electrolyte interface into metal atoms. This process involves electrons flow from the counter-electrode to the working electrode. An electronic transfer occurs at the working-electrode/electrolyte interface. The charges are then consumed by the metal cations (in the case of metal cations, we talk about a reduction to obtain the metal) following the reduction reaction below (*reaction III-1*), leading to the deposition of metal on the working electrode.

$$\mathbf{A^{x+}_{(aq)} \cdot\ yH_2O + xe^- \rightarrow A_{(s)} + yH_2O} \qquad \text{Reaction III-1}$$

where the dot indicates an electrostatic interaction.

Electrodeposition also serves to metal coating by an electroplating process, consisting of the immersion of the desired object/metal to be coated in an electrolyte bath[19] (*i.e.,* a solution with dissolved metal cations serving as sacrificial metal). This method aims mainly to change the physical-chemical properties of an object to protect it from corrosion, increasing its resistance, changing magnetic and conductivity properties, or aesthetic aspects (*i.e.,* decoration).

During the redox process, the current circulating at the working-electrode/solution interface is called the Faradic current, depending on the mass transport and kinetic. The Faradic current describes the speed rate at which the redox reactions take place at the electrode according to the following equation:

$$\mathbf{I} = \frac{\mathbf{dQ}}{\mathbf{dt}}$$ Equation III-1

Faraday's law reads if the reduction yield is 100%, the product of the number of reduced moles by the charge corresponding to 1 mole (*i.e.,* n.F):

$$\mathbf{Q} = \mathbf{n}.\mathbf{e}^{-} \times \mathbf{F} \times \mathbf{n}_{(\mathbf{moles})}$$ Equation III-2

In electrodeposition (or electroplating), electrons transfer is directly proportional to the product formed. The deposited metal mass is equal to the number of moles times the molar mass of the species. We can also extract the value of volume from the product of the electrode surface by the thickness of the deposited material. This brings us to define the deposit density as follows (if the reaction yield is 100%):

$$\boldsymbol{\rho} = \frac{\mathbf{n}_{(\mathbf{moles})} \times \mathbf{M}}{\mathbf{S} \times \mathbf{e}}$$ Equation III-3

Combining both *equation III-2* and *equation III-3*, we will be able to determine the thickness of the deposited metal according to *equation III-4* below:

$$\mathbf{e} = \frac{\mathbf{n}_{(\mathbf{moles})} \times \mathbf{M}}{\mathbf{S} \times \boldsymbol{\rho}} = \frac{\mathbf{Q} \times \mathbf{M}}{\mathbf{n} \times \mathbf{F} \times \mathbf{S} \times \boldsymbol{\rho}}$$ Equation III-4

[19] One should note that temperature, concentration (*i.e.,* pH value), and chemical composition of the bath affect how effective the electroplating process is.

where:

M: molar mass in g/mol;

ρ: Density in g/cm^3;

F: The Faraday constant, its accepted value reads 96485.33 C/mol;

Q: Quantity of electric charge in Coulomb (C);

e: Thickness in cm;

S: Electrode surface in cm^2.

I.2 Examples of electrodeposition methods

As a well-known process developed all over the past decades, the electrochemical deposition method is one of the most attractive template filling techniques for the growth of metallic nanostructures, and mainly nanowires. There are three different ways to deposit nanowires inside nanoporous templates uniformly (*e.g.,* anodic aluminum oxide templates), taking into account the template parameters (pore size, pore density, and porosity).

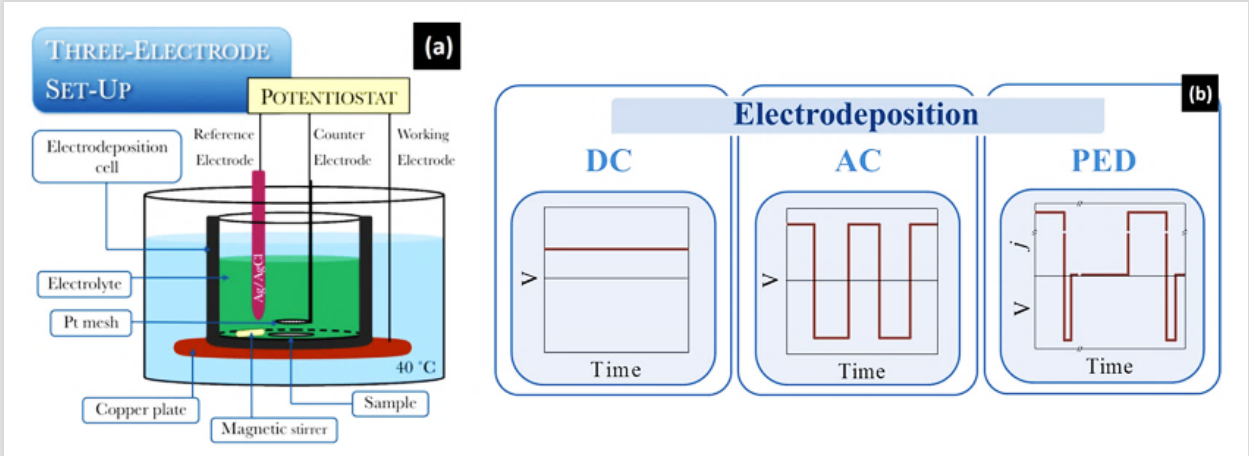

Figure III-2: Schematic illustration of a) Electrodeposition setup using a three-electrode system; b) Illustration of the three different electrodeposition methods to fill nanoporous templates. Reprinted from reference [4].

I.2.1 Direct-Current (DC) Electrodeposition

Under a two- or three-electrodes system, potentiostatic deposition allows working at a constant potential; the current that crosses the circuit is recorded (on the other hand, galvanostatic deposition in which a fixed current is applied while the evolution of the potential is recorded). The current response enables monitoring of the deposition process.

Using Faraday's law (*Equation III-4*), we can estimate and, hence to vary, the amount or thickness of metal deposited during electrodeposition. Several materials have been deposited in AAO membranes using DC electrodeposition, including NWs of single elements such as Ni, Co, Fe, alloys, multilayered NWs, and NTs [4]. According to *Sousa et al.* investigation, nanostructure deposition using the DC electrodeposition method is not a suitable technique for industrial applications due to the laborious template processing required and its limited applicability to thick membranes only (>20 µm).

I.2.2 Alternating-Current (AC) Electrodeposition

In this method, AC electrodeposition inside the AAO membrane, the barrier layer might not be removed entirely, leading to lower electrical conduction at the bottom of the AAO. In this case, we tend to use high voltages and frequencies [5]. It is widely used in industry and offers the possibility of producing NWs of very small lengths. In contrast, the filling fraction of AAO nanopores utilizing this method is generally low due to the high potentials applied that lead to hydrogen evolution and consequently inhibit deposition [6].

I.2.3 Pulsed Electrodeposition (PED)

As alluded to in the literature and known as an exception to both methods cited above, pulsed electrodeposition may improve the quality of metal deposition, enhancing the mechanical and physical properties of films with an increase in the deposition rate. Applying a pulsed potential will allow alternating deposition time and relaxation time (t_{on} and t_{off}), during which the electrode/electrolyte interface is replenished with the metal salt to be reduced. At the relaxation time t_{off}, the concentration of electroactive species is regenerated by the diffusion of the cations within the electrolyte.

In PED mode, more parameters are added compared to DC and AC mode since the pulse and pause times are added to the existing variables, making the process more complex to use and optimize accordingly (*e.g.,* signal amplitude, signal shape, and frequency).

The commonly used forms of modulated electrical regimes are shown in *figure III-4* below and described as follows:

a) The simple pulsed current regime (*figure III-3-a*): a cathodic current I_c is imposed during a time T_c, and the current drops to I=0 during a fixed pause time t_{off} (relaxation at zero current).

b) The pulsed current regime with periodic inversion of the current (*figure III-3-b*), defined by a cathodic current I_c imposed during time T_c and an anodic current I_a (of opposite sign) during time T_a.

c) The pulsed current regime with inversion then the interruption of the current (*figure III-3-c*) [7].

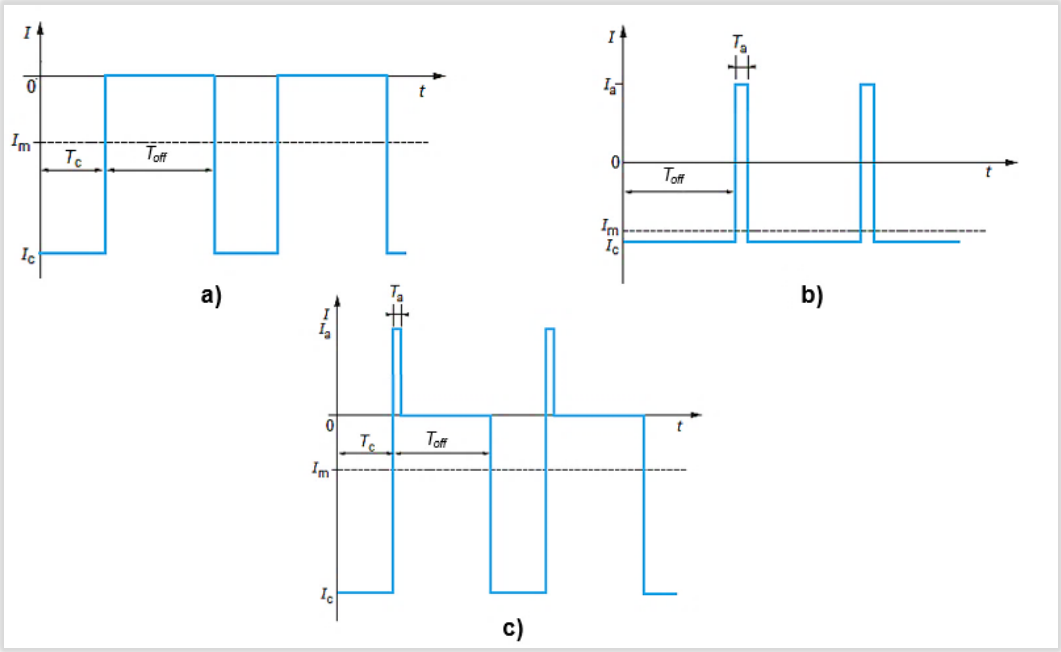

Figure III-3: Current (I) *vs.* Time (t) plot of the most common pulsed current regimes: a) The simple pulsed current regime, b) Pulsed current with polarity reversing, and c) The pulsed current regime with inversion then the interruption of the current. Reprinted and edited from reference [7].

However, the main advantages of PED rely on its flexibility in adjusting the amplitude and time duration of the voltage/current pulses, offering the possibility to introduce a delay pulse to refresh the concentration of metallic ions at the deposition interface, increasing the NWs growth uniformity. Also, it offers a reduction in porosity and internal stress, improves the current distribution, lowers the gas content, improves the purity, results in fine-grained deposits, and deposits having low electrical resistance and good corrosion resistance. Many studies have been conducted in the context of optimizing PED

conditions, and uniform high aspect ratio NWs of different materials such as Ni, Fe, Cu, or Ag were obtained [2][4][6][8][9].

I.3 Nanowires synthesis as functional materials through Electrodeposition

Metal deposition inside the AAO template was first developed by *Cobini* and his coworkers [10]. For the past decades, nano-scale engineering has been powered by conventional lithographic and contact printing techniques. Fabrication of nanostructures and tailoring their physical or chemical properties on this scale is quite challenging [11]. For instance, nanowires find applications in various high technology applications because of their unique properties: magnetic (*e.g.,* coercivity and magnetization, wear resistance, heat conductivity, energy harvesting, and electrocatalytic properties [9].

At that point, the template-assisted technique offers a particular interest in ordered growth of continuous (or segmented) metal/alloys nanowires (see *figure III-4*).

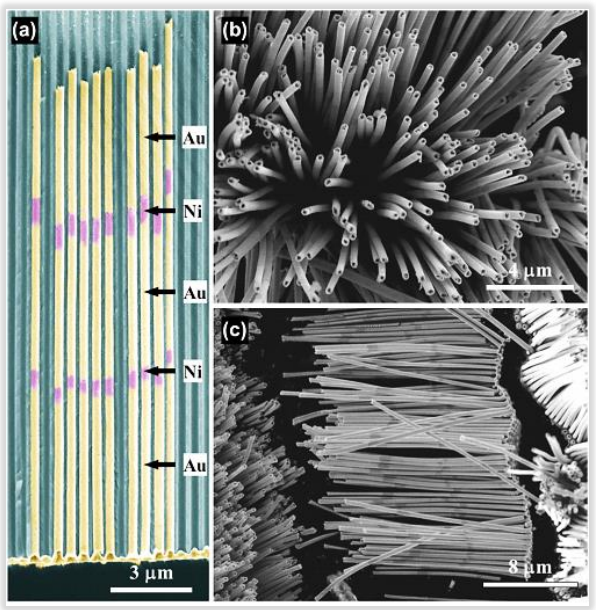

Figure III-4: SEM images of multisegmented metal nanotubes with a stacking configuration of Au/Ni/Au/Ni/Au along the nanotube axis: a) false-colored cross-sectional SEM image of as-prepared metal nanotube-AAO composite. b, c) SEM images of multisegmented metal nanotubes after removing the AAO template [12].

Basically, geometrical features provided by AAO make it a successful and tunable sacrificial mold to nanostructures growth and nanowires electrodeposition as depicted in *figure III-5* below, offering precise control over the size, shape, and configuration.

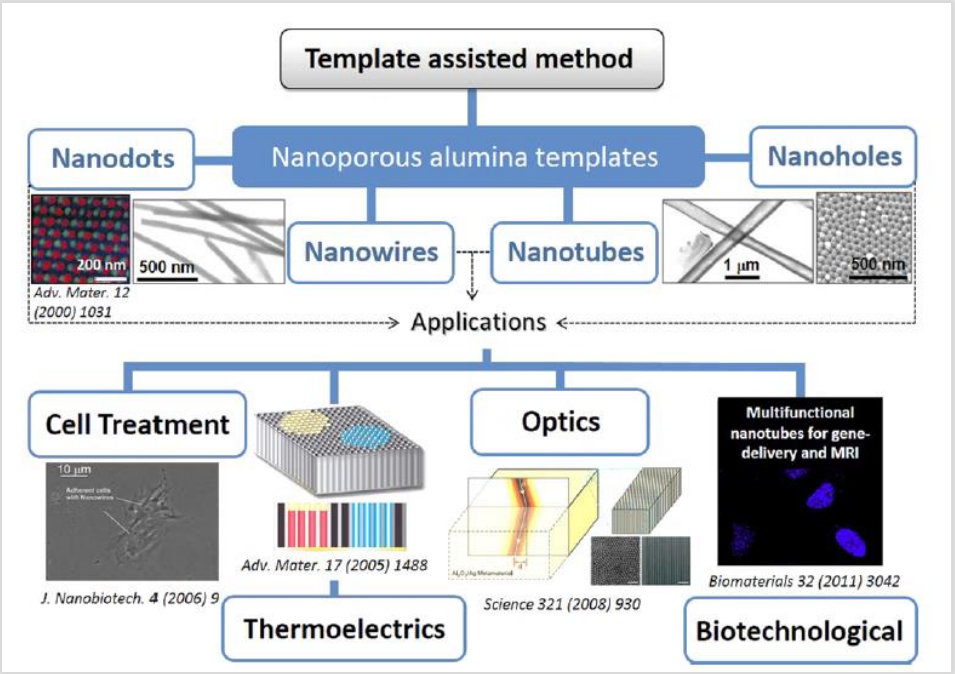

Figure III-5: Organogram summarizing several technological applications of nanostructures grown in AAO templates. Reprinted from reference [4].

Shifting gears toward NiNWs growth inside AAO/Si templates, many research teams have already worked on the electrochemical deposition of nickel, whether by DC electrodeposition, AC electrodeposition, or pulsed electrodeposition [2][13][14][15].

Combining both the tunable geometry of AAO and the control of the pore filling (*i.e.,* growth homogeneity) offered by the PED technique leads to uniform, fast grown, vertically aligned, and well-ordered arrays of NiNWs. *Gösele et al.* [2] focused on the uniform nickel pulsed electrodeposition into ordered alumina pores in aqueous deposition solutions. They assumed that the PED is reliable for deposition into high aspect materials by compensating for the slow diffusion-driven transport in the pores.

The electrolyte that many research groups have agreed upon is the so-called Watts bath solution, a mixture of $NiSO_4x6H_2O$, $NiCl_2x6H_2O$, and H_3BO_3 as a buffer. The concentration of each component is displayed in *table III-1* below [16][17].

Watts bath composition	
Nickel(II) sulfate - $NiSO_4$, $6H_2O$	220 to 300 g/L
Nickel(II) chloride - $NiCl_2$, $6H_2O$	35 to 65 g/L
Boric acid - H_3BO_3	35 to 45 g/L
Cathodic current density	0.02 A/cm² to 0.1 A/cm²
Temperature °C	35 à 55 °C
pH	3 to 5

Table III-1: Composition of the Watts Bath as a nickel solution for nanowires electrodeposition.

Moreover, the template-assisted DC electrodeposition of nickel was studied by *S. Wen* and *J.A. Szpunar* [18]. Slightly uniform nickel nanowires were directly deposited into the nanoporous alumina template film on an Au-coated silicon wafer (see *figure III-6*). A high current of 0.02 A was initially applied for 5 seconds and then lowered to 0.01 A for 30 seconds to deposit nanowires along the nanopores.

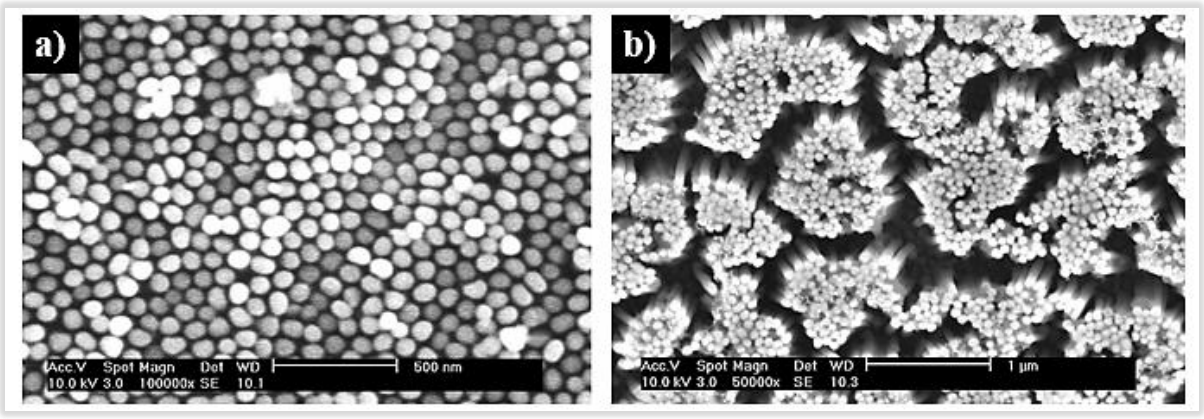

Figure III-6: SEM images of nickel nanowires after electropolishing a) embedded in the alumina template and b) after removing the alumina template in NaOH 20%. Reprinted from reference [18].

The NiNWs growth inside nanoporous AAO has also been reported by *B. Marquardt* and his coworkers [19]. Since the barrier layer at the bottom of the pores (see *paragraph II.2.4*) reveals an insulating behavior, the applied electrodeposition voltage is increased to a value high enough to overcome the barrier layer resistance in all pores, leading to a quasi-uniform NiNWs length. They related the length variation of the nanowires to the

barrier layer thickness variation since the filling rate depends on the barrier layer's thickness: the lower the barrier layer thickness, the lower the resistance, and thus the higher the electrodeposition current.

Furthermore, many research teams have carried out the electrodeposition of NiNWs or Ni-alloy nanowires onto porous membranes based on the techniques cited above in *paragraph I.2* and by varying the electrodeposition parameters [20][21][22].

Throughout our experiments, nickel nanowires will be electrodeposited into porous alumina templates to create ordered nanowires. Because of the higher aspect ratio of AAO and to keep the concentration of nickel cations relatively constant at the bottom of the pores, pulsed electrodeposition is adopted. To control the length of the nanowire under constant-current conditions, the nanowires growth rate is proportional to the applied current density according to Faraday's law, by knowing the electrodeposition yield.

The next paragraph will be devoted to describing the NiNWs growth protocol followed in this work through electrodeposition inside AAO from an aqueous solution containing Ni metallic ions. The PED method consists of short periodic pulses of current repeating itself for a fixed number of pulses until the desired length of nanowires is achieved.

II. Experimental Results: Template-assisted growth of Nickel nanowires inside the nanoporous anodic aluminum oxide

The experiment was carried out in the same homemade electrochemical cells developed at the lab for AAO fabrication (*Experimental setup III.1).* The metal salt of nickel was solubilized in the electrolyte (Watts Bath). A difference in potential is applied between two insoluble electrodes: the anode (Pt-Ir gauze) and the cathode (AAO/Si), where silicon acts as an electrical contact. In a highly concentrated electrolyte, the metal species are then reduced to the cathode and the rate of Ni electrodeposition is limited by charge transfer and/or convection. Accordingly, the reduction rate is controlled by the applied cathodic current density, which depends mainly on metallic species concentration. Precise control of these parameters leads to adjusted deposition kinetics.

II.1 PED of nickel nanowires inside AAO

For optimized and flexible use of a porous anodic alumina template, the pores must be filled with a conducting or semiconducting material. It is very much in our interest to have good physical contact between the alumina and p-type silicon wafer to ensure the uniform growth of nickel nanowires. A post-fabrication treatment was necessary for the uniform growth of nanowires: the AAO thermal treatment at 450°C in N_2 atmosphere at a pressure of 10 mbar for one hour to get rid of the organic impurities, followed by a deoxidation step in HF vapor to remove the silicon native oxide from the bottom of the pores.

In this thesis, we have chosen the pulsed electrochemical deposition (PED) in an aqueous solution for NiNWs growth. PED's main advantages, which allowed better control over the deposition parameters and the length of NiNWs, rely on its flexibility to adjust the amplitude and duration of the voltage pulses. It offers the possibility of introducing a delay pulse to refresh the metallic ions concentration at the deposition interface, promoting uniform nanowire growth [2].

II.1.1 Electrolyte preparation

Metallic species in their various forms (anionic, cationic, or neutral) are reduced to the cathode (local deposition offering no loss of material) after transport in the electrolyte by diffusion, migration, and/or convection.

Nickel nanowires were grown in AAO mold, using the Watts bath solution: a mixture of 300 g/L $NiSO_4.6H_2O$, 45 g/L $NiCl_2.6H_2O$, and 45 g/L H_3BO_3. The magnetic stir bar was put in the container containing the solution to be stirred at 35-40°C. The stirring speed was adjusted to ensure sufficient stirring. The pH of the solution was measured to be 4. It has been suggested that boric acid stabilizes the pH and enhances metal deposition. The prominent redox couples present in the solution are reported in the *table III-2* below:

Redox couples	E° (V *vs.* SHE)
$S_2O_2^{-8}$ /SO^{2-}	+2.01
O_2/H_2O	+1.23
H^+/H_2	0
Ni^{2+}/Ni	-0.257

Table III-2: Standard electrode potential for redox couples present in a nickel solution.

Sulfur is very complex from an electrochemical point of view. Sulfate ions are present both as an oxidizing and reducing agent. They are considered electronegative species, and they cannot react. They are only involved in current transport during ions migration [23].

Since the standard potential of the couple O_2/H_2O is higher than Ni^{2+}/Ni, the oxygen in the solution is reduced and may inhibit the cathodic reduction of nickel: we may have an added cathodic current which reduces the yield of Ni deposition:

$$\mathbf{O_{2_{(g)}} + 4H^{+}_{(aq)} + 4e^{-} \rightarrow 2H_2O_{(l)}}$$ Reaction III-2

Therefore, nitrogen was bubbled through the solution to keep the solution essentially free of oxygen. Also, considering the low standard potential of the couple Ni^{2+}/Ni compared to H^+/H_2, hydrogen emission is likely to occur in the electrolyte (H^+ protons reduction to H_2), leading to a decrease in the yield of Ni deposition: $\mathrm{I_{cathodic}} = \mathrm{I_{H_2}} + \mathrm{I_{Ni}}$).

II.1.2 NiNWs pulsed electrodeposition (Ni PED)

This work consists of depositing the nickel by an electrochemical reduction in an electrolytic bath where the reduction of Ni^{2+} ions is achieved through an external current. Thus, the sample is maintained inside an adequate homemade electrochemical cell (same electrochemical cell as the one used for aluminum anodization) where the electrical contact between the electrolyte and the working electrode is ensured at the bottom of nanopores on the conductive silicon substrate (*noticia:* the front side of the silicon wafer supporting the alumina membrane is used as the cathode, the rear side is for the electrical contact).

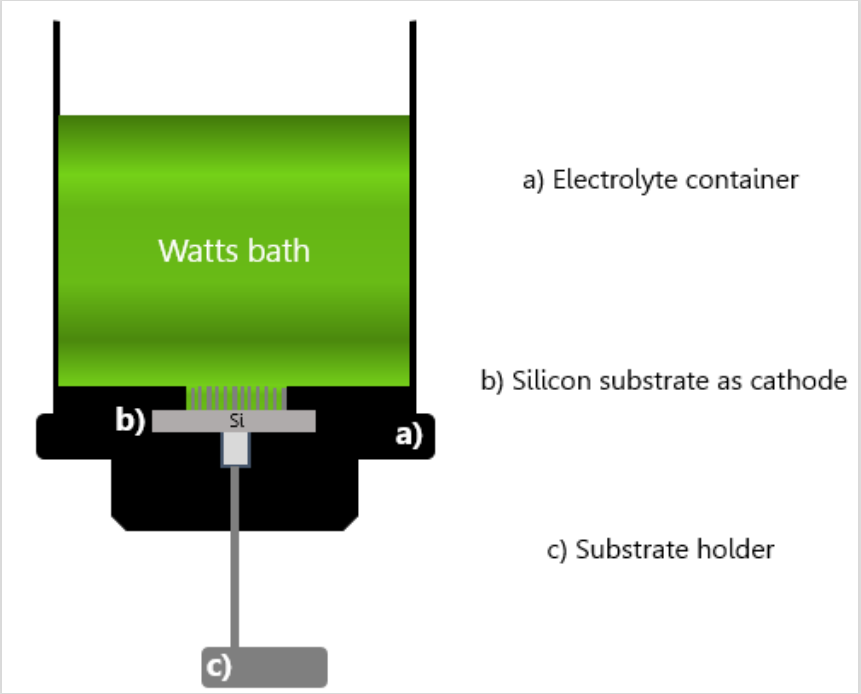

Figure III-7: Schematic illustration of the electrochemical cell used for nickel nanowires electrodeposition on the AAO template.

Due to simultaneous hydrogen evolution during PED, the faradaic efficiency must be below 100%. For electrochemical calculations in this work, we will assume that faradaic efficiency is ~100%. NiNWs were deposited on silicon by square-wave galvanostatic pulses because of: **i/** the high aspect ratio of the cylindrical as evidenced before, **ii/** Keeping Ni^{2+} ions concentration nearly constant at the bottom of AAO pores, **iii/** constant current allows controlling the charge **Q** injected in the system assuming that there are no parasite reactions such as hydrogen production (*i.e.,* the amount of the deposited material or the thickness with a Ni(II) reduction yield equals to 100%) as follows:

$$\mathbf{Q = n_{e^-} \times n_{deposit} \times F} \qquad \text{Equation III-5}$$

where:

n_{e^-}: is the number of electrons exchanged in the redox reaction;

$n_{deposit}$: the amount of substance (nickel) deposited in moles;

F: The Faraday constant, its currently accepted value is F = 96485 C/mol.

The Ni PED process was optimized during this work after several trials. Since we aim to reduce nickel, a constant negative current (I_{pulse-}) is applied on the cathode during a short time t_{on-} allowing the flow of a defined amount of charge Q leading to the reduction of

nickel ions. This step is followed by a constant positive current (I_{pulse+}) during a short positive pulse t_{on+} follows to discharge the double-layer capacitance (*i.e.,* the interface between the conductive electrode and the adjacent nickel electrolyte, and to reoxidize H_2 produced during t_{on-}). Subsequently, a relatively long-time t_{off} is applied to ensure ions' concentration to recover at the pore tips and for the deposition interfaces to be supplied with ions. *Figure III-8* shows a schematic current-time transients pulses used for the pulsed electrodeposition of nickel alongside the PED parameters used in this thesis.

The total charge injected into the system is given as follow:

$$\mathbf{Q = I_{Pulse^-} \times t_{on^-} \times n_{Pulses}} \qquad \text{Equation III-6}$$

where $n_{pulses-}$ is the total number of galvanic pulses.

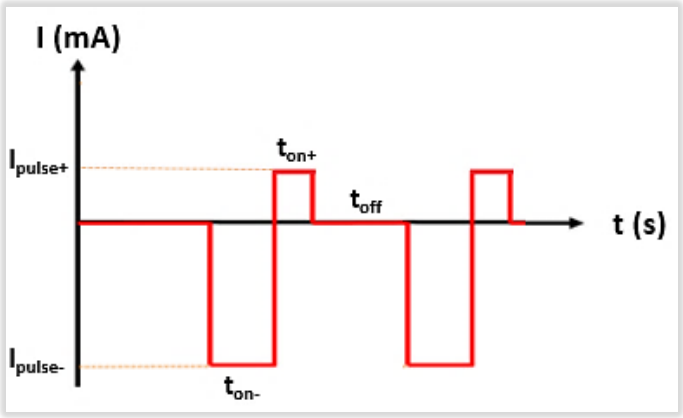

PED Parameters	Value
I_{pulse-}	80 mA/cm²
t_{on-}	52 ms
I_{pulse+}	30 mA/cm²
t_{on+}	10 ms
t_{off}	1 s

Figure III-8: Schematic diagram of the time evolution of current during pulsed electrodeposition. Applied parameters in this thesis: Each high current pulse I_{pulse-} is applied for a time t_{on-} followed by a lower current pulse I_{pulse-} for a shorter time, then a concentration recovery time t_{off} of 1s. This process is repeated for 135, the experimental number of pulses.

In that regard, and prior to electrodeposition, it is possible to have a glimpse of the rate of filling of the pores, *i.e.,* the number of charges **Q** passing through the working electrode, relying on the porosity of anodic aluminum oxide mold. In the case of AAO small nanopores (**D_p=50-60 nm**, **e=400 nm**), the obtained porosity was estimated at **35%.**

The theoretical number of pulses n_{pulses} is calculated according to the desired length, thus to completely fill pores, using Faraday's law (*equation III-6*):

$$n_{pulses} = \frac{\rho_M \times \%P \times e \times n_{e^-} \times F}{M_M \times t_{on-} \times I_{pulse^-}}$$ Equation III-7

where:

Notation	Physical properties	Value
ρ_M	Nickel density	8,902 g/cm^3 at 25°C
e	Alumina thickness	4.10^{-7} m
F	Faraday's constant	96485,33 A.s/mol
M_M	Ni molar mass	58,69 g/mol
%P	Porosity	35%
T_{on-}	Pulse time	0.052 s
I_{pulse-}	Current pulse	0,08 A/cm²

Table III-3: Notations of physical properties and their standard value.

Using *equation III-7*, the calculated number of pulses is 146 pulses, which is more or less in line with the experimental number of 135 pulses performed with a *Biologic©* Potentiostat and controlled with *EC-Lab©* software.

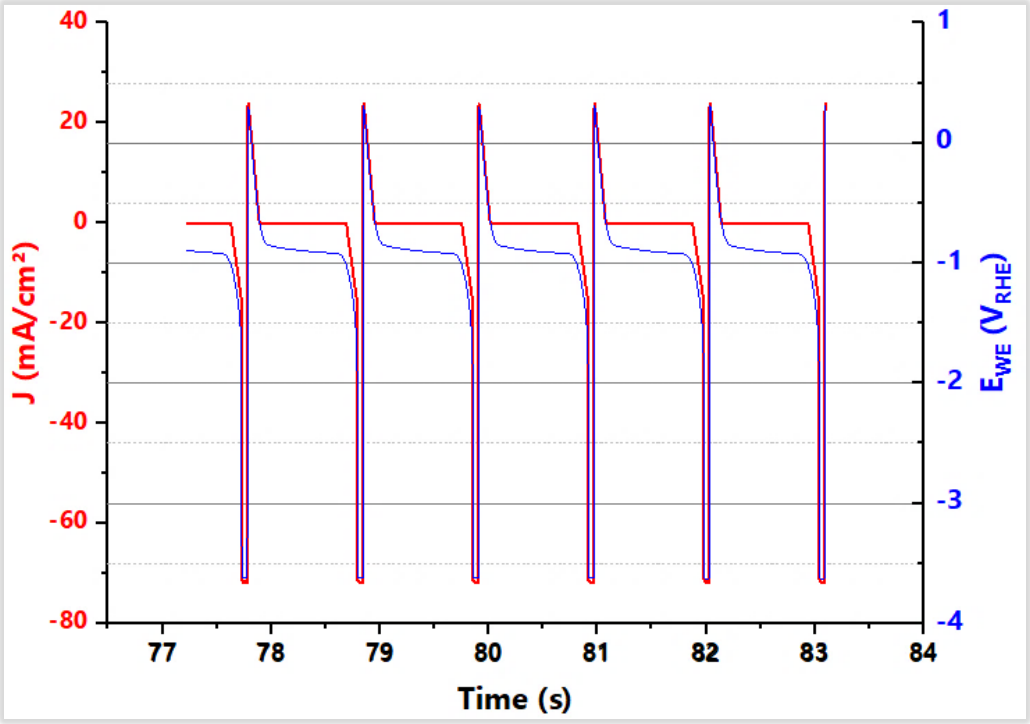

Figure III-9: Experimental plot of the evolution of the current density (red plotting) and the potential response (blue plotting) over time during the nickel's pulsed electrodeposition.

Once we exceed the experimental value of pulses number, we tend to have an overgrowth of the NiNWs. Each nanowire emerges in the form of micrometric agglomerates, as displayed in *figure III-10* below.

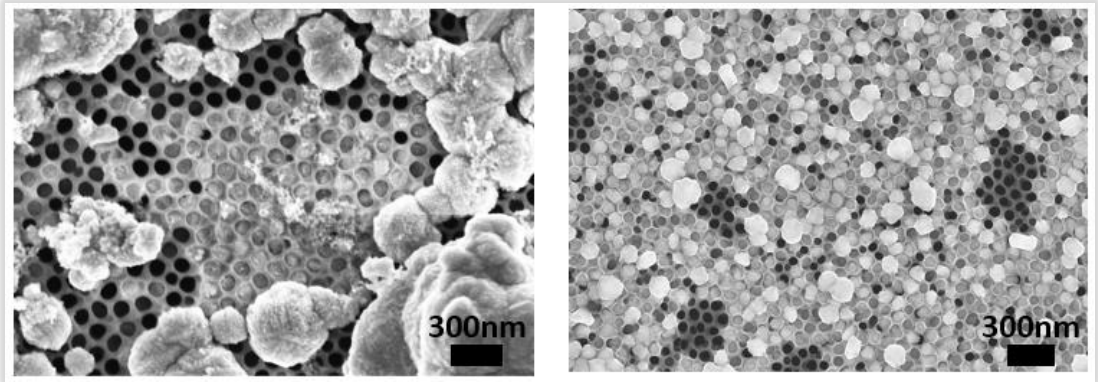

Figure III-10: Top view scanning electron microscopy images (SEM) of nickel overgrowth on nanoporous aluminum oxide template.

II.2 NiNWs structural characterization

Nickel was electrodeposited into porous alumina templates to create ordered nanowires. Pulsed currents helped improve the deposits' quality (smooth surface may be due to Ni oxidation during t_{on+}, and good adherence to the substrate). The deposition time was varied to control the length of the nanowires.

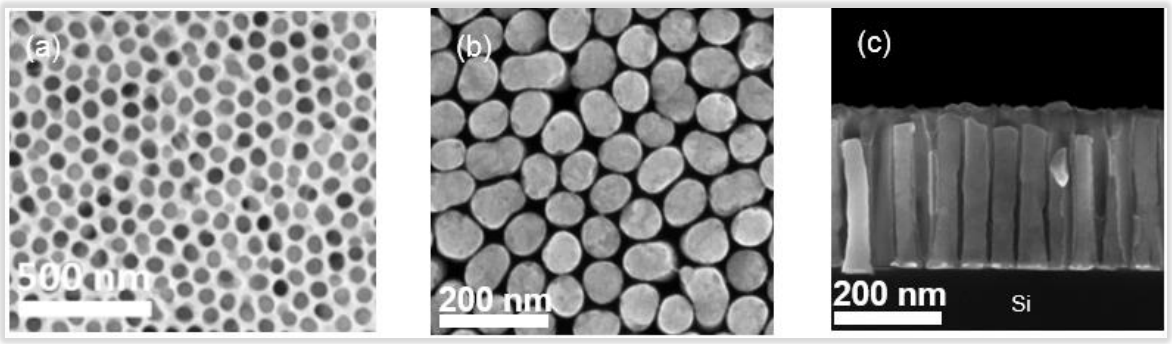

Figure III-11: Scanning Electron Microscopy (SEM) observations of Nickel nanowires grown inside porous anodic alumina template (PAAT), a) SEM top view of Nickel nanowires before alumina etching, b) SEM Top view of Nickel nanowires after alumina etching, and c) SEM cross-sectional view of Nickel nanowires after alumina etching.

The slight difference in NiNWs length in *figure III-11-a)* is attributed to the aluminum deposition's surface unevenness on silicon. To investigate the effect of increasing t_{on+} to 50ms on the deposition, the morphology analysis by SEM of nickel nanowires shown in *figure III-12* depicts the formation of nickel fragments (around 100-200 nm in length).

A more extended discharge period of time may be the origin of an abrupt of the injected number of charges carrying Ni ions revealing an inhomogeneous continuity of the nanowire.

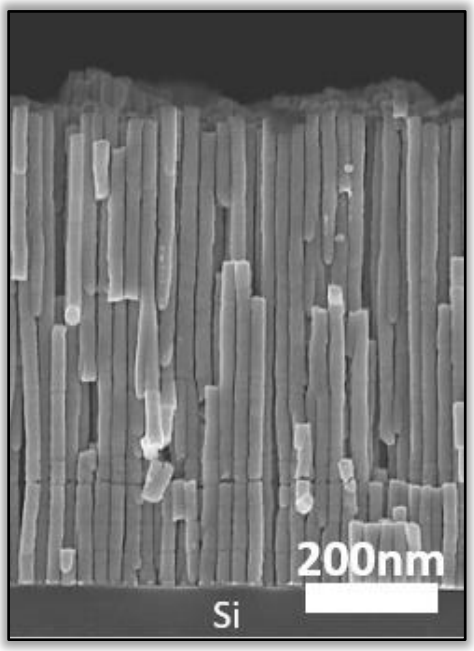

Figure III-12: SEM cross-sectional image of non-confined multisegmented nickel nanowires on silicon synthesized at t_{on+}=52 ms, t_{on-}=52 ms.

To examine the usefulness of HF deoxidation, I carried out two separate experiments with the same parameters where "sample A" was deoxidized while "sample B" was not. We can clearly observe from *figure III-13-B)* the heterogeneous growth of NiNWs. This is attributed to the presence of thin native silicon oxide on the silicon surface at the bottom of the pores. Thus, after SiO_2 deoxidation, the deposition rate has been strikingly improved in terms of height and filling ratio. Therefore, the removal of this layer was mandatory to a uniform NiNWs growth.

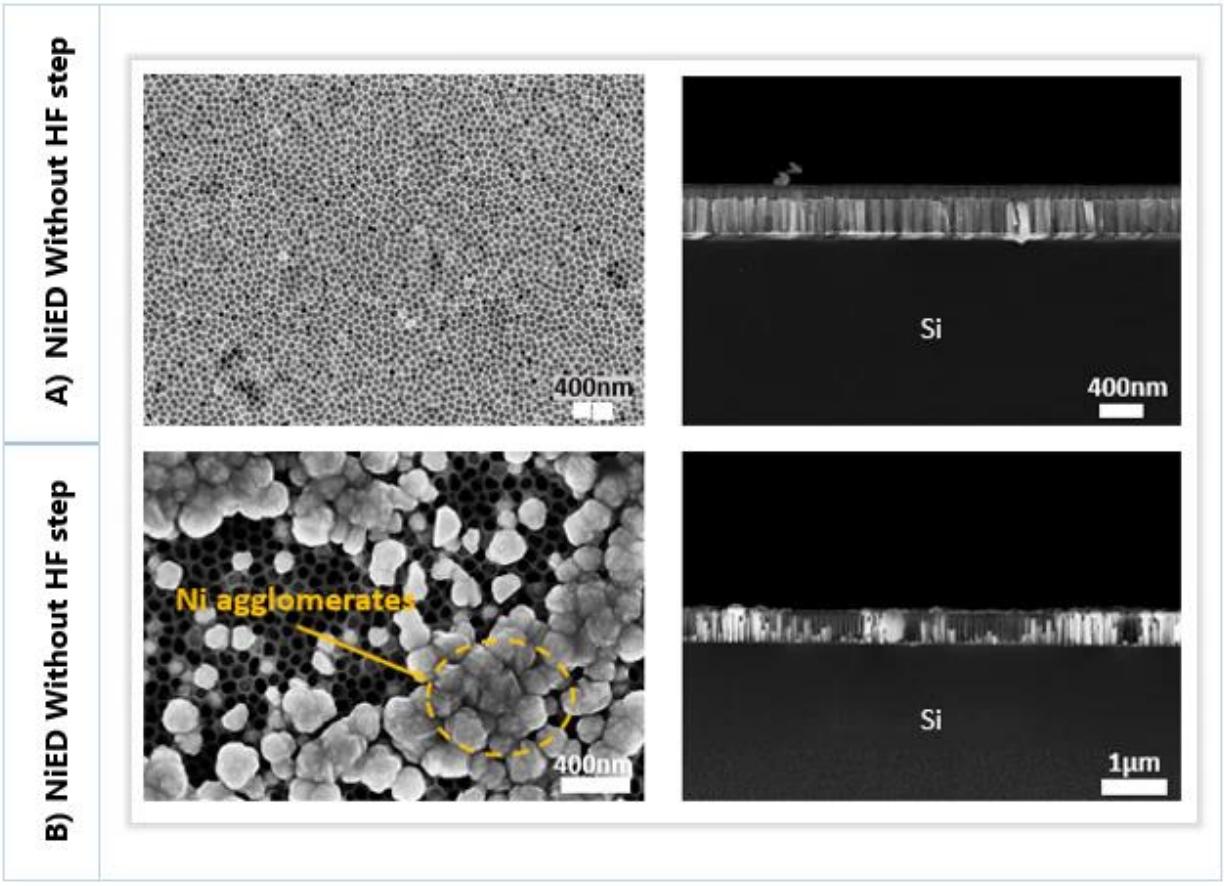

Figure III-13: SEM micrographs of top and a cross-sectional view of NiNWs growth inside anodic aluminum oxide A) with HF deoxidation step and B) without HF deoxidation step.

Conclusion:

In this part of the thesis, we have performed the electrodeposition of nickel nanowires at the bottom of the nanoporous aluminum oxide template pores using pulsed current electrodeposition. A homogeneous and reproducible deposition, height control, and filling ratio were obtained after the HF pre-deoxidation process of the native SiO_2 layer at the bottom of nanopores. The following section will provide an in-depth study of Pt galvanic displacement reaction with nickel nanowires in a confined and non-confined system (after AAO etching).

III. Bibliographic Synthesis: Platinum Galvanic Displacement as an electrochemical way to fabricating PtNi electrocatalyst

For its unique set of advantages, platinum is widely used in medicine, microelectronics, and as a catalyst. It is the main element that can meet performance requirements while enhancing slow reaction kinetics and limiting proton exchange membrane (PEM) system degradation [24]. To dig deeper into the improvement of activity of pure Pt, many investigations have been conducted to elaborate binary Pt-X electrocatalysts (X stands for transition metals: Co, Cu, Ru, Ni, etc...), with different morphological shapes, whether by alloying, layering, dealloying and/or core-shell approaches. Tuning the geometry of Pt-M-based electrocatalysts allowed a significant increase in catalytic activity.

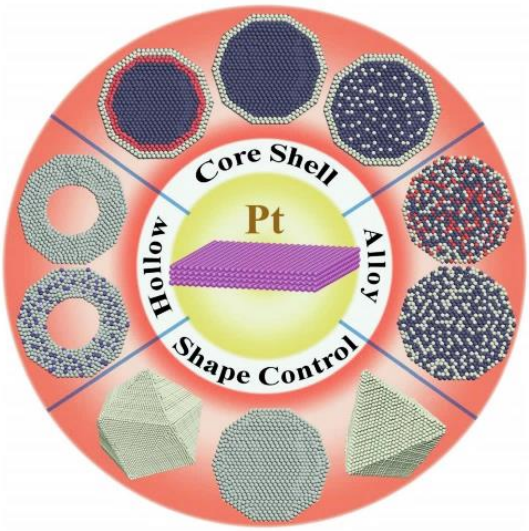

Figure III-14: Recent important advances in new active and durable Pt-based nanostructures for improved ORR catalysis. Reprinted from reference [25].

Among the various transition metals, alloying platinum with nickel has shown exceptional oxygen reduction reaction (ORR) mass activities and promising durability in rotating disk electrode (RDE) experiments, as evidenced in *figure III-15* below [26]. As a matter of comparison, a record ORR specific activity of 11.5 mA/cm^2_{Pt} at 0.9 V vs. RHE (*i.e.,* 33 times higher than a commercial Pt/C) was reported in 2016 on jagged Pt nanowires formed by complete dealloying of PtNi nanowires, thereby confirming that high ORR activity can be obtained [27].

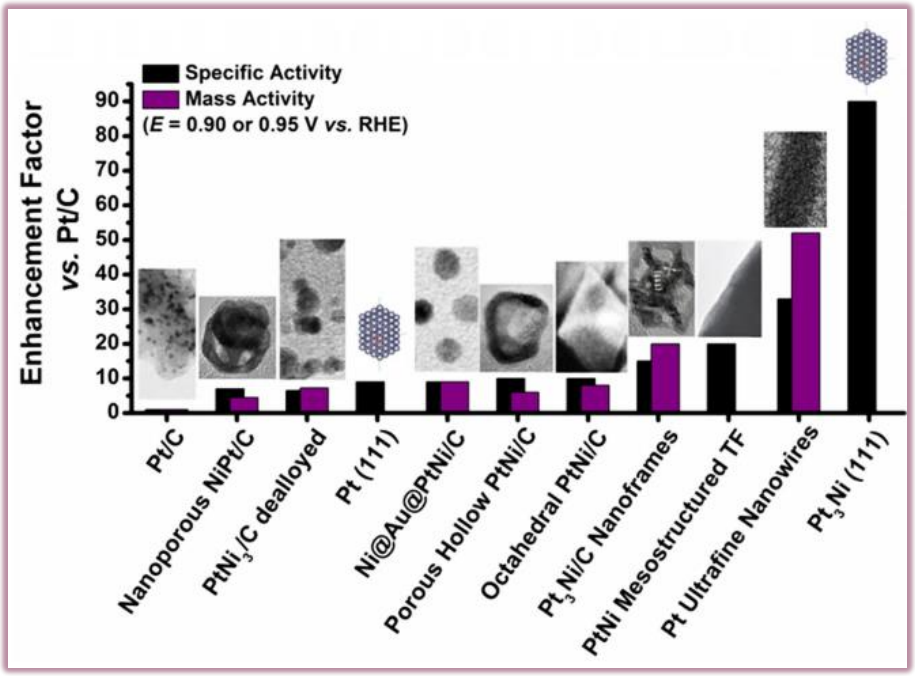

Figure III-15: Enhancement of the ORR kinetics vs. Pt/C for several electrocatalysts in 0.1 M $HClO_4$, *i.e.,* commercial Pt/C, nanoporous NiPt/C, dealloyed $PtNi_3$/C, porous hollow PtNi/C, octahedral PtNi/C, and Pt ultrafine nanowires. Reprinted from reference [26].

Pt-alloys are state-of-the-art materials for high activity oxygen reduction catalysts. In this chapter, we will be discussing notably the various structures of Pt-Ni alloys as electrocatalysts for the PEMFC obtained by the galvanic displacement route.

III.1 Why alloying Pt with transition metals? Vulcano Plot, d-band theory, and DFT calculations

Platinum is known to be the most active and stable electrocatalyst used for both anode and cathode of a PEMFC to promote HOR and ORR at the anode and the cathode, respectively. Clinging to the Sabatier[20] principle, which states that for a two-step reaction passing through an adsorbed intermediate (O, OH, and OOH species), the adsorption energy (E_{M-H} kJ/mol) should be neither too high nor too low. If it is is too high (endothermic), adsorption is slow and limits the overall rate; if it is too low (exothermic), desorption is slow [28].

[20] Sabatier, F. La catalyse en chimie organique ; Berauge : Paris, 1920.

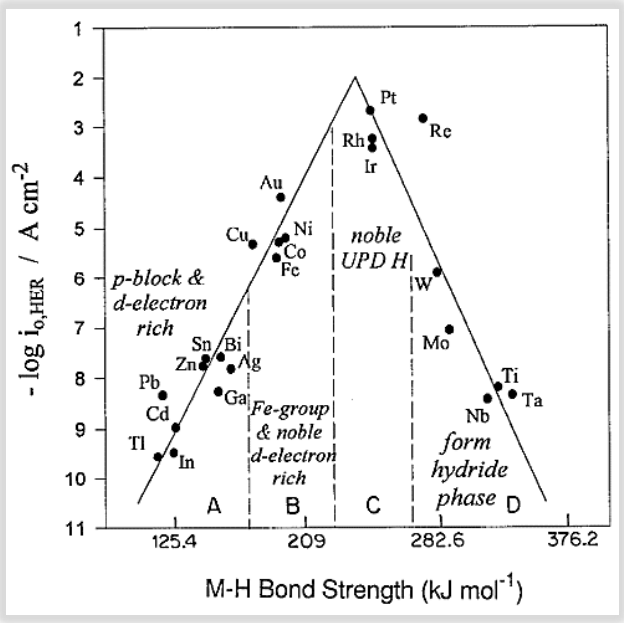

Figure III-16: Volcano plot of Trasatti for log(i_0) values for the Hydrogen Evolution Reaction as a function of M-H bond energy reprinted from reference [29].

How alloying Pt with 3d-transition metals tunes the electronic structure? Until the late 80's when *Paul Stoneheart* veered toward the elaboration of Pt alloys with a transition metal, demonstrating significantly higher performance for oxygen reduction than does bulk platinum [30]. *Nørskov et al.* also revealed the reasons why Pt showed significant performance compared to other metals and gave insights into the electrochemical reduction of dioxygen. Their results stemmed from the density functional calculations (DFT) shown in *figure III-17 below* [31].

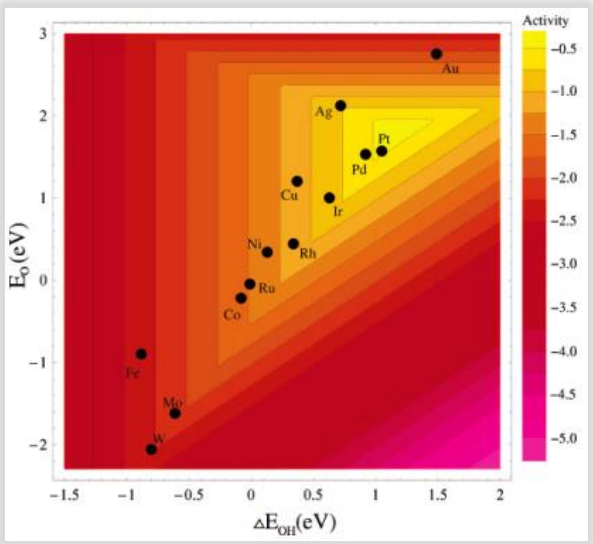

Figure III-17: Trends in oxygen reduction activity plotted as a function of both the O and the OH binding energy. Reprinted from reference [31].

Stamenkovic and his co-workers [32] reported that alloying Pt-X alloys (X stands for Ti, V, Fe, Co, Ni) exhibit a higher ORR activity than pure Pt based on both theoretical calculations (DFT) and experiments. They assumed that Pt alloys tune the electronic structure, hence modifying the surface reactivity to change the performance for the ORR according to: **i/** strain effect, which is evidenced while alloying Pt with smaller atomic size elements, inducing a contraction of the Pt-lattice, thus downshifting the Pt d-band center; **ii/** Ligand effect as a result of the change in the electronic structure of the catalytic sites by the close transition metal atoms.

Let it be emphasized here that *Stamenkovic et al.* [32] have reported from their RDE results that the $Pt_3Ni(111)$ surface is 10-fold more active for the ORR than the corresponding Pt(111) surface and 90-fold more active commercial Pt/C catalysts, believing that the key parameter that determines the unusually catalytic activity of $Pt_3Ni(111)$ is the low coverage by OH_{ad} (see *figure III-18* below)**.** The characterization of Pt-Ni(hkl) alloy surfaces summarized that the different low-index surfaces have a markedly different activity for the ORR: $Pt_3Ni(100)$-skin < $Pt_3Ni(110)$-skin << $Pt_3Ni(111)$-skin.

Besides the transition metals cited above, several Pt-X catalysts have been studied, including, PtAl, PtCr, PtPb, Pt_5Gd, Pt_3Y, and some corresponding ternary compounds [33][34].

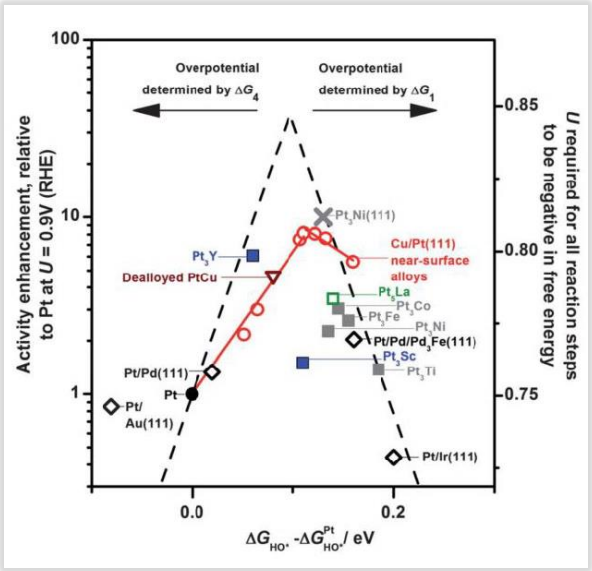

Figure III-18: Volcano plot depicting the rate of the oxygen reduction reaction and activity enhancement on Pt-based alloys as a function of hydroxyl binding energy, ΔG_{HO*}, both relative to pure Pt. All data are at U= 0.9 V, with respect to a reversible hydrogen electrode (RHE) from reference [35].

Further and deeper studies on the optimization of various Pt-based catalysts allowed the understanding of the oxygen reduction reaction activity. *Figures III-19-a and b* summarizes the reported half-cell activity and stability of recent Pt-M catalysts, demonstrating the breakthrough provided by highly ordered Pt-M intermetallic catalysts. *Figures III-19-c) and d)* further compare PEMFC performance (mass activities) of PGM cathodes, showing significantly reduced Pt loading in MEAs using structurally ordered Pt-M intermetallic catalysts. This exciting performance improvement suggests that practical applications in the PEMFC industry should emerge quickly [33].

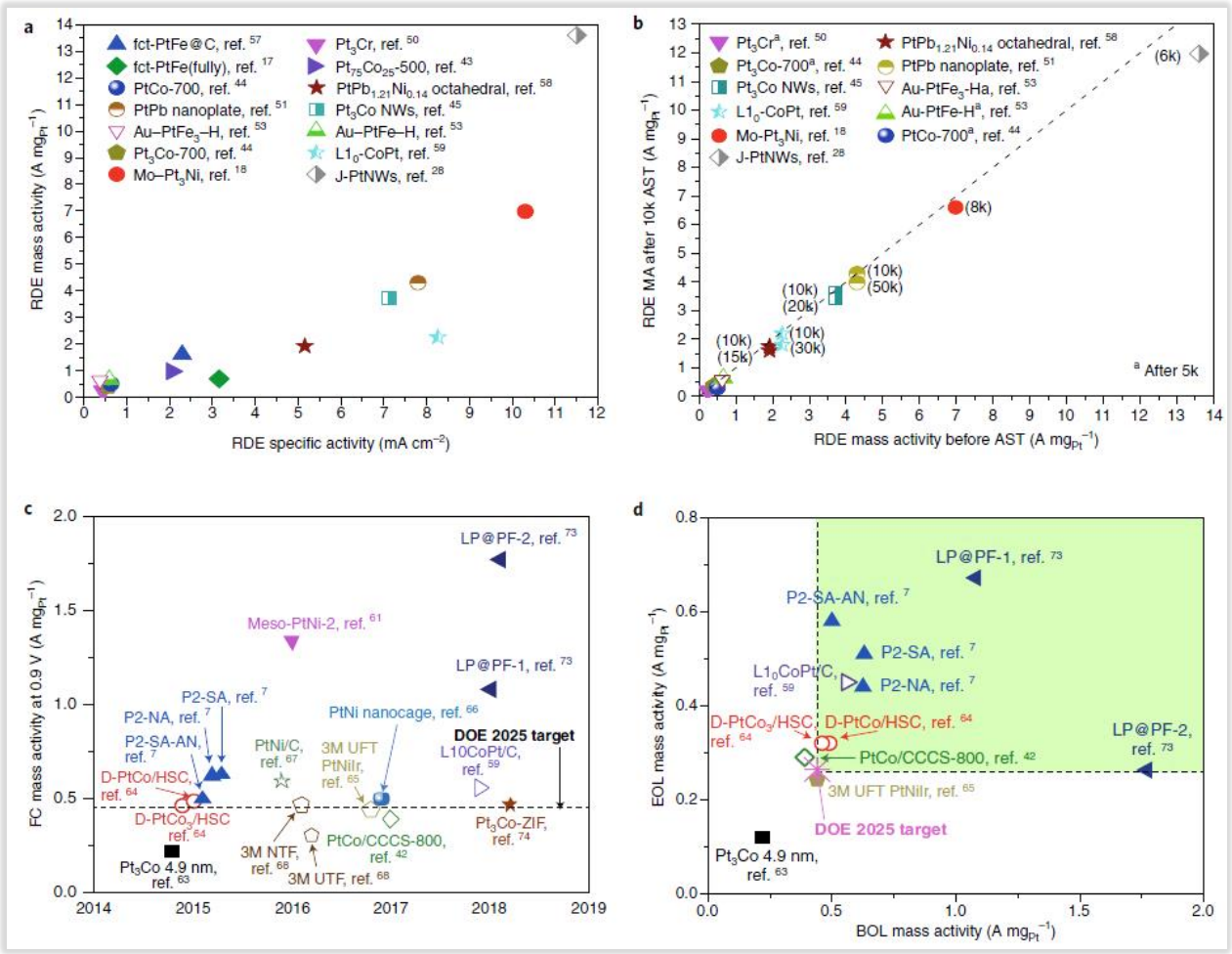

Figure III-19: Current development of PGM catalysts: a) Specific activity and mass activity at 0.9 V for different Pt-M intermetallic catalysts in aqueous electrolytes via RDE tests. b) Mass activity at 0.9 V before and after 10,000 potential cycling Accelerated Stress Tests. c) Mass activity at 0.9 V for low-PGM catalysts, calculated from PEMFC performance using H_2/O_2, 1.0 bar, 80°C, and 100 %RH. d) Mass activity at 0.9 V at the beginning of life (BOL) tests and end of life (EOL) tests after 30,000 potential cycles in PEMFCs. Reprinted from reference [33].

However, getting a grip on a low-cost and effective fabrication method of Pt-based electrocatalyst, galvanic displacement reaction of a transition metal by Pt provides a practical approach: this is the following paragraph's aim.

III.2 Galvanic displacement: A versatile electrochemical process

Galvanic displacement is a redox process in which a sacrificial metal with low standard redox potential is corroded by the ions of a second metal with a higher standard potential redox in an electrolyte. Suppose a solution containing noble metal salt ions M^{x+} (with higher standard redox potential) is in contact with a less noble metal X (with lower standard redox potential), a galvanic exchange occurs spontaneously; the noble metal M is deposited on the surface of the metallic metal X that is oxidized and formed cations. *Table III-4* below summarizes the reduction potentials of metals commonly used in GD experiments.

Redox Reaction	**E° (V *vs.* SHE)**
$Co^{2+} + 2e^- \rightarrow Co_{(s)}$	-0.28
$Ni^{2+} + 2e^- \rightarrow Ni_{(s)}$	-0.25
$Cu^{2+} + 2e^- \rightarrow Cu_{(s)}$	0.34
$Ag^{+} + e^- \rightarrow Ag_{(s)}$	0.80
$Pd^{2+} + 2e^- \rightarrow Pd_{(s)}$	0.95
$Pt^{2+} + 2e^- \rightarrow Pt_{(s)}$	1.18
$Au^{3+} + 3e^- \rightarrow Au_{(s)}$	1.50

Table III-4: Standard reduction potentials of various metals relative to the standard hydrogen electrode (SHE) for ideal conditions at 25 °C and 1 atm.

Galvanic displacement offers a particularly effective and versatile approach due to its ability to control the size and shape and tune the composition, internal structure, and morphology of the resultant nanostructures. As a result, the final product typically exhibits various shapes: whether a shape is closely resembling that of the original template with a slight increase in dimensions, a hollow nanostructure, or a porous morphology. The

overall process covers two main key subprocesses: **i/** alloying: Involved in the initial stage of a GD reaction when a thin layer of metal M is deposited on the template composed of metal X; **ii/** and dealloying: which plays an important role in the later stages of a GD reaction, especially in controlling the porosity of the wall, when the metal with a lower reduction potential is selectively removed from the alloyed wall, either by adding more of the metal ions involved in the galvanic replacement or by utilizing a conventional wet etchant [36].

As a matter of example, to investigate the synthesis of hollow Pt-Ni/C nanoparticles scrupulously, via a one-pot process involving galvanic displacement and the nanoscale Kirkendall effect, *Laetitia D.* and coworkers [37] achieved 6- and 9-fold enhancement in mass and specific activity for the ORR, respectively over standard solid Pt/C nanocrystallites of the same size (see *figure III-20)*.

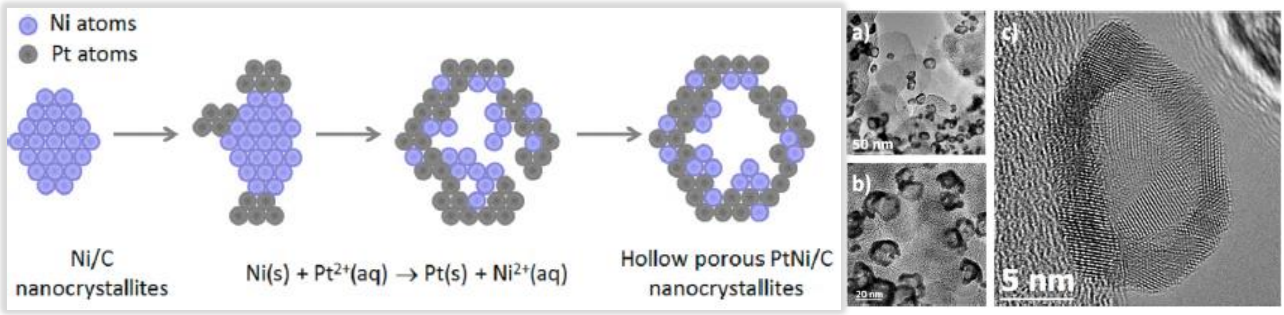

Figure III-20: Left: Schematic illustration of the galvanic displacement procedure used to synthesize hollow Pt-rich nanoparticles as described in reference [37]. Right: Aberration corrected HR-TEM images of the hollow PtNi(1:3)/C nanoparticles. a) and b) Assemblies of PtNi (1:3)/C nanoparticles imaged at 250.000 and 400.000× nominal magnification, respectively. c) an HR-TEM image of a single PtNi (1:3)/C nanoparticle [37].

III.3 Nanostructures of PtNi electrocatalysts: State-of-the-art

Alongside specific activity, the platinum specific surface area (S_{Pt}) of the catalyst is considered a key element to increasing the catalytic activity of an electrocatalyst for the ORR. From single crystals to nanomaterials, nanostructuring highly efficient electrocatalysts have shown a drastic increase in S_{Pt}, thus enhancement of the specific surface area (SA). Performance optimization is ensured by tuning the nanocatalyst's surface structure, composition, and size control, as displayed in *figure III-21* below.

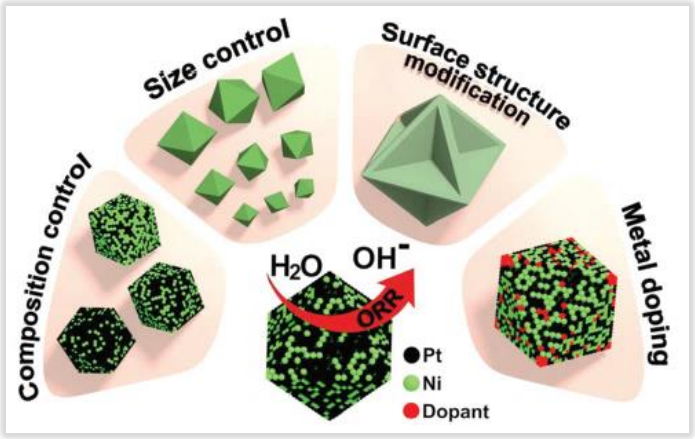

Figure III-21: Engineering of PtNi octahedra as ORR catalysts from reference [38].

PtNi-based electrocatalysts offered substantial advantages as excellent ORR electrocatalysts owing to the compressed Pt–Pt interatomic distances, favorable chemisorption of the OH species onto the Ni sites, and downshift of the Pt d-band center [38]. Consequently, various 1D, 2D, and 3D PtNi nanostructures with preferential facets have been studied and developed for the past decades. The following is a roundup of some of the latest scientific studies on the novel PtNi electrocatalysts.

III.3.1 Shape-Controlled PtNi nanoparticles

In 1998, *Toda et al.* [39] reported surface-oriented studies of various Pt alloy catalysts, showing an activity increase up to 2-fold over pure Pt. *U.A. Paulus et al.* [40] carried out further studies on Pt-Ni alloy catalysts compared to pure Pt catalysts dispersed on carbon-supported in 2002 using ex-situ characterization (thin-film RRDE method). Oxygen reduction reaction revealed a quite unstable behavior of this catalyst is in the ORR potential region and significant activity enhancement per geometric area on electrodes with equal overall metal loading, very similar particle size, and a very identical Pt surface atom density. The observed structural changes in PtNi particles' morphology become more "Pt-like", probably indicative of Ni's leaching from the surface, hence the instability of the PtNi catalyst in the ORR environment.

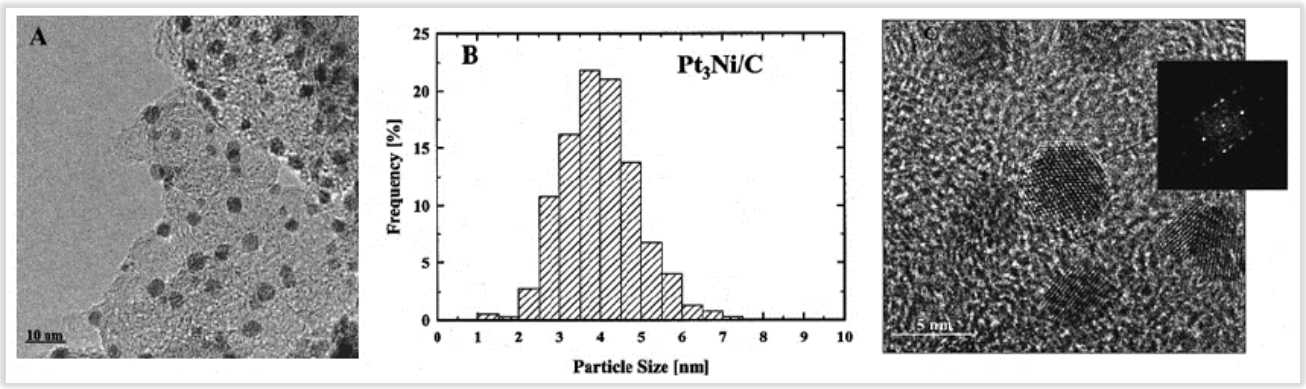

Figure III-22: a) Low-magnification high-resolution episcopic microscopy (HREM) micrograph, b) Particle size distribution determined by HREM micrographs, c) HREM micrograph with an atomic resolution of the Pt_3Ni catalyst [40].

In 2010, *J. Zhang* and co-workers [41] reported a new route to synthesize monodisperse and highly active Pt_3Ni nanoctahedra and nanocubes terminated with {111} and {100} facets by means of a new wet chemical approach (a high-temperature organic solution chemistry approach) using tungsten hexacarbonyl $W(CO)_6$ as reducing agent and oleylamine and oleic acid as solvent and capping agents respectively (*figure III-23*).

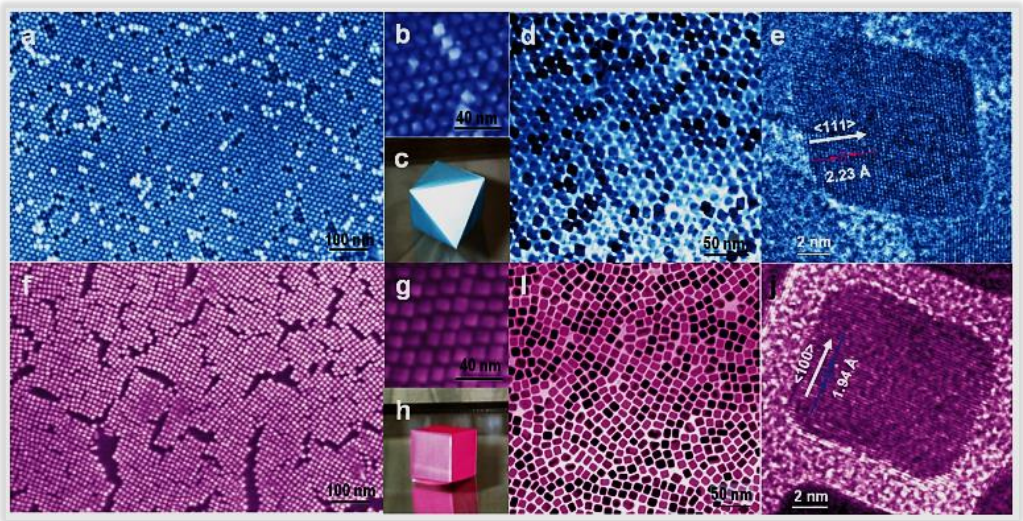

Figure III-23: a-e) Images for Pt_3Ni nanoctahedra. f-j) Images for Pt_3Ni nanocubes. a, f) Field-emission SEM images. b, g) High-resolution SEM images. c) 3D illustration of an octahedron. d, i) TEM images. e, j) High-resolution TEM images of single NCs. h) 3D image of a cube [41].

According to the ex-situ experiments, the group suggested that controlling the shape of nanocatalyst might be an effective way to improve ORR activity and develop highly active electrocatalysts according to the ex-situ experiments as evidenced in *figure III-24.* PtNi

octahedra achieved 5 and 7-fold enhancement in specific activity (2.8 and 4-fold enhancement in mass activity) relative to the nanocubes and commercial Pt/C.

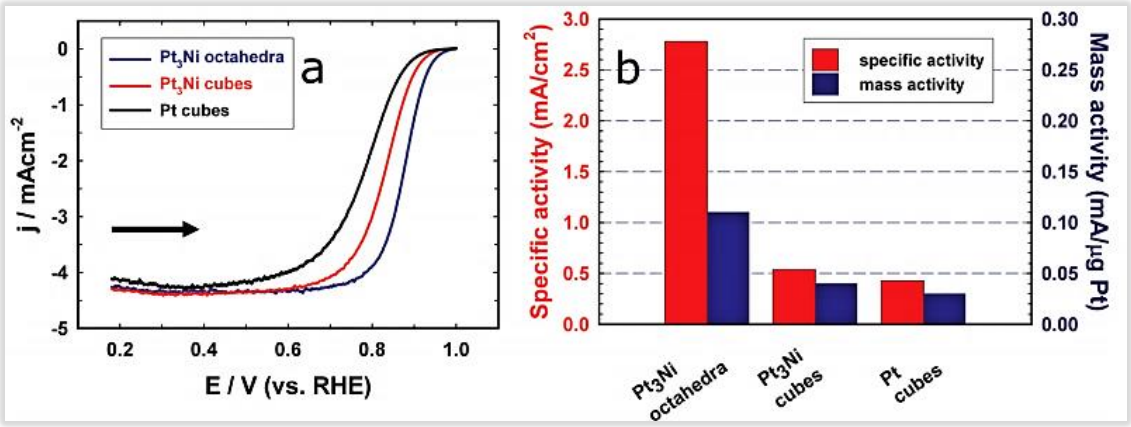

Figure III-24: a) Polarization curves for ORR on Pt_3Ni nanoctahedra, Pt_3Ni nanocubes, and Pt nanocubes supported on a rotating glassy carbon disk electrode in O_2 saturated 0.1 M $HClO_4$ solution at 295K; scan rate, 20 mV/s; rotation rate, 900 rpm. Catalyst loading in terms of Pt mass: Pt_3Ni octahedra, 3.0 µg; Pt_3Ni cube, 2.0 µg; Pt cube, 1,1 µg. The current density was normalized to the glassy carbon geometric surface area (0.196 cm^2). The arrow indicates the potential scan direction. b) Comparison of the OR activities on the three types of catalysts. Specific activity and mass activity were all measured at 0.9 V *vs.* RHE at 295 K [41].

For the past decade, fine-tuning the geometry and the size of PtNi octahedra, including bimetallic, core-shell, and multi-metallic nanostructures via various chemical routes and etching techniques, featured enhancement in electrocatalytic activity of this particular type of nanomaterials for the ORR [42][43][44], in a reproducible manner in ex-situ experiments as summarized in *table III-5* below.

Pt/Ni ratio of PtNi octahedra	Shape directing agent	MA @ 0.9 V_{RHE} ($A.mg_{Pt}^{-1}$)	SA @ 0.9 V_{RHE} ($mA.cm_{Pt}^{-2}$)
Pt_3Ni_1	CO gas	1.1	2.8
$Pt_{2.5}Ni$	CO gas in benzyl ether	3.3	7.3
$Pt_{1.5}Ni/C$*	CO/H_2 gas	1.96	3.99
PtNi	Metal precursor ligand	1.45	3.14
Pt_3Ni/C*	Benzoic acid	1.62	2.53

* PtNi octahedra directly grown on carbon supports.

Table III-5: Summary of the ORR activities of PtNi octahedra synthesized by adding different shape-directing agents. Reprinted and edited from references [45].

Finally, incorporating a third metal to PtNi octahedra (Co, Mo, Rh, Rh, Pd) could significantly suppress the long-term deactivation, shape deformation, and composition decay to ensure higher and more stable catalysts [46]. However, Ni atoms seem to leach out from the octahedral structure under stability tests leading to a significant surface activity loss.

III.3.2 Core-Shell PtNi nanoparticles

A new strategy to overcome leaching issues of the transition metal, affording higher stability of the catalyst, is the tunable core-shell structure. The latter consists of Pt-rich layers (shell) deposited over a core metal (mainly a pure metal or an alloy) to utilize platinum better. *M. Oezaslan et al.* [47] conclusively reported that the Pt shell thickness is a key parameter for controlling the activity of core-shell nanocatalysts, usually based on the chemical leaching and electrochemical dealloying methods. Dealloying and acidic leaching (or selective dissolution) can be distinguished from each other as two distinctly different atomic processes.

In general, dealloying is the electrochemical dissolution of the less noble metal from a uniform multimetallic alloy in acid. A strong depletion of the less noble metal results from the dealloying process, leading to the formation of a thicker Pt-enriched surface

consisting of several atomic layers. In contrast, acid leaching only attacks the near-surface region of the alloyed material. An overview of the different approaches and strategies for the preparation of Pt-based core–shell nanocatalysts is presented in *figure III-25* below, reprinted from reference [47].

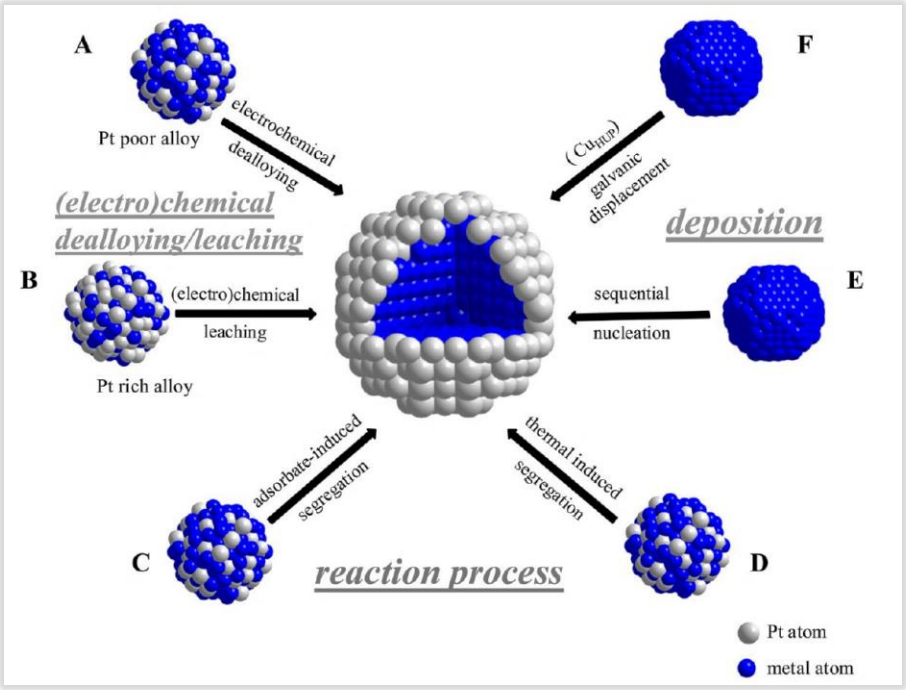

Figure III-25: Illustration of basic synthesis approaches for the preparation of core–shell nanoparticle catalysts. Electrochemical (acid) dealloying/leaching results in A) dealloyed Pt bimetallic core-shell nanoparticles and B) Pt-skeleton core-shell nanoparticles, respectively. Reaction process routes generate segregated Pt skin core–shell nanoparticles induced either by C) strong binding to adsorbates or D) thermal annealing. The preparation of E) heterogeneous colloidal core-shell nanoparticles and F) Pt monolayer core-shell nanoparticles is via heterogeneous nucleation and Under-Potential Deposition (UPD) followed by galvanic displacement, respectively. Reprinted from reference [47].

Furthermore, the experimentally observed ex-situ activities of PtNi core-shell nanoparticle catalysts from a selected set of reports are summarized in *table III-6* below [47].

Core@shell catalyst	Synthesis method[a] (*Figure III-25*)	Particle size (nm)	MA[b]	SA[b]	Metal precursor salts
$PtNi_3$@Pt	A	6-7	7	6.7	Pt/C, $Ni(NO_3)_2$
$PtNi_3$@Pt	B	~5	-	9	$Pt(acac)_2$, $Ni(acac)_2$

a Synthesis methods as described in *Figure III-24*.
b ORR improvement factors were determined by comparing Pt mass-based activity (i_m: mA/mg_{Pt}) or Pt specific-surface-area-based activity (i_s: $\mu A/cm_{Pt}^2$) with those for pure Pt catalyst with comparable particle size at identical reaction conditions and reference potentials, taken from the same paper.

Table III-6: Collection of different synthesis methods for the preparation of PtNi core-shell nanoparticles and their resulting ORR activity (MA: mass activity, SA: specific activity) improvement factors.

As part of their experiments, the research group concluded that due to the low dissolution potentials of 3d-transition metals, they tend to dissolve in contact with strong acids and anodic potentials of up to 1V *vs.* RHE, which results in an increase in the Pt shell thickness. The improved ORR activities of core-shell nanoparticles present in the early stage of the catalyst life cycle gradually decrease due to the thicker Pt shell. They, therefore, resemble more and more the performance of a pure Pt surface [47].

Drawing on the dealloying method, *Strasser et al.* [48][49] synthesized a variety of dealloyed core-shell Pt_xNi_{1-x} (*figure III-26*) obtained by potential cycling. Pt alloys with varying near-surface compositions manifest distinctly different ORR activities and exhibit enhanced ORR activities compared to a commercial 3-5 nm Pt/C NPs catalyst. Dealloyed $PtNi_3$ nanoparticles showed the highest mass activity and specific activity (5-fold and 10-fold enhancement over Pt/C catalyst, respectively). The highest residual Ni content underlines the importance of retaining a high content of the transition metal in the dealloyed NPs to achieve optimal ORR activity [48].

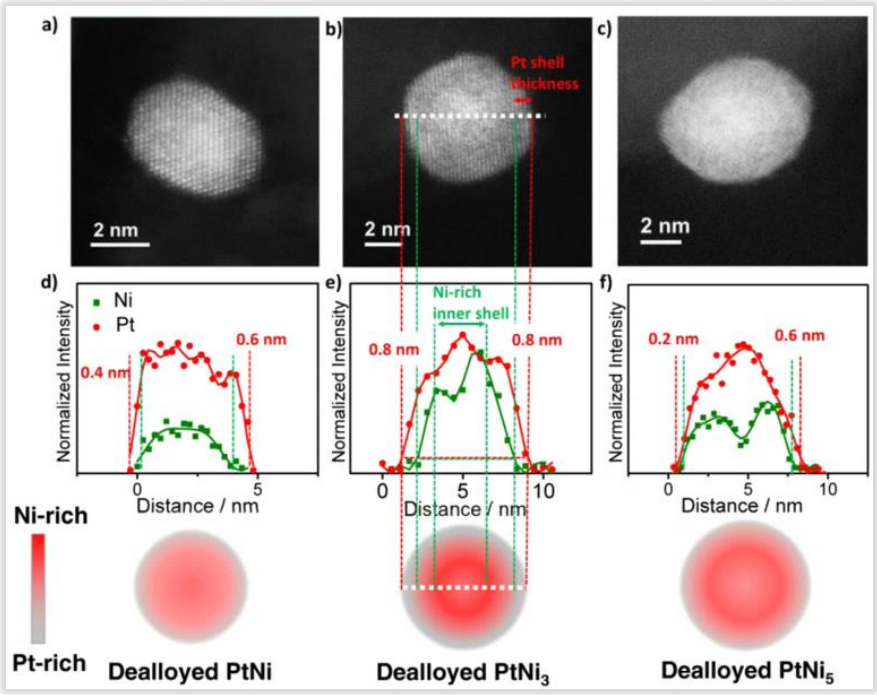

Figure III- 26: High-resolution HAADF-STEM images of dealloyed PtNi a), $PtNi_3$ b), and $PtNi_5$ Nanoparticles (NPs) c), and EELS line compositional profiles d-f) across the NPs, respectively. Bottom line: Structural model of distinctly different compositional core-shell fine structures of dealloyed Pt_xNi_{1-x} catalysts. Extracted from reference [48].

Subsequently, *Wang et al.* [50] highlighted the critical role of Pt shell thickness in varying the ORR activities, where higher initial Ni compositions in Pt_xNi_{1-x} (from Pt_3Ni to $PtNi_3$) were reported to result in a higher extent of Ni dissolution and thereby thicker pure Pt shells, which lowers ORR activity. Additionally, the distribution of transition metals at and below the surface (down to ~10 atomic layers from the surface) appeared to play a more critical role in controlling lattice strain and, hence, catalytic reactivity of the outermost Pt layer.

III.3.3 Hollow Pt-Ni nanoparticles

As a firsthand use of the core@shell nanostructure in electrocatalysis, *H-P Liang et al.* [51] have developed Pt hollow nanosphere catalysts for direct methanol fuel cell (DMFC) at room temperature in a homogeneous solution with Co nanoparticles as sacrificial templates. Unlike the core@shell nanoparticles, hollow PtNi NPs obtained by the galvanic replacement process display a void or porosities in the center of the particle due to the chemical dealloying process, which involves removing the less-noble metal core exhibiting a lower standard potential comparing to Pt. Depending on the initial particle

size, the nanocavities' formation relies on the dealloying process parameters (*e.g.,* electrolyte type, temperature, media, time), leading to a well-defined and controllable size and shape hollow NPs. Nevertheless, their poor morphology is still a matter of debate. The dealloying mechanism invokes two main sequential chemical stages: galvanic replacement, Kirkendall effect, and Ostwald ripening [36].

In 2012, leaning towards PtNi alloys, *S. J. Bae* and coworkers [52] reported a simple method for the preparation of carbon-supported and highly uniform PtNi hollow nanoparticles with higher ORR activity than a commercial Pt/C (~3 and ~8-fold enhancement of mass and specific activity for the ORR relative to Pt/C, respectively) as laid out *figure III-27-A) and B)*.

Two years later, *L. Dubau et al.* [53] synthesized hollow carbon-supported Pt_xNi_{1-x}/C nanoparticles with low Ni content via Ni atoms' galvanic replacement by Pt atoms and the nanoscale Kirkendall effect. These nanoparticles have shown improved and sustainable ORR specific activity in a liquid electrolyte and PEMFC operating conditions (see *figure III-27-C) and D))*. The same research group [54][55][56], alongside *R. Chattot* and *T. Asset* Ph.D. works have been studying the formation and growth mechanism of hollow PtNi/C NPs via several chemicals methods, indicating that ORR activity can be tuned by nanostructuring and suggested that targeting structural disorder is a promising approach to improve the electrocatalytic properties of mono- or bimetallic nanocatalysts.

In the same year, *V.R. Stamenkovic et al.* [57][58] synthesized one of the most attractive PtNi hollow nanostructures, a highly active and durable class of electrocatalysts, by transforming solid $PtNi_3$ polyhedral nanoparticles into an open-cell three-dimensional (3D) frame (see *figure III-27-E) and F))*. According to RDE measurements, hollow Pt_3Ni nanoframes with Pt(111)-skin-like surface have exhibited greatly enhanced mass and specific activity at 0.95V compared to commercial Pt/C (~36 and 22-fold enhancements in mass and specific activity). However, what is striking here is that real PEMFC tests have shown a drastic drop in SA and MA, probably due to nickel instability in the acidic medium.

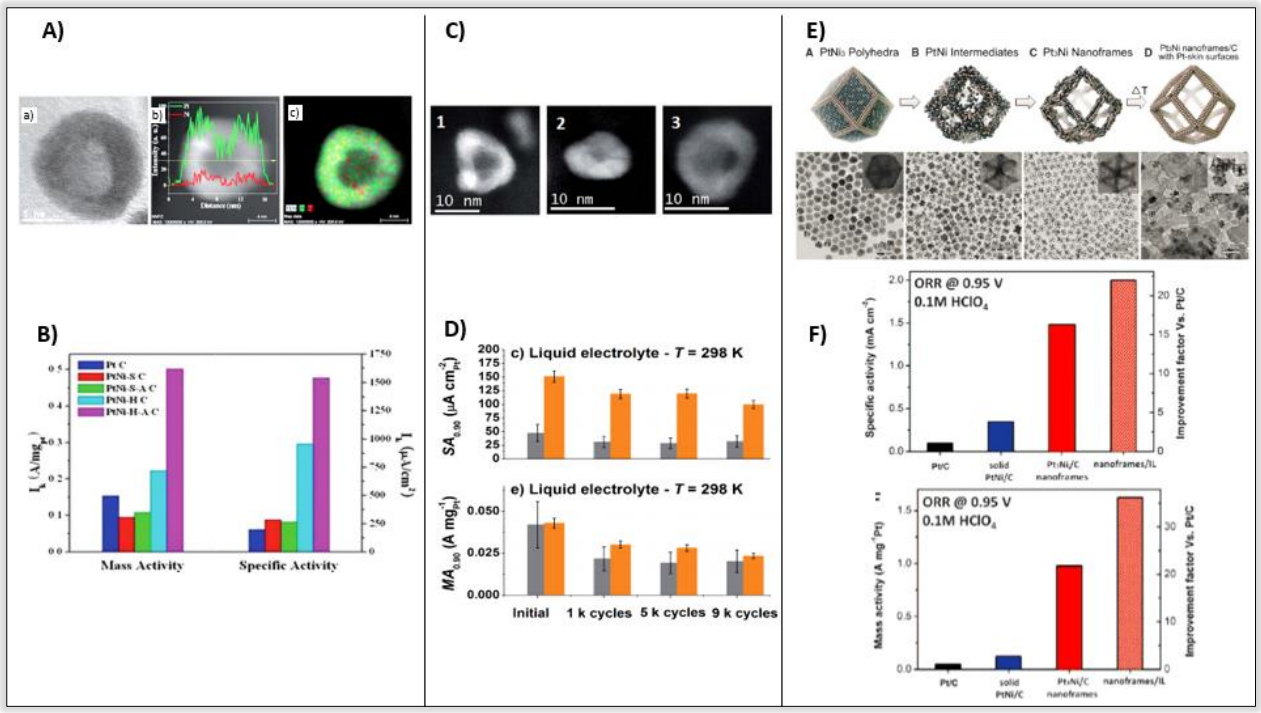

Figure III-27: TEM images of PtNi hollow nanoparticles and their electrochemical properties (mass and specific activities) compared to commercial Pt/C: A) (a) TEM, (b) STEM image, and (c) overlaid version of elemental mapping on the TEM image of PtNiH-A/C. (b and e) Inset figures are EDX line-scanning profiles along a single hollow particle indicated by the arrow for PtNi /C. B) Comparison of mass and specific activities at 0.9 V. C) aberration-corrected HAADF-STEM images and X-EDS spectra measured on the as-synthesized Pt–Ni/C and the Pt–Ni/C-AT nanoparticles. D) The ORR specific activity and the ORR mass activity during an accelerated stress test consisting of potential cycles between 0.60 and 1.05 V vs. RHE. E) samples obtained at four representative stages during the evolution process from polyhedra to nanoframes: (A) Initial solid PtNi3 polyhedra, (B) PtNi intermediates, (C) Final hollow Pt_3Ni nanoframes, (D) Annealed Pt_3Ni nanoframes with Pt(111)-skin-like surfaces dispersed on high–surface area carbon and F) Specific activities and mass activities measured at 0.95 V, and improvement factors versus Pt/C catalysts.

III.3.4 PtNi aerogels

Other types of nanomaterials exhibiting exceptional activity for the ORR have also been synthesized. *S. Henning et al.* [59] have tested a novel class of unsupported bimetallic alloy catalysts (Pt_3Ni aerogels; *figure III-28-A*) as the cathode material in polymer electrolyte fuel cells. The catalyst was prepared by a simple co-reduction route of $NiCl_2{\cdot}6H_2O$ and H_2PtCl_6 with $NaBH_4$ in an aqueous solution under ambient conditions (room temperature, air).

Electrochemical measurements of the aerogels' catalytic activity toward oxygen reduction in RDE measurements revealed a 3-fold specific activity increase when compared to

commercial Pt/C catalysts as evidenced in *figure III-28-B) and C)*. The ECSA of the aerogels estimated to be ≈30 m^2/g_{Pt} [59].

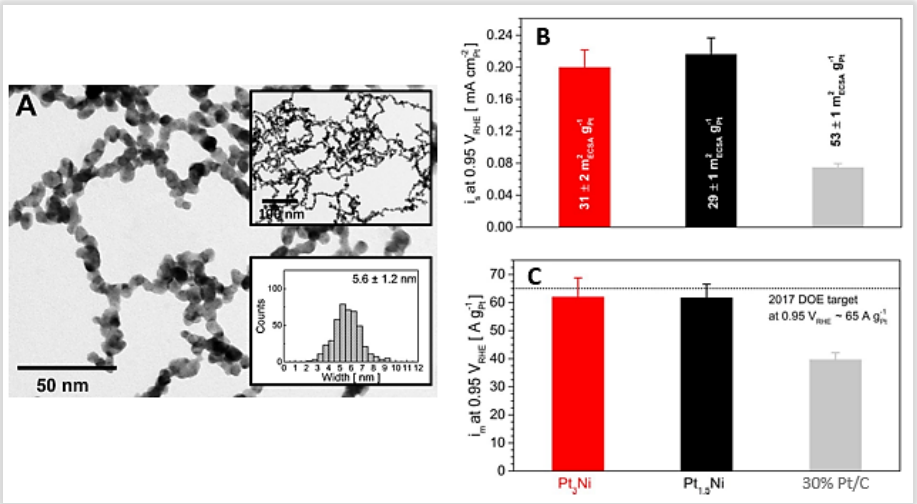

Figure III-28: A) TEM images of Pt_3Ni aerogel; the insets show the corresponding distributions of nanochain diameters and TEM images with lower magnification. B-C) Mass and specific ORR activity values at 0.95 V_{RHE} for Pt-Ni aerogels and Pt/C. The dotted line represents the DOE ORR activity target at 0.95 V *vs.* RHE, extrapolated from the benchmark value of 440 A/g_{Pt} at 0.9 V vs. RHE assuming a Tafel slope of 60 mV/dec. Activity values were extracted from anodic polarization curves in O_2-saturated 0.1 M $HClO_4$ electrolyte (5 mV/s), corrected for IR-drop, and mass transport losses [59].

The group has extended his work by investigating PtNi aerogels' stability under PEFC relevant working conditions, comparing their behavior to that of commercial Pt/C catalysts, and verifying the stability enhancement expected from the absence of carbon support in these novel materials (see *figure III-28*). Average electrochemical activity values for both PtNi aerogels and commercial Pt/C are summarized in *table III-7* below:

	Pt_3Ni Aerogel	**Pt/C (47 wt%, TKK) 0.4 mg_{Pt}/cm^2_{geom}**
MA (A/g_{Pt})	113	120
SA ($\mu A/cm_{Pt}^2$)	526	233
ECSA (m^2/g_{Pt})	29	69

Table III-7: Average values of the beginning-of-life mass activity (MA) and surface activity (SA) at 0.9 V *vs.*RHE, 80°C, 100% RH, H_2/O_2, 1.5 bar_{abs}, and ECSA at 25°C of Pt_3Ni aerogel and Pt/C MEAs [60].

Accelerated stress tests (beginning- and end-of-life tests, start-stop degradation) applied for the Pt_3Ni aerogel have shown significant loss of activity. In addition to the increase in particle sizes (*figure III-29*), the catalyst also undergoes significant Ni dissolution (≈60%) from the alloy phase, decreasing both MA and SA. Based on these results and the overall fuel cell power output (*figure III-30)*, Pt_3Ni aerogel is a promising PEMFC catalyst for the automotive application that warrants high durability in case of fuel starvation and cell start-up/shut-down events.

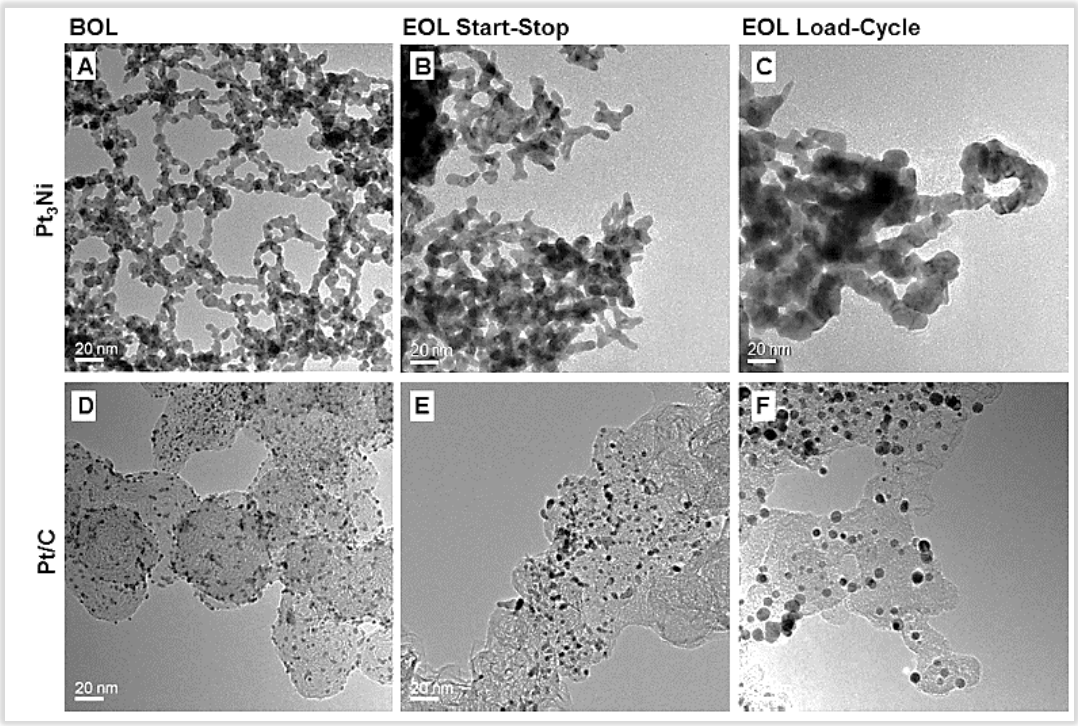

Figure III-29: Representative TEM images of the Pt_3Ni aerogel (top row) and Pt/C catalyst (bottom row) at the beginning-of-life A, D) and after start-stop B, E) and load-cycle degradation C, F) [60].

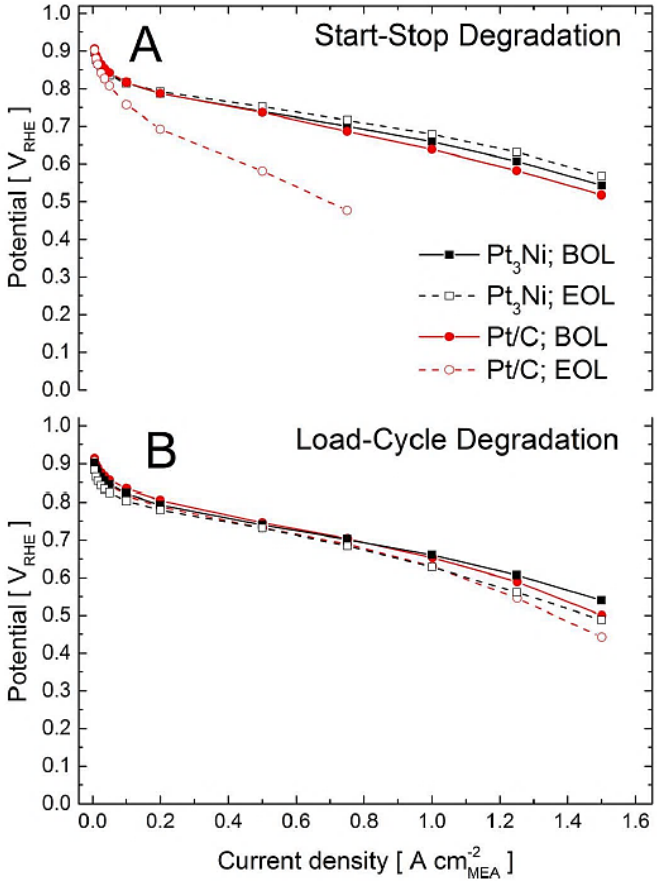

Figure III-30: Beginning- and end-of-life I(E) curves at 80°C, 100% RH, in H_2/air at 1.5 bar_{abs} for the start-stop (A) and load-cycle degradation (B) of Pt_3Ni and Pt/C MEAs (cathode loadings of 0.3–0.4 mg_{Pt}/cm^2_{geom}).

In the same year, the research group [60] has optimized an akin electrocatalyst, which has demonstrated a high current PEMFC performance commensurate with that of a carbon-supported benchmark (Pt/C). Aerogel catalyst layers were optimized by adding K_2CO_3 (a filler material that creates a CL with increased porosity after the acid washing step) to the catalyst ink, which was later removed by acid washing the catalyst-coated membrane (CCM). The performance improvement caused by the addition of K_2CO_3 is explained by increased porosity and average pore size. Moreover, optimized Pt_3Ni MEAs showed ~2.5-fold increased surface-specific ORR activity with respect to Pt/C and displayed excellent stability during an AST of 10.000 potential cycles between 1.0 and 1.5 V *vs.* RHE.

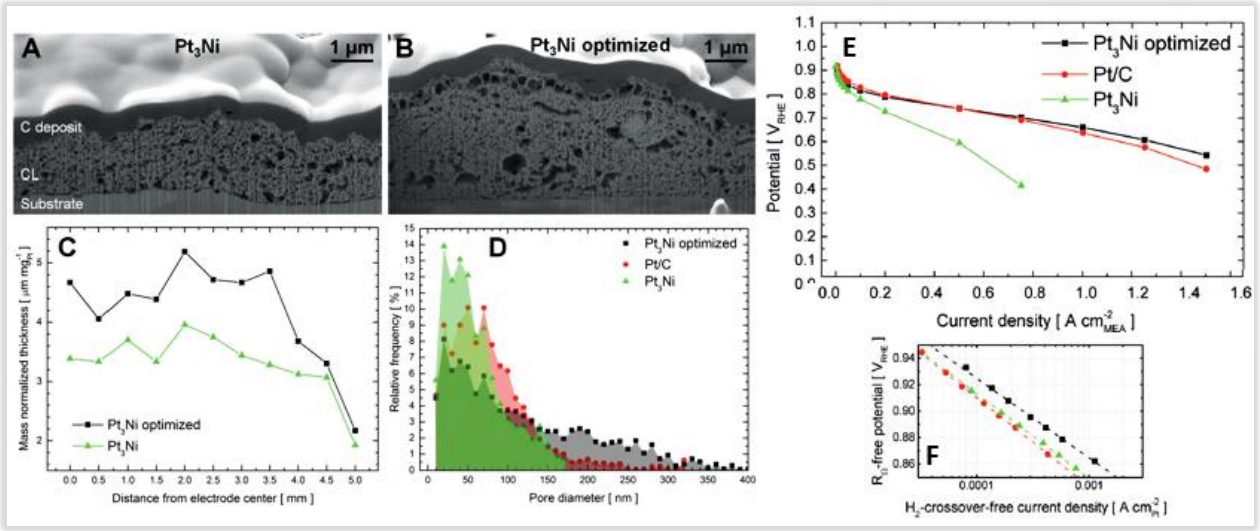

Figure III-31: A-B) Representative cross-section SEM images and C) thickness as a function of the distance from the electrode center for catalyst layers of Pt_3Ni (0.48 mg_{Pt}/cm^2_{geom}) and Pt_3Ni optimized (0.53 mg_{Pt}/cm^2_{geom}). D) Pore size distributions derived from FIB-SEM tomography for Pt_3Ni, Pt_3Ni optimized, and Pt/C catalyst layers. E) Polarization curves at 80°C, 100% RH in H_2/air at 1.5 bar_{abs}, and F) Tafel plots in H_2/O_2 for Pt_3Ni optimized, Pt_3Ni, and Pt/C MEAs (~0.31 mg_{Pt}/cm_{geom} for all cathodes) [60].

III.3.5 Nanostructured Thin Film Electrocatalysts (NSTF)

Since 1995, the *3M company* has been developing an alternative PEM fuel cell catalyst approach, referred to as NSTFC (nanostructured thin film catalysts), consisting of ultrathin electrode layers of thin-film Pt catalysts vacuum coated over a monolayer of crystalline whiskers [61][62].

The NSTF binary and ternary catalysts (PtCoMn, PtCoFe, PtNiFe, PtCo, PtZr, and PtNi) were formed by a vacuum sputter-deposition metal multi-layers onto a supported monolayer of oriented crystalline organic-pigment whiskers (perylene based heterocyclic organic solid nanowhiskers). The latter is obtained via the CVD method (Chemical Vapor Deposition) following a <111> growth direction. These nanowhiskers are electrically insulated and are considered to have no impact on the ORR. Catalysts sputter-coated on top of the whiskers encapsulates them as a polycrystalline thin film. The crystallinity of the organic nanowhiskers makes it possible to direct the platinum deposit on their surface, thus increasing the roughness of the surface of the catalyst and, therefore, its specific surface. For most of the catalyst alloys coated onto those whisker supports, the catalysts were sputter deposited in a batch-loaded vacuum chamber with multiple sputtering targets chosen for the particular alloy composition to be made, allowing a wide variety of

catalyst composition (see *figure III-32*). The catalyst-coated whiskers are embedded in the surface of the PEM to make the CCM [63].

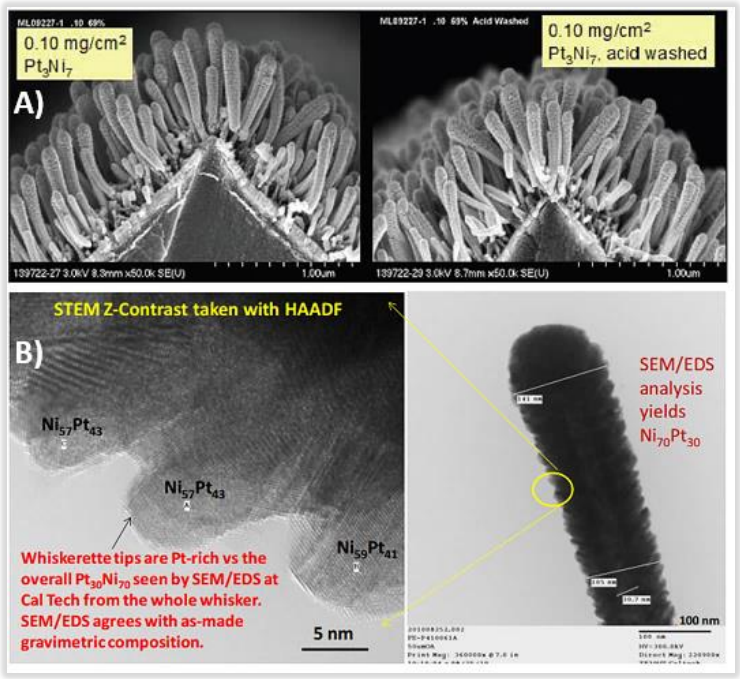

Figure III-32: A) SEM images, at originally 50 kX, of the NSTF catalysts with Pt_3Ni_7 coatings as-made (left) and after acid washing (right). B) TEM images of roll-good fabricated Pt_3Ni_7 alloy coated NSTF whiskers showing the composition of the whiskerettes on the whiskers' sides have a Pt-rich composition versus the overall as-made composition and composition determined from EDS of the whole whisker. Reprinted from reference [63] and [64].

The advanced NSTF with Pt_3Ni or Pt_3Co catalysts exhibit a 2-fold increase in activity, while with the use of PtNi, the activity is 4 times higher. When the latter has undergone thermal annealing to evaporate the nanowhiskers' organic core, the activity is 8-fold higher compared to commercial Pt/C with the same Pt loading. Furthers studies on $Pt_{1-x}Ni_x$ have shown an extraordinarily sharp peak in ORR activity (measured in 50 cm^2 CCMs electrode assemblies) as a function of the as-made composition around x=0.7 determined gravimetrically.

The ORR mass activity of the Pt_3Ni_7 is ~60% higher than for the NSTF standard $Pt_{68}Co_{29}Mn_3$ alloy [65][64][66]. *Figure III-33-B)* shows the full current density range of many of the polarization curves shown in part in *figure III-33-A)*, revealing that the Pt_3Ni_7 alloys suffer from much reduced limiting current density compared to the PtCoMn and Pt_3Ni_1. As observed from the plots, limiting current decreases as the amount of transition metal increases while acid washing of the catalyst before making the CCM increases the

limiting current significantly. This is understood to be due to the significant amount of dealloying and dissolution of the excess Ni into the membrane [63].

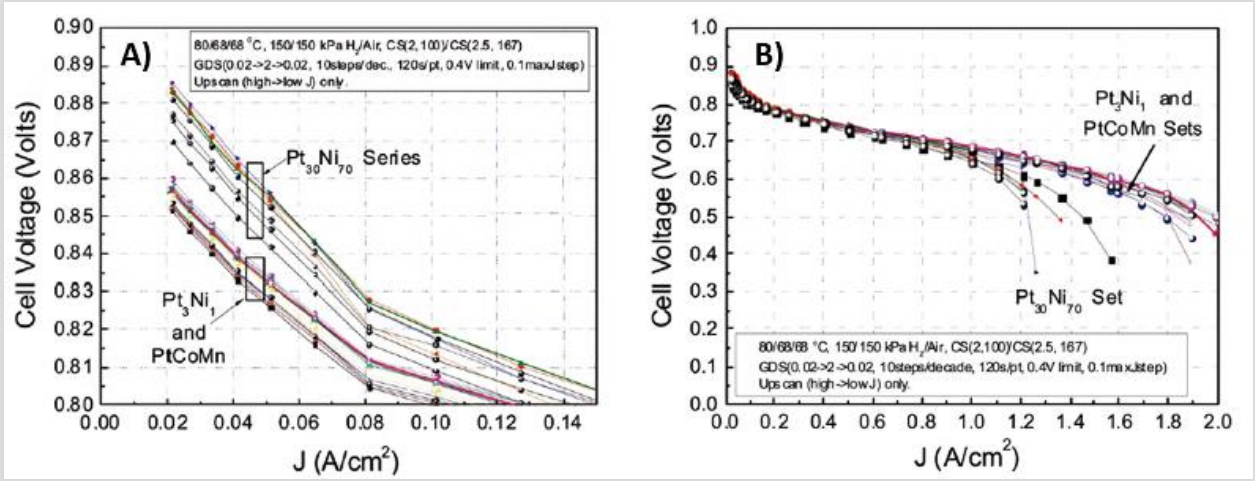

Figure III-33: A) Hydrogen/air galvanodynamic polarization curves (GDS) in the kinetic region at the conditions shown in the inset for various NSTF Pt_xNi_y compositions compared to Pt_3Ni_1 and the NSTF standard PtCoMn. B) H_2/air GDS polarization curves at the conditions shown in the inset for NSTF MEA's with the Pt_3Ni_7 composition versus the Pt_3Ni_1 and standard PtCoMn. Reprinted from reference [63].

The main shortcomings of this technology are: **i/** Excess Ni cations in the membrane affects the net water transport across the membrane from anode to cathode, resulting in increased flooding of the NSTF cathodes and increased oxygen mass transfer overpotential, and **ii/** cost limitation per kW of a stack (24$/kW) mainly due to processes of vacuum deposition of the catalyst [63][65].

III.3.6 PtNi nanowires: Ex-situ tests and operating fuel cell tests

The first appearance of PtNi nanowires fabrication dates back to 2005 when the *S.Z. Chu* group [67] successfully fabricated integrated nanowire arrays of PtNi on glass substrates by subsequent anodization and electrodeposition. As a route for developing core-shell structure, long Pt-shell $PtNi_5$ nanowires (see *figure III-34*) have been made by the electrospinning method as described in reference [68]. The study indicated that nanowires after a mild acid wash and proper heat treatment formed a core-shell structure with a Pt-rich shell capable of protecting Ni from dissolution in strong acid at 60°C.

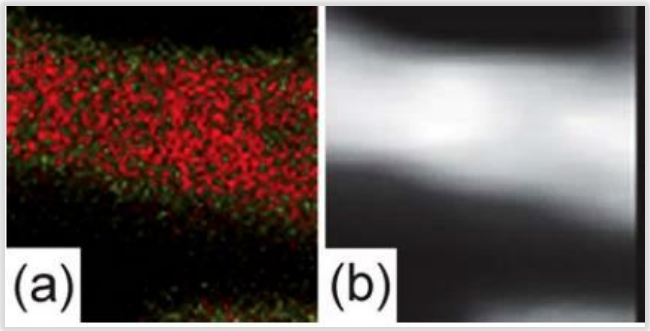

Figure III-34: $PtNi_5$ after core-shell structure treatment and acid test: (a) In the overlapped mapping, the red points indicate Ni, and the green points are Pt. (b) The wire where mapping was executed.

In 2014, *Shaun M. Alia* and coworkers [69] extended the study of PtNiNWs structure to electrocatalysis for oxygen reduction (ORR) in rotating disk electrode half-cells with an acidic electrolyte and compared to carbon-supported Pt.

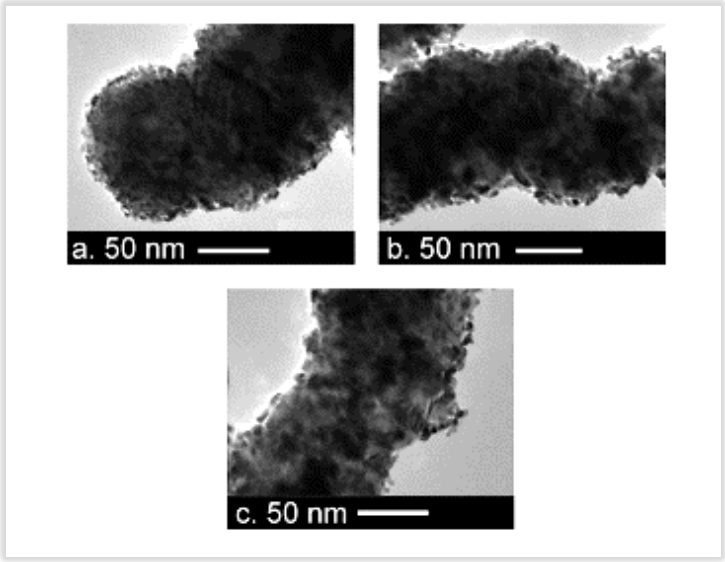

Figure III-35: TEM images of PtNiNWs (9.6 wt % Pt) a) as-synthesized, b) following RDE break-in, and c) following RDE durability testing (30 000 cycles, 0.6–1.0 V *vs.* RHE) [69].

Pt-coated NiNWs (with diameters of 150−250 nm and lengths of 100−200 µm, maintaining the morphology of initial NiNWs) were synthesized by the spontaneous galvanic displacement of NiNWs by exposure to potassium tetrachloroplatinate (K_2PtCl_4). Higher levels of Pt displacement were achieved by adding hydrochloric acid (HCl), presumably due to the presence of a Ni oxide layer and the ability of the added acid to etch this layer, thereby exposing unoxidized Ni. Catalysts containing less than 20%wt Pt were found to have high activity and durability in electrochemical testing. As shown in

figure III-36, the ECSA reached a value of ~90 m^2/g_{Pt} and allowed PtNiNWs to produce a maximum ORR mass activity 3.0 times greater than Pt/C.

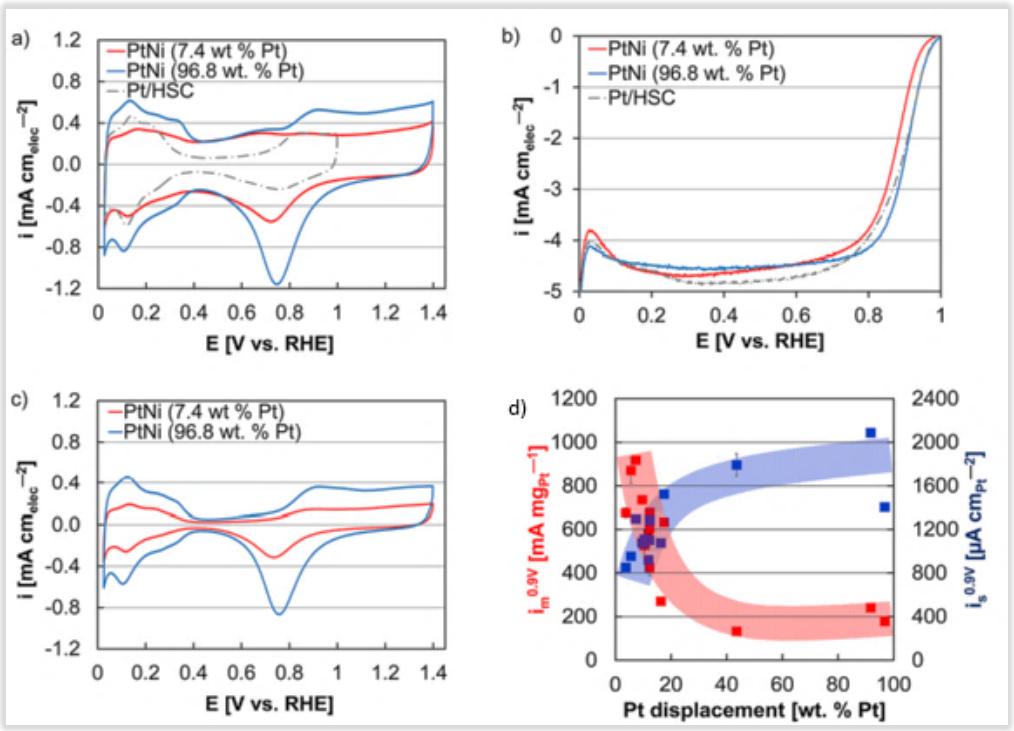

Figure III-36: a) Cyclic voltammograms and b) ORR polarization curves of PtNiNWs (7.4 and 96.8 wt % Pt, with graphitized carbon nanofibers 60 wt % added to the inks) and Pt/HSC. c) Cyclic voltammograms of PtNiNWs (7.4 and 96.8 wt % Pt, without graphitized carbon nanofibers). Catalyst loadings on the RDE tip were the following: PtNiNWs (7.4 wt % Pt) 33.7 $\mu g_{PtNi}/cm_{elec}^2$; PtNiNWs (96.8 wt % Pt) 38.9 $\mu g_{PtNi}/cm_{elec}^2$; and Pt/HSC 17.8 $\mu g_{Pt}/cm_{elec}^2$. d) Mass and specific ORR activities of PtNiNWs as a function of percent Pt displacement. The inks used to prepare the RDE tips contained graphitized carbon nanofibers (60 wt %) and a Nafion ionomer (4 µL/mL). ORR activities were corrected for internal resistance and the partial pressure of oxygen at 0.9 V *vs.* RHE (1600 rpm, 20 mV/s) in an oxygen-saturated 0.1 M $HClO_4$ electrolyte.

The same research group investigated PtNiNWs as methanol oxidation reaction (MOR) catalysts for direct methanol fuel cells (DMFCs) in rotating disk electrode (RDE) half-cells under acidic conditions. Annealing the NiNWs to 200°C in an oxygen atmosphere resulted in the highest MOR performance. At 0.5 V *vs.* RHE, the annealed catalyst produced a 65% greater mass activity than PtRu/C (which has long been the state-of-the-art MOR catalyst DMFCs). Following potential cycling, the activity of the PtNiNWs was more than 24 times greater [70].

Similarly, the impact of the thermal treatment of PtNiNWs electrocatalysts in oxygen was examined to determine the effect on oxygen reduction (ORR) activity, durability for PEMFCs, and minimize Ni dissolution. After annealing, NiO layer growth offers improvements in durability. According to durability testing, the retention of activity improved with increased temperature to 200°C and was the highest observed (3 times greater than Pt/C) [71].

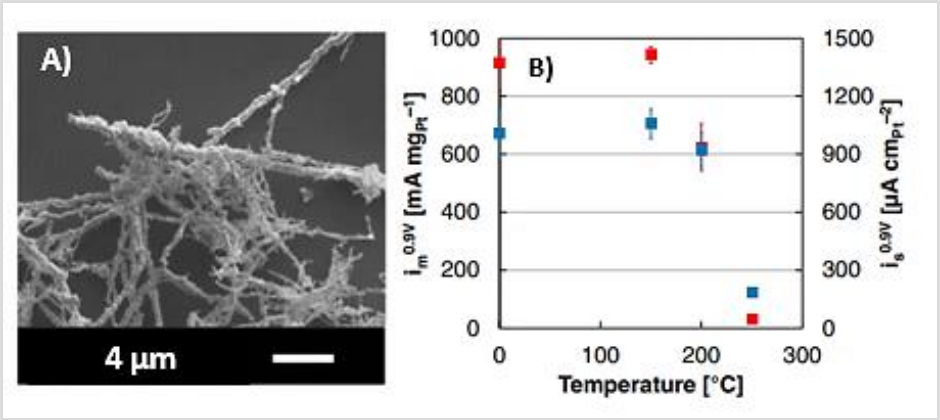

Figure III-37: A) SEM images of Pt-Ni nanowires (7 wt% Pt) annealed in oxygen to 200°C following Pt displacement. B) Mass and specific ORR activities of PtNi nanowires as a function of annealing temperature, with the untreated Pt-Ni nanowires included at 0°C. ORR activities were determined during anodic polarization scans at 1600 rpm and 20 mV/s in oxygen-saturated 0.1 M perchloric acid. As the annealing temperature increased, ORR activity decreased, and by 250°C, the activity was significantly reduced [71].

A more in-depth investigation and profound study of the same research group led to the synthesis of PtNiNWs through a series of post-synthesis optimization steps: **i/** PtNi nanowires annealed in hydrogen at 250°C produced a 3-fold specific activity increase in RDE half-cells, **ii/** Ex-situ acid exposure using concentrated nitric acid or sulfuric acid significantly improved catalyst durability and minimized Ni dissolution, **iii/** Oxygen annealing minimized activity losses in durability testing and decreased Ni dissolution, attributed to the increased prevalence of Ni oxide (NiO) near the nanowire surface as demonstrated before [71].

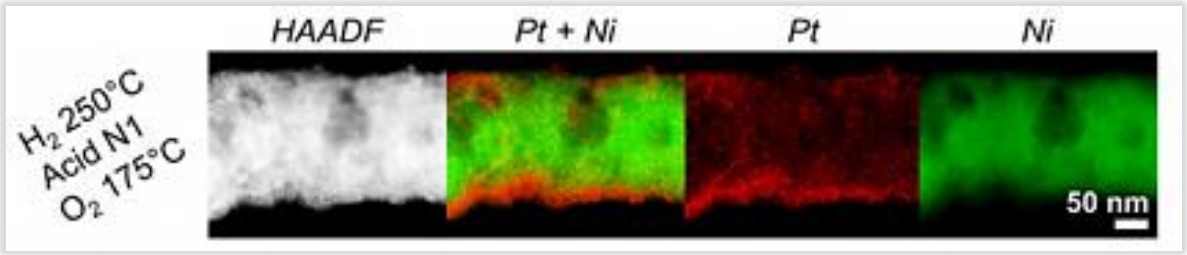

Figure III-38: STEM-HAADF of PtNi nanowires (7.3 ± 0.3 wt% Pt); annealed in hydrogen to 250 °C and ex-situ acid-leached in a mixture of acetic and sulfuric acid, then and annealed in oxygen to 175°C.

These materials exhibited both high specific activity of >6000 µA/cm_{Pt} at 0.9 V and high surface areas up to 90 m^2/g_{Pt} in RDE half-cells in 0.1 M perchloric acid. Unfortunately, they were limited in terms of their specific activity and durability upon exposure to relevant electrochemical test conditions (*figure III-39*) [72].

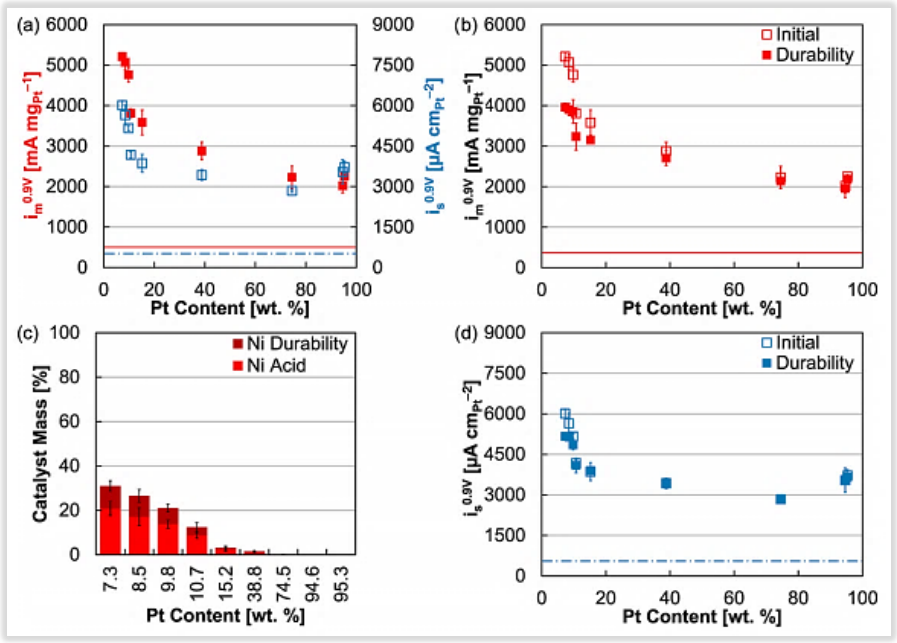

Figure III-39: a) ORR mass (*red*) and site-specific (*blue*) activities of PtNi nanowires (7.3 ± 0.3 wt % Pt), annealed in hydrogen to 250 °C and acid leached to a variety of compositions, at 0.9 V *vs.* RHE. The solid red line and dashed blue line were included for the mass and site-specific activity of Pt/HSC. c) Amount of catalyst lost to the electrolyte after acid exposure (Ni Acid) and potential cycling (Ni durability), as determined by ICP-MS. b) Mass and d) site-specific ORR activities of PtNi nanowires annealed in hydrogen before (initial) and after durability (durability). Horizontal lines were included for the mass (*red*) and site-specific (*blue*) activities of Pt/HSC after durability testing. Durability consisted of 30 000 cycles in the potential range of 0.6–1.0 V *vs.* RHE in 0.1 M perchloric acid. ORR activities were taken during anodic polarization scans at 20 $mV.s^{-1}$ and 1600 rpm and were corrected for internal resistance and mass transport [72].

Up until 2018, *Scott A. Mauger et al.* [73] have successfully incorporated PtNiNWs into high-performance membrane electrode assemblies, as evidenced in *figure III-40 and figure III-42* below. They were prepared through spontaneous galvanic displacement and then annealed to 250°C in a hydrogen environment as demonstrated by *Shaun M. Alia* before since the activity is influenced by additional annealing treatments of the material following synthesis. The nanowires' structure exhibited up to 10's of microns in length (as-synthesized) with diameters between 100 and 300 nm. The cathode catalyst is made of a mixture of Pt/HSC (TKK TEC10E50E) inks and PtNiNWs with the desired PtNi:Nafion ratio using an ultrasonic spray-coated onto Nafion©212 membranes. The platinum loading of the cathodes was between 0.1 and 0.2 mg Pt/cm², while the anodes with loadings of approximately 0.25 mg Pt/cm².

For some MEAs, Ni was leached from the PtNiNWs prior to MEA incorporation (pre-leaching) by soaking the PtNiNWs in 1M H_2SO_4. To fathom more profoundly the effect of Ni contamination, select MEAs were submerged in 1L of 0.01 M H_2SO_4 at room temperature for 17 hours in order to exchange Ni^{2+} with H^+. After soaking, the MEA was repeatedly rinsed with deionized water and dried on a vacuum plate at 50°C until dry. *Figure III-40 a) and b)* show SEM images of the cross-section of an MEA along with a top-down image of the PtNiNW cathode.

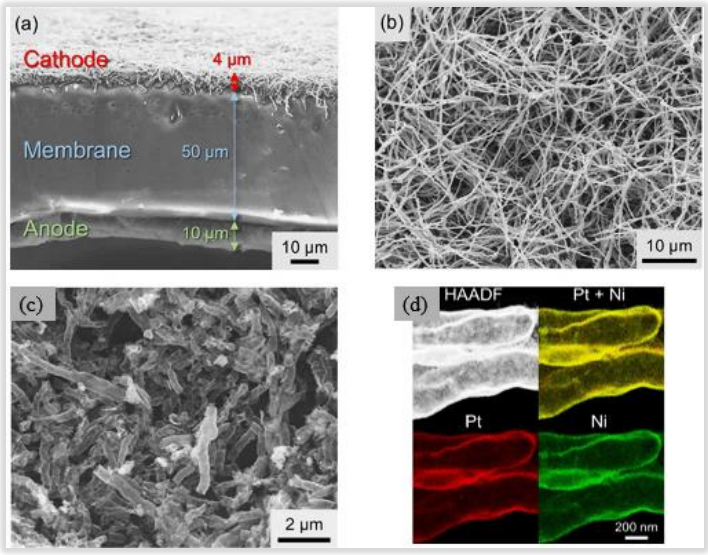

Figure III-40: Scanning electron microscope images of the 16 wt% Nafion MEA recorded for the as-prepared MEA in a) cross-sectional and b) top-down of the cathode. c) Top-down SEM of the pre-leached PtNiNW cathode. d) HAADF STEM of 81 wt% Pt PtNiNWs and EDS maps for Pt-Ni, Pt, and Ni. Reprinted from reference [73].

Before the ion exchange procedure, the research group assumed that the PtNiNWs showed no catalytic activity because Ni atoms have blocked sulfonic acid sites in the cathode, as shown in cycling voltammograms in *figure III-41-a)*. Ion exchange procedure always had an influence on decreasing the high-frequency resistance (HFR) from 480 $m\Omega/cm^2$ to 118 $m\Omega/cm^2$ and a significant increase in mass activity. Also, metal ion contamination has been shown to increase oxygen transport resistance in the ionomer, which would result in mass-transport losses. MEA (with 9%wt Nafion content) tests covered in this study have shown, at highest performance on a mass activity basis, 133 mA/mg_{Pt} (0.9 $V_{IR\text{-}free}$). For comparison, PtNi nanoparticles supported on carbon have achieved mass activities over 600 mA/mg_{Pt}, so additional refinements in the catalyst processing and electrode design are needed to improve the performance of these PtNiNWs in MEAs.

Finally, comparing both MEAs (before and after pre-leaching of PtNiNWs), the initial polarization curve (*figure III-41-f*) showed significantly higher current densities could be achieved in this MEA with the pre-leached PtNiNWs than any of the MEAs with unleached PtNiNWs even after multiple ion exchange processes, both with a low ionomer content to minimize oxygen transport limitations.

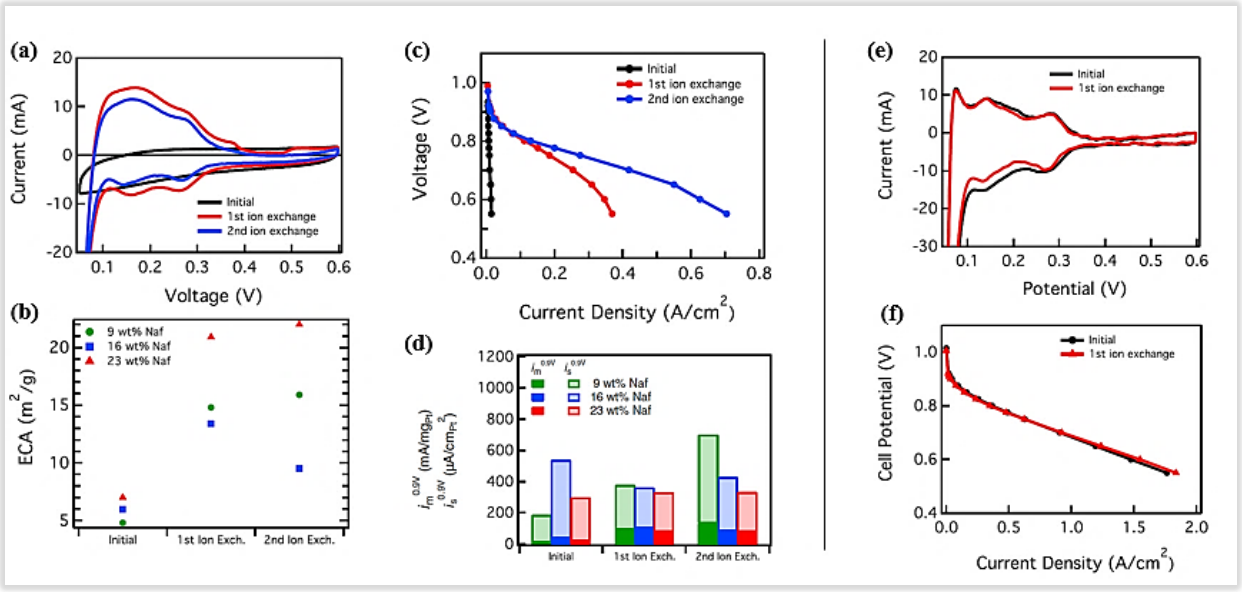

Figure III-41: Summary of electrochemical tests on PtNiNWs: a) Cycling voltammograms of PtNiNW MEA with 16 wt% Nafion in the cathode. Voltammograms were measured at 50 mV/s after the initial testing cycle and testing cycles following ion exchange in 0.01 M H_2SO_4. b) Electrochemical surface areas (ECSAs) for the entire PtNiNWs MEAs. c) Oxygen polarization curve for the 16 wt% Nafion MEA measured initially and after soaking in 0.01 M H_2SO_4 baths. d) Mass ($i_m^{0.9V}$) and specific ($i_s^{0.9V}$) activities measured at 0.9 V for PtNiNW MEAs with 9 wt%, 16 wt%, and 23 wt% Nafion. e) Cyclic voltammograms and f) oxygen polarization curves of the pre-leached PtNiNW MEA measured without any additional processing of the MEA (initial) and after ion exchanging the MEA in sulfuric acid. The platinum loading of the cathodes was between 0.1 and 0.2 mg_{Pt}/cm^2. Hydrogen/Oxygen polarization curves were measured at 80°C, 100%RH, 150 kPa_{abs}, and 0.4 slpm (standard liter per minute).

Probing the PtNiNWs nanostructure deeply, extended investigations have been carried out by the same research group one year later. The combination of X-ray Spectroscopies, Transmission X-ray microscopy alongside electron microscopy provided unprecedented detail of the evolution of the nanowire-based extended surface catalyst and electrode structure guiding the targeted design of high-performance electrodes based on this class of materials [74].

III.3.7 PtNi nanotubes as a new architecture of electrodes for the ORR

As it was covered by *Shaun. M. Alia,* in his previous work [72], using galvanic displacement to deposit thin Pt layers onto NiNWs, post-synthesis processing parameters were mandatory to improve the catalytic activity of PtNiNWs, including thermal treatment under reducing and oxidizing conditions and acid leaching to remove Ni selectively. Ex-situ acid exposure was used to explore the potential impacts of Ni leaching on

performance, durability, and the morphology of the desired structure of PtNi. It was shown that higher acid concentrations during acid leaching resulted in higher degrees of Ni removal where many nanowires were broken into shorter segments (0.5–1 µm) and exhibited hollow and porous nanotubes as depicted in *figure III-42* [72].

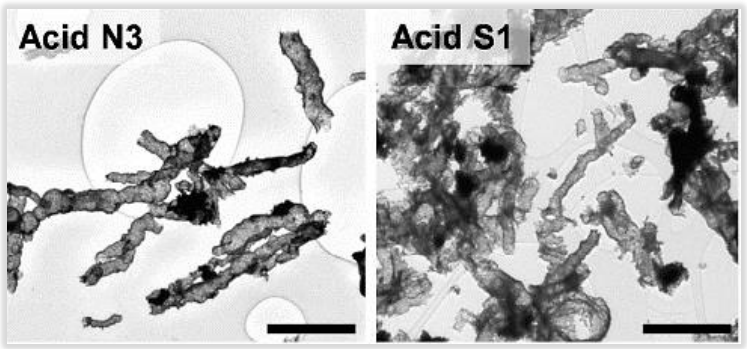

Figure III-42: TEM of Pt-Ni nanowires (7.3 ± 0.3 wt. % Pt), annealed in hydrogen to 250°C, and acid leached with nitric acid (N3: 3M) and sulfuric acid (S1: 1M) at room temperature for 2 hours [72].

In 2019, *C. Fan et al.* [75] from the College of Science at *Shanghai University* studied the elaboration of PtNi nanotubes (PtNiNTs) alloy catalyst with a one-dimensional nanotube structure via a galvanic replacement reaction combined with the Kirkendall effect (*figure III-43*). The synthesis was carried out according to the following process: **i/** The metallic Ni nanofibers were synthesized through an electrospinning process, **ii/** A thermal oxidation 450°C in the air for 4 hours, **iii/** the hydrogen reduction in H_2/N_2 (10% H_2) at 350°C for 3 hours, **iv/** the Pt deposition by a galvanic replacement reaction in a K_2PtCl_4 aqueous solution, **v/** the thermal treatment in N_2 at 360°C for 2 hours, and finally **vi/** an acid leaching process whereby the PtNiNWs were stirred in 0.5 M H_2SO_4 at 55°C for 20 min to synthesize the PtNiNTs [75].

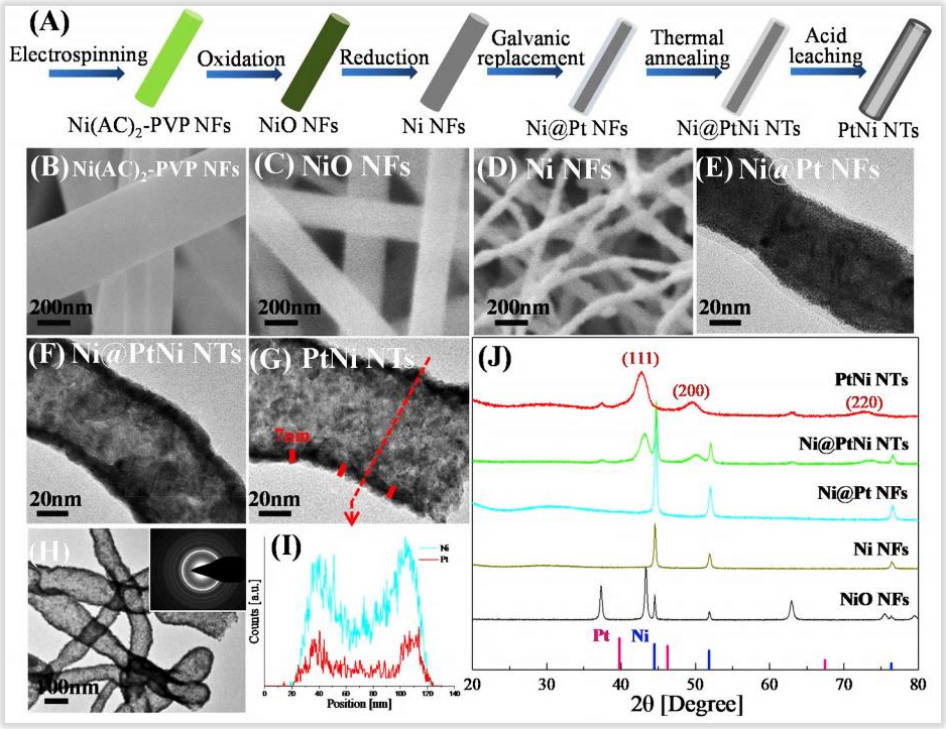

Figure III-43: A) The synthetic schematic process for the $PtNi_{2.2}$ NTs. The SEM/TEM images of the intermediates after the different synthetic steps of B) electrospinning, C) oxidation, D) reduction, E) galvanic replacement process, F) thermal annealing, and G) acid leaching, respectively. H) The TEM image and (inset) electron diffraction pattern of the $PtNi_{2.2}$ NTs. I) The EDS spectroscopy line-scan profiles of Pt-L and Ni-K along the indicated direction in G). J) The XRD patterns of the intermediates and the $PtNi_{2.2}$ NTs at different synthetic steps. Extracted from reference [75].

The PtNiNTs with a wall thickness of 19 nm and the atomic ratio of Ni to Pt of 2.2 have revealed significant improvements in the activity according to ex-situ experiments (see *figure III-44* below). They have shown a 6.2-fold increase in specific activity compared to the commercial Pt/C, and interesting durability translated to only 8.6% loss in mass activity maintained after 10.000 cycles. The ORR activity improvement is essentially attributed to the alloying effect by introducing Ni to the Pt lattice, the Pt-rich surface, and the shape effect of the unique one-dimensional hollow tube structure [75].

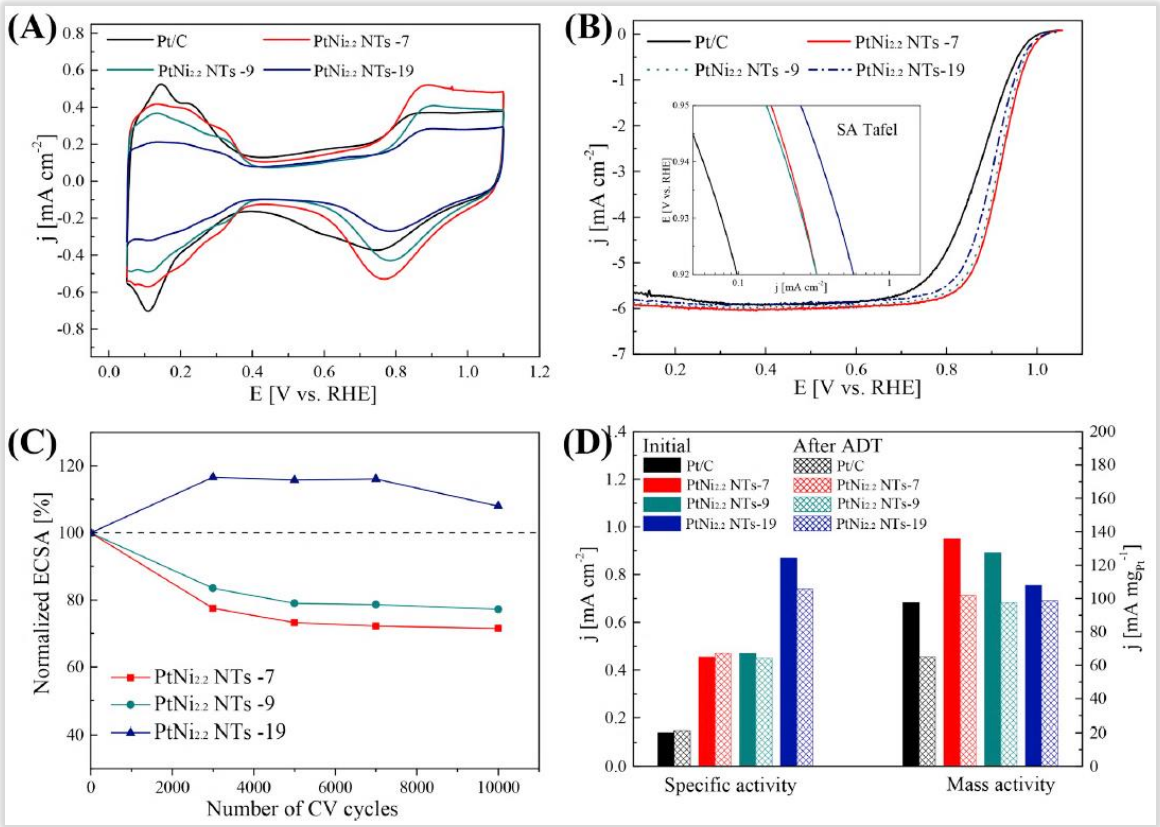

Figure III-44: The electrochemical performance of the Pt/C and the $PtNi_{2.2}$ NTs with the wall thicknesses of 7 nm, 9 nm, and 19 nm, respectively. A) CVs and ECSAs (inset) measured in N_2-saturated 0.1 M $HClO_4$ electrolyte at a scan rate of 50 mV/s. For the CV, the currents for Pt/C is multiplied by a factor of 0.5 to facilitate comparison with the PtNi NTs. B) LSVs and SA Tafel plots (inset) measured in O_2-saturated 0.1 M $HClO_4$ electrolyte at a 10 mV/s, 1600 rpm scan rate. C) Normalized ECSAs with a number of the CV cycles. D) The MA and SA were estimated from the LSVs at 0.90 V *vs.* RHE during the stability testing. The Pt loadings are 28 $\mu g_{Pt}/cm^2$ for the PtNi NTs and 20 $\mu g_{Pt}/cm^2$ for the Pt/C (ADT stands for Accelerated degradation tests).

The interest of an electrocatalyst for the ORR depends mainly on its intrinsic activity in a real fuel cell. Therefore, as presented by the polarization curve in *figure III-45*, the research group has performed investigating the MEA performance of the $PtNi_{2.2}$NTs (with 19 nm in wall diameter) in passive direct methanol fuel cells (DMFCs). Compared with the commercial Pt/C, $PtNi_{2.2}$NTs displayed activation polarization in the low current density region, where the polarization is primarily affected by activation related to the catalyst activity. In terms of maximum power density, it is 18.6 mW/cm^2 for the Pt/C and 25.1 mW/cm^2 for the $PtNi_{2.2}$NTs, which is a 35% enhancement than that of Pt/C. These results demonstrate that the PtNiNTs have a better MEA performance than commercial Pt/C, which is desirable to decrease the usage of noble metal in MEAs [75].

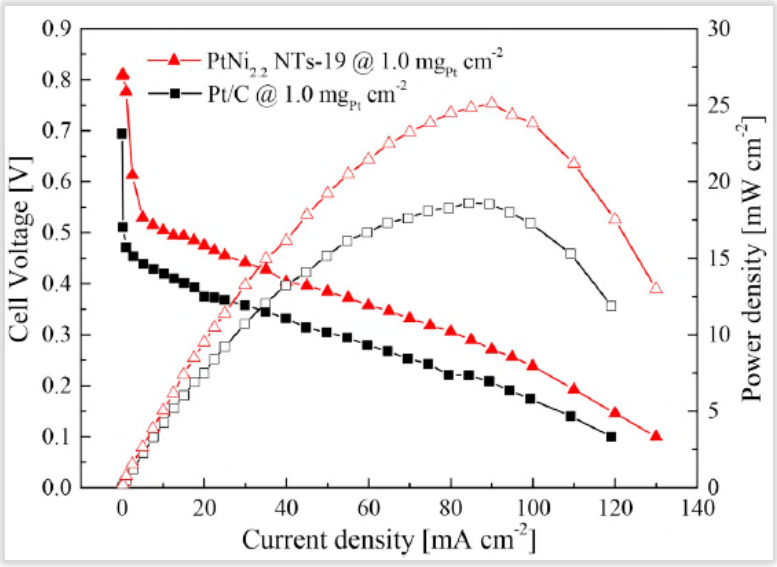

Figure III-45: Polarization curves of the DMFCs with the $PtNi_{2.2}$NTs and 20% Pt/C as the cathode catalysts when fed with 4.0 M methanol solution.

It should be noted that many other research works have been carried out to investigate the activity improvements of PtNi nanowires using ex-situ measurements such as RDE tests and have been the focus of extensive research [76][77][78].

Conclusion:

This paragraph has discussed the most commonly used electrode architectures made of PtNi electrocatalyst with different shapes and structures. Only a few research groups have been able to test the ORR activity of PtNi in a fuel cell. Besides the electrochemical route, it was reported in literature various techniques leading to tuning the architecture of the fuel cell's electrocatalysts and enhancing its activity (see **Appendix A**).

The following paragraph describes the complete protocol followed in this thesis to synthesize PtNi nanowires and PtNi nanotubes with the GD process accompanied by post-treatments: heat treatment and acid leaching process. The synthesized electrodes will further be transferred to MEA then evaluated and applied as the cathode catalysts for a single differential cell.

IV. Experimental Results: Platinum galvanic displacement as a route to PtNi Nanowire and Nanotubes fabrication

As previously stated, transition metals such as Ni have attracted considerable attention due to their potential use in electrocatalysis. In the current paragraph, PtNi nanowires and nanotubes, templated from nickel nanowires grown inside a sacrificial mold of porous anodic alumina template, were synthesized by the galvanic replacement process. Experiments held in this part of the thesis strive to expand our understanding of combining/splitting galvanic displacement (GD) and acid leaching (AL) processes in a confined (NiNWs inside AAO) and a non-confined system (self-standing NiNWs on Si substrate):

a) Reaction with the addition of HCl (combined GD and HCl): The Pt solution is diluted in a solution of HCl at different concentrations. NiNWs are exposed to this solution, and Ni atoms are exchanged with Pt atoms at a higher kinetic rate in the acid medium.

b) Reaction without the addition of HCl (splitted GD and AL): The Pt solution is diluted in ultra-pure water. The GD takes place at a slow rate. Pt tends to cover the surface of the NiNWs (Pt-shell@Ni-core). Later on, and once the process is over, the AL process is carried out after a thermal treatment to remove the excessive Nickel in the core.

For this purpose, the GD's process is twofold: the nickel nanowires were exposed to Pt salt solution in a confined environment, on the other hand, in a non-confined environment, where the AAO was completely etched. The flow-chat below depicts the followed paths held in this work.

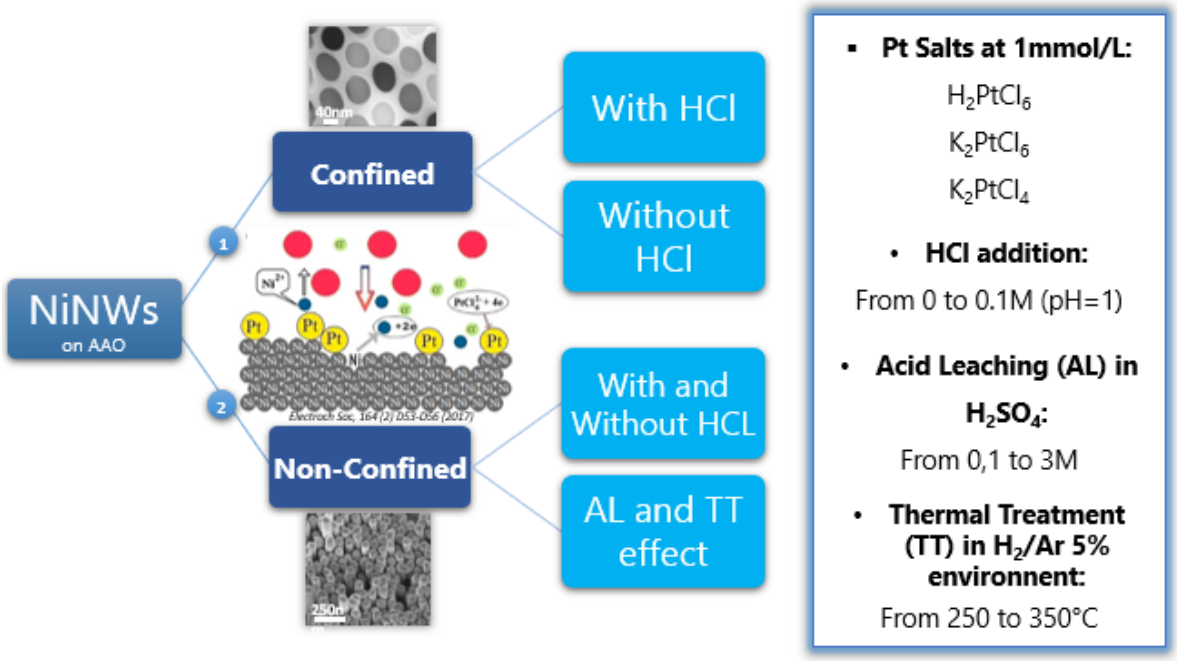

Figure III-46: Flowchart of the study of PtNi nanotubes and PtNi nanowires elaboration proposed in this Ph.D. TT refers to Thermal Treatment, AL refers to Acid Leaching.

IV.1 Galvanic Displacement: Electrochemical reactions

For all experiments reported in this part, the platinum salt concentration was fixed at 1mM. The latter were made initially from a hexachloroplatinic acid hexahydrate ($H_2PtCl_6.6H_2O$), Potassium hexachloroplatinate IV (K_2PtCl_6), and Potassium tereachloroplatinate II (K_2PtCl_4), as received from *Merck KGaA*.

We will then explore the effect of all the parameters cited in *figure III-46* above on the growth of PtNi nanostructures. Since the redox potential of nickel is lower than that of Pt, metallic Ni tends to be corroded (*i.e.,* oxidized) spontaneously, delivering electrons, which lead to the deposition of metallic Pt followed by the release of Ni^{2+} cations.

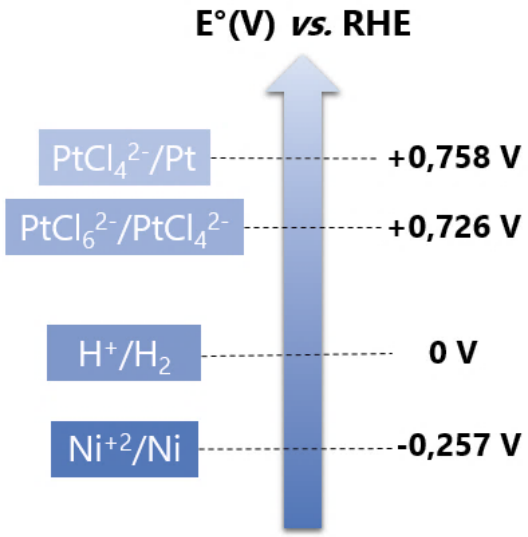

Figure III-47: Standard redox potentials (E°) in volts of platinum and nickel, relative to the standard hydrogen electrode at 298.15 K and 1atm.

The reduction equations for Pt salts used in this work are as follows in *table III-8* after the precursor dissociates in water (K_2PtCl_4 as an example):

$$\mathbf{K_2PtCl_{4(aq)} \rightarrow PtCl_{4(aq)}^{2-} + 2K_{(aq)}^{+}} \qquad \text{Reaction III-3}$$

Pt Salt	Involved Electrochemical Reactions
K_2PtCl_6	$K_2PtCl_{6\ (aq)} \rightarrow PtCl_6^{2-}{}_{(Aq)} + 2K^+_{\ (Aq)}$ $2Ni + PtCl_6^{2-} \rightarrow 2Ni^{2+} + Pt_{\downarrow} + 6Cl^-$
K_2PtCl_4	$K_2PtCl_{4\ (aq)} \rightarrow PtCl_4^{2-}{}_{(Aq)} + 2K^+_{\ (Aq)}$ $Ni + PtCl_4^{2-} \rightarrow Ni^{2+} + Pt_{\downarrow} + 4Cl^-$
H_2PtCl_6	$H_2PtCl_{6\ (aq)} \rightarrow PtCl_6^{2-}{}_{(Aq)} + 2H^+_{\ (Aq)}$ $2Ni + PtCl_6^{2-} \rightarrow 2Ni^{2+} + Pt_{\downarrow} + 6Cl^-$

Table III-8: Pt Salts and their involved electrochemical reactions with nickel during the galvanic displacement process.

It is worth noting that in the case of using K_2PtCl_6 or H_2PtCl_6, the formation of metallic platinum from $PtCl_6^{2-}$ might go through a $PtCl_4^{2-}$ intermediate reaction:

$$\mathbf{PtCl_6^{2-} + 2e^- \rightarrow PtCl_4^{2-} + 2Cl^-} \qquad \text{Reaction III-4}$$

IV.2 Galvanic Displacement in a confined and non-confined system without the addition of Hydrochloric acid

This part of the chapter will report a systematic analysis of the GD reaction and its effect on NiNWs grown on AAO with small pores (D_p=50-55 nm, D_{int}=90-100 nm, e=400 nm) as previously described in *paragraph III.2.* The resulting AAO geometry exhibits a porosity of ~35%. The theoretical number of pulses is therefore esteemed to be around 140. In our study of NiNWs growth, using a *Biologic©* potentiostat at a pulsed current of 52mA, we have imposed 135 pulses in order to avoid any overflow phenomenon (*i.e.,* nanowires overgrowth where each nanowire emerges from the top of the AAO).

In particular, the choice of different Pt salts was motivated by the exchange of 1Pt atom at the expense of 1Ni atom in the case of K_2PtCl_4, and 1 Pt atom at the expense of 2 Ni atoms in the case of H_2PtCl_6 or K_2PtCl_6. The Ni dissolution was expected to start from the top of the NiNWs according to the reactions described in the table below:

Exposing the confined and non-confined NiNWs to 1mM H_2PtCl_6, K_2PtCl_6, and K_2PtCl_4 solutions, respectively, without HCl and 1mM HCl in room temperature, the GD reaction did not take place at long exposure time (from 1 to 24 hours). We can ascribe this to the possibility of the presence of an oxide layer (NiO) on the surface of nanowires, as previously discussed by *Shaun M. Alia* [69].

It is necessary here to clarify exactly that the GD reaction occurred without HCl in a K_2PtCl_4 solution at 80°C. (*Cf., paragraph IV.3.2.1*).

Also, the GD reaction was probably not likely to happen, presumably due to the low Pt anions diffusion alongside the Ni nanowires. Moreover, proceeding with the GD at room temperature may slow down the kinetic rate of the reaction.

IV.3 Galvanic Displacement: Effect of Hydrochloric acid addition

IV.3.1 Path I: GD in a confined system

It has conclusively been shown in a previous study by *O. Marconot et al.* [79] that PtCu nanotubes could be elaborated in a confined environment. As a matter of inspiration for my Ph.D. work, I tried the same strategy to make sure to keep the same organization of the structure. The results were surprising because, according to my experiments, it

seemed difficult for Pt cations to diffuse along the nanowires length. This ambiguous result drove my curiosity to extend investigations in a non-confined environment.

IV.3.1.1 Reaction without the addition of HCl

This pathway involves using first GD in different Pt solutions without the addition of HCl at room temperature, at 60°C and 80°C. Theoretically, due to the E° difference between Ni and Pt, a galvanic reaction should occur spontaneously between the two metals. The SEM coupled EDX analysis of the samples has shown that there was no significant deposition of Pt on NiNWs (*figure III-48*). This somewhat contradictory result may be due to the presence of a Ni oxide layer on the nanowires' surface, which prevents the reaction from taking place. Moreover, increasing the Pt solution concentration to 10 mmol/L did not show any other difference.

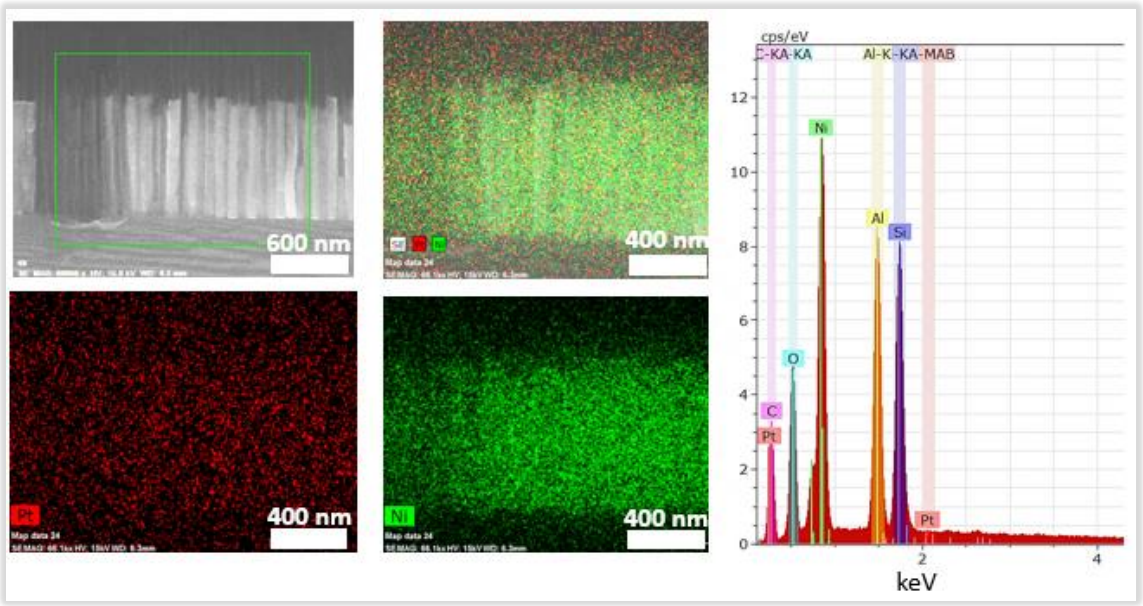

Figure III-48: Scanning Electron Microscopy (SEM) with Energy Dispersive X-Ray analysis (EDX) scan map of a confined galvanic displacement of NiNWs. Elemental identification peaks did not show the presence of platinum.

This result has further strengthened our conviction that the addition of an amount of HCl would serve as an etcher to the assumed NiO shell. Deeper insights into the structure of PtNiNWs after galvanic displacement were obtained using TEM analysis and EDX elemental map, as depicted in *figure III-49* below. The analysis was performed by Laure GUETAZ from The Nanocharacterization Platform (PFNC), CEA-Minatec.

We can clearly observe that an oxide shell serving as a Ni protective shell from the deposition of Pt cations during the galvanic displacement.

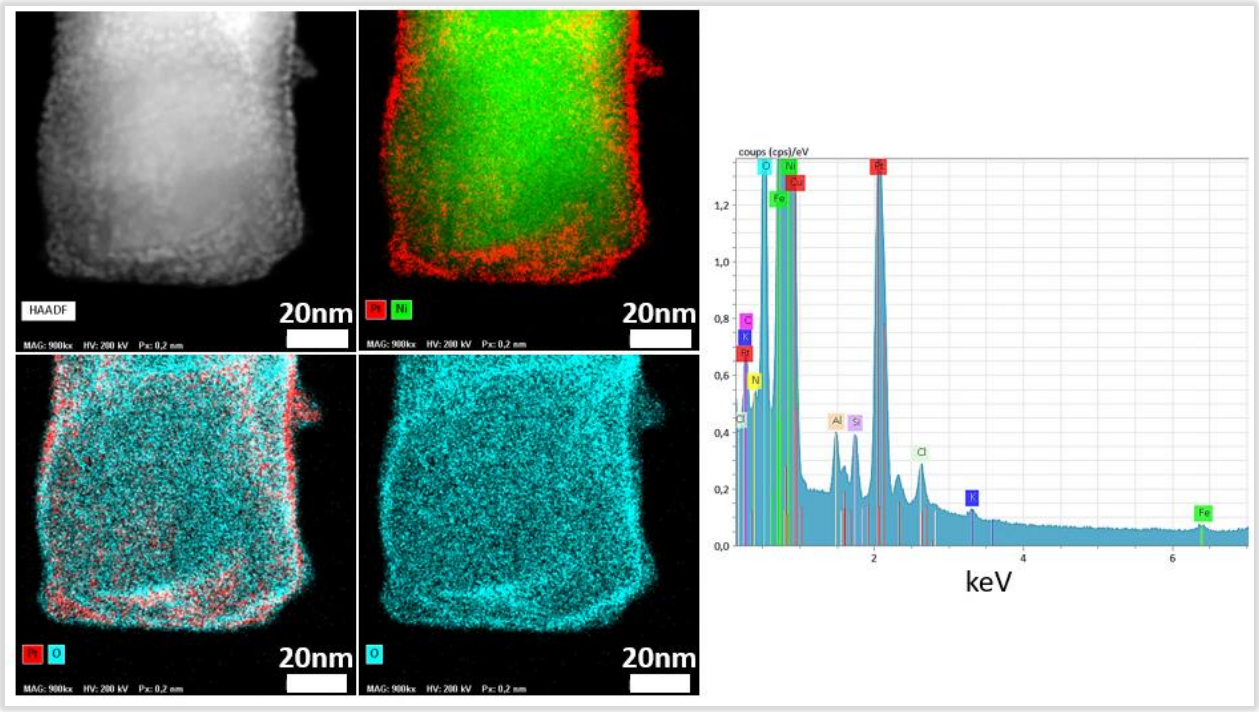

Figure III-49: High-angle annular dark-field imaging (HAADF)-TEM coupled EDX analysis of cross-sectioned PtNiNWs as-synthesized (without HCl addition), obtained after galvanic displacement in K_2PtCl_4 at 80°C. Red mapping refers to Pt, Green mapping refers to Nickel, and blue mapping refers to Oxygen.

Therefore, we considered the inspirational results reported by *O. Marconot et al.* [79] (elaboration of PtCu Nanotubes) and *Shaun M. Alia* [72] (elaboration of PtNi nanowires) as a critical strategy to combine GD and AL in order to tackle the Pt displacement issue. To elucidate the effect of HCl addition, *Shaun M. Alia* reported that higher Pt displacement was only achieved by adding hydrochloric acid to a K_2PtCl_4 solution, presumably due to the presence of a Ni oxide layer and the ability of the added acid to etch this layer, thereby exposing unoxidized Ni.

IV.3.1.2 Reaction with the addition of HCl

This pathway involves combining the GD and the acid leaching process simultaneously. For each Pt solution diluted in HCl (by varying its concentration from 0.01 M to 0.1 M, pH=2–1 from Pourbaix diagram), we have investigated the effect of the GD on the exposed NiNWs.

a- H_2PtCl_6 at 0.01 M HCl solution

The experiment was held at room temperature for 1 hour, 2 hours, and 4 hours. The SEM analysis below has clearly shown that the GD reaction did not occur since the morphology of the NiNWs remained intact. The GD reaction was probably not likely to happen, presumably due to the low Pt anions diffusion alongside the Ni nanowires. Also, according to the Pourbaix diagram, Ni could be corroded in acidic media.

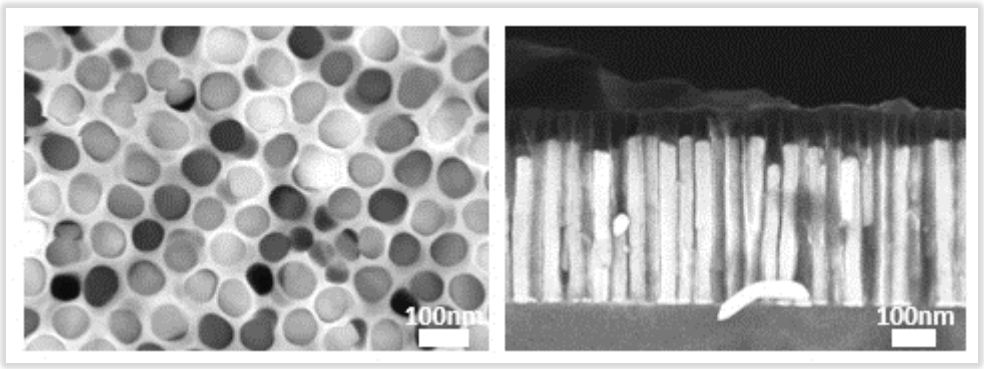

Figure III-50: SEM top-view and cross-sectional view analysis of intact NiNWs after 2 hours GD reaction in H_2PtCl_6 solution at 0.01 M HCl at room temperature.

b- H_2PtCl_6 at 0.1 M HCl solution

By increasing HCl concentration to 0.1 M, the GD reaction for 5 minutes occurred from the top of NiNWs to the bottom, leading to broken PtNi structures into shorter segments inside the AAO template and uncontrolled re-deposition of Pt agglomerates at the top of AAO. According to the TEM coupled EDX analysis displayed in *figure III-51*, PtNi alloy nanostructures were drop-casted on a TEM grid to determine the composition:

- Top: 88,3 at% of Pt – 11,7 at% of Ni;
- Down: 72 at% of Pt – 28 at% of Ni.

These preliminary results have shown the possibility of the formation of PtNi core-shell nanostructure. The galvanic displacement is believed to occur on the top of Nickel nanowires and spreads along the nanowires' length.

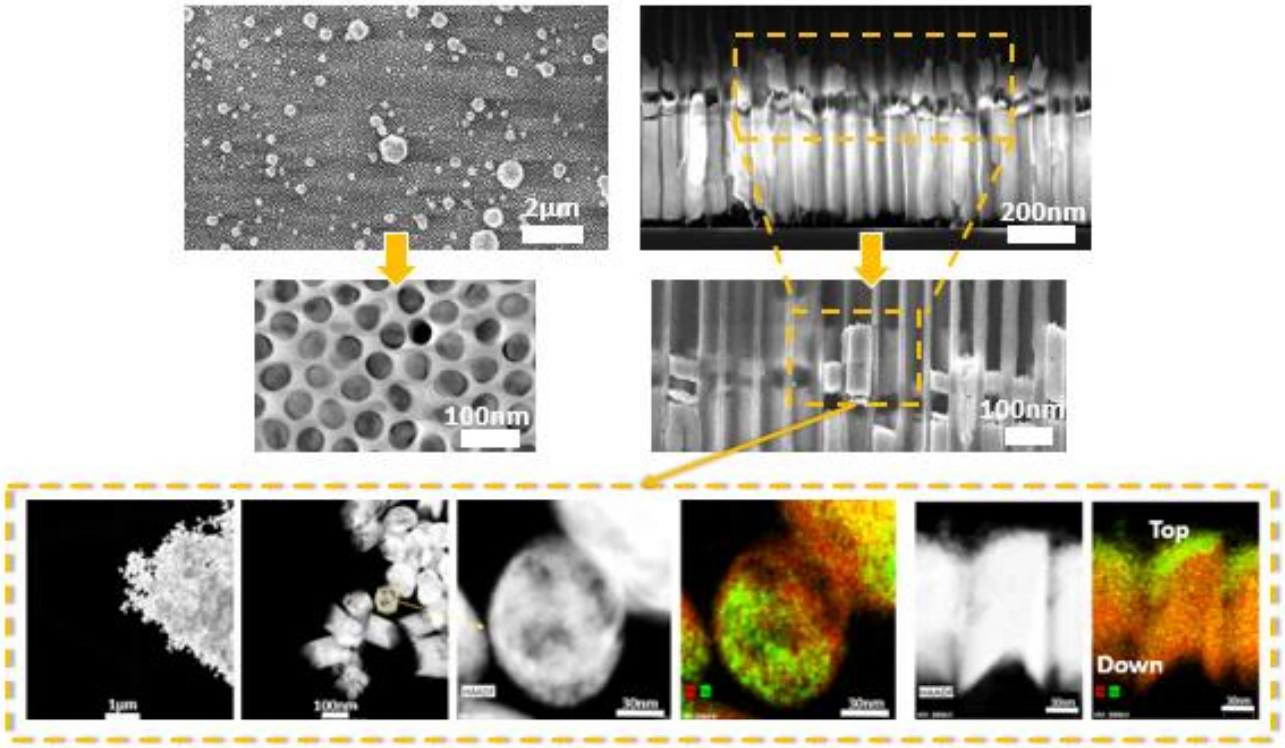

Figure III-51: SEM top-view and a cross-sectional view of PtNi nanowires in an H_2PtCl_6 solution at 0.1 M HCl at room temperature for 5 minutes. TEM coupled EDX mapping of PtNiNWs arrays illustration.

To go further in exposure time, the same experiment was held but at one hour. The GD was too violent, uncontrolled over time, and led to the complete detachment of the nanowires with a Pt delocalized redeposition at the template's surface, as displayed in *figure III-52* below. We may attribute this phenomenon to cementation which usually gives pulverulent deposits on the sacrificial material; the reaction stops once we no longer have anodic sites (all Ni is corroded by platinum after the exchange between Pt(II) and Ni).

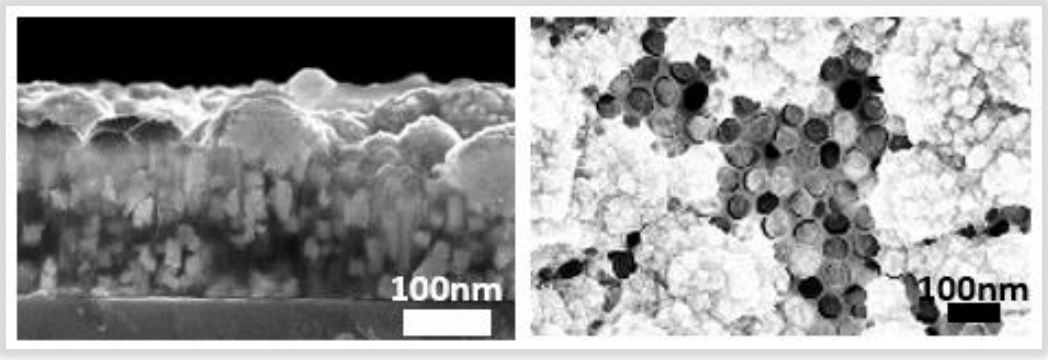

Figure III-52: SEM cross-sectional and top-view and images of the confined NiNWs galvanic displacement reaction in an H_2PtCl_6 solution at 0.1 M HCl at room temperature for 60 minutes.

Throughout these experiences, the counter-ion from H_2PtCl_6 and by varying the concentration of HCl, the shortcomings of GD have been clearly recognized as follows: **i/** uncontrolled GD reaction at different HCl concentration and exposure time, **ii/** the major defect in the experiments is the detachment of the nanowires, **iii/** re-deposition of platinum on the top of the AAO template, **iv/** and HCl is mandatory to achieve a GD reaction, but its concentration should be controlled and used with the appropriate Pt salt.

According to the present structural results, it could conceivably be hypothesized that using a different Pt salt rather than an acid would be favorable for the formation of PtNiNWs or PtNiNTs.

c- K_2PtCl_6 at 0.01 M HCl solution

Since H_2PtCl_6 did not show significant results in the formation of reproducible and controlled structures, it is desirable to shed light on the effect of Potassium hexachloroplatinate salt. Confined NiNWs on AAO were immersed in a K_2PtCl_6 solution at 0.01 M HCl (pH~2). The first five minutes of the GD reaction at room temperature revealed the beginning of detachment at the top of the nanowires, as evidenced below (*figure III-53*):

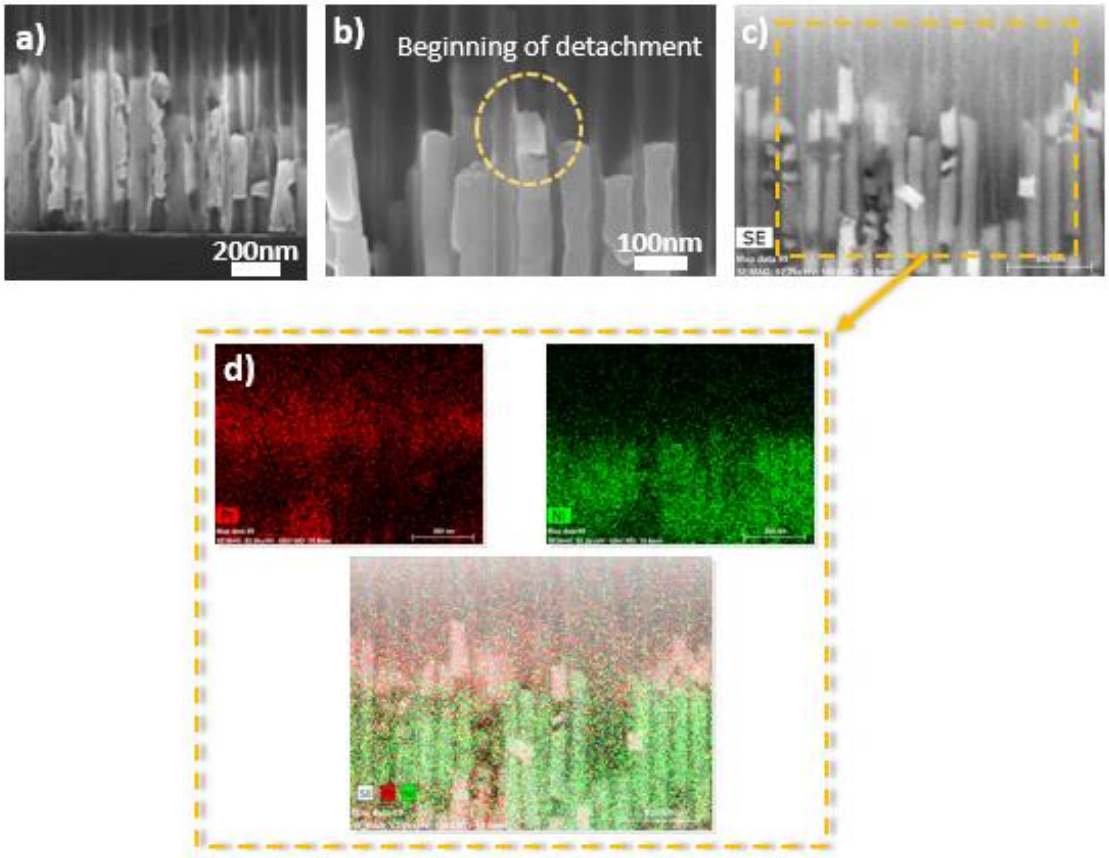

Figure III-53: SEM/EDX cross-sectional and top-view schematic illustration of the morphological changes of the confined NiNWs after 5 minutes galvanic displacement reaction in a K_2PtCl_6 solution at 0.01 M HCl at room temperature.

Further tests have been carried out at a longer exposure time (10 and 30 minutes) at room temperature. They have shown that the reaction only occurs at the top of the nanowire and does not spread all along the nanowire. At 30 minutes of exposure, a PtNi foam-like structure was obtained, as depicted in *figure III-54* below:

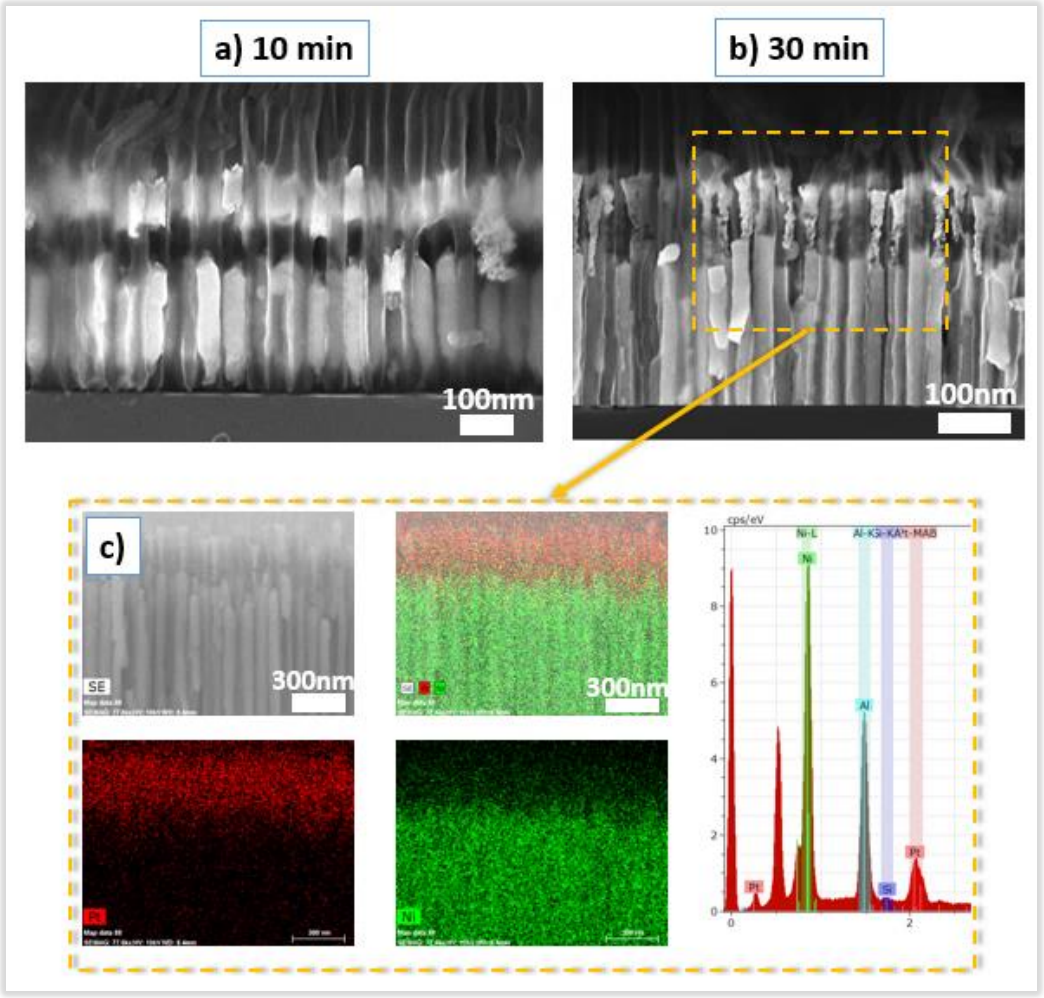

Figure III-54: SEM/EDX cross-sectional illustration of the morphological changes of the confined NiNWs after 30 minutes galvanic displacement reaction in a K_2PtCl_6 solution at 0.01 M HCl at room temperature.

Since time exposure at 0.01M HCl did not provide the desired controlled structure, we have tried a new experiment with the same initial NiNWs sample in AAO at a higher concentration.

d- K_2PtCl_6 at 0.1 M HCl solution

Following the same experimental process, K_2PtCl_6 was dissolved in highly purified water then diluted in a 0.1 M HCl solution (pH~1). As can be seen from the structural characterization, certain drawbacks associated with HCl use at higher concentration: SEM-cross section analysis has shown the fragmented PtNi structure into shorter segments. Long exposure time (1 hour) of GD lead to a complete breaking of the nanowires in smaller fragments alongside the redepositing of Pt on the surface of the AAO. If

considering what was reported by *Shaun M. Alia et al.* [72], we can attribute these results to the sensitivity of Ni in acidic media, and the concentration of H^+ could increase the kinetic rate of the GD reaction. (*i.e.,* high nickel sensibility to HCl concentration at room temperature; the ionic conductivity of the bath increases when [HCl] increases).

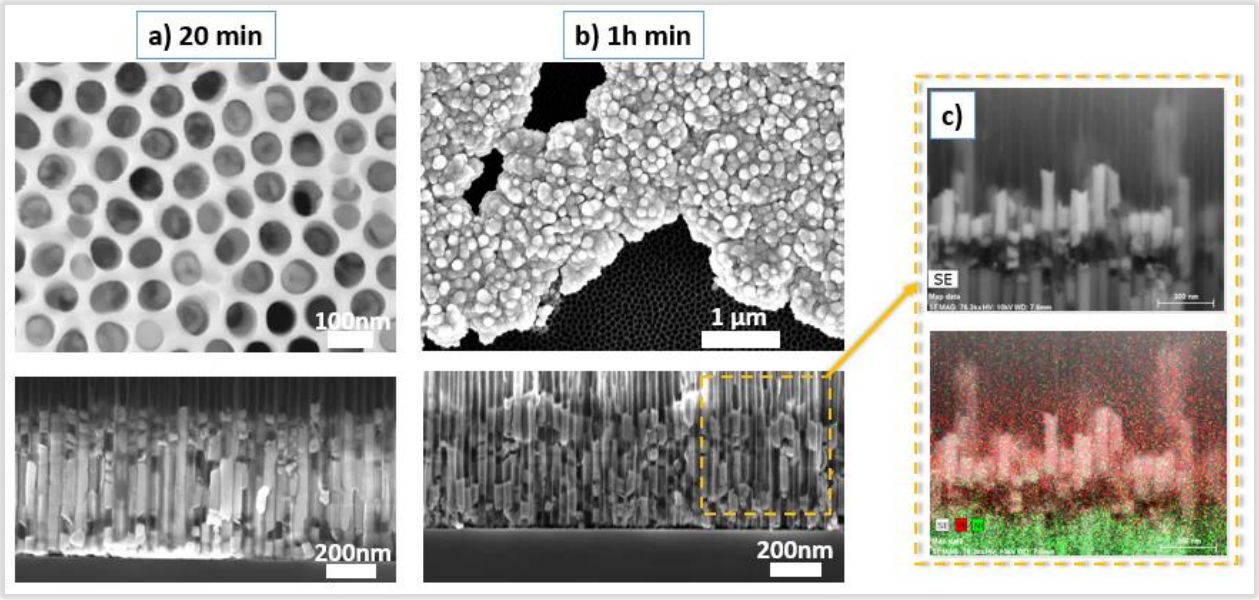

Figure III-55: SEM/EDX cross-sectional illustration of the morphological changes of the confined NiNWsafter after galvanic displacement reaction for a) 20 minutes and b) 1 hour in a K_2PtCl_6 solution at 0.01 M HCl at room temperature. c) EDX elemental map of fragmented representative PtNiNWs.

e- K_2PtCl_4 at 0.01 M HCl solution

Although we have varied Pt salt (H_2PtCl_6 and K_2PtCl_6) and HCl concentration, we did not get the desired results: reproducible PtNiNWs and PtNiNTs. There is still some considerable controversy surrounding the effect of the acidic medium and the right Pt salt. Interestingly, we have expanded our tests to the use of a different Pt salt (K_2PtCl_4). At room temperature, the GD reaction in the 0.01 M HCl solution did not occur at 2 hours, 6 hours, and 8 hours.

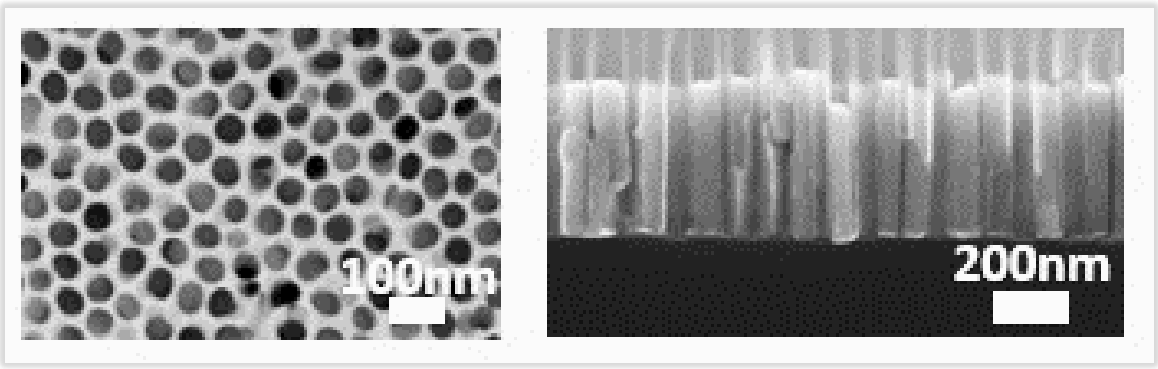

Figure III-56: SEM cross-sectional and top-view and images of the confined NiNWs galvanic displacement reaction in a K_2PtCl_4 solution at 0.01 M HCl at room temperature for 6 hours.

By keeping the same process but instead, this time at 50°C for only 10 minutes, an uncontrolled GD reaction led to an unconfined PtNi alloy on the surface of the AAO. The utility of increasing temperature thus underlined further evidence on its impact on the GD reaction.

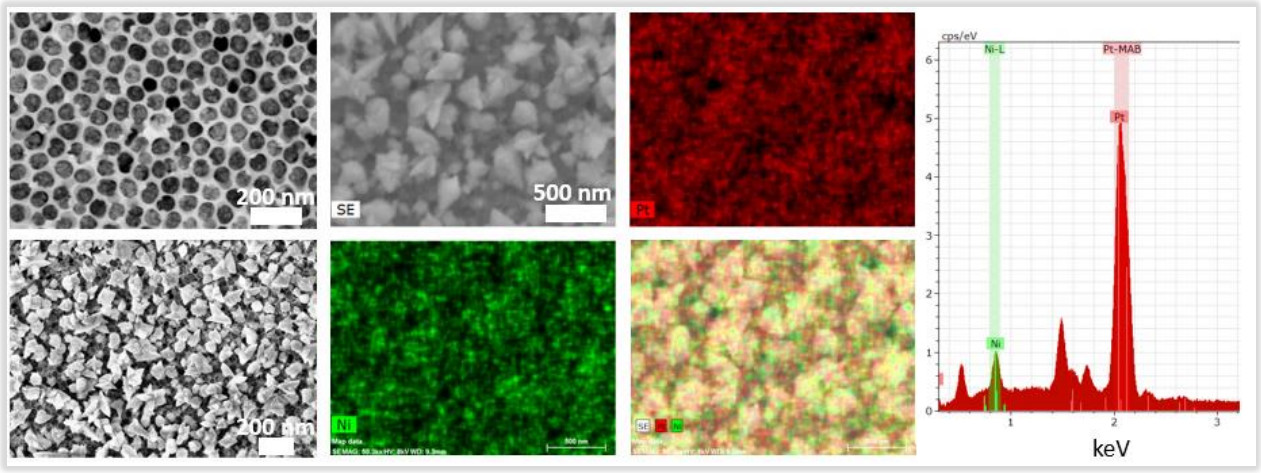

Figure III-57: SEM top-view images of the confined NiNWs galvanic displacement reaction in a K_2PtCl_4 solution at 0.01 M HCl at 50°C for 10 minutes.

These results offer evidence of fine-tuning the HCl concentration/temperature duality. Our next experiments were held with careful attention to these two critical parameters and their direct effect on the PtNi morphology. The upshot of this adjustment is the necessity of decreasing temperature to 35°C and increasing the HCl concentration to 0.05 M. *Figure III-58* below illustrates an SEM coupled EDX analysis of the obtained interconnected PtNi nanowires, which seem to be clogged from the top.

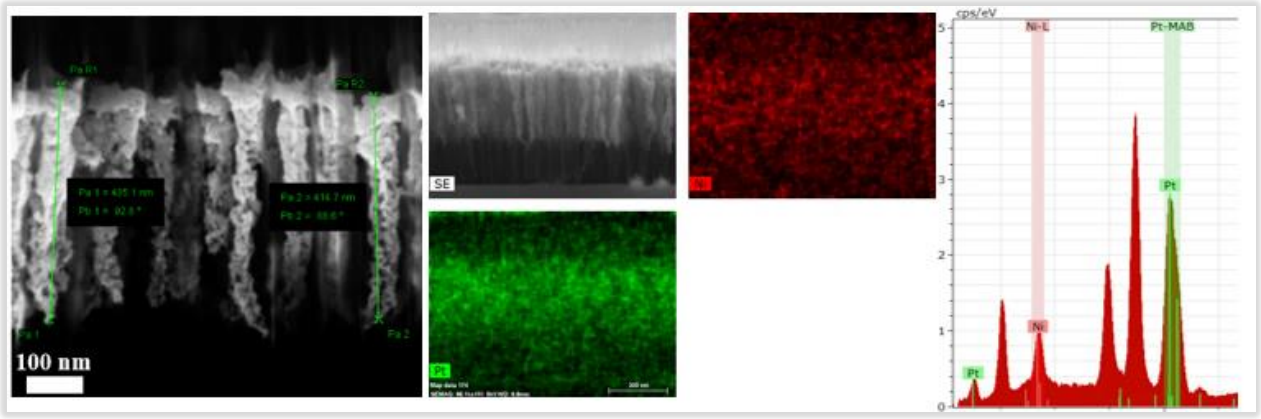

Figure III-58: Scanning electron microscopy (SEM) coupled Energy-dispersive X-ray spectroscopy (EDX) structural characterization of PtNi interconnected nanowires obtained in K_2PtCl_4 solution containing 0.05 M of HCl at 30°C in 10 minutes.

To highlight the GD process's evolution over time, *figure III-59* below depicts the steps involved from initial NiNWs to intertwined PtNiNWs inside AAO.

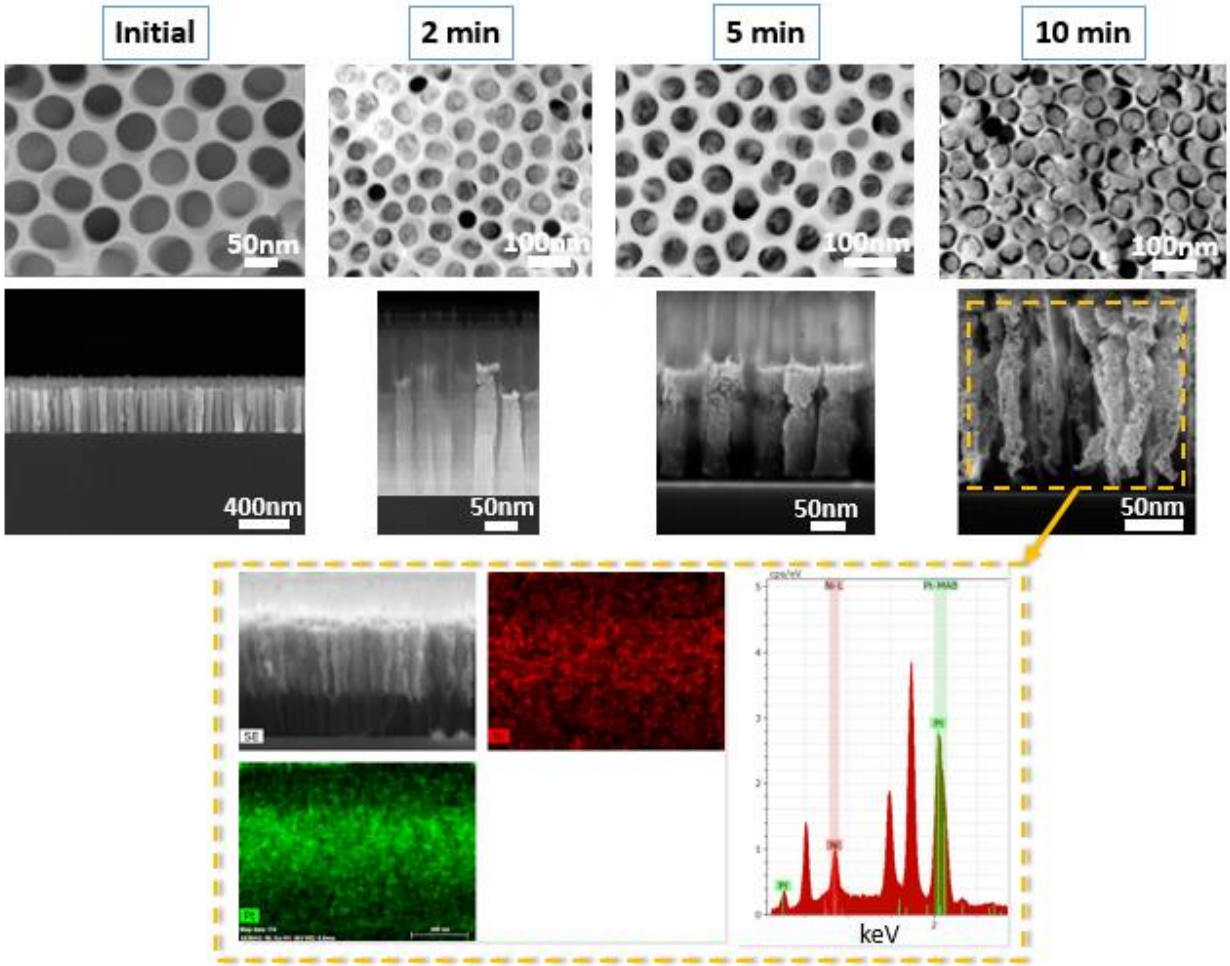

Figure III-59: SEM top-view and cross-sectional images of the GD reaction's evolution over time of confined NiNWs in K_2PtCl_4 solution at 0.01 M HCl at 30°C.

f- K_2PtCl_4 at 0.1 M HCl solution

Despite the previous experiments and to call into question the validity of the right concentration of HCl, I have also examined the effect of a slight increase in HCl concentration to 0.1 M at room temperature. Interesting results were obtained after 1.5 hours of GD reaction, leading to foam-like PtNi nanostructures with a close resemblance to those reported previously at 0.05 M HCl. However, a closer inspection on the surface of AAO revealed the redepositing of Pt agglomerates on its surface, as displayed in the figure below.

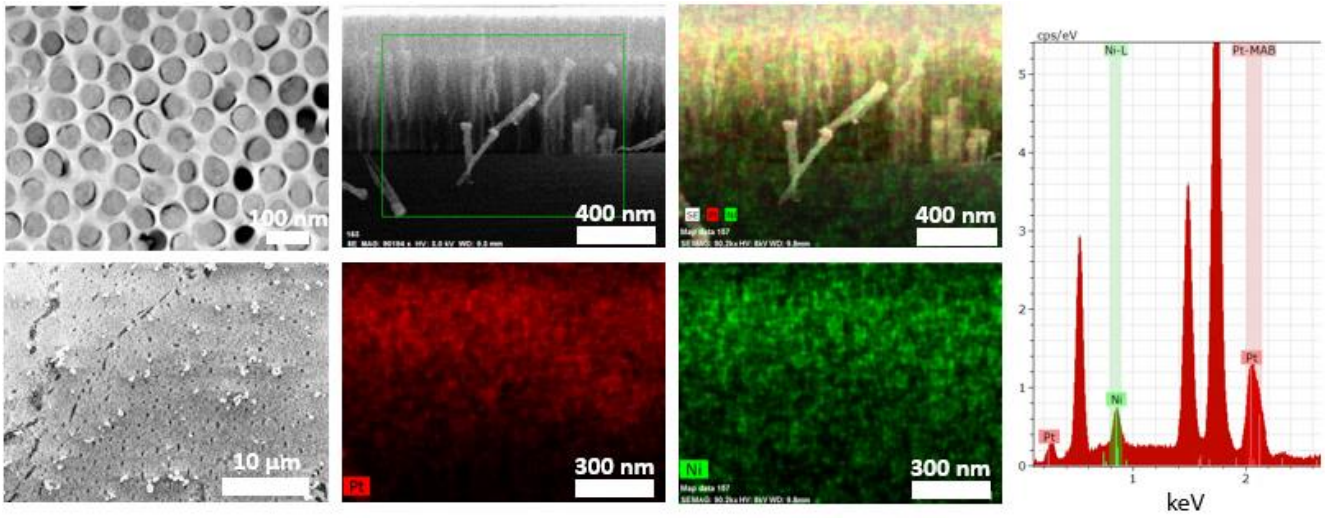

Figure III-60: SEM top-view and cross-sectional images of the GD reaction result of confined NiNWs in K_2PtCl_4 solution at 0.1 M HCl at 1.5 hours at room temperature.

IV.3.1.3 Conclusion: GD in a confined system

Regarding the experiments I held in a confined system (where the GD reaction should occur inside AAO), varying HCl concentration led to different results according to SEM structural analysis. Also, in a confined system, the study has demonstrated that the GD reaction is non-trivial and tricky due to its sensitivity to several parameters such as concentrations, exposure time, temperature, and HCl concentration.

In summary, most of the experiments have shown that the GD reaction in a confined system is hard to control neither with H_2PtCl_6 nor with K_2PtCl_6, with and without acid. The nanotubes were not obtained, which indicates that the nickel's stability is strongly influenced by the presence of an acid. Nevertheless, in the confined system, reproducibility was achieved solely for samples exposed to 1mM K_2PtCl_4 solution in

0.05 M HCl concentration at 30°C. As observed by SEM imaging in *figure III-59* above, PtNi foam-like nanorods were obtained after 10 minutes of GD reaction and disconnected from the bottom of the silicon substrate.

IV.3.2 Path II: GD in a non-confined system

As reported earlier, a non-confined system refers to the etching of the AAO template in an alkaline etching medium (1M NaOH solution) at room temperature, where freestanding and aligned Ni nanowires on a silicon substrate have been exposed to different Pt solutions.

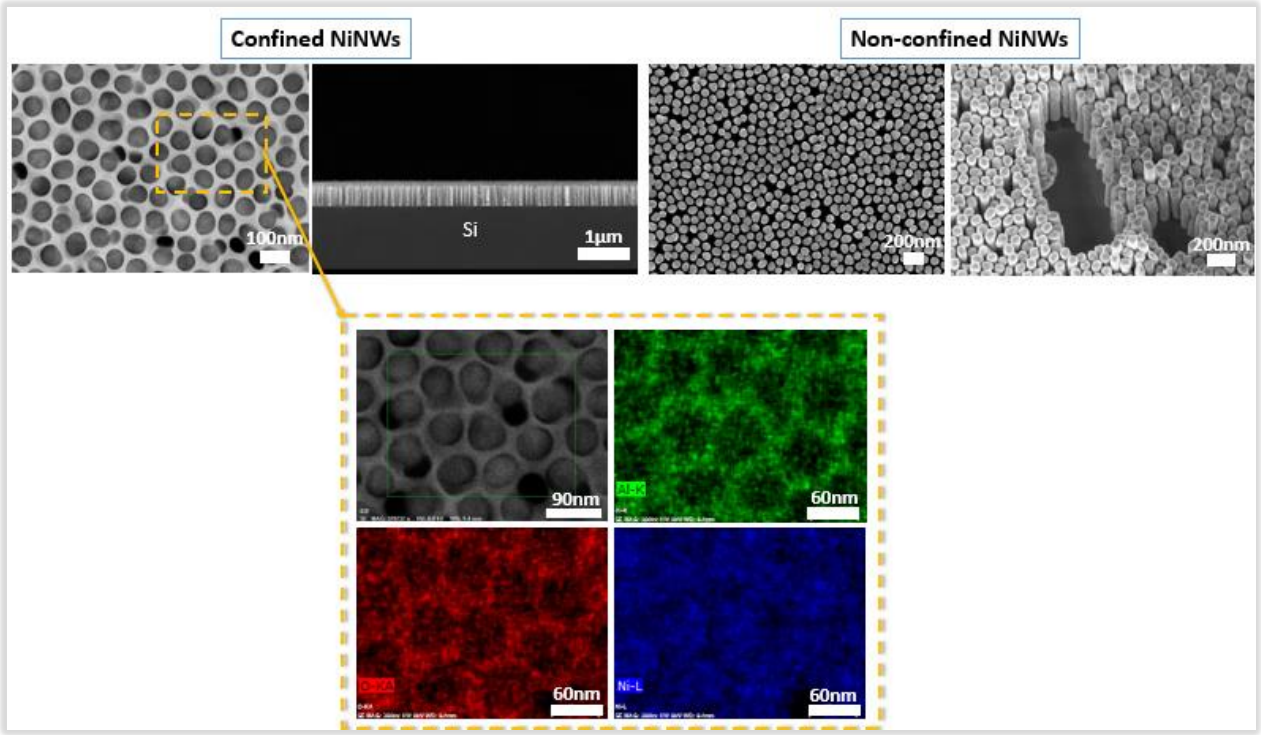

Figure III-61: SEM images of NiNWs inside AAO membrane and after etching AAO membrane. Energy-dispersive X-ray spectroscopy map of the surface of NiNWs embedded inside the AAO membrane.

It should be borne in mind that the stability of the synthesized material towards the etching solution of AAO must be checked beforehand; otherwise, the nanowires will be altered or destroyed as the dissolution proceeds. In our case, nickel and nickel-based alloys are well known for their ability to resist corrosive environments, even under severe operating conditions. Specifically, in the case of resisting highly concentrated NaOH, nickel ranks next to silver. For this reason, nickel and its alloys are widely used in NaOH service [80].

IV.3.2.1 Reaction without the addition of HCl: Thermal treatment and acid leaching effect

In this part, we evaluated the GD in a non-confined system without the addition of HCl. To assess the effect of the GD on NiNWS, repeated experiments at different exposure times and various Pt salts have been carried out. Results were not satisfying; inhomogeneous deposits of Pt on the surface of AAO or non-occurring reactions were obtained. Even in HCl at a low concentration (1 mmol/L), the GD reaction did not occur. This is exemplified, for instance, for a GD reaction in a K_2PtCl_4 solution for 1 hour where Pt agglomerates on the top of NiNWs, which *figure III-62* below illustrates this point clearly.

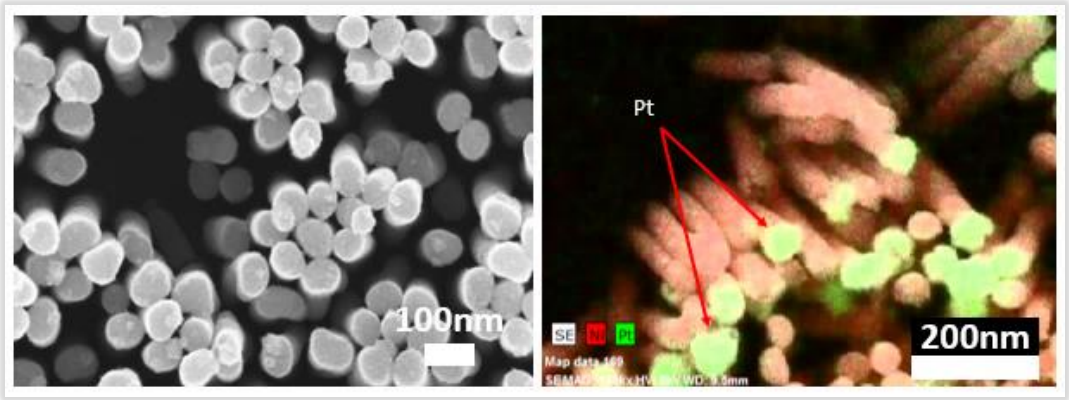

Figure III-62: SEM coupled EDX elemental map analysis of the galvanic displacement reaction of NiNWs in K_2PtCl_4 solution for 1 hour at room temperature.

Unexpectedly, and amid our experiences, *C. Fan et al.* [75] have presented in their article a viable multi-process method to elaborating PtNi alloy catalyst with one-dimensional nanotube structure via a galvanic replacement reaction combined with Kirkendall effect. We believed this solution would help achieve our desired electrode architecture made of PtNiNTs and is worth further investigation.

To highlight our presented work, only K_2PtCl_4 1mM was used as a source of Pt cations, where the Pt cations would be reduced to metallic Pt at the expense of the sacrificial Ni according to the following reaction:

- Precursor dissociates in water: $\mathbf{K_2PtCl_{4(aq)} \rightarrow PtCl_4^{2-}{}_{(aq)} + 2K_{(aq)}}$
- Pt deposition: $\mathbf{Ni + PtCl_4^{2-} \rightarrow Pt + Ni^{2+} + 4Cl^-}$

A non-confined Pt galvanic displacement process at a temperature range from 60° to 90°C (slow and high evaporation of water, respectively) was performed. Exposure time to Pt salt solution has been investigated, as shown in *figure III-63* below. Non-confined NiNWs samples were exposed to 1 mM K_2PtCl_4 solution at 60°C for one to 6 hours. Elemental integrated EDX spectrum was used for semi-quantitative composition estimation (*figure III-63* below) and showed an increase in the Pt/Ni atomic ratio over exposure time.

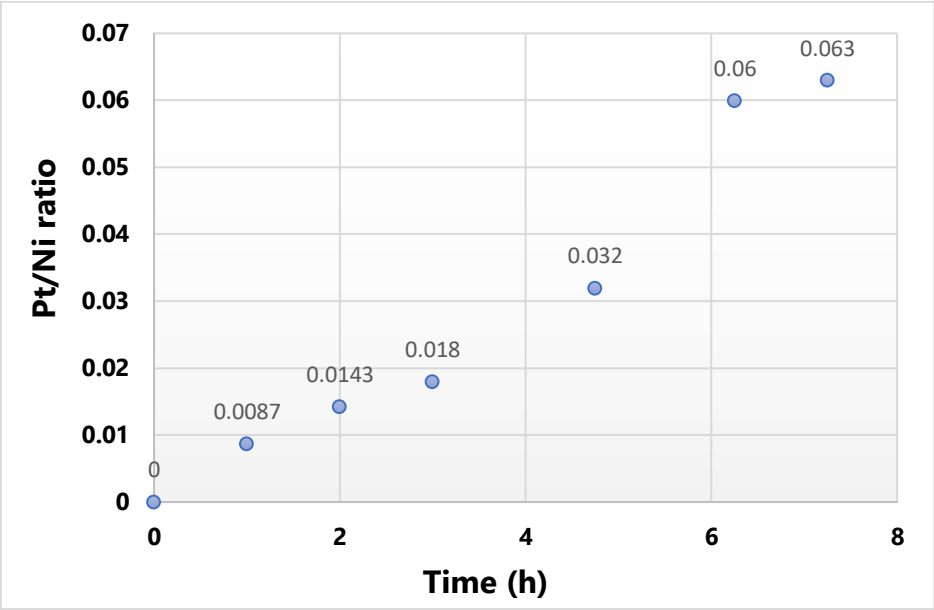

Figure III-63: The evolution of the Pt/Ni atomic ratio obtained from EDX analysis during the GD reaction over time in 10^{-3}M K_2PtCl_4 solution at 60°C.

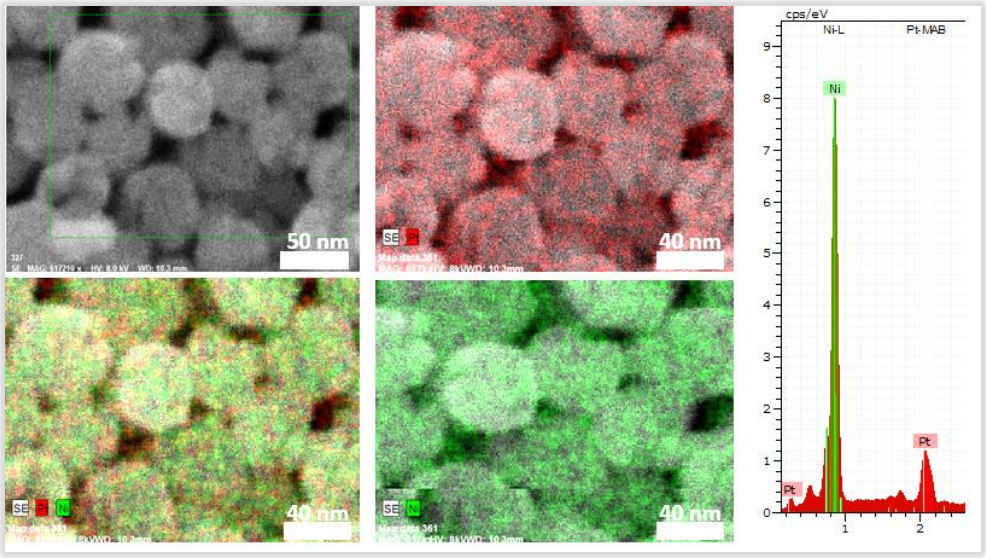

Figure III-64: SEM-EDX elemental mapping of the top of the PtNi nanowires after exposing the sample to a K_2PtCl_4 solution at 60°C for 5 hours.

As shown in *figure III-65* below, a longer exposure time to the Pt solution (10 to 20 hours) led to an overgrowth of the platinum on the top of the nanowires, which is well consistent with SEM/EDX analysis.

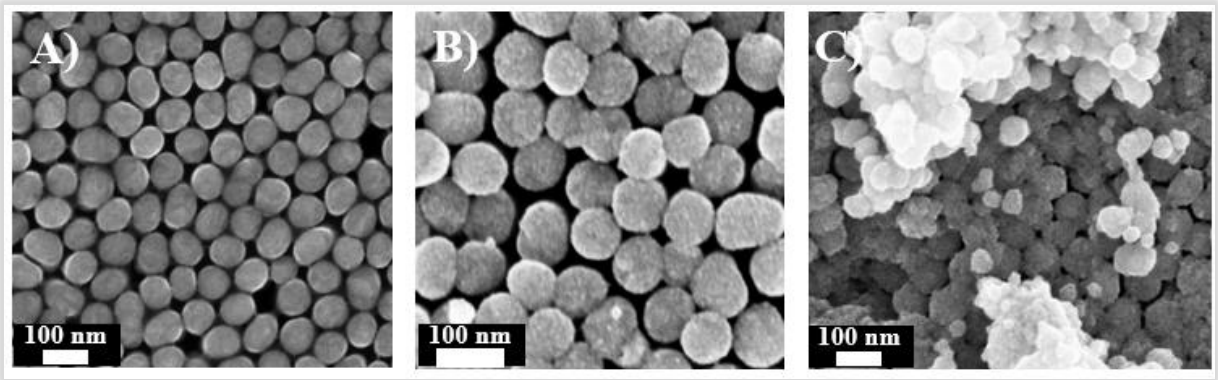

Figure III- 65: A top view scanning electron microscope (SEM) image showing the effect of Pt solution exposure time on the morphology of the NiNWs. A) Non-confined nickel nanowires, B) 5 hours galvanic displacement reaction at 60°C, and C) 10 hours galvanic displacement reaction at 60°C.

To optimize the process for a shorter time, I carried out the same experiment at a higher temperature [80-85°C] for 1.5 hours. We believe that temperature has a significant effect on the rate of a chemical reaction.

Based on the SEM-coupled EDX semi-quantitative composition estimation, a Pt/Ni atomic ratio was approximately 2-3%. During the GD process, Pt atoms are believed to nucleate and grow into very small particles, ultimately growing into a thin Pt-shell around nickel nanowires. Ni^{2+} and $PtCl^{4-}$ (or $PtCl^{6-}$) diffuse continuously across the shell until we stop the reaction.

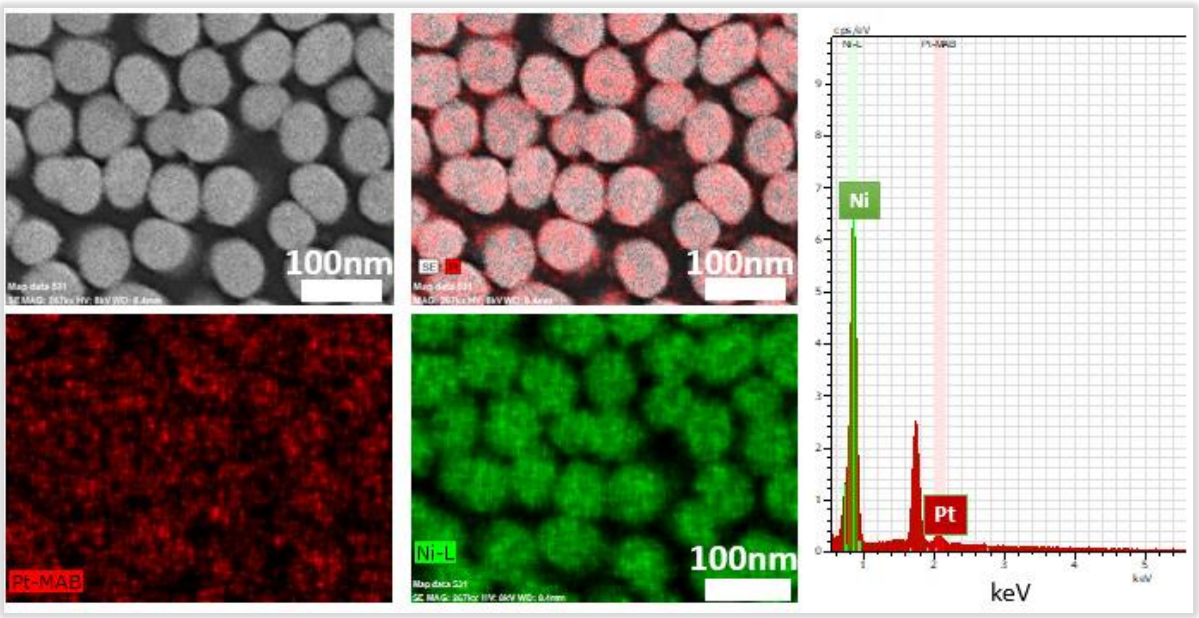

Figure III-66: SEM/EDX elemental mapping of the top of the PtNi nanowires after exposing the sample to a K_2PtCl_4 solution at 80°C for 1.5 hours.

The structural analysis of the Pt coated NiNWs was assessed by a TEM analysis coupled with an Energy-dispersive X-ray spectroscopy map. As evidenced in *figure III-67*, the GD reaction had led to the deposit of a thin Pt layer of ~4-5 nm onto the Ni nanowires.

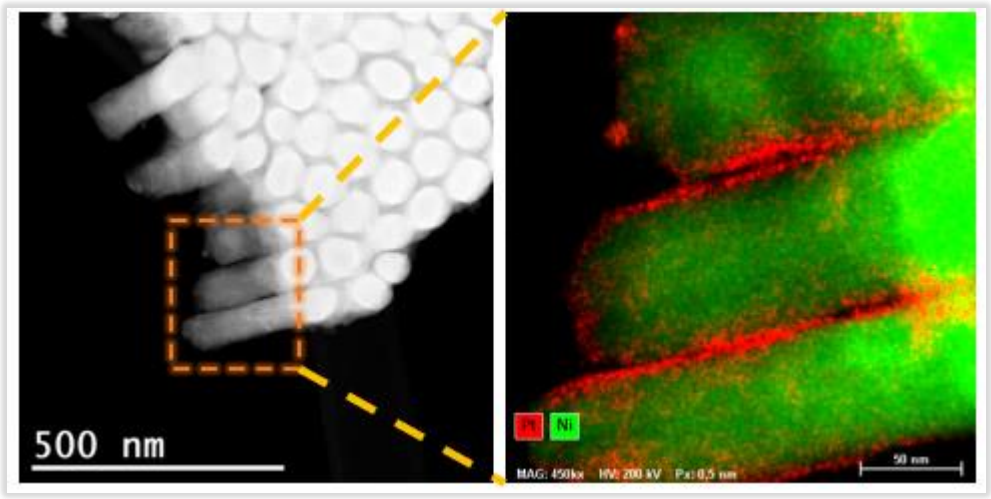

Figure III-67: Transmission electron micrograph and its corresponding elemental map of Pt and Ni for PtNiNWs (intermediate step before the formation of PtNiNTs) Pt species are in red, and Ni species are in green.

The samples were further characterized by X-ray diffraction (XRD) to investigate the crystallinity of the metal phases. Measurements were performed via PANalytical Empyrean diffractometer with a diffracted-beam monochromator (Cu K-α radiation, λ = 0.15406 nm)

using the θ-2θ configuration scan. The diffraction patterns were acquired by Olivier SICARDY at the Nanocharacterization Platform (PFNC), CEA-Minatec.

Based on the diffraction of X-rays on these PtNiNWs (*i.e.*, Pt-shell surrounding the Ni-core), measurements exhibit two broad peaks related to the face-centered cubic Nickel, with angular positions 44.5° and 51.8°, corresponding respectively to Ni(111) and Ni(200) crystalline planes as displayed in *figure III-68* below. Also, an apparent peak could be detected at 39.83°, which might refer to the pure Pt(111) peak.

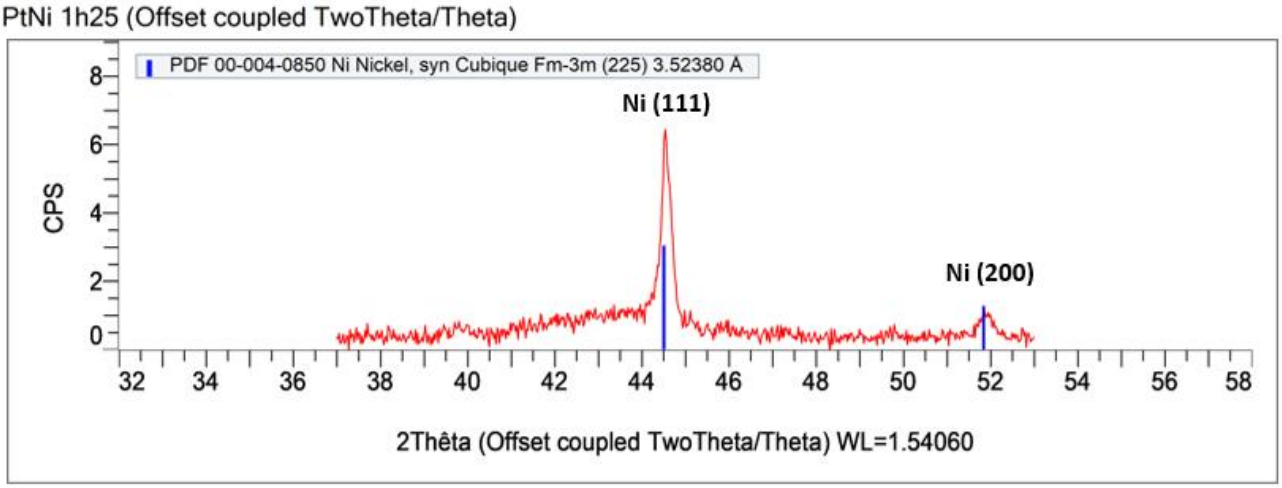

Figure III-68: XRD measurements performed on PtNiNWs at low Pt deposition where Ni peaks are clearly visible. PtNi nanowires were obtained after exposing the NiNWs sample to a K_2PtCl_4 solution at 80°C for 1.5 hours.

Based on the previous works of *T. Asset* et *al.* [54]*, S. M. Alia* et *al.* [72]*,* and *C. Fan* et *al.* [75], the thermal treatment under H_2/Ar atmosphere and the acid leaching is playing a pivotal role in the formation of a porous structure of PtNi nanowires, thus forming hollow nanotubes. PtNiNWs were annealed in an attempt to improve the incorporation of Ni into the Pt phase.

After the GD reaction, the PtNiNWs annealing was conducted using a thermal quartz tube furnace under H_2/Ar 5% atmosphere. A complete purge of the furnace was set for 2 hours. The increased rate of temperature in the furnace is 10°C/min until reaching the desired temperature. Once the annealing process ends, the temperature decreases until it reaches room temperature. A schematic diagram of the annealing process of PtNiNWs in the RTA system is shown in *figure III-69*.

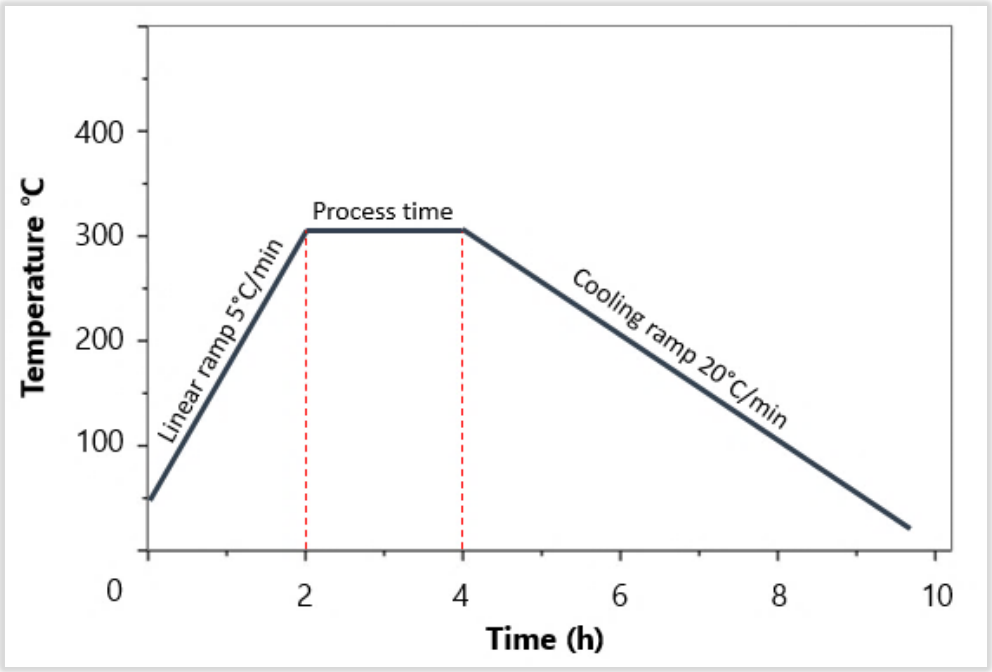

Figure III-69: A schematic diagram of the annealing process in RTA (Rapid Thermal Annealing) temperature.

The next step consists of an **acid leaching treatment**. The chemical dealloying consisted of the PtNiNWs samples exposure to a 0.5-2 M sulfuric acid solution at 30-50°C for 3 to 10 minutes. This step has to remove excessive Ni located in the core of the PtNiNWs, thus forming PtNi nanotubes. During the AL process and before the formation of PtNiNTs, the latter have peeled off from silicon due to the acid environment. However, once they are detached from the substrate, their integration into the Nafion® turned out to be impossible. To alleviate the problem, we suggested two solutions:

a) Thermal pre-treatment of the non-confined NiNWs on silicon: We believed that this step would allow the diffusion of Ni atoms through the silicon substrate. Thus, it would be a very good attachment to the substrate, thereby alleviating the PtNi detachment from Si [81]. Unfortunately, the tangled relationship between thermal treatment and detachment from silicon led to the reoccurrence of the problem again after AL. A slight dealloying occurred in the core of the PtNiNWs before they detach entirely from the silicon substrate as demonstrated in *figure III-70* below.

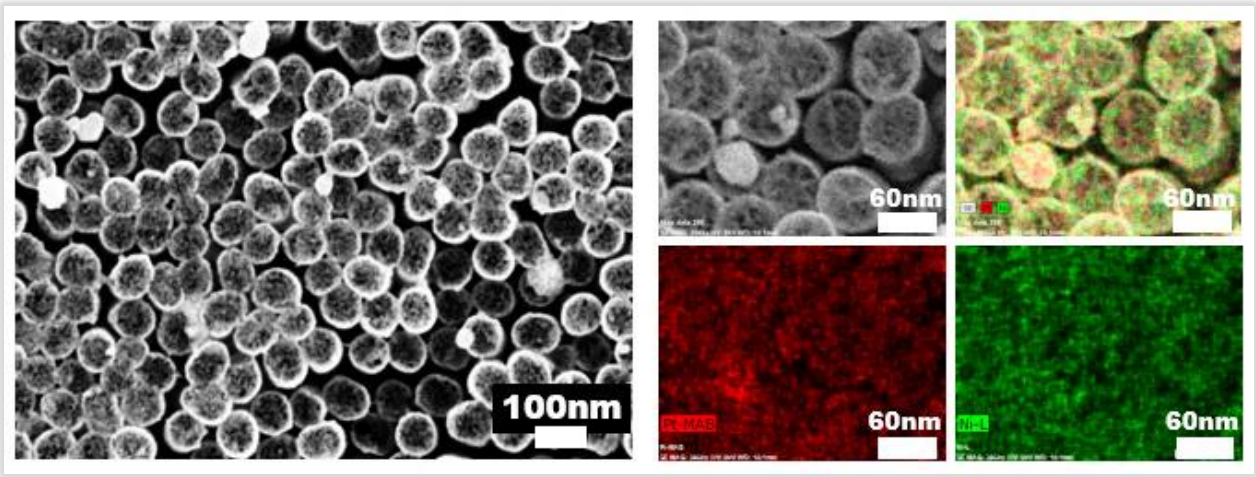

Figure III-70: SEM top-view image of quasi-porous PtNiNWs before the complete detachment from the silicon substrate and its corresponding EDX analysis.

b) The second method represented a viable alternative to the previous one. It consists of transferring the annealed PtNiNWs onto the Nafion® HP membrane (thickness: 22 µm) by the hot-pressing process (see *paragraph I.1.3* for further details). Once the PtNi nanowires were entirely transferred to the ionomer membrane, the latter is then immersed in the sulfuric acid solution for dealloying, re-acidifying the membrane, and helps to tear off gently the polymer from the silicon substrate. For the AL, however, the goal was not to remove all of the nickel but the soluble nickel of the PtNiNWs that was not alloyed to the Pt.

Morphological characterization of the obtained PtNiNTs samples was carried out by SEM-EDX analysis. *Figure III-71* below shows the PtNi nanotubes formed onto the Nafion® surface after acid leaching in a sulfuric acid solution heated to 30°C.

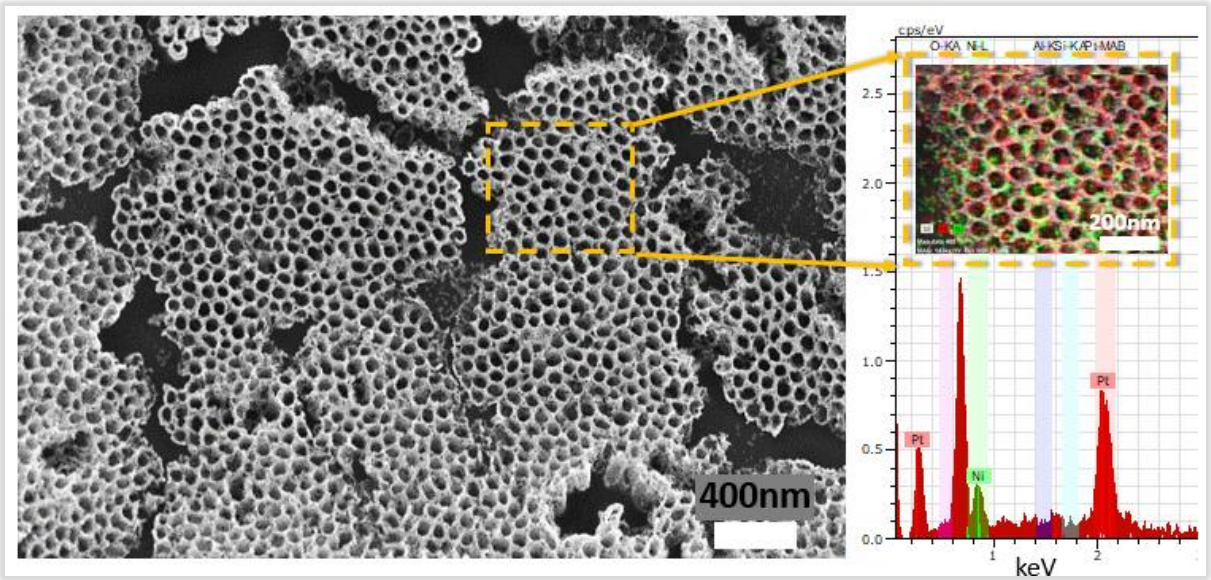

Figure III-71: SEM top of PtNi nanotubes transferred to Nafion© membrane, obtained in a non-confined system in K_2PtCl_4 solution heated to 80°C for 1.5 hours. After GD, the PtNiNWs were heated under H_2/Ar atmosphere for 2 hours at 250°C. After that, PtNiNWs were transferred to the Nafion© membrane by a hot-pressing process followed by an acid-leaching process in a sulfuric acid solution. According to the EDX quantitative analysis, the atomic ratio of Pt:Ni is 3:1.

To characterize the synthesized PtNiNTs, the energy dispersive X-ray (EDX) analysis was performed using transmission electron microscopy (TEM) indicated the formation of a porous structure (*figure III-72)* of the nanotube and their integration onto the Nafion® membrane.

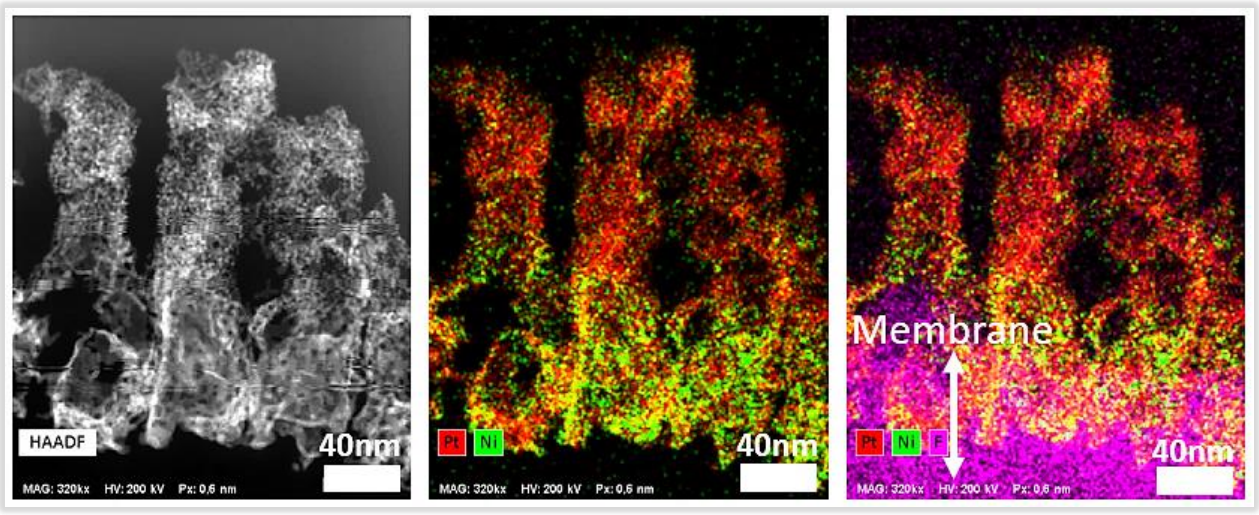

Figure III-72: HAADF-TEM micrograph and its EDX elemental mapping of the porous PtNiNTs embedded onto the Nafion® membrane.

A TEM coupled EDX analysis was used to build an elemental map, giving insights on the sample morphological properties as depicted in *figure III-73*. The higher Pt content at the top of the nanotubes indicates that the acid leaching occurred more at this region and spread less toward the embedded area onto the membrane with a higher Ni concentration inside it as evidenced in the following figure:

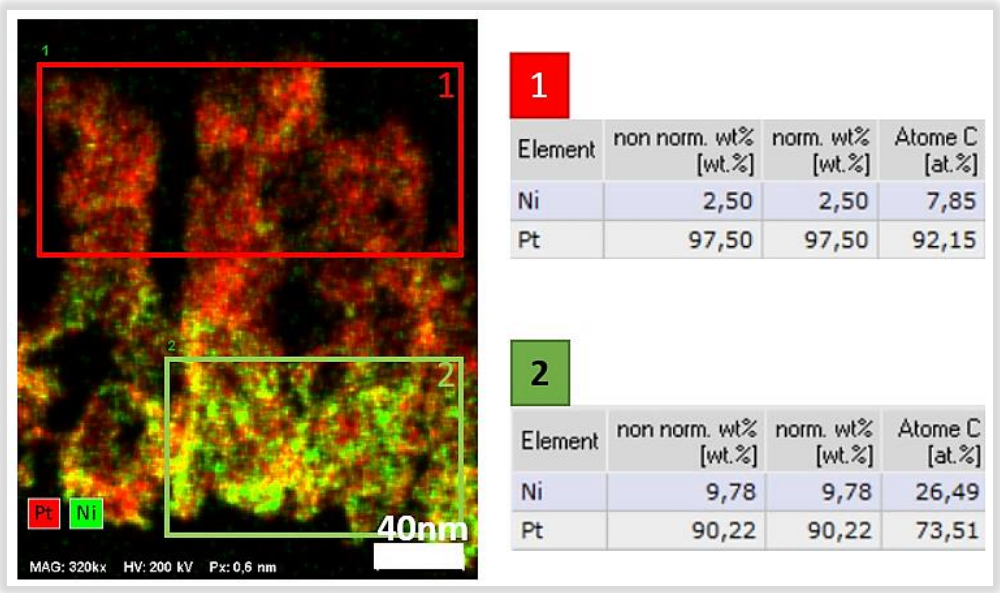

1

Element	non norm. wt% [wt.%]	norm. wt% [wt.%]	Atome C [at.%]
Ni	2,50	2,50	7,85
Pt	97,50	97,50	92,15

2

Element	non norm. wt% [wt.%]	norm. wt% [wt.%]	Atome C [at.%]
Ni	9,78	9,78	26,49
Pt	90,22	90,22	73,51

Figure III-73: The corresponding TEM-EDX elemental map for a cross-sectional view of the PtNiNTs embedded onto the Nafion® membrane and their acquired quantification, showing the acid leaching gradient along the nanotubes.

XRD experiments were performed on this sample (PtNiNTs embedded onto the Nafion® membrane). The obtained pattern (*figure III-74*) revealed a very low signal at 39.8° matching that for the pure Pt(111), indicating a low concentration of Pt in the sample.

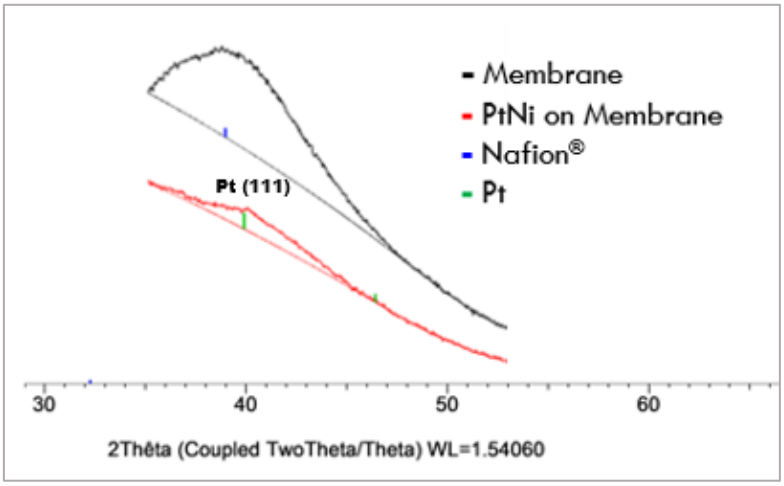

Figure III- 74: XRD measurements performed on PtNiNTs embedded onto the Nafion® membrane.

To sum up, several steps were involved in the formation of PtNiNTs. After every step, a SEM/EDX analysis was performed to investigate the evolution and the effect of each process. The flowchart below (*figure III-75*) represents an overview of the complete process involved in the fabrication of PtNiNTs.

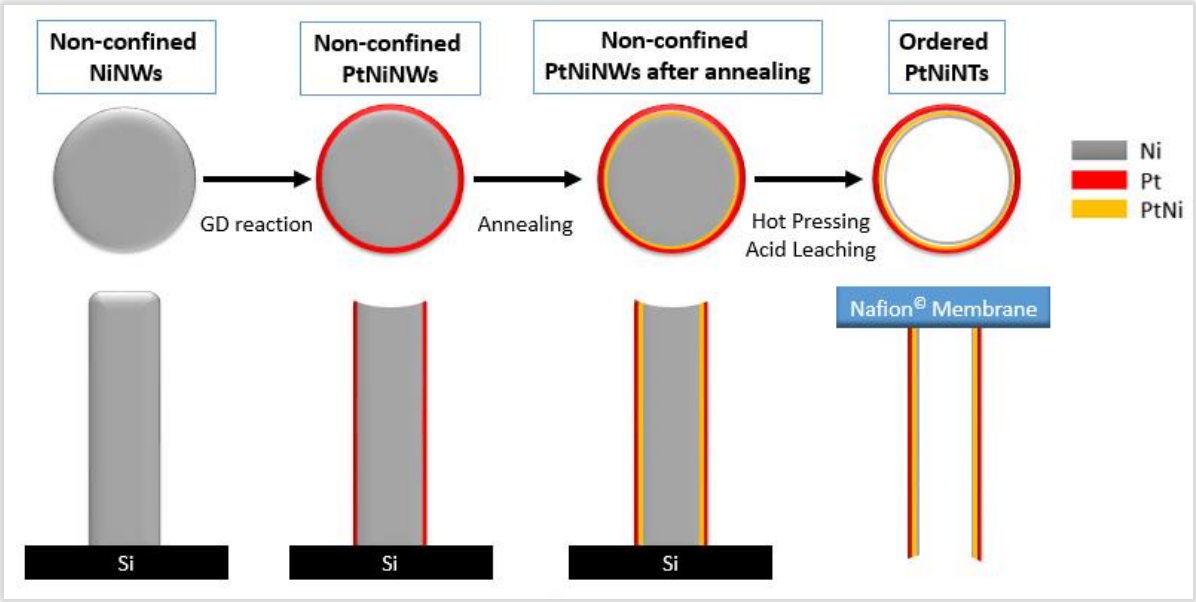

Figure III-75: A schematic illustration of the complete process of the steps involved in the elaboration PtNi nanotubes.

IV.3.2.2 Reaction with the addition of HCl

Similar to the process described previously, the GD reaction of non-confined NiNWs was carried out in the same conditions (Pt counter-ion salts and HCl at different concentrations), as stated before.

In H_2PtCl_6, the GD did not occur without HCl, with 0.001 M HCl, nor with 0.01 M HCl at room temperature. Only at 0.1 M HCl for 30 minutes, partial GD reaction occurred at the top of NiNWs but did not spread all along with them, as shown in *figure III-76* below.

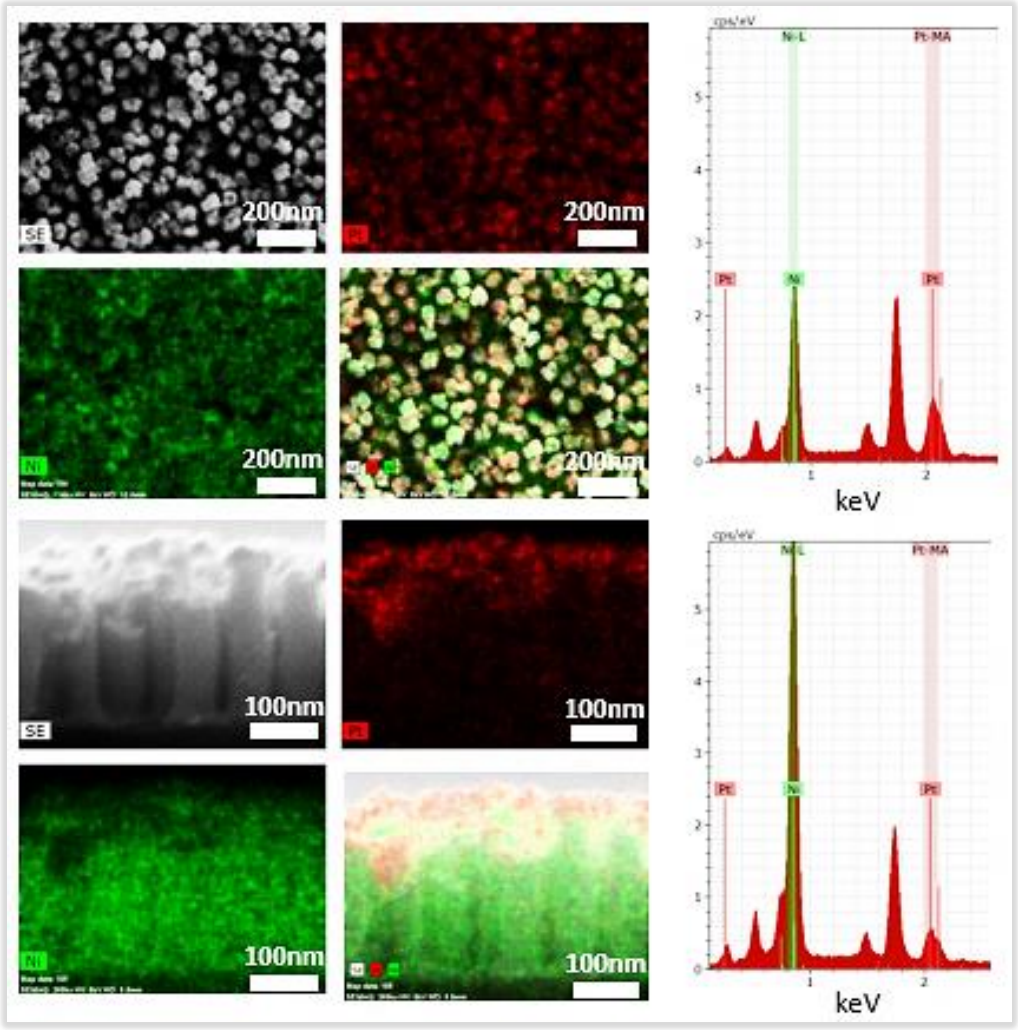

Figure III-76: Top-view and cross-sectional SEM coupled EDX analysis of the result of NiNWs GD reaction in H_2PtCl_6 solution in 0.1 M HCl HCl for 30 minutes.

Switching to K_2PtCl_6 as a Pt counter-ions source, GD reaction at room temperature at different HCl concentrations. Only while increasing the solution's temperature to 30°C, the reaction occurred solely when using HCl at a concentration of 0.1 M. The single most striking observation to emerge from SEM analysis, PtNiNWs exhibited a foam-like structure in their core. The issue related to the obtained structure is the full detachment of the nanostructures from silicon, as clearly evidenced in *figure III-77* below.

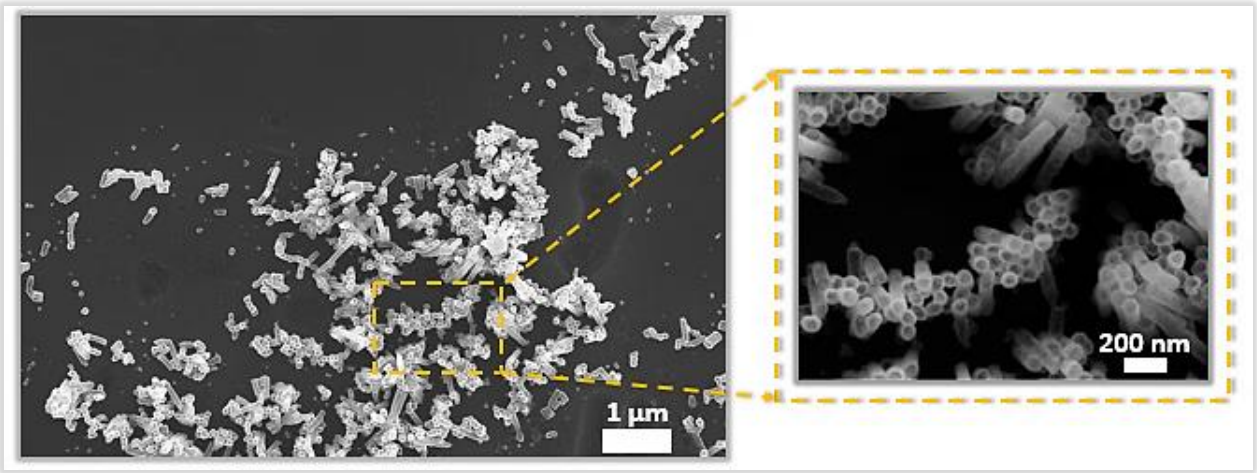

Figure III-77: SEM top-view image of detached PtNiNWs from the silicon substrate. The GD reaction was carried out in a K_2PtCl_6 solution in 0.1 M HCl at 30°C for 5 minutes.

Similarly, K_2PtCl_4 salt in [0.001-0.01 M] HCl was not useful in elaborating PtNiNWs by GD. Increasing HCl concentration to 0.1 M at room temperature for 45 minutes has shown a reproducible fabrication of PtNiNWs with less detachment rate from Si, as displayed in *figure III-78* below.

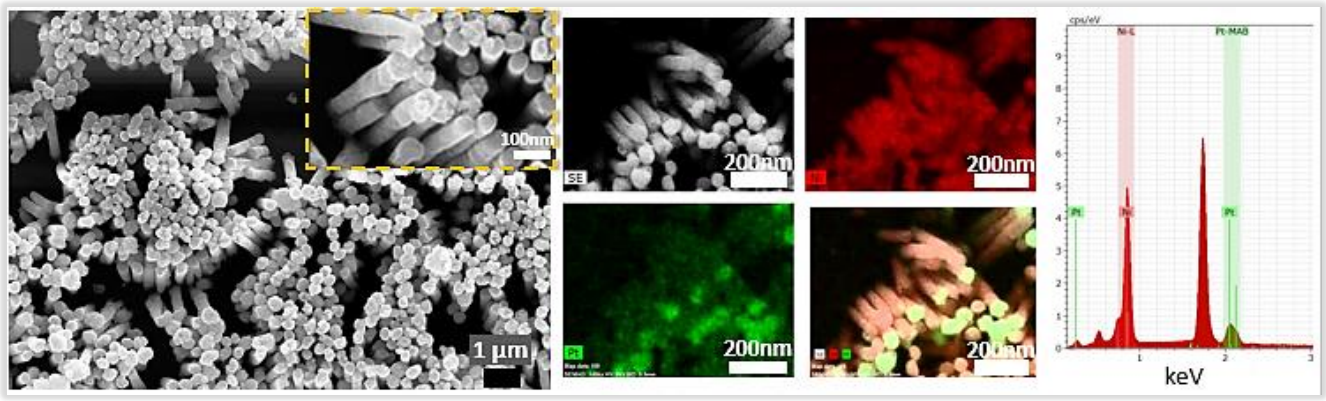

Figure III-78: Top-view SEM coupled EDX analysis of PtNiNWs after the GD reaction in K_2PtCl_4 solution in 0.1 M HCl for 45 minutes at room temperature.

The study has gone some way towards enhancing our understanding of the effect of HCl and temperature. To examine this issue, I increased HCl concentration to 0.05 M while I increased the temperature to 35°C between 2 and 15 minutes. As a consequence, reproducible PtNiNWs have been synthesized successfully. Moreover, PtNiNWs did not detach from the substrate, which will make it easier to be transferred into the ionomer membrane by hot-pressing.

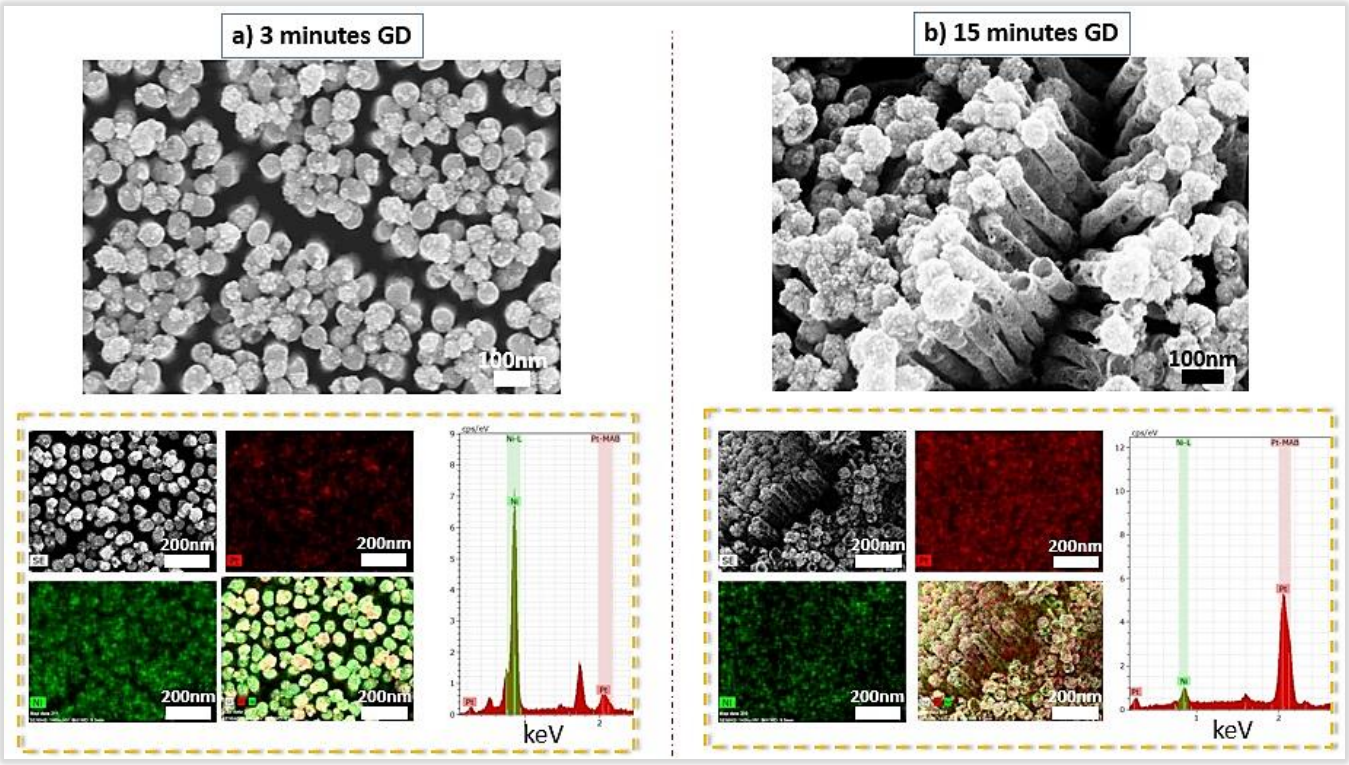

Figure III-79: Scanning electron microscopy (SEM) structural characterization coupled with Energy-dispersive X-ray spectroscopy (EDX) mapping of PtNiNWs obtained in K_2PtCl_4 solution containing 0.05 M of HCl at 30°C in a) 3 minutes and b) 15 minutes of galvanic displacement.

Throughout this thesis and according to the methodology outlined above, reproducible PtNiNWs that will be used in fuel cell tests are obtained after 8 minutes GD reaction at 35°C in K_2PtCl_4 solution with HCl 0.05 M (*figure III-80*). The resulting NWs have shown an atomic ratio Ni=1/Pt=3 (Pt_3Ni) and are directly transferred into the ionomer membrane by hot-processing, as will be demonstrated in the next chapter. The surface roughness of the Pt shell could be related to the vacancies formed by the dissolution of Ni.

Figure III-80: SEM top-view structural characterization coupled with EDX elemental mapping of PtNiNWs after exposing NiNWs to a K_2PtCl_4 solution in 0.05 M HCl at 35°C for 8 minutes.

For a deeper morphological analysis, the PtNiNWs were peeled off from the Si substrate and dispersed in a Copper transmission electron microscopy grid. The performed TEM-EDX quantitative microanalysis evidenced the formation of Pt_2Ni foam-like nanowires, displaying the distribution of Pt within the nickel as we can clearly observe in *figure III-81* below.

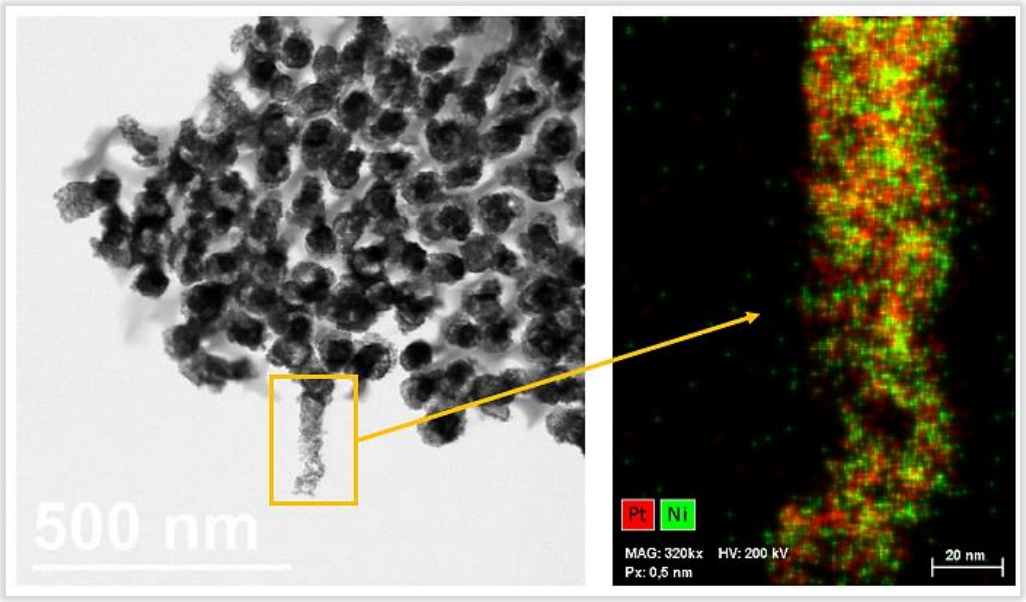

Figure III-81: Representative TEM-coupled EDX analysis of Pt_2NiNWs prepared after exposing NiNWs to a K_2PtCl_4 solution in 0.05 M HCl at 35°C for 8 minutes.

According to the XRD pattern obtained in *figure III-82* below, the analysis presents a shift to higher 2θ values with respect to pure Pt due to the solid solution formation. Shifted peaks positioned at 2θ values of 40.09°, 46.9°, 82.91° and 86.89° are indexed to the (111), (200), (311) and (222) reflections of the face-centered cubic (fcc) crystal lattice of PtNi (compared to pure Pt: peaks positioned at 2θ values of 39.98°, 46.49°, 67.81°, 81.67° and 85.99° are indexed to the (111), (200), (220), (311) and (222) reflections of the face-centered cubic (fcc) crystal lattice). As displayed in the XRD pattern, no characteristic peaks indicating the existence of Ni or NiO crystal structures are apparent. The absence of any sharp peaks confirms the amorphous nature of the PtNiNWs. For this sample, the lattice constant was found to be 3.88 Å, which corresponds to a solid solution alloy of $Pt_{1-x}Ni_x$ with x = 0,14.

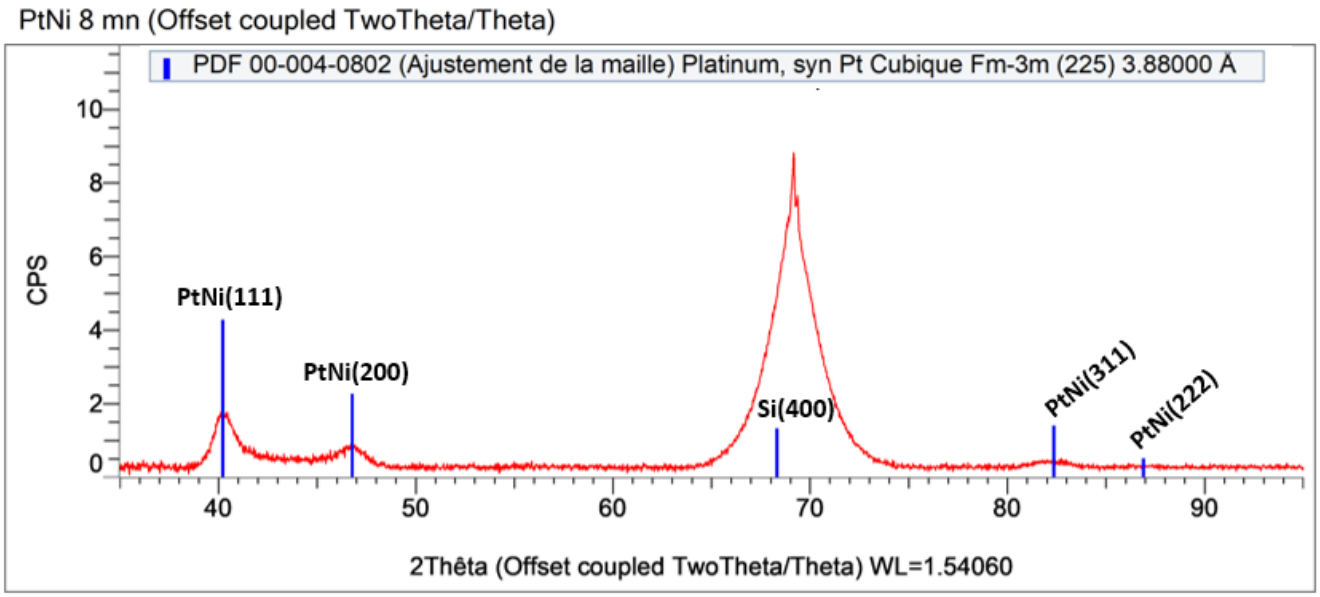

Figure III-82: XRD measurements performed on the as-prepared PtNiNWs supported on p-Si(100) synthetized in a K_2PtCl_4 solution in 0.05 M HCl at 35°C for 8 minutes.

Ultimately, after several trials to finally achieve a reproducible way to elaborating PtNiNWs, we summarize the previous reproducible process as follows:

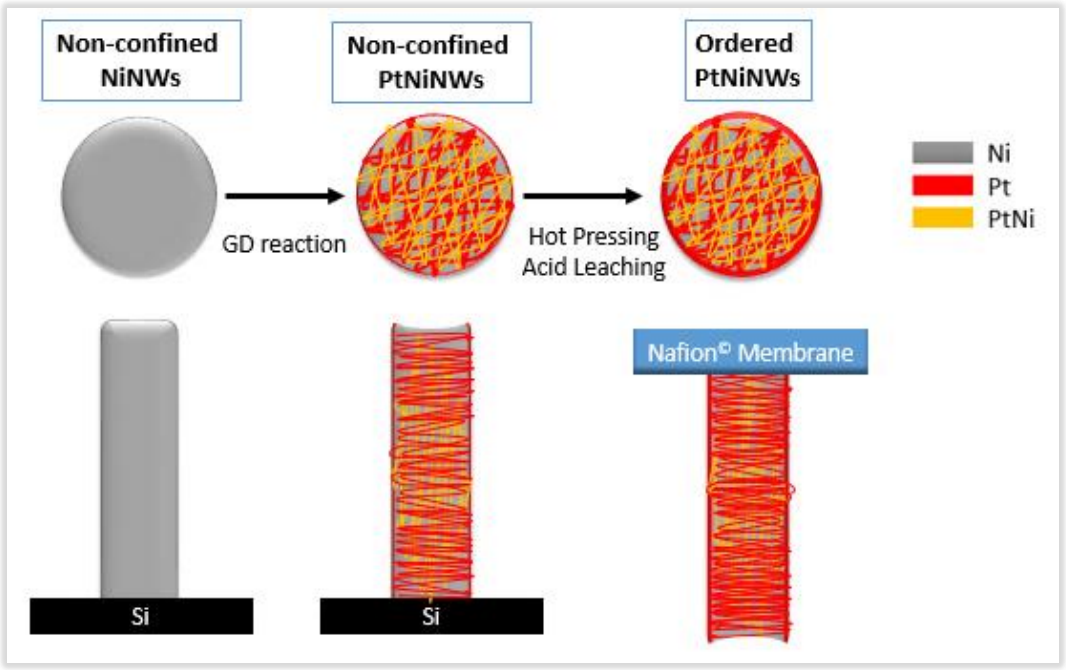

Figure III-83: Schematic illustration of various stages involved in fabricating PtNiNWs through a galvanic displacement process at 35°C in K_2PtCl_4 in 0.05 M HCl for 5-10 minutes.

V. Conclusion

One of the most significant findings to emerge from this study is that we have pursued the synthesis of a novel cathode structure made only of PtNiNWs and PtNiNTs as an electrocatalyst. Nickel nanowires' growth was carried out with the template-assisted technique. The template was then removed to obtain self-standing NiNWs on a silicon substrate. Later on, the non-confined nickel nanowires have been exposed to a Pt solution at different conditions, where Pt ions were reduced by metallic Ni. The acid leaching process emerged as reliable and mandatory to removing excessive bulk Ni, thus avoiding the ionomer membrane's poisoning. The formation of voids inside the NiNWs can be ascribed to the leaching of the Ni-rich core. According to the galvanic displacement process combined with the thermal treatment process and acid leaching, the structures were synthesized and transferred onto the Nafion® membrane.

Taken together, these results suggest the sensibility of the Pt galvanic displacement of nickel to acidic medium and temperature. This study offered insights into tackling the fractured PtNiNWs and the PtNiNTs detachment from the silicon substrate. This more extensive study may offer a base for future studies of PtNi nanostructures fabrication with the combination of the galvanic displacement process, thermal treatment, and acid leaching.

List of figures and tables

References

[1]. M.P. Proenca, C.T. Sousa, J. Ventura, M. Vazquez, J.P. Araujo, Ni growth inside ordered arrays of alumina nanopores: Enhancing the deposition rate, Electrochimica Acta. 72 (2012) 215–221.

[2]. K. Nielsch, F. Müller, A.-P. Li, U. Gösele, Uniform Nickel Deposition into Ordered Alumina Pores by Pulsed Electrodeposition, Advanced Materials. 12 (2000) 582–586.

[3]. Y. Yu, X. Wang, Chapter 9 - Semiconductor Nanowires for Energy Harvesting, in: S.A. Dayeh, A. Fontcuberta i Morral, C. Jagadish (Eds.), Semiconductors and Semimetals, Elsevier, 2016: pp. 297–368.

[4]. C.T. Sousa, D.C. Leitao, M.P. Proenca, J. Ventura, A.M. Pereira, J.P. Araujo, Nanoporous alumina as templates for multifunctional applications, Applied Physics Reviews. 1 (2014) 031102.

[5]. A.J. Yin, J. Li, W. Jian, A.J. Bennett, J.M. Xu, Fabrication of highly ordered metallic nanowire arrays by electrodeposition, Appl. Phys. Lett. 79 (2001) 1039–1041.

[6]. N.J. Gerein, J.A. Haber, Effect of ac Electrodeposition Conditions on the Growth of High Aspect Ratio Copper Nanowires in Porous Aluminum Oxide Templates, J. Phys. Chem. B. 109 (2005) 17372–17385.

[7]. Bernadette NGUYEN, Électrodéposition par courants pulsés, Matériaux | Traitements des métaux, Techniques de l'Ingénieur M1627 V1, 01 February 2016.

[8]. J.M. Baik, M. Schierhorn, M. Moskovits, Fe Nanowires in Nanoporous Alumina: Geometric Effect versus Influence of Pore Walls, J. Phys. Chem. C. 112 (2008) 2252–2255.

[9]. M. Subramanian, N. Dhanikaivelu, R. Rama Prabha, Pulsed electrodeposition of cobalt and nickel alloy, Transactions of the IMF (2007) Vol 85, 5 274–280.

[10]. V. Caboni, Italian Patent 339 232, 1936.

[11]. H. Chik and J.M. Xu, Nanometric superlattices: non-lithographic fabrication, materials, and prospects, Materials Science and Engineering. R 43 (2004) 103–138.

[12]. W. Lee, R. Scholz, K. Nielsch, U. Gösele, A Template-Based Electrochemical Method for the Synthesis of Multisegmented Metallic Nanotubes, Angewandte Chemie International Edition. 44 (2005) 6050–6054.

[13]. T. Borkar, S.P. Harimkar, Effect of electrodeposition conditions and reinforcement content on microstructure and tribological properties of nickel composite coatings, Surface and Coatings Technology. 205 (2011) 4124–4134.

[14]. A.I. Vorobyova, E.A. Outkina, A.A. Khodin, Nickel/alumina nanocomposites by AC electrochemical processing, Appl. Phys. A. 122 (2016) 130.

[15]. C.T. Sousa, D.C. Leitão, M.P. Proença, A. Apolinário, J.G. Correia, J. Ventura, J.P. Araújo, Tunning pore filling of anodic alumina templates by accurate control of the bottom barrier layer thickness, Nanotechnology. 22 (2011) 315602.

[16]. P. Benaben, F. Durut, Electrolytic nickel coating, Techniques de l'Ingénieur M1611 (2003).

[17]. George A. Di Bari, Book: Electrodeposition of nickel, Modern Electroplating, Fifth Edition Edited by Mordechay Schlesinger and Milan Paunovic, (2010) 79–114.

[18]. S. Wen, J.A. Szpunar, Direct electrodeposition of highly ordered magnetic nickel nanowires on silicon wafer, Micro & Nano Letters. 1 (2006) 89–93.

[19]. Marquardt, L. Eude, M. Gowtham, G. Cho, H.J. Jeong, M. Châtelet, C.S. Cojocaru, B.S. Kim, D. Pribat, Density control of electrodeposited Ni nanoparticles/nanowires inside porous anodic alumina templates by an exponential anodization voltage decrease, Nanotechnology. 19 (2008) 405607.

[20]. L.A. Meier, A.E. Alvarez, S.G. García, M.C. del Barrio, Formation of Cu and Ni Nanowires by Electrodeposition, Procedia Materials Science. 8 (2015) 617–622.

[21]. R. Oriňáková, A. Turoňová, D. Kladeková, M. Gálová, R.M. Smith, Recent developments in the electrodeposition of nickel and some nickel-based alloys, J Appl Electrochem. 36 (2006) 957–972.

[22]. K.S. Napolskii, I.V. Roslyakov, A.A. Eliseev, D.I. Petukhov, A.V. Lukashin, S.-F. Chen, C.-P. Liu, G.A. Tsirlina, Tuning the microstructure and functional properties of metal nanowire arrays via deposition potential, Electrochimica Acta. 56 (2011) 2378–2384.

[23]. J. Descarpentries, D. Buttard, L. Dupré, T. Gorisse, Highly conformal deposition of copper nanocylinders uniformly electrodeposited in nanoporous alumina template for ordered catalytic applications, Micro & Nano Letters. 7 (2012) 1241–1245.

[24]. O.T. Holton, J.W. Stevenson, The Role of Platinum in Proton Exchange Membrane Fuel Cells, Platinum Metals Review. 57 (2013) 259–271.

[25]. W. Xia, A. Mahmood, Z. Liang, R. Zou, S. Guo, Earth-Abundant Nanomaterials for Oxygen Reduction, Angewandte Chemie International Edition. 55 (2016) 2650–2676.

[26]. T. Asset, R. Chattot, M. Fontana, B. Mercier-Guyon, N. Job, L. Dubau, F. Maillard, A Review on Recent Developments and Prospects for the Oxygen Reduction Reaction on Hollow Pt-alloy Nanoparticles, ChemPhysChem. 19 (2018) 1552–1567.

[27]. V.R. Stamenkovic, B. Fowler, B.S. Mun, G. Wang, P.N. Ross, C.A. Lucas, N.M. Marković, Improved Oxygen Reduction Activity on Pt3Ni(111) via Increased Surface Site Availability, Science. 315 (2007) 493–497.

[28]. P. Quaino, F. Juarez, E. Santos, W. Schmickler, Volcano plots in hydrogen electrocatalysis – uses and abuses, Beilstein J Nanotechnol. 5 (2014) 846–854.

[29]. B.E. Conway, G. Jerkiewicz, Relation of energies and coverages of underpotential and overpotential deposited H at Pt and other metals to the volcano curve for cathodic H2 evolution kinetics, Electrochimica Acta 45 (2000) 4075–4083.

[30]. P. Stonehart, "Development of Advanced Noble Metal-Alloy Electrocatalysts for Phosphoric Acid Fuel Cells (PAFC)," Berichte Der Bunsengesellschaft Für Physikalische Chemie. 94 (1990) 913–921.

[31]. J.K. Nørskov, J. Rossmeisl, A. Logadottir, L. Lindqvist, J.R. Kitchin, T. Bligaard, H. Jónsson, Origin of the Overpotential for Oxygen Reduction at a Fuel-Cell Cathode, J. Phys. Chem. B. 108 (2004) 17886–17892.

[32]. V. R. Stamenkovic, B. Fowler, B. S. Mun, G. Wang, P. N. Ross, C. A. Lucas, N. M. Markovic, Improved Oxygen Reduction Activity on $Pt_3Ni(111)$ via Increased Surface Site Availability, Science 315 26 (2007) 493–496.

[33]. X.X. Wang, M.T. Swihart, G. Wu, Achievements, challenges and perspectives on cathode catalysts in proton exchange membrane fuel cells for transportation, Nat Catal. 2 (2019) 578–589.

[34]. M. Escudero-Escribano, A. Verdaguer-Casadevall, P. Malacrida, U. Grønbjerg, B.P. Knudsen, A.K. Jepsen, J. Rossmeisl, I.E.L. Stephens, I. Chorkendorff, Pt5Gd as a Highly Active and Stable Catalyst for Oxygen Electroreduction, J. Am. Chem. Soc. 134 (2012) 16476–16479.

[35]. I.E.L. Stephens, A.S. Bondarenko, U. Grønbjerg, J. Rossmeisl, I. Chorkendorff, Understanding the electrocatalysis of oxygen reduction on platinum and its alloys, Energy Environ. Sci. 5 (2012) 6744.

[36]. X. Xia, Y. Wang, A. Ruditskiy, Y. Xia, 25th Anniversary Article: Galvanic Replacement: A Simple and Versatile Route to Hollow Nanostructures with Tunable and Well-Controlled Properties, Advanced Materials. 25 (2013) 6313–6333.

[37]. L. Dubau, T. Asset, R. Chattot, C. Bonnaud, V. Vanpeene, J. Nelayah, F. Maillard, Tuning the Performance and the Stability of Porous Hollow PtNi/C Nanostructures for the Oxygen Reduction Reaction, ACS Catal. 5 (2015) 5333–5341.

[38]. N.K. Chaudhari, J. Joo, B. Kim, B. Ruqia, S.-I. Choi, K. Lee, Recent advances in electrocatalysts toward the oxygen reduction reaction: the case of PtNi octahedra, Nanoscale. 10 (2018) 20073–20088.

[39]. T. Toda, H. Igarashi, M. Watanabe, Role of Electronic Property of Pt and Pt Alloys on Electrocatalytic Reduction of Oxygen, J. Electrochem. Soc. 145 (1998) 4185–4188.

[40]. U.A. Paulus, A. Wokaun, G.G. Scherer, T.J. Schmidt, V. Stamenkovic, V. Radmilovic, N.M. Markovic, P.N. Ross, Oxygen Reduction on Carbon-Supported Pt−Ni and Pt−Co Alloy Catalysts, J. Phys. Chem. B. 106 (2002) 4181–4191.

[41]. J. Zhang, H. Yang, J. Fang, S. Zou, Synthesis and Oxygen Reduction Activity of Shape-Controlled Pt 3 Ni Nanopolyhedra, Nano Lett. 10 (2010) 638–644.

[42]. C. Cui, L. Gan, H.-H. Li, S.-H. Yu, M. Heggen, P. Strasser, Octahedral PtNi Nanoparticle Catalysts: Exceptional Oxygen Reduction Activity by Tuning the Alloy Particle Surface Composition, Nano Lett. 12 (2012) 5885–5889.

[43]. M. Ahmadi, C. Cui, H. Mistry, P. Strasser, B. Roldan Cuenya, Carbon Monoxide-Induced Stability and Atomic Segregation Phenomena in Shape-Selected Octahedral PtNi Nanoparticles, ACS Nano. 9 (2015) 10686–10694.

[44]. M.K. Carpenter, T.E. Moylan, R.S. Kukreja, M.H. Atwan, M.M. Tessema, Solvothermal Synthesis of Platinum Alloy Nanoparticles for Oxygen Reduction Electrocatalysis, J. Am. Chem. Soc. 134 (2012) 8535–8542.

[45]. N.K. Chaudhari, J. Joo, B. Kim, B. Ruqia, S.-I. Choi, K. Lee, Recent advances in electrocatalysts toward the oxygen reduction reaction: the case of PtNi octahedra, Nanoscale. 10 (2018) 20073–20088.

[46]. V. Beermann, M. Gocyla, E. Willinger, S. Rudi, M. Heggen, R.E. Dunin-Borkowski, M.-G. Willinger, P. Strasser, Rh-Doped Pt–Ni Octahedral Nanoparticles: Understanding the Correlation between Elemental Distribution, Oxygen Reduction Reaction, and Shape Stability, Nano Lett. 16 (2016) 1719–1725.

[47]. M. Oezaslan, F. Hasché, P. Strasser, Pt-Based Core–Shell Catalyst Architectures for Oxygen Fuel Cell Electrodes, J. Phys. Chem. Lett. 4 (2013) 3273–3291.

[48]. L. Gan, M. Heggen, S. Rudi, P. Strasser, Core–Shell Compositional Fine Structures of Dealloyed Pt x Ni 1– x Nanoparticles and Their Impact on Oxygen Reduction Catalysis, Nano Lett. 12 (2012) 5423–5430.

[49]. P.Strasser, S.Kühl, Dealloyed Pt-based core-shell oxygen reduction electrocatalysts, Nano Energy 29 (2016) 166–177167.

[50]. C. Wang, M. Chi, D. Li, D. Strmcnik, D. van der Vliet, G. Wang, V. Komanicky, K.-C. Chang, A.P. Paulikas, D. Tripkovic, J. Pearson, K.L. More, N.M. Markovic, V.R. Stamenkovic, Design and Synthesis of Bimetallic Electrocatalyst with Multilayered Pt-Skin Surfaces, J. Am. Chem. Soc. 133 (2011) 14396–14403.

[51]. H.-P. Liang, H.-M. Zhang, J.-S. Hu, Y.-G. Guo, L.-J. Wan, C.-L. Bai, Pt Hollow Nanospheres: Facile Synthesis and Enhanced Electrocatalysts, Angewandte Chemie. 116 (2004) 1566–1569.

[52]. S.J. Bae, S.J. Yoo, Y. Lim, S. Kim, Y. Lim, J. Choi, K.S. Nahm, S.J. Hwang, T.-H. Lim, S.-K. Kim, P. Kim, Facile preparation of carbon-supported PtNi hollow nanoparticles with high electrochemical performance, J. Mater. Chem. 22 (2012) 8820.

[53]. L. Dubau, M. Lopez-Haro, J. Durst, L. Guétaz, P. Bayle-Guillemaud, M. Chatenet, F. Maillard, Beyond conventional electrocatalysts: hollow nanoparticles for improved and sustainable oxygen reduction reaction activity, J. Mater. Chem. A. 2 (2014) 18497–18507.

[54]. T. Asset, R. Chattot, J. Drnec, P. Bordet, N. Job, F. Maillard, L. Dubau, Elucidating the Mechanisms Driving the Aging of Porous Hollow PtNi/C Nanoparticles by Means of CO ads Stripping, ACS Appl. Mater. Interfaces. 9 (2017) 25298–25307.

[55]. R. Chattot, T. Asset, J. Drnec, P. Bordet, J. Nelayah, L. Dubau, F. Maillard, Atomic-Scale Snapshots of the Formation and Growth of Hollow PtNi/C Nanocatalysts, Nano Lett. 17 (2017) 2447–2453.

[56]. L. Dubau, J. Nelayah, S. Moldovan, O. Ersen, P. Bordet, J. Drnec, T. Asset, R. Chattot, F. Maillard, Defects do Catalysis: CO Monolayer Oxidation and Oxygen Reduction Reaction on Hollow PtNi/C Nanoparticles, ACS Catal. 6 (2016) 4673–4684.

[57]. C. Chen, Y. Kang, Z. Huo, Z. Zhu, W. Huang, H.L. Xin, J.D. Snyder, D. Li, J.A. Herron, M. Mavrikakis, M. Chi, K.L. More, Y. Li, N.M. Markovic, G.A. Somorjai, P. Yang, V.R. Stamenkovic, Highly Crystalline Multimetallic Nanoframes with Three-Dimensional Electrocatalytic Surfaces, Science. 343 (2014) 1339–1343.

[58]. V.R. Stamenkovic, N.M. Markovic, V.A.2 Nanosegregated Cathode Alloy Catalysts with Ultra-Low Platinum Loading, FY 2013 Annual Progress Report, DOE Hydrogen and Fuel Cells Program (2015) 7.

[59]. S. Henning, L. Kühn, J. Herranz, J. Durst, T. Binninger, M. Nachtegaal, M. Werheid, W. Liu, M. Adam, S. Kaskel, A. Eychmüller, T.J. Schmidt, Pt-Ni Aerogels as Unsupported Electrocatalysts for the Oxygen Reduction Reaction, J. Electrochem. Soc. 163 (2016) F998–F1003.

[60]. S. Henning, H. Ishikawa, L. Kühn, J. Herranz, E. Müller, A. Eychmüller, T.J. Schmidt, Unsupported Pt-Ni Aerogels with Enhanced High Current Performance and Durability in Fuel Cell Cathodes, Angewandte Chemie International Edition. 56 (2017) 10707–10710.

[61]. M.K. Debe, R.J. Poirier, Postdeposition growth of a uniquely nanostructured organic film by vacuum annealing, Journal of Vacuum Science & Technology A. 12 (1994) 2017–2022.

[62]. M.K. Debe, A.R. Drube, Structural characteristics of a uniquely nanostructured organic thin film, Journal of Vacuum Science & Technology B: Microelectronics and Nanometer Structures Processing, Measurement, and Phenomena. 13 (1995) 1236–1241.

[63]. M.K. Debe, A.J. Steinbach, G.D. Vernstrom, S.M. Hendricks, M.J. Kurkowski, R.T. Atanasoski, P. Kadera, D.A. Stevens, R.J. Sanderson, E. Marvel, J.R. Dahn, Extraordinary Oxygen Reduction Activity of Pt3Ni7, J. Electrochem. Soc. 158 (2011) B910.

[64]. M.K. Debe, R.T. Atanasoski, A.J. Steinbach, Nanostructured Thin Film Electrocatalysts - Current Status and Future Potential, ECS Trans. 41 (2019) 937–954.

[65]. M.K. Debe, Nanostructured Thin Film Electrocatalysts for PEM Fuel Cells - A Tutorial on the Fundamental Characteristics and Practical Properties of NSTF Catalysts, ECS Transactions. 45 (2012) 47–68.

[66]. D. van der Vliet, C. Wanga, M.K. Debe, R. Atanasoski, N.M. Markovic, V.R. Stamenkovic, Platinum-alloy nanostructured thin film catalysts for the oxygen reduction reaction, Electrochimica Acta 56 (2011) 8695–8699.

[67]. S.Z. Chu, S. Inoue, K. Wada, K. Kurashima, Fabrication of integrated arrays of ultrahigh density magnetic nanowires on glass by anodization and electrodeposition, Electrochimica Acta 51 (2005) 820–826.

[68]. J.-L. Shui, J.-W. Zhang, J.C.M. Li, Making Pt-shell Pt30Ni70 nanowires by mild dealloying and heat treatments with little Ni loss, J. Mater. Chem. 21 (2011) 6225.

[69]. S.M. Alia, B.A. Larsen, S. Pylypenko, D.A. Cullen, D.R. Diercks, K.C. Neyerlin, S.S. Kocha, B.S. Pivovar, Platinum-Coated Nickel Nanowires as Oxygen-Reducing Electrocatalysts, ACS Catal. 4 (2014) 1114–1119.

[70]. S.M. Alia, S. Pylypenko, K.C. Neyerlin, S.S. Kocha, B.S. Pivovar, Platinum Nickel Nanowires as Methanol Oxidation Electrocatalysts, J. Electrochem. Soc. 162 (2015) F1299–F1304.

[71]. S.M. Alia, S. Pylypenko, A. Dameron, K.C. Neyerlin, S.S. Kocha, B.S. Pivovar, Oxidation of Platinum Nickel Nanowires to Improve Durability of Oxygen-Reducing Electrocatalysts, J. Electrochem. Soc. 163 (2016) F296–F301.

[72]. S.M. Alia, C. Ngo, S. Shulda, M.-A. Ha, A.A. Dameron, J.N. Weker, K.C. Neyerlin, S.S. Kocha, S. Pylypenko, B.S. Pivovar, Exceptional Oxygen Reduction Reaction Activity and Durability of Platinum–Nickel Nanowires through Synthesis and Post-Treatment Optimization, ACS Omega. 2 (2017) 1408–1418.

[73]. S.A. Mauger, K.C. Neyerlin, S.M. Alia, C. Ngo, S.K. Babu, K.E. Hurst, S. Pylypenko, S. Litster, B.S. Pivovar, Fuel Cell Performance Implications of Membrane Electrode Assembly Fabrication with Platinum-Nickel Nanowire Catalysts, J. Electrochem. Soc. 165 (2018) F238–F245.

[74]. S. Shulda, J.N. Weker, C. Ngo, S.M. Alia, S.A. Mauger, K.C. Neyerlin, B.S. Pivovar, S. Pylypenko, 2D and 3D Characterization of PtNi Nanowire Electrode Composition and Structure, ACS Appl. Nano Mater. 2 (2019) 525–534.

[75]. C. Fan, G. Wang, L. Zou, J. Fang, Z. Zou, H. Yang, Composition- and shape-controlled synthesis of the PtNi alloy nanotubes with enhanced activity and durability toward oxygen reduction reaction, Journal of Power Sources 429 (2019) 1–8.

[76]. T.-W. Chen, J.-X. Kang, D.-F. Zhang, L. Guo, Ultralong PtNi alloy nanowires enabled by the coordination effect with superior ORR durability, RSC Adv. 6 (2016) 71501–71506.

[77]. F. Chang, G. Yu, S. Shan, Z. Skeete, J. Wu, J. Luo, Y. Ren, V. Petkov, C.-J. Zhong, Platinum–nickel nanowire catalysts with composition-tunable alloying and faceting for the oxygen reduction reaction, J. Mater. Chem. A. 5 (2017) 12557–12568.

[78]. J.-L. Shui, J.-W. Zhang, J.C.M. Li, Making Pt-shell Pt30Ni70 nanowires by mild dealloying and heat treatments with little Ni loss, J. Mater. Chem. 21 (2011) 6225.

[79]. O. Marconot, N. Pauc, D. Buttard, A. Morin, Vertically Aligned Platinum Copper Nanotubes as PEM Fuel Cell Cathode: Elaboration and Fuel Cell Test, Fuel Cells. 18 (2018) 723–730.

[80]. M. Komath, Hot corrosion of nickel in anhydrous sodium hydroxide, Materials Chemistry and Physics 45 (1996) 171-175.

[81]. N. Yarykin, J. Weber, Nickel in silicon: Room-temperature in-diffusion and interaction with radiation defects, Physica Status Solidi c. 14 (2017) 1700005.

Chapter 4

Membrane Electrode Assembly – Fuel Cell tests of Pt/C, PtNiNWs, and PtNiNTs electrodes (Performance and durability tests)

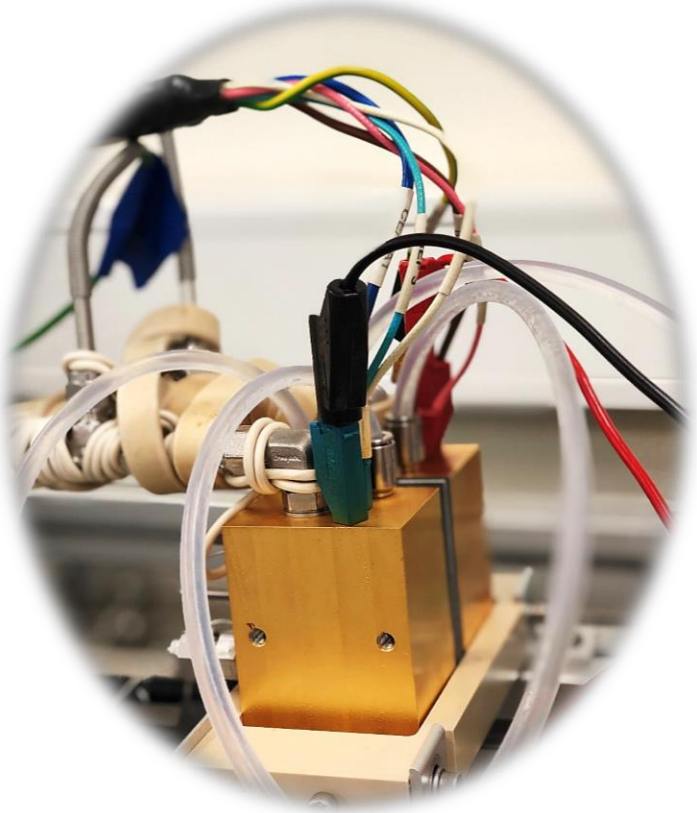

"My brain is only a receiver; in the Universe, there is a core from which we obtain knowledge, strength, and inspiration."

-Nikola Tesla

Table of Content

This chapter will depict a relevant experimental protocol for MEAs' characterization made of conventional Pt/C catalyst at low Pt loading, PtNiNWs, and PtNiNTs as cathodes. Studies have been completed and intended to quantify the performance compared with standard Pt/C electrodes and quantify the activity and transport limitations in different operating conditions, especially in dry or wet conditions. The robustness towards the accelerated stress test has also been evaluated.

Furthermore, it is worth mentioning that to overcome the disparity between MEA and RDE performance characterizations, we did not cover RDE tests in this thesis for two reasons: **i/** It was difficult, if not impossible, to transfer the PtNi oriented nanostructure into an RDE apparatus to perform electrochemical measurements. This would have required fabricating the nanostructure onto a glassy carbon electrode or developing a new transfer method that might need a lot of effort. This could be done once a relevant nanostructure is obtained for further understanding; **ii/** we wanted to determine the performance in real conditions because RDE measurements are not very representative, then to compare the various electrodes.

I. Fundamental Fuel Cell Test on Pt/C conventional electrodes: Performance, Activity, and Degradation

In this section, we will display the fabrication process of a standard Pt/C electrode in order to compare the performance and activity under real PEMFC conditions. We targeted to fabricate a low Pt-loading cathode exhibiting substantially the same ECSA as the cathodes made of PtNiNWs and PtNiNTs using the same Nafion® membrane.

I.1 Low Pt-loading Pt/C electrode fabrication

I.1.1 Ink preparation

The MEA used in this work was fabricated in-house. The cathode-type Pt/C catalytic ink was prepared by mixing: 0.7 g of catalyst powder TEC10V50E (47.2 w%Pt Tanaka® Pt NPs (~3 nm) deposited onto carbon support Vulcan XC72 (~40-50 nm)), 4.5 g of Nafion® solution D520, 20 mL of Propanol as a solvent and 20 mL Ultrapure water 18.2 MΩ.cm.

The ink preparation was held in a glovebox because of safety issues related to the handling of nanopowders. The weight ratio between ionomer and carbon is 67%. After the dispersion, the ink was stirred for 72 hours with a magnetic stirrer.

Before depositing the ink onto a PTFE (250 µm) substrate, the ink was premixed in a sonicator bath beforehand for 10 minutes at room temperature to improve its homogeneity. Using the ultrasonic coating process provided by Sono-Tek© (*figure IV-1*), the ink was sprayed onto the PTFE substrate.

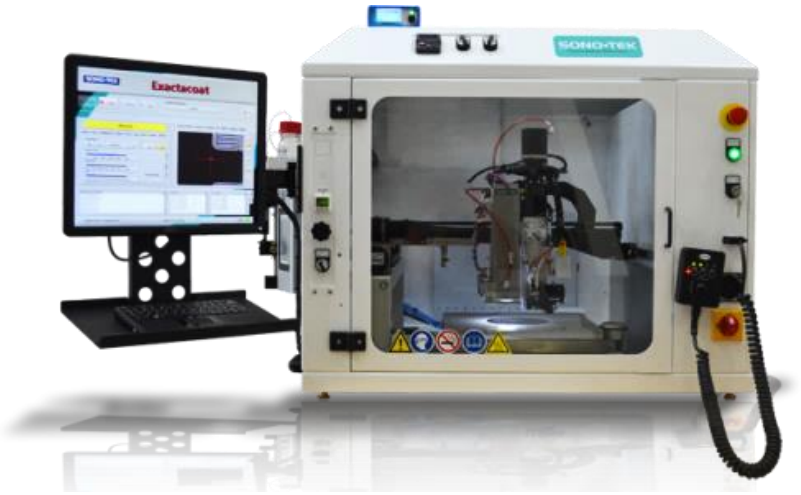

Figure IV-1: Sono-tek® benchtop coating system with coordinated XYZ motion control using Windows-based software and user-friendly teach pendant with a trackball.

I.1.2 Catalyst loading measurement

We quantified the Pt loading by two methods: UV–Visible Spectroscopy and X-ray Fluorescence spectroscopy (XRFS). Both techniques demonstrated a final loading of about 35-40 $\mu g_{Pt}/cm^2$.

I.1.3 Hot-pressing transfer and MEA preparation

The Pt/C electrode was fabricated by the decal-transfer method on the Nafion® membrane by hot-pressing, where the Nafion® membrane was put over the PTFE inside two plates. The process was performed at 150°C and 2 MPa for 10 minutes.

The overall system is composed, as evidenced in the *figure IV-2* below, of the following components: **i/** Gas Diffusion Layer (GDL) 24BC (235 µm), **ii/** PTFE (150 µm) and PEN (25 µm) wedges as mechanical reinforcements and to ensure a good gas sealing, placed

between the monopolar plates and the MEA, leaving only the active area to exposed to gases. Also, the wedges require a *ca.* 25% compression to the GDL, **iii/** in-house made Gas Diffusion Electrode (GDE) as an anode (Pt/C TKK 50 %wt on Vulcan carbon NPs, 0.1 mg/cm² on GDL Sigracet 24BC from SGL).

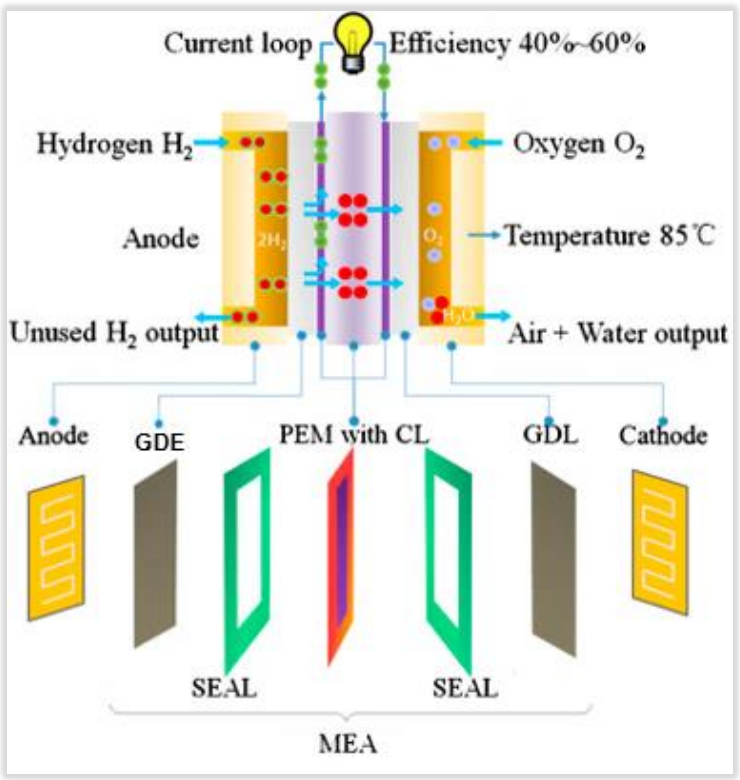

Figure IV-2: Schematic illustration of the main components of a polymer electrolyte membrane fuel cell (PEMFC).

A cross-sectional view of the MEA used in this work is given in *figure IV-3* below:

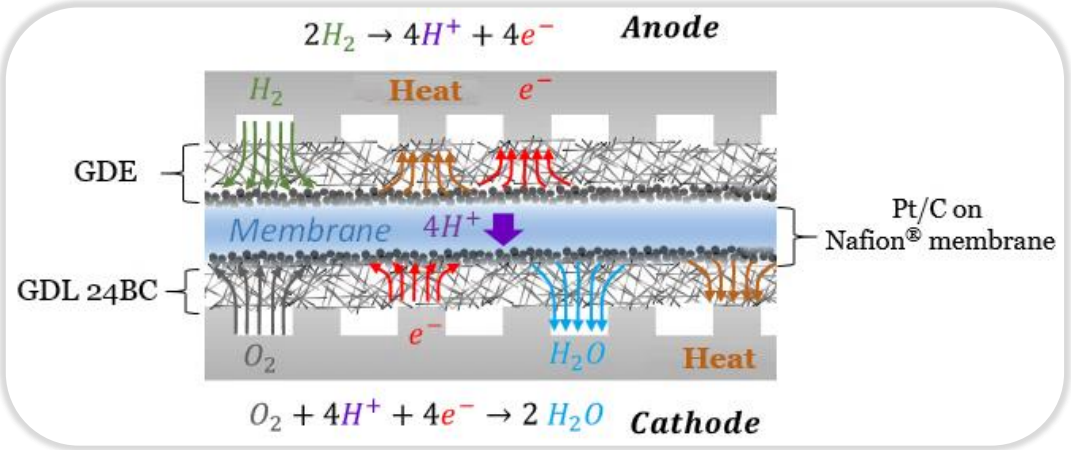

Figure IV-3: A cross-sectional schematic illustration of the mono-cell assembly used in a differential cell test.

The fabricated MEA was then placed in a differential fuel cell allowing its study under homogeneous and well-defined conditions of relative humidity (RH), cell temperature, and gas flow, as pinpointed in the image below:

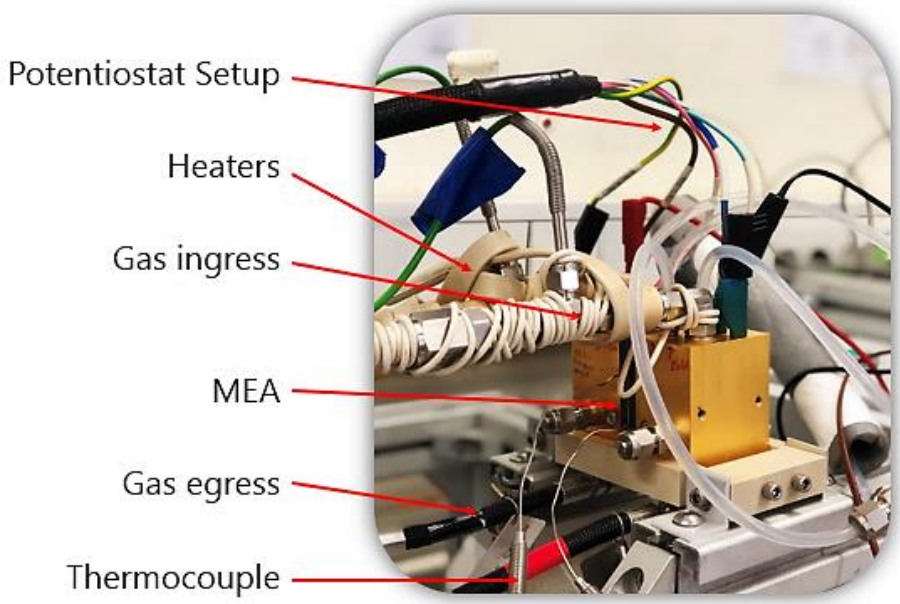

Figure IV-4: Experimental setup of an operating home-made differential fuel cell.

Reduced dimensions and high stoichiometric ratios characterize this type of cell. A differential cell's purpose is not to be operated as a technical device but to emulate the local conditions of a larger device and study the effect of different operating parameters at a local scale without the disturbance of along the channel effects [1]. Graphite flow fields with multi-straight and parallel channels are used on both the anode and the cathode side. The geometry of the cell used in this work is defined as follow:

Active Surface	1.2 x 1.5 = 1.8 cm²
Multiple parallel straight Channels	1.2 cm long
Channel Width	250 µm
Channel Depth	400 µm
Rib Width	250 µm

Table IV-1: Geometry of the differential cell used in this work.

The cell was mounted in an in-house test stand. The latter allows a precise control of the conditions protocol during operation, as summarized below:

	Experimental values	
Operating conditions	**Anode**	**Cathode**
Relative Humidity (%HR)	50% – 100% HR	50% – 100% HR
Cell Temperature	40 – 80 °C	
Absolute Pressure (P_{tot})	1 – 3 bar	
Gas	H_2 N_2 – Inert gas	O_2 or Air N_2 – Inert gas
Gas flow rates	10-35 NL/h	10-35 NL/h

Table IV-2: Operating conditions offered by the in-house test stand for testing differential cells.

The cell could be heated via a hot water flow through a water circulation network. During the test, the active gases used are Air or Oxygen at the cathode and Hydrogen at the anode. To dry the cell's components, a purge under N_2 gas flow is required to getting rid of active gases.

The test stand allows the possibility of reproducing local conditions of a real fuel cell and providing precise control of operating conditions as mentioned in *table IV-2* above. The partial pressures of reactants (*i.e.,* active gases) are not fully homogeneous. We try to make it as homogeneous as possible from the gas inlet to the outlet, hence the high stoichiometry.

Relative humidity (φ) is defined as the ratio of the partial pressure of water vapor at a specified temperature to the equilibrium vapor pressure of water at the same temperature.

$$\boldsymbol{\varphi = \frac{P_{vap}(H_2O)(T)}{P_{sat}(H_2O)(T)}}$$

Equation IV-1

I.2 Pt/C Cathode: Electrochemical characterization in operating conditions

Prior to testing, the MEA was pre-conditioned (break-in step) via voltage cycling using a lab-developed protocol. The MEA conditioning was carried out in H_2/O_2 at 1.5 bar and relative humidity of 100% (fully humidified gases) at 80°C for several hours to reach the maximum performance of the cell.

I.2.1 Electrochemical surface area measurement

The ECSA measurement aims to determine the specific active surface area, which refers to the catalyst's surface in contact with the electrolyte and accessible to protons from the membrane and electrically connected to the carbon support. Cyclic voltammograms (CVs) were measured after the break-in process at 40°C and 80°C at 100% RH under a pressure of 1 bar. Since the available ECSA might be small due to the Pt low-loading, we have recorded the CVs at a scan rate of 200 mV/s to be able to measure it: Varying the working electrode's potential between 0.1 to 1.2 V_{RHE}, assuming that the counter-electrode potential is fixed at 0 V.

The experiment was carried out with a *Biologic©* potentiostat monitored by the *EC-Lab* program, with a fully humidified flow of H_2 and N_2 at the anode and the cathode, respectively. The current is measured and recorded during the scan. After that, the active electrochemical surface area (ECSA) was averaged from the hydrogen underpotential deposition (H_{UPD}) region of cyclic voltammograms (the H-adsorption and H-desorption charges between 0.1 and 0.4 V_{RHE}). The shape of the curve obtained is comparable to those found in literature, as illustrated in *figure IV-5* below.

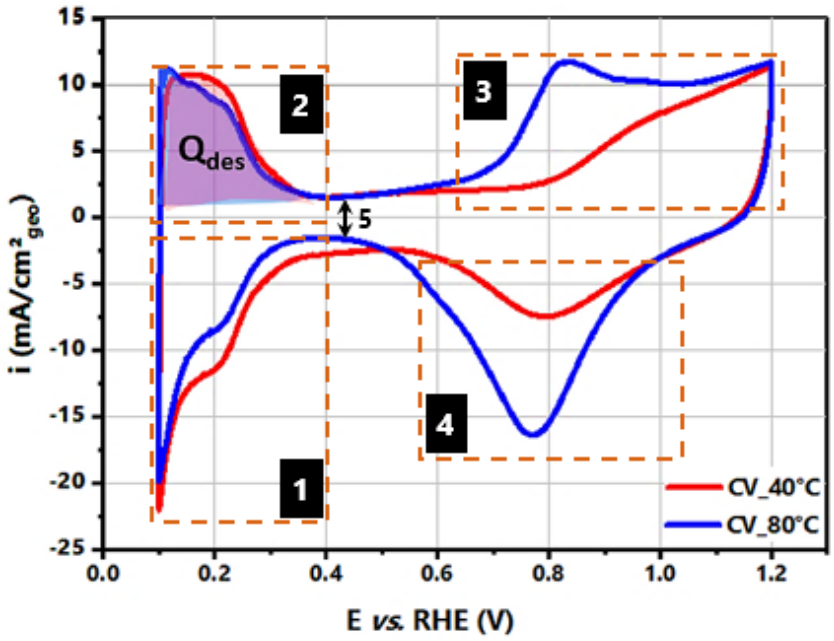

Figure IV-5: Cyclic voltammogram in fully humidified H_2/N_2 of the Pt/C electrode with low Pt-loading at the cathode (35 $\mu g_{Pt}/cm^2$). Data were recorded at a scan speed of 200 mV/s, 40°C (red curve), and 80°C (blue curve) with a 1 bar total pressure. The blue and red areas (in the 0.1 – 0.4 V_{RHE} potential range) correspond to hydrogen desorption.

The voltammogram illustrated above depicts various regions and are associated with:

- Region 1 (from 0.4 V to 0.1 V): Refers to the H^+ adsorption (reduction);

$$\mathbf{Pt + H^+ + e^- \rightarrow Pt - H} \qquad \text{Reaction IV-1}$$

- Region 2 (from 0.1 V to 0.4 V): Identifies the H^+ desorption (oxidation). Once the potential is increased, the hydrogen atoms are then desorbed;

$$\mathbf{Pt - H \rightarrow Pt + H^+ + e^-} \qquad \text{Reaction IV-2}$$

- Region 3 (from 0.6 V to 1.2 V): Pt oxidation (Pt oxidation and formation of Pt oxides);

$$\mathbf{Pt + H_2O \rightarrow Pt - OH + H^+ + e^-} \qquad \text{Reaction IV-3}$$

$$\mathbf{Pt - OH \rightarrow Pt - O + H^+ + e^-} \qquad \text{Reaction IV-4}$$

- Region 4 (from 1.2 V to 0.5 V): Pt oxides reduction

$$\mathbf{Pt - O + H^+ + e^- \rightarrow Pt - OH} \qquad \text{Reaction IV-5}$$
$$\mathbf{Pt - OH + H^+ + e^- \rightarrow Pt + H_2O}$$

- Region 5 (between 0.4 V and 0.5 V): Corresponds to the electrochemical double-layer capacitance current where no faradic reactions occur.

The formation and reduction of Pt oxides (*region 4 from figure IV-5, reaction IV-*5) are presented figuratively by the reaction, including PtO. However, different oxide species such as PtOH or PtO_2 are present depending on the upper potential sweep limit and catalyst material [2]. Hydrogen is adsorbed on the Pt surface after reducing the proton at a lower potential (from 0.4 to 0.1 V). Once the potential is increased, the hydrogen atoms are then desorbed.

Subsequently, by measuring the coulometry of the desorption of hydrogen, we can estimate the number of hydrogen atoms that were adsorbed, which is proportional to the number of adsorption sites on the electrode's surface.

Thus, the ECSA is measured by integrating the blue area displayed in figure IV-5. Experimentally, it is determined by integrating the hydrogen adsorption/desorption areas (Q_{des}) of the cyclic voltammogram (assuming that 0.210 mC/cm^2_{Pt} after double-layer correction is the electrical charge related to one monolayer adsorption of Hydrogen on a Pt(111) surface) [3][4]. The expression of Q_{des} (in Coulombs) could be calculated with *EC-lab®* software, and it is defined as:

$$\mathbf{Q_{des}} = \int_{t_2}^{t_2} \mathbf{I}.\,\mathbf{dt} = \frac{1}{v}\int_{E_1}^{E_2} \mathbf{I}.\,\mathbf{dE} \qquad \text{Equation IV-2}$$

where: v refers to the rate scan in mV/s.

In our experiment performed on the low Pt-loading Pt/C electrode, the value of Q_{des} reads ~4,2 mC. According to the following expression (*equation IV-3*), we could determine the value of the ECSA (reported in terms of cm^2_{Pt}/cm^2_{geo}):

$$\mathbf{ECSA} = \frac{\mathbf{Q_{des}}}{\mathbf{0.21 \times S_{electrode}}} \qquad \text{Equation IV-3}$$

where: -$S_{electrode}$ refers to the geometric surface area of the electrode in cm^2_{geo};

-ECSA: the electrochemical surface area in cm^2_{Pt}/cm^2_{geo};

-Q_{des}: charge obtained by integrating the dashed blue area in mC;

I.2.2 Study of the polarization curve and impedance measurements

Generally, both electrical work and heat are generated during fuel cell operation. Thermodynamically, we refer to the total reaction heat by the change in enthalpy ΔH, while the overall electrical energy output is proportional to ΔG (change in Gibbs' free energy: the maximum electrical work that the fuel cell can generate). To determine the free energy variation, we subtract the amount of energy lost to entropy (ΔS) from the total energy change of the system (ΔH) as described in *equation IV-4* below, assuming that the only product at a given temperature is liquid water [3]:

$$\mathbf{\Delta G(T,P) = \Delta H(T,P) - T.\Delta S(T,P)} \quad \text{Equation IV-4}$$

At standard conditions, the values of enthalpy, entropy, and the free energy read:

$$\mathbf{\Delta G^{R^\circ}_{H_2O}(298\ K) = -237.2\ kJ/mol} \quad \text{Equation IV-5}$$

$$\mathbf{\Delta S^{R^\circ}_{H_2O} = -163\ J/(mol \cdot K)} \quad \text{Equation IV-6}$$

$$\mathbf{\Delta H^{R^\circ}_{H_2O} = -285.8\ kJ/mol} \quad \text{Equation IV-7}$$

At the thermodynamic equilibrium where only liquid water is produced at the standard conditions, the reversible potential can be defined as follows:

$$\mathbf{E_{rev}(T) = -\frac{\Delta G^{R}_{H_2O}(T)}{n_e - \times F}} \quad \text{Equation IV-8}$$

Theoretical Thermodynamic Electrode Potential:

The overall electrochemical reaction between H_2 and O_2 can be written as follows:

$$\mathbf{H_2 + \frac{1}{2}\,O_2 \leftrightarrow H_2O} \quad \text{Reaction IV-6}$$

Assuming that this reaction is in equilibrium, the thermodynamic potential at the OCV could be obtained by the Nernst equation below, taking into account that the value $\mathbf{E^\circ_{O_2/H_2O} - E^\circ_{H_2/H^+}}$ reads 1,229 V_{RHE} under standard conditions (1 atm and 298 K):

$$\mathbf{E_{eq} = (E_{O_2/H_2O} - E_{H_2/H^+}) + 2,303.\frac{RT}{2F}.\log\left(\frac{a_{H_2}\cdot\sqrt{a_{O_2}}}{a_{H_2O}}\right)} \quad \text{Equation IV-9}$$

Where T is the working temperature in Kelvin; R is the universal gas constant that reads 8.314 J/K.mol; F is Faraday's constant (96487 C/mol); and $\mathbf{a_{H_2O}}$, $\mathbf{a_{O_2}}$ and $\mathbf{a_{H_2}}$ refer to the

partial pressures $\frac{P_{H_2O}}{P^\circ}$, $\frac{P_{O_2}}{P^\circ}$, and $\frac{P_{H_2}}{P^\circ}$, respectively (P° is the standard pressure). Note that the calculated fuel cell OCV is not the real OCV in a practical fuel cell and usually is lower than the theoretically expected value due to the catalyst mixed potential and hydrogen crossover [3].

Under operation, the observed cell voltage of a PEMFC cell with the contribution of the various voltage losses may be described as follows:

$$E_{cell} = E_{eq} + \eta_{ORR} - \eta_{HOR} - \eta_{Ohm} \quad \text{Equation IV-10}$$

Where:

- E_{eq} is the thermodynamic equilibrium potential as a function of temperature and gas partial pressure;
- η_{Ohm} refers to the ohmic losses, equals to $R_{Ohm}.i$ (where i is the applied current; R_{Ohm} is the relative humidity dependent cell resistance (the sum of the RH-dependent membrane proton resistance ($R_{membrane}$), and the RH-independent contact and bulk electronic resistances (R_{e-});
- η_{HOR} and η_{ORR} are the anode and cathode kinetic overpotentials;

Moreover, it is difficult to define the equilibrium voltage due to the contribution of various activities of products and reagents on the catalyst's surface [4].

Theoretical Thermodynamic Electrode Potential:

The overpotentials due to the electrochemical reactions' kinetics can be expressed, for each half-reaction (HOR and ORR), by the Butler-Volmer's law, which implies simplifying hypotheses:

$$j = j_a + j_c = j_0\left(-e^{\frac{-\alpha_c nF\eta}{RT}} + e^{\frac{\alpha_a nF\eta}{RT}}\right) \quad \text{Equation IV-11}$$

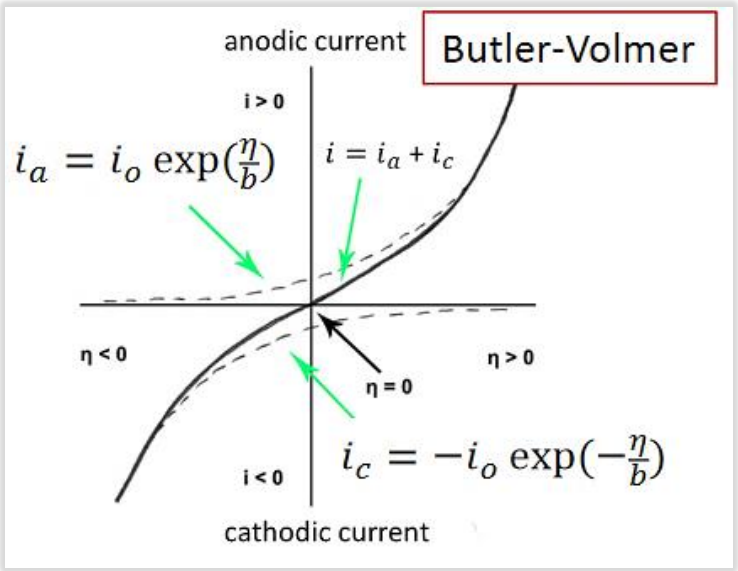

Figure IV-6: Butler-Volmer plot: the current density as a function of the overpotential η. The anodic and cathodic current densities are shown as i_a and i_c, respectively.

This law is only valid in the case where the kinetically limiting step is the charge transfer step to an electron. In most cases, charge transfer coefficients (which can hardly be obtained experimentally) are considered to satisfy the relation: $\boldsymbol{\alpha_c = 1 - \alpha_a}$. For relatively high overpotentials, one of the two terms from the Butler-Volmer equation can be neglected. For instance, higher reduction overpotential is satisfied when $\boldsymbol{\eta \ll -\frac{RT}{nF}}$, the Butler-Volmer equation reads:

$$\mathbf{j = -j_0 \left(e^{\frac{-\alpha_c nF\,\eta}{RT}} \right)} \qquad \text{Equation IV-12}$$

From the Butler-Volmer simple equation (*i.e.,* limiting case of the Butler-Volmer equation), we can extract the Tafel curve; *i.e.,* the logarithm of the current density as a function of the overpotential ($\eta = \log_{10}(j)$), can be plotted after correcting the various transport losses, and reads:

$$\boldsymbol{\eta = \frac{RT}{nF\alpha_c} \ln\left(\left| \frac{j}{j_0} \right| \right)} \quad \text{or:} \quad \boldsymbol{\ln(|j|) = \frac{\alpha_c nF}{RT} \cdot \eta + \ln(j_0)} \qquad \text{Equation IV-13}$$

We can thus extract the Tafel slope that provides insights about the charge transfer kinetic process and the reaction mechanism, and it is defined as follows:

$$\mathbf{b = \frac{2{,}303 * R * T}{\alpha * F}} \qquad \text{Equation IV-14}$$

By linear regression, it is possible to obtain the current exchange j° for η=0.

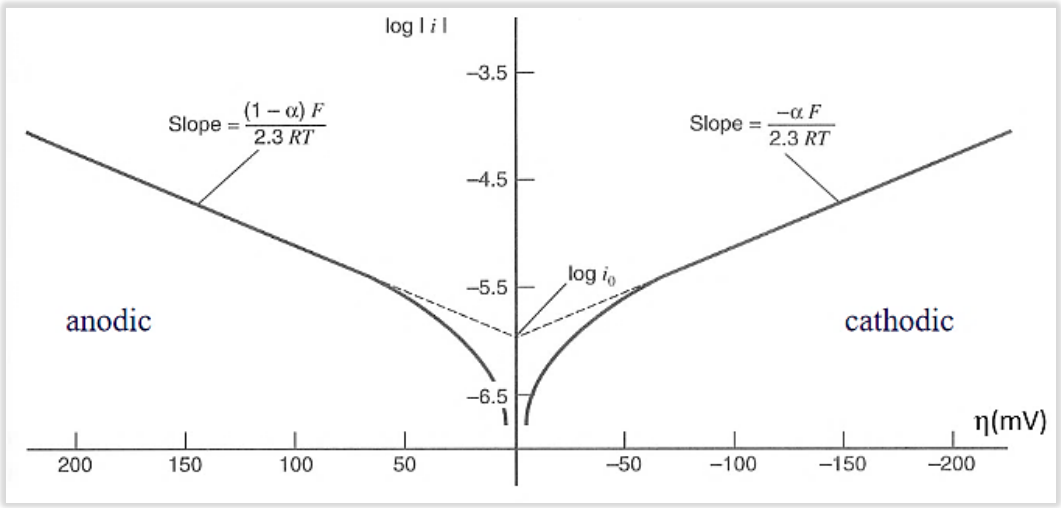

Figure IV-7: Schematic graph showing the logarithm of the current density as a function of the overpotential: Tafel plot.

Previous studies have reported that it is necessary to determine the kinetically limiting intermediate reaction in order to define the exchange coefficient **α**. It has been demonstrated that the slope value usually varies between 60 mV/decade and 20 mV/decade depending on Pt facet crystallinity and working conditions [5][6].

MEA Performance: Polarization curve in H_2/O_2

Firstly, we performed a break-in protocol to the MEA in order to achieve optimum performance.

In this work, we have tested the fuel cell's performance under wet H_2/O_2 gas flow at different relative humidity values (100% RH, 80% RH, 80-100% RH, and 100-80% RH), different total pressure (from 1.26 bar to 1.5 bar), and a cell temperature of 80°C. The performance is better at fully humified conditions because the ionomer's conductivity in both the membrane and the electrode increases with RH. In the membrane, it decreases the ohmic resistance, while in the electrode it improves protons' accessibility to the catalytic sites, which leads to better utilization of platinum.

On the other hand, the performance of the MEA significantly improved after conditioning, as we can clearly see in *figure IV-8*. Some researchers have attributed this increase in performance to changes in the MEA microstructures [7]. From our viewpoint, this increase

might be related to the ionomer swelling and reorganization, removal of pollutants, reorganization of the catalytic sites, or to the reorientation of active facets of Pt. It is worth noting that at 0.65 V, the current density improved after the break-in and ohmic loss correction from 0,35 A/cm^2_{geo} to 0.62 A/cm^2_{geo}. The OCV value reads in this case: $\mathbf{E_{OCV} = 0,928\ V}$.

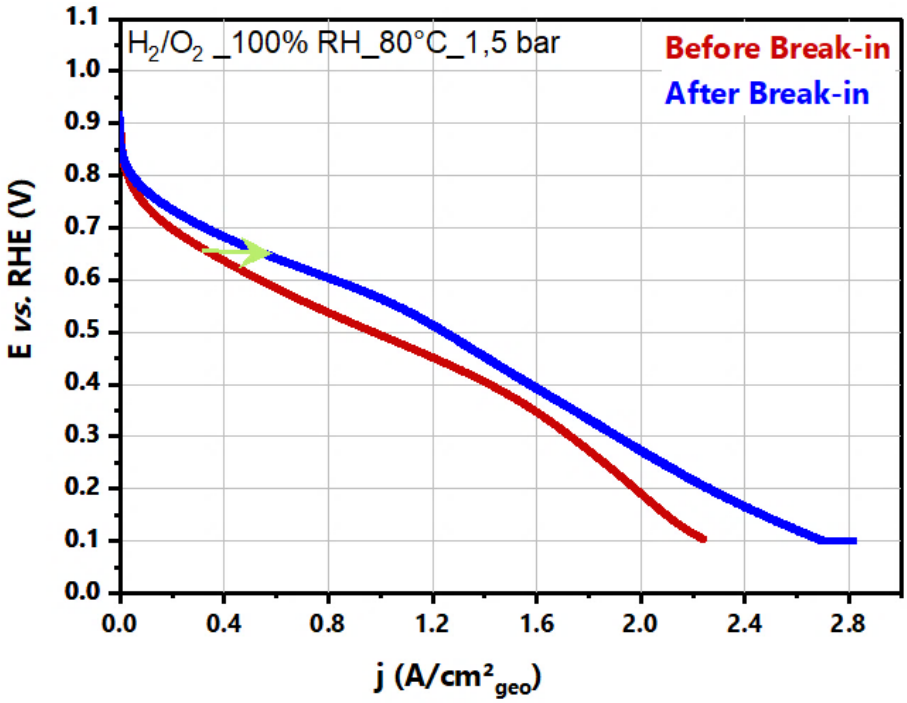

Figure IV-8: Measured polarization curve as a function of geometrical current density at T_{cell}=80°C, 100% RH (dew points), wet H_2/O_2 gas flow, and a total pressure 1.5 bar. Red-curve: original un-corrected polarization curve, Blue-curve: polarization curve after the break-in, The homemade catalyst layer is made of Pt/Carbon (0.1 mg_{Pt}/cm^2 - 0.035 mg_{Pt}/cm^2 at the anode and the cathode, respectively.

Electrochemical Impedance Spectroscopy

This technique provides information about the overall ohmic resistance of the system when the latter is in equilibrium at a steady-state condition (*i.e.*, fixed potential). At 0.4 V under H_2/N_2 gas flow, where no faradic reaction is taking place, we apply a sinusoidal frequency perturbation ω to the current. We could then measure the potential response and vice-versa. The system functioning is assumed to be quasi-stationary (system invariant during the measurement time).

Considering the different kinetics in the fuel cell, EIS measurements are recorded on a wide range of frequencies (see *table IV-3* below). Slow mechanisms are associated with

low frequencies and fast mechanisms with high frequencies. This allows you to dissociate the mechanisms that have different time constants.

Electrochemical phenomena	Frequency response
H^+/e^- transports in membrane/GDL	10 kHz - 1 MHz
Proton transport in the CL	1 – 10 kHz
Charge transfer	100 Hz – 1 kHz
O_2 transfer	It varies from ~few 100 Hz to 10 MHz, depending on the desired region of the FC

Table IV-3: Frequency response of different electrochemical phenomena associated with the EIS measurements.

In our work, we aimed to characterize the ohmic resistance of the cell and the effective proton resistance of the CL. PEIS was held from 200 kHz to 100 Hz at 0.4 V, where no adsorption/desorption reactions are observed in this region, as confirmed by the absence of redox peaks in the CV. We performed measurements in a potentiostatic mode, where a perturbation around a fixed value of voltage (10 mV) is applied. Simultaneously, its current response is measured (the amplitude of the applied signal should be small to be in the linear regime).

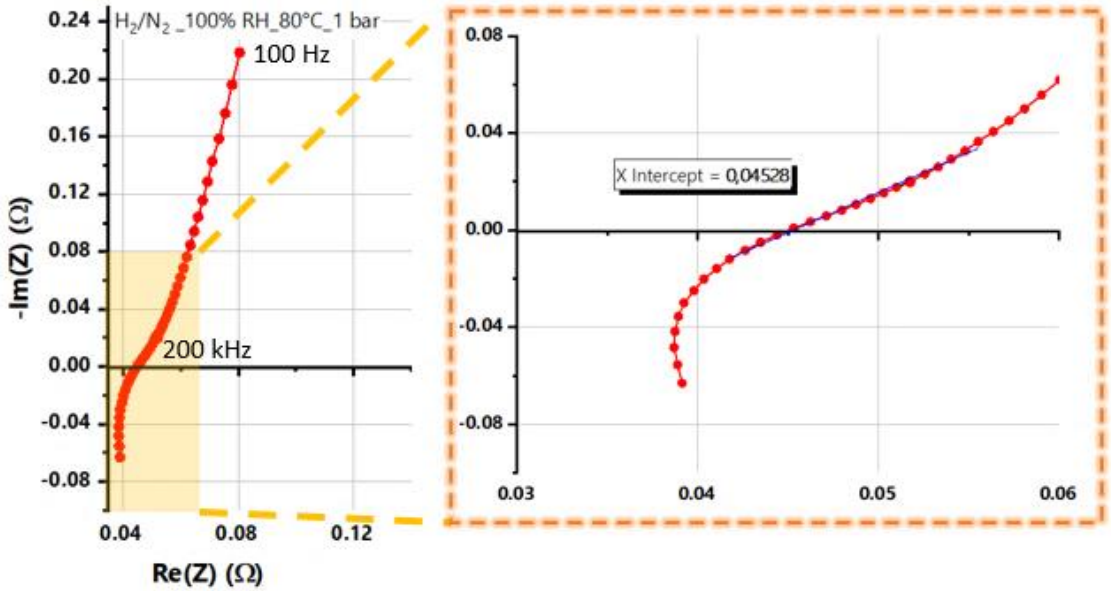

Figure IV-9: Experimental results of the performed EIS at 0.4 V in fully humidified H_2/N_2 at 40°C, recorded from 200 kHz to 100 Hz. The intersection of the curve with the abscissa axis refers to the overall ohmic resistance. The frequency corresponding to the intersection of the plot at the x-axis is 15 kHz.

Considering the few PEIS experiments carried out in this work and the very thin CL used in the cathode, we could not dissociate the losses coming from transport issues. Thus, we will settle for the high-frequency resistance (the value of impedance for which the imaginary part is equal to zero at high frequency) to correcting the polarization curves, denoted R_{ohmic}. We report an overall ohmic resistance R_{ohmic} that reads a value of ~0.046 Ω (taking into account the geometrical surface area of the electrode (1.8 cm^2), the value reads ~0.082 Ω.cm^2).

In a standard EIS experiment held after the polarization curve in H_2/O_2 and H_2/Air (*figure IV-10* below pinpoints the EIS principle with its associated Nyquist plot with the main physical phenomena extracted), various impedance spectra were registered at different operating points (at 300 mV, 600 mV, 650 mV, 750 mV, and 850 mV), for numerous frequencies (ranging from 200 kHz to 100 mHz) to explore the occurring electrochemical phenomena. At each operating point, a representative Nyquist shape is plotted, from which we can extract the overall ohmic resistance.

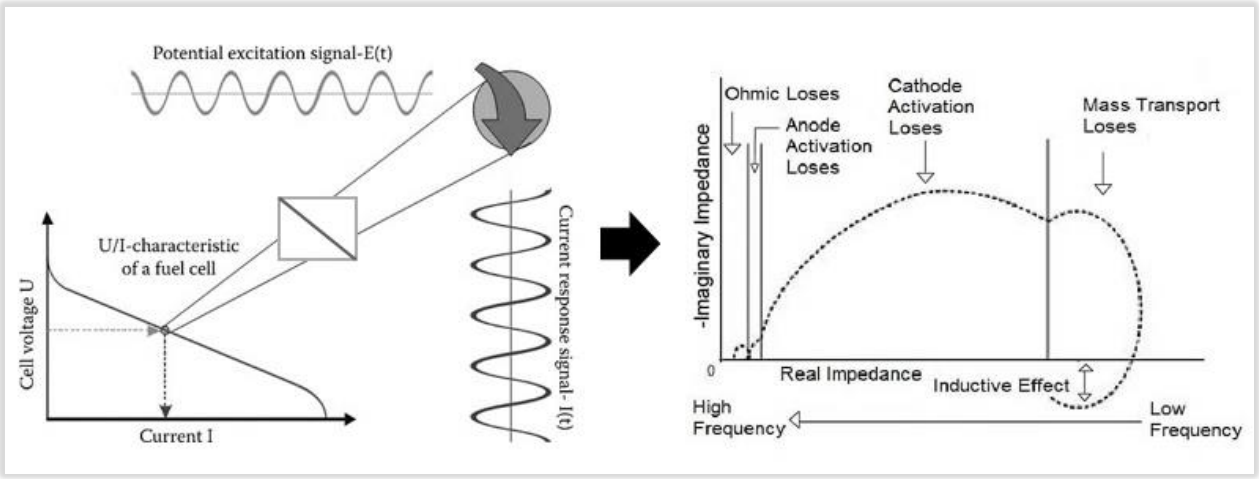

Figure IV-10: Illustration displaying the principle of the electrochemical impedance spectroscopy as a perturbative characterization of the dynamics of an electrochemical process and the Nyquist plot with the main physical phenomena extracted.

We noticed a significant decrease of the ohmic resistance after the break-in: it dropped from 0.040 Ω to 0.035 Ω, which might be attributed to a possible hydration of the membrane's ionomer or the removal of cationic impurities from the membrane.

Figure IV-11 below highlights the Nyquist plots for each voltage operating point. As evidenced in this figure, alongside *figure IV-12* below, the ohmic resistance remains more or less constant at each working area as the voltage decreases (*i.e.,* when the current density increases). This might be due to the homogeneous hydration of the membrane at a given voltage due to different currents. We also notice a closer value of the resistance in H_2/Air compared to H_2/O_2 (*i.e.*, at different cathode gas).

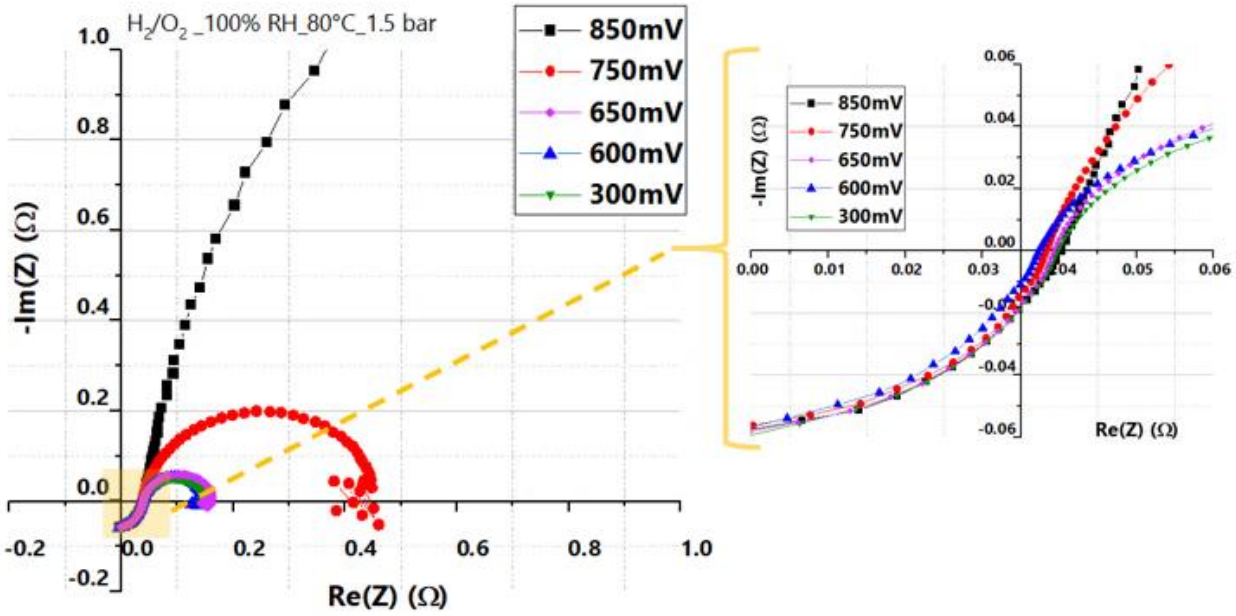

Figure IV1-11: Electrochemical Impedance Spectroscopy (EIS) was performed at various voltage values, at T_{cell}=80°C, 100% RH, wet H_2/O_2 gas flow, and a total pressure of 1.5 bar.

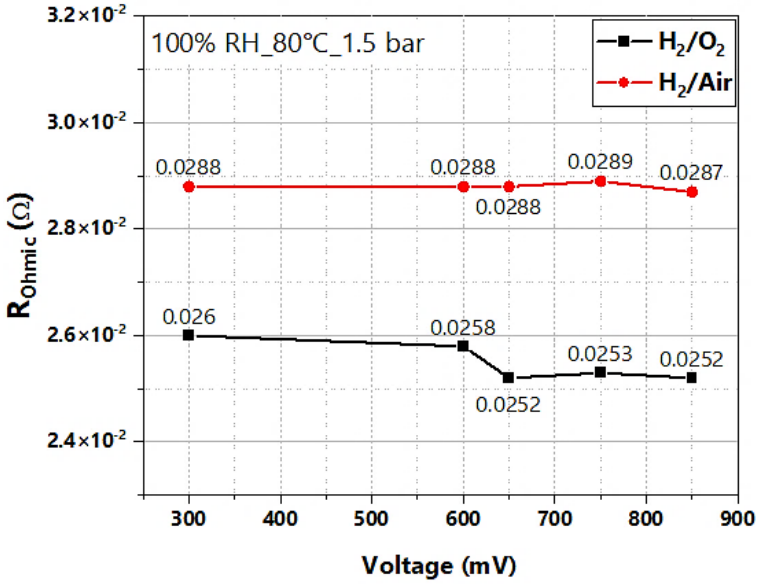

Figure IV-12: The ohmic resistance values obtained at different functioning points in H_2/O_2 and H_2/Air in a fully humidified gas flow at 80°C and 1.5 bar.

In the future results, we will choose the R_{ohmic} from the Nyquist plot obtained at a fixed voltage of 650 mV, in accordance with the set value of voltage in the polarization curve, in order to correct the ohmic drop in polarization curves and to compare the performance accurately.

In addition, the heterogeneous aspect of the thin catalyst layer makes probing its deeper electrochemical analysis under operation extremely challenging, thus the complexity of

revealing protons' transport resistance. Concomitantly, neglecting the anode's contribution, the cell's voltage depends only on the effective ohmic resistance of the catalyst layer.

$$E_{cell,iR-free} = E_{measured} + R_{Ohm} \cdot I \qquad \text{Equation IV-15}$$

The figure below displays the polarization curve (PC) at the aforementioned conditions after the ohmic drop correction. The PC displays the evolution of the voltage as a function of current density and allows the quantification of the cell's performance.

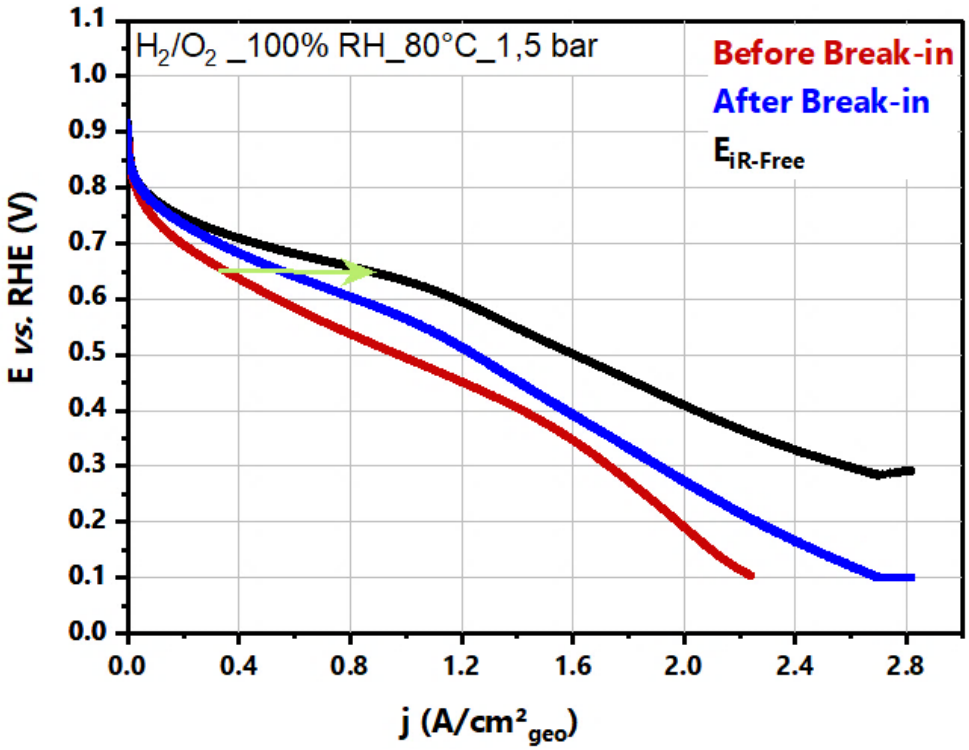

Figure IV-13: Measured polarization curve as a function of geometrical current density at T_{cell}=80°C, 100% RH (dew points), wet H_2/O_2 gas flow, and a total pressure of 1.5 bar. Red-curve: original un-corrected polarization curve, Blue-curve: polarization curve after the break-in, and Black-curve: The resistance-corrected cell voltage ($E_{iR-free}$). The homemade catalyst layer is made of Pt/C (0.1 mg_{Pt}/cm^2 - 0.035 mg_{Pt}/cm^2 at the anode and the cathode, respectively).

MEA Performance: Polarization curve in H_2/Air

Figure IV-14 below shows a second polarization curve realized in H_2/Air: (in green) with the ohmic drop corrected curve (orange plot). The potential at the OCV reads $E_{OCV} = 0.887$ V, with a 41 mV lower than the characterization in H_2/O_2. Also, at 0.65 V, the current density shows a value of ca. 0.15 A/cm^2_{geo}. The drop of performance in the air

is attributed to the low O_2 concentration (~5 times less) in the air. After the ohmic drop correction, it is clear that the ohmic resistance has a negligible part of the total air losses.

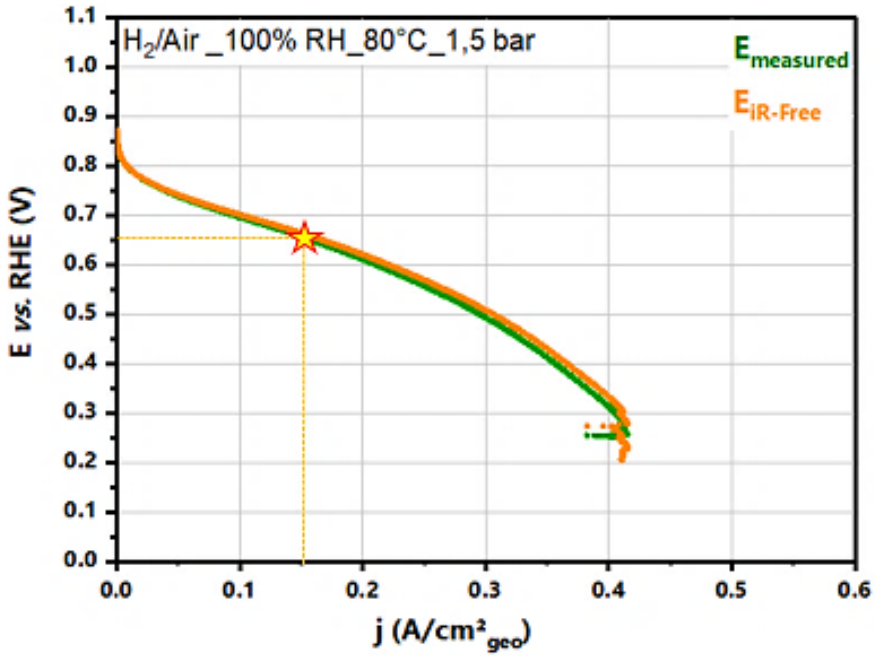

Figure IV-14: Measured polarization curve as a function of geometrical current density at T_{cell}=80°C, 100% RH (dew points), wet H_2/Air-gas flow, and a total pressure of 1.5 bar. Green-curve: original un-corrected polarization curve, and Orange-curve: The resistance-corrected cell voltage ($E_{iR\text{-}free}$).

I.3 Accelerated Stress Test (AST): Degradation of the MEA

Drawing upon the degradation of the catalyst layer at the cathode side, the purpose of this study was to assess its durability under harsh conditions: cycling potential from 0.6 V_{RHE} to 1.0 V_{RHE}, at a T_{cell} of 80°C, under H_2/N_2 at 100% RH and a total pressure of 1 bar. In this potential range, only platinum oxidation and reduction occur, causing dissolution and redeposition of the catalyst, inducing low carbon corrosion (which takes place at a higher potential range >1.2 V_{RHE}). It also allows assessing the catalyst's stability in these conditions. The AST test was carried out according to the "AST Protocol from the DOE", as described **Appendix B**.

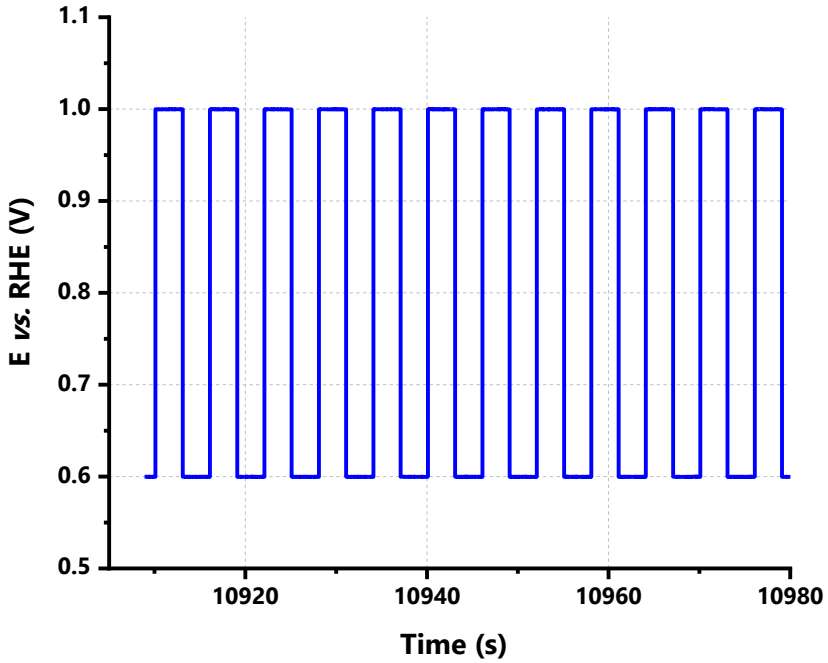

Figure IV-15: Cell voltage *vs.* time during voltage cycling from 0.6 V_{RHE} to 1.0 V_{RHE} to fasten the dissolution of Pt.

In literature, it has been shown that the classical degradation mechanisms of the Pt/C catalyst in operating conditions involve various electrochemical processes, including **i/** the carbon corrosion, leading to the densification of the CL, **ii/** the Pt nanoparticles degradation via the Ostwald ripening (small Pt particle dissolution under higher chemical potential, and reduction (or coalescence) on larger particles), **iii/** Pt dissolution; **iv/** migration of Pt nanoparticles from the carbon support; **v/** and the decrease of the ECSA as well. *Figure IV-16* provides a schematic illustration of the mechanisms involved in the degradation of Pt/C electrocatalysts [8].

It is worth pointing out that the Nafion® membrane is also vulnerable to chemical degradation due to the hydrogen permeation across the membrane from the anode to the cathode, implying a decrease in the OCV of the fuel cell. Such a reaction could lead to the production of peroxide radicals, causing the degradation of both the PEM and the catalyst layer. Hydrogen crossover increases when the temperature, pressure, and humidity of the cell rise.

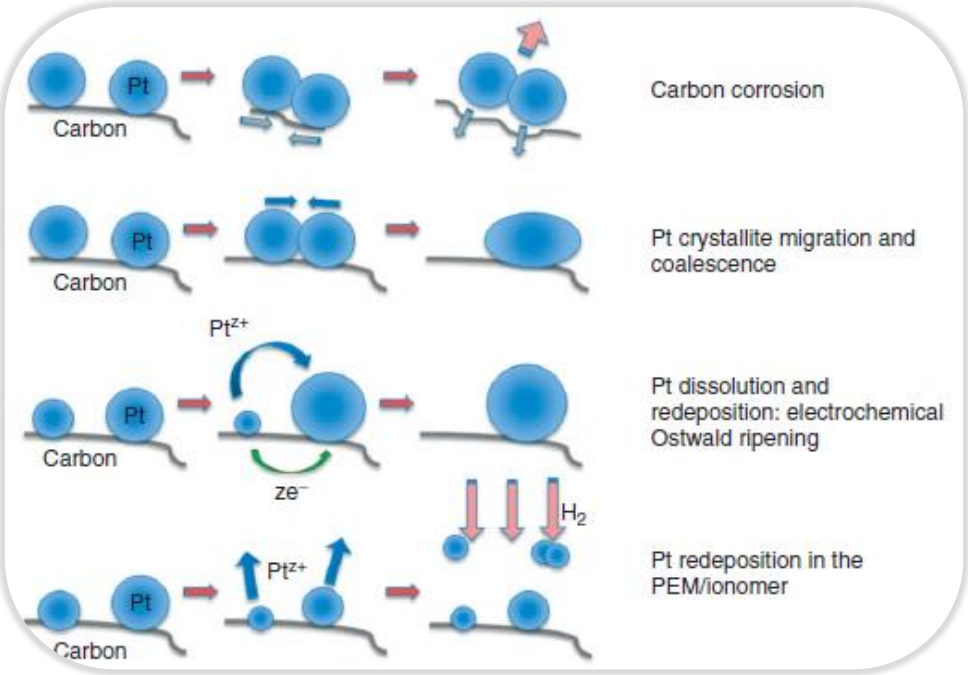

Figure IV-16: Schematics of the four main processes of Pt/C nanoparticles degradation during PEMFC operation. Reprinted from reference [8].

As displayed in *figure IV-17*, the load cycle protocol of 50.000 potential cycles at 200 mV/s leads to a drastic drop of the H_{UPD} area, yielding to lower ECSA and consequently decreasing the PEMFC performance. After degradation, a loss of almost 97% of the specific surface (from ~12 cm^2_{Pt}/cm^2_{geo} to 0.34 cm^2_{Pt}/cm^2_{geo}). This might be attributed mainly to the reorganization of Pt nanoparticles and their dissolution/redeposition to form bigger NPs in the electrode, which lead to the decrease in the specific surface for the same amount of Pt. Or, the precipitation might occur within the membrane, and thus the Pt is no longer electrically connected to the electrodes.

We also notice from the CV's comparison that after aging, the double-layer capacitance had decreased far less than the ECSA, which would indicate that the carbon was not too affected during the degradation.

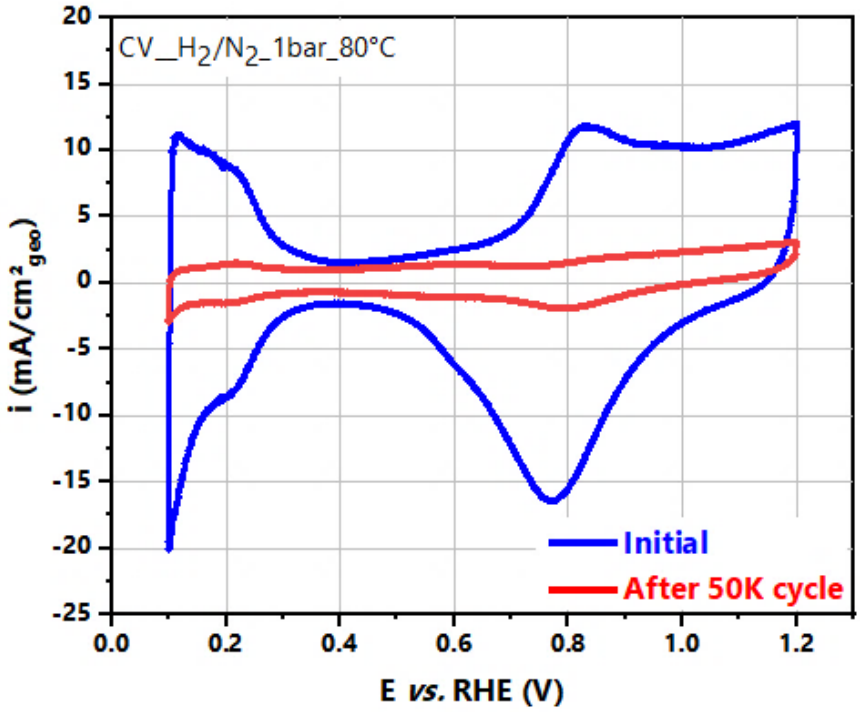

Figure IV-17: Comparison of voltammograms before degradation (blue plot) and after 50K voltage cycles (red plot) conducted in H_2/N_2 at 80°C and relative humidity of 100%, and a total pressure of 1 bar, recorded at a potential sweep rate of 200 mV/s.

In addition, we took advantage of comparing the overall ohmic resistance according to PEIS measurements before and after degradation at 0.4 V under H_2/N_2. From the graph depicted in *figure IV-18* below, we observe a decrease in the cell's overall ohmic resistance 0.046 Ω to 0.022 Ω (~52%), which might be due to the hydration of the ionomer, or the alteration in the MEA's thickness (*i.e.*, better contact between the MEA components).

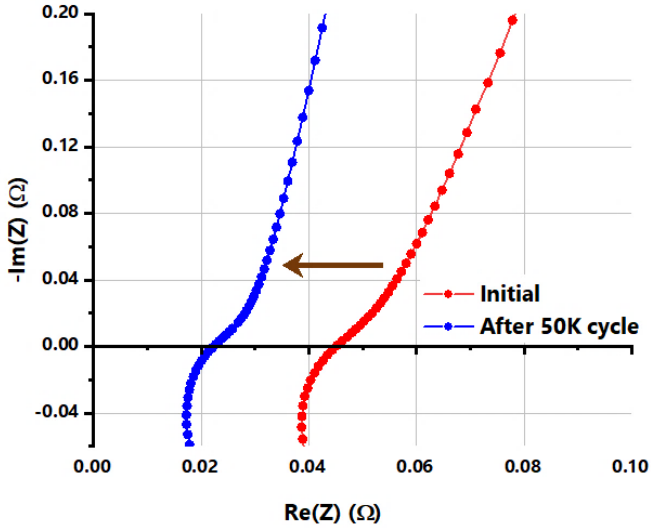

Figure IV-18: Comparison of the impedance spectra obtained from the Nyquist plot before degradation (red plot) and after 50K voltage cycles (blue plot) conducted in H_2/N_2 at 80°C and relative humidity of 100% and a total pressure of 1 bar.

Performance analysis after degradation has been held under wet reactive gases (H_2/O_2 and H_2/Air) and compared to initial polarization curves at 80°C, 100% RH, and a total pressure of 1.5 bar. At 0.65 $V_{iR\text{-}free}$ as our comparison working point, a drastic drop in performance was observed, as depicted in *figure IV-19* below. A drop of 97% in H_2/O_2 and 95% in H_2/Air.

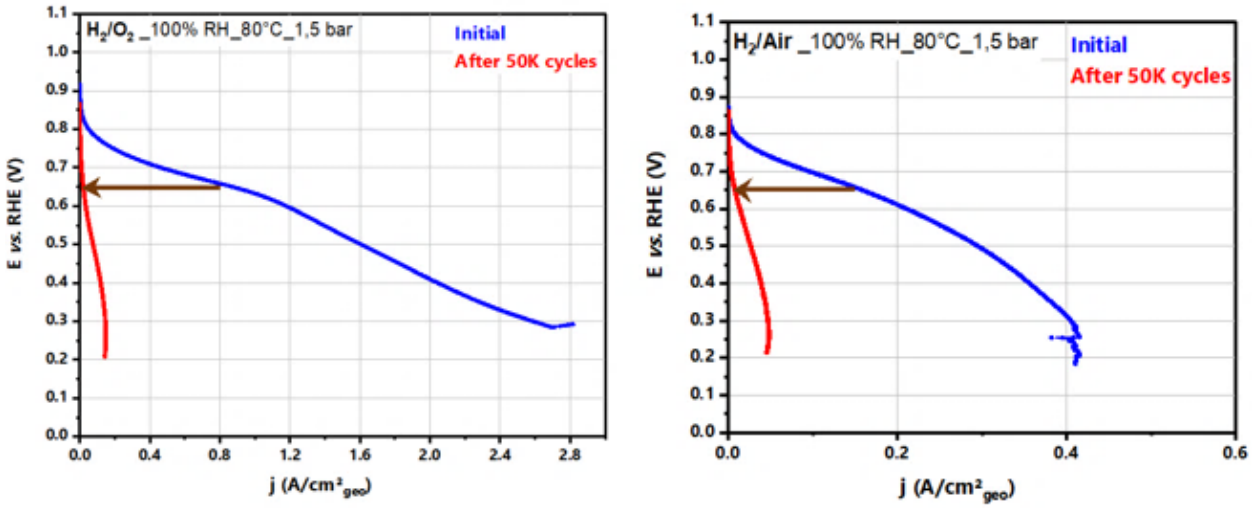

Figure IV-19: Performance comparison of the measured polarization curves ($E_{iR\text{-}free}$ as a function of geometrical current density) at T_{cell}=80°C, 100% RH, wet H_2/O_2 (left side) and H_2/Air (right side) gas flow and a total pressure of 1.5 bar, before aging (blue curve) and after 50K cycles of AST (red curve).

After degradation, the OCV has shown a slight drop in H_2/O_2 and H_2/Air. However, this potential drop of the OCV does not, in any case, mean that the activity had decreased.

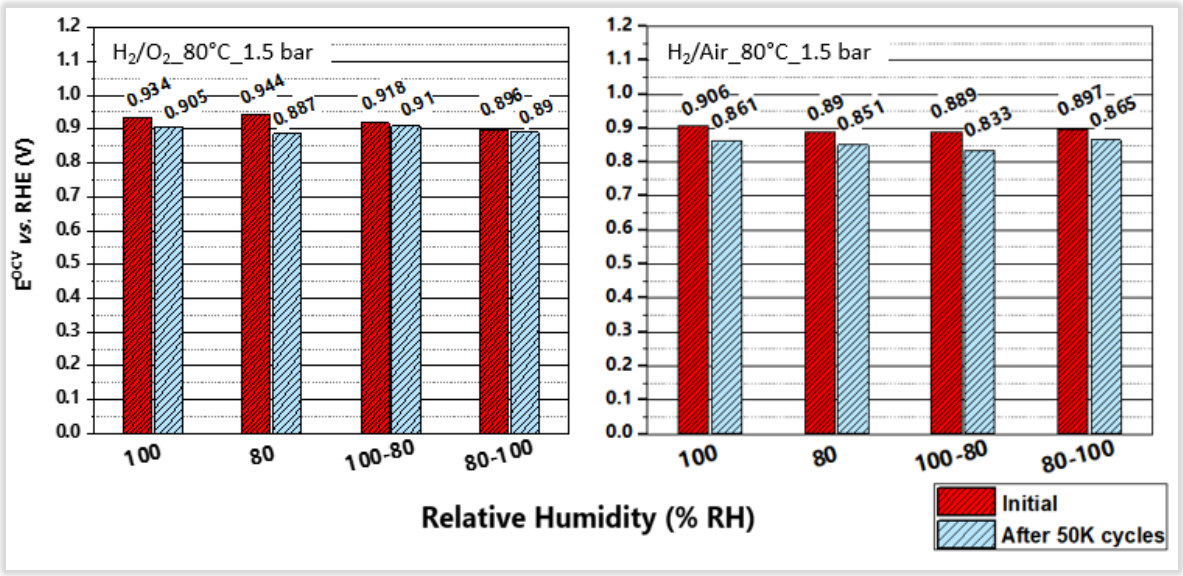

Figure IV-20: Evolution of the OCV values before and after 50K voltage cycles degradation in H_2/O_2 and H_2/Air.

Also, the performance at 0.65 V_{RHE} has decreased sharply after degradation by a factor of 97% and 95% in H_2/O_2 and H_2/Air, respectively, as evidenced in *figure IV-21* below.

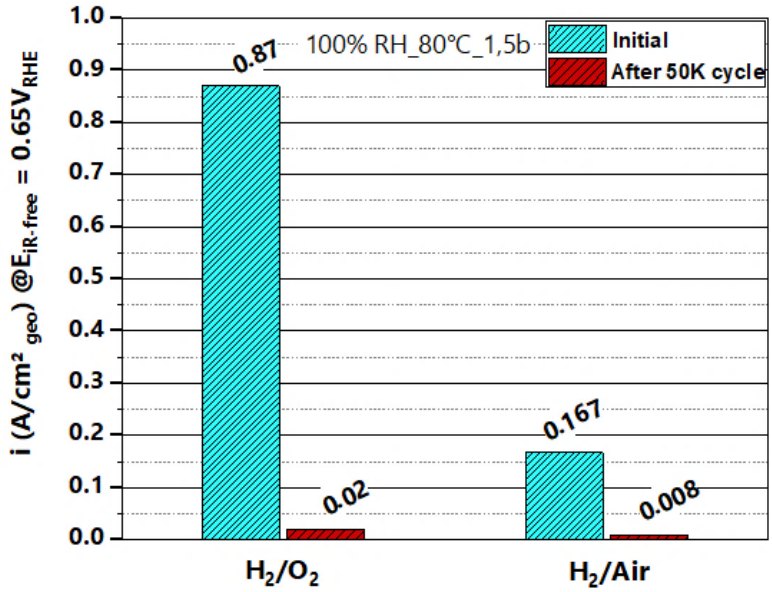

Figure IV-21: Evolution of the current density at 0.65 V_{RHE} before and after degradation.

To examine the impact of the pronounced loss in ECSA after degradation on the performance, we compared the polarization curves before and after degradation as a function of the specific current (A/cm^2_{Pt}). At 0.65 V_{RHE}, the activity decreased by a factor of ~70% after the AST test.

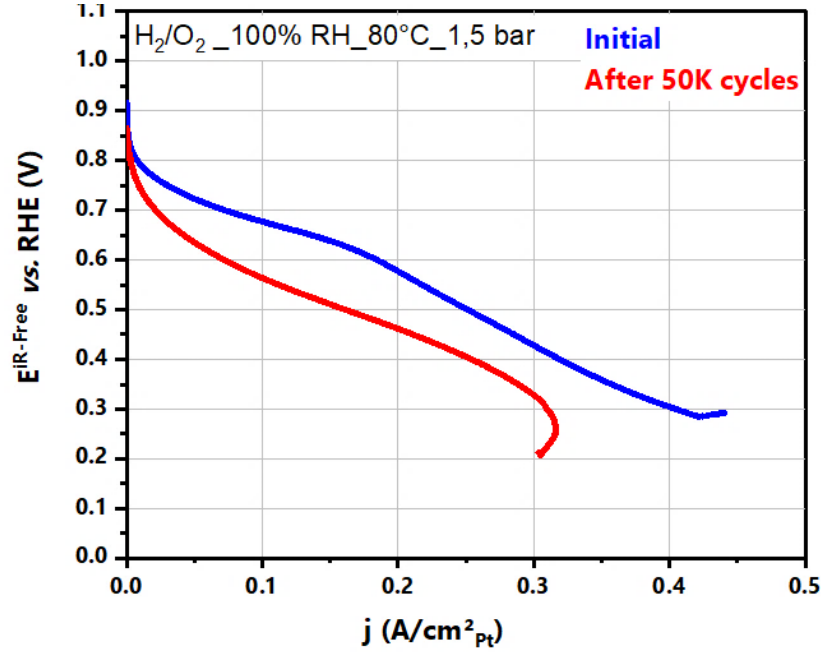

Figure IV-22: Evolution of the polarization curve as a function of the specific current density before aging (blue curve) and after aging (red curve) at Tcell=80°C, 100% RH, wet H_2/O_2 gas flow, and a total pressure of 1.5 bar.

Also, we compared the evolution of the ohmic resistance before and after degradation under 100% RH H_2/N_2 gas flow and 80°C.

	Initial	**After 50K cycles**
Ohmic Resistance (Ω)	0.045	0.024
Ohmic Resistance (Ω.cm²)	0.081	0.043

We noticed a significant decrease in the ohmic resistance. This result, therefore, needs to be interpreted with caution. The reason is not clear; it might show that **i/** there is probably no significant pollution of the ionomer of the membrane by cationic Pt^{2+}; **ii/** a better contact between the electrode and the membrane; **iii/** thinning of the membrane; or **iv/** better hydration of the ionomer. However, due to time limitations, further electrochemical experiments and structural analysis need to be done to confirm our hypothesis.

From the results emerging from *figure IV-23* below, it can thus be suggested that the decrease in performance is mainly due to a reduction of the ECSA. Also, the drop-in activities is assessed by comparing the mass and specific ORR activities and the loss of the electrochemical surface area due to the severe aging process.

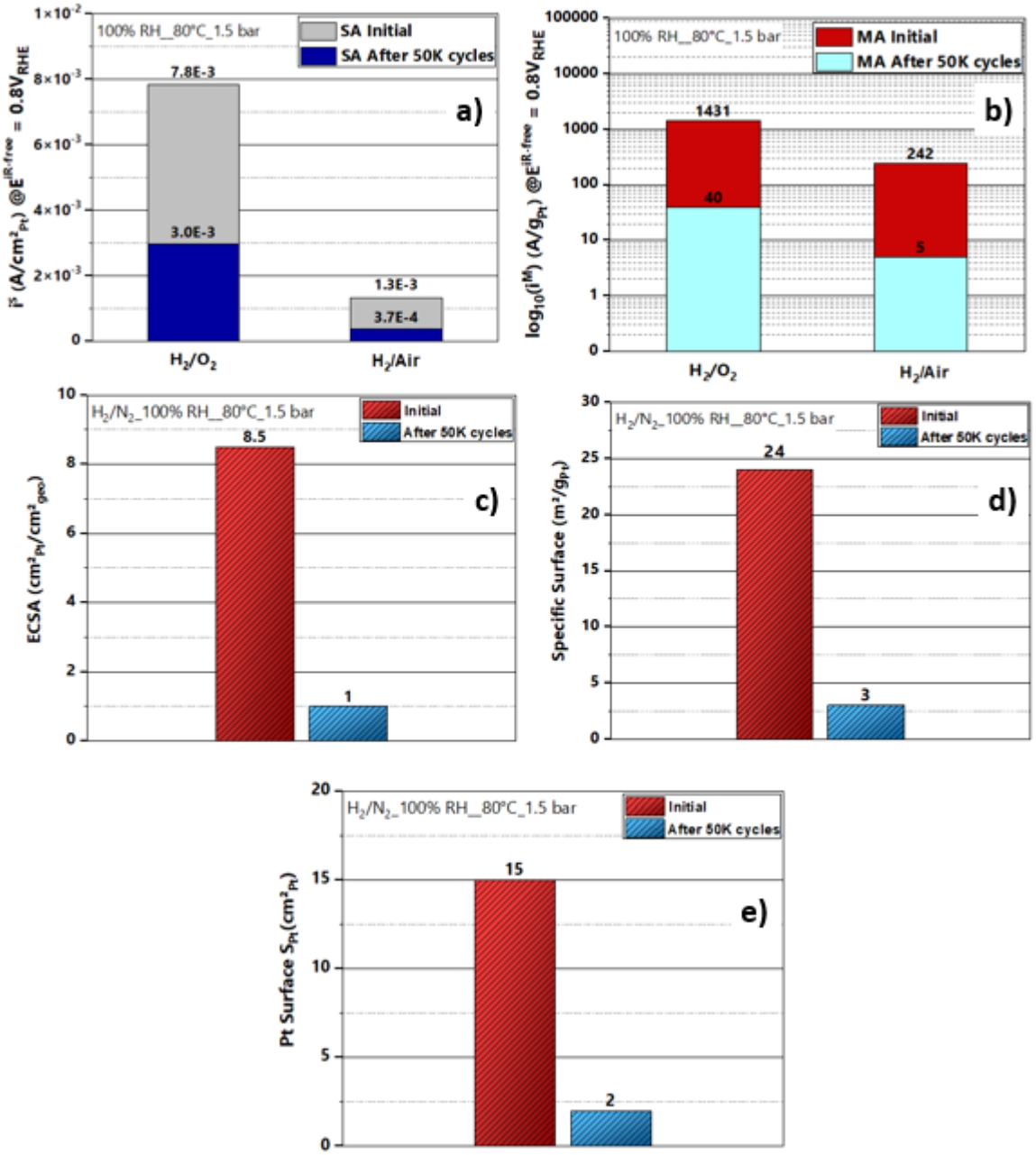

Figure IV-23: Performance comparison of Pt/C electrodes at a cathode loading of 35 $\mu g_{Pt}/cm^2$ before degradation and after 50K potential cycles in H_2/O_2, H_2/Air, and H_2/N_2: a) and b) specific activity and mass activity data recorded (in logarithm scale) at $E_{iR\text{-}free}$=0.8 V_{RHE}, c) ECSA values before and after degradation, d) Specific surface in m^2/g_{Pt}, and e) Platinum total surface before and after degradation.

These results from the AST assessed a drastic loss in performance of the Pt/C catalyst. The latter is poorly resistant to aging and exhibits a high degradation rate under potential cycles affecting its durability. Another aspect of concern is that separation of transport losses of thin electrodes might be hard due to problems of discontinuities in the conductive carbon phase or in the proton-conducting ionomer.

The performance losses under both H_2/O_2 and H_2/Air stem mainly from the loss of active surface area during aging. Therefore, we aimed to test the new architecture of the cathode made of ordered and self-supported carbon-free PtNi nanowires and nanotubes, as we shall see in the next paragraph. These structures might offer the following advantages:

- To unravel the ORR sluggish kinetics reasons;
- Easier access of reactants to catalytic sites;
- To enhance durability and performance under a fuel cell working environment;

II. PtNiNWs and PtNiNTs as cathode for the PEMFC: Electrochemical characterization

II.1 PtNiNWs and PtNiNTs electrodes' fabrication

II.1.1 Final geometry structure of the PtNiNWs and PtNiNTs

Now that the desired nanostructures for the cathode are elaborated, the last step of the whole process is their complete integration into a functional MEA. The AME integration of the PtNi nanotubes and nanowires electrodes is presented in this paragraph. The electrodes tested in this part have the following geometry:

PtNi NWs/NTs Diameter (nm)	50 - 60
Thickness (nm)	350 - 400
Interpore distance D_{int} (nm)	80 - 120

Table IV-4: The final geometry of the PtNi nanowires and PtNi nanotubes after integration onto the Nafion® membrane.

II.1.2 Membrane hot-pressing

This part focuses initially on integrating these nanostructures onto a Nafion® HP membrane using the conventional hot-pressing process. The hot-pressing process was optimized to transfer the nanostructures onto the membrane completely. It required many attempts to have a reproducible transfer of the whole electrode by varying the overall applied stress, time, and temperature.

The hydraulic press (*Model SYNTAX)* used in assembling MEAs consists of two pedestals heated to 150°C. A loading force was imposed on the upper pedestal to apply stress of 1 MPa for 13 minutes. GDLs and gaskets are used to compensate for eventual unevenness or misalignment on the pedestal surfaces.

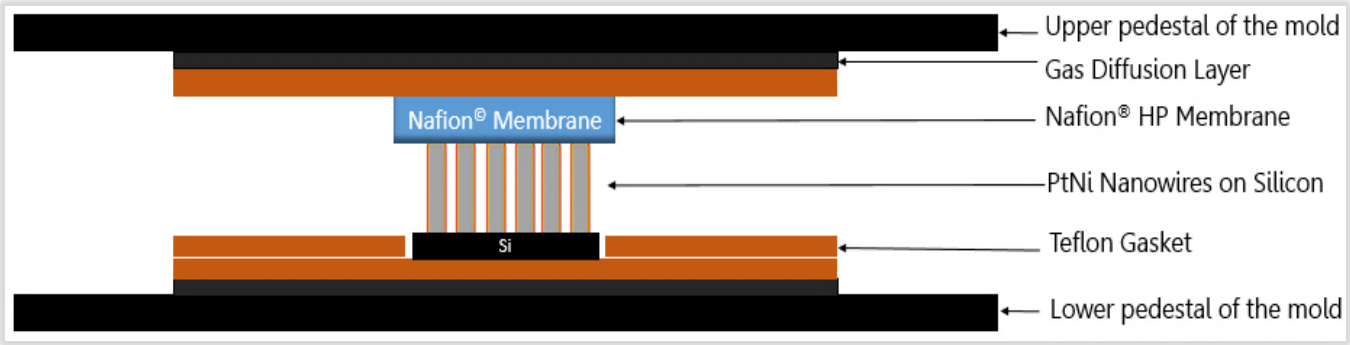

Figure IV-24: Schematic illustration of the hot-pressing process of PtNiNWs and PtNiNTs electrodes on a silicon substrate.

Once the pressing process is over, we recover the membrane gently with silicon substrate stuck into it. The latter is washed in sulfuric acid H_2SO_4 0.5 M for three reasons: **i/** facile removal of silicon substrate from the ionomer membrane without tearing it up, **ii/** nickel leaching, and **iii/** membrane re-acidifying.

The SEM images below show the cathode's final self-supported nanostructures after the complete integration of PtNiNWs and PtNiNTs on the Nafion® HP membrane.

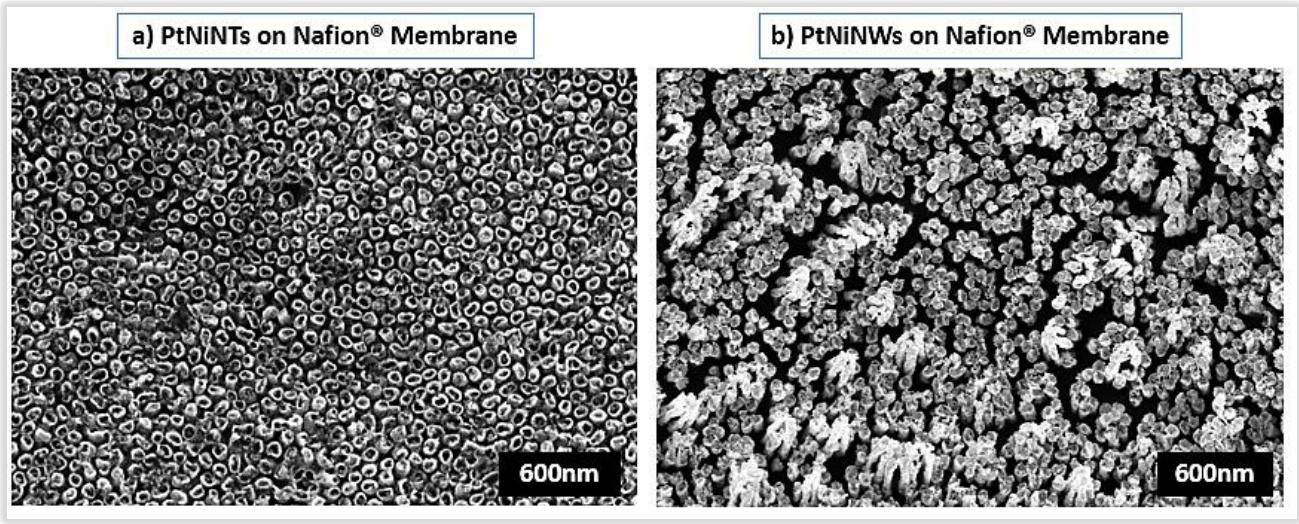

Figure IV-25: SEM top-view structural analysis of a) PtNiNTs and b) PtNiNWs array structures transferred onto the Nafion® membrane by the hot-pressing process.

The carbon-free electrodes thus developed were placed at the cathode of a differential fuel cell that allows studying the MEA under homogeneous and well-defined conditions for in-depth local characterization. A conventional commercial gas diffusion electrode (GDE) was used on the anode side, composed of Pt/C catalyst (0.1 mg/cm²). MEAs were assembled into differential following the same aforementioned protocol assembly for the Pt/C (the suggested assembly is highlighted in *figure IV-26*).

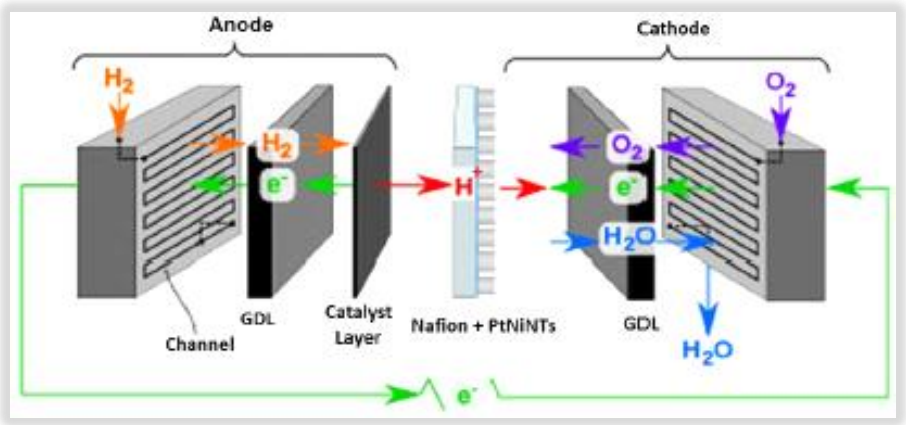

Figure IV-26: The proposed Fuel Cell's structure with a conventional GDE on the anode side and PtNiNWs/PtNiNTs on the cathode side.

The following section will provide a performance analysis of the elaborated cathode made of PtNiNWs and PtNiNWs integrated into a Nafion® membrane (as shown in detail in *the experimental part of Chapter III*). The membranes thus elaborated are mounted in a single test cell. A cross-sectional MEA structure is depicted in the *figure IV-27* below:

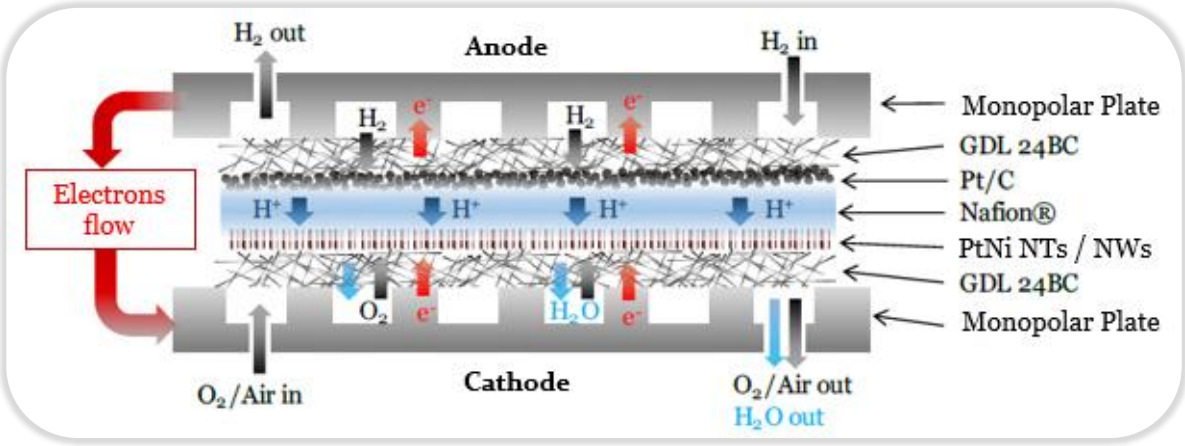

Figure IV-27: Schematic illustration of the single-cell test cell with Platinum nanotubes/nanowires embedded on a Nafion® membrane on the cathode side and a conventional Pt/C catalyst on the anode side (0.1 mg_{Pt}/cm^2).

Like the standard MEA made of Pt/C previously tested, MEA with PtNiNTs/NWs cathodes followed the same break-in protocol and performance characterization process.

II.2 Fuel cell test of the PtNiNWs as a novel carbon-free cathode

The PtNiNWs have been characterized using methods similar to those disclosed previously for the Pt/C MEA. As defined by UV-vis and X-ray fluorescence, the cathode Pt-loading ranged from 0.08 to 0.1 mg_{Pt}/cm^2. In this section, we will also try to understand the effect of RH on the performance of the PtNi nanostructures. In an attempt to avoid changing two parameters at the same time (RH and total pressure), we adapted the RH to the total pressure by adjusting the partial pressure of O_2.

II.2.1 The electrochemical surface area and the internal resistance of the CL

At first hand, we performed cyclic voltammetry to investigate the electrochemical surface area under fully humidified H_2/N_2 gas flow at a total pressure of 1 bar at 40 and 80°C, combined with the electrochemical impedance spectroscopy to determine the overall ohmic resistance. The measured ECSA was derived from the H_{UPD} adsorption/desorption peak red area (0.1 V < E < 0.4 V), and reads 19 cm^2_{Pt}/cm^2_{geo}.

As it can be seen in *figure IV-28* below, a strong difference in H_{UPD} and Pt oxidation/reduction peaks between 40°C and 80°C was noticed. All the tested PtNiNWs cathodes have shown this same behavior. Also, an apparent shift in the typical peaks (blue plot) of the hydrogen adsorption/desorption is observed. This might be attributed to the pure Pt atoms organization in the outer layer of the catalyst or a less leaching of Ni at 40°C.

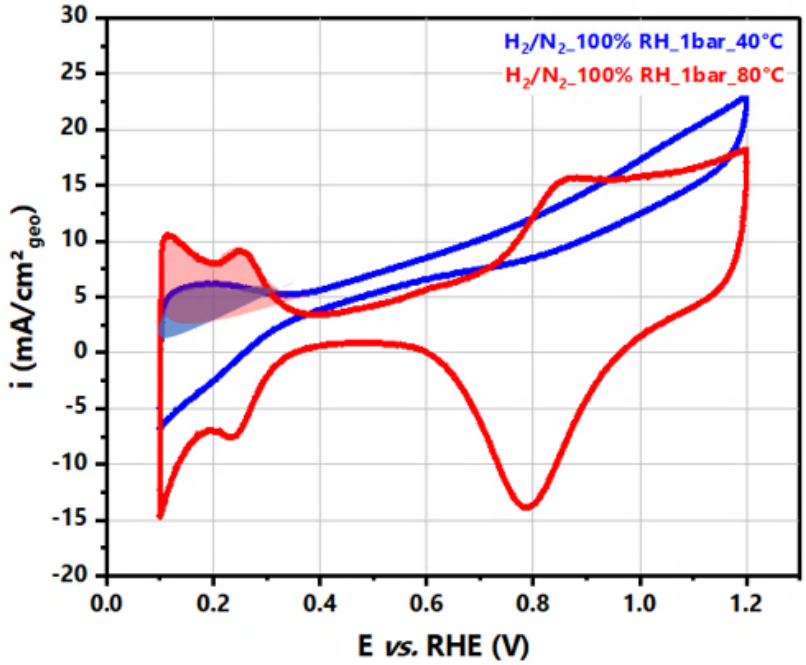

Figure IV-28: Cyclic voltammetry (CV) of PtNiNWs, recorded in fully humidified H_2/N_2 gas flow from 0.1 V_{RHE} to 1.2 V_{RHE} at 40°C (blue plot) and 80°C (red plot) with a sweep rate of 200 mV/s.

The major features of this CV could be attributed to: **i/** a shunt or resistive behavior from 0.4 V to 0.7 V as indicated by a linear slope, probably due to the fabrication process that punches the membrane contact between the two electrodes (*i.e.*, transferring the PtNiNWs by hot-pressing from the silicon substrate); **ii/** the surface that is accessible to protons and electrons is larger at 80°C than at 40°C (absence of the peaks associated to Pt area accessible to protons and electrons at 40°C). I observed that this phenomenon is irreversible because after measuring the ECSA back again at 40°C, I tend to get a similar plot as the red one. At 80°C, the membrane is softer and swells more with better contact (between the CL and microporous layer of the GDL), or there might be cleaning of Ni at 80°C. Another most probable hypothesis is either the better proton transport at 80°C because of the larger swelling of the ionomer compared to 40°C or due to reorganization of the ionomer with better contact with the PtNiNWs [9].

The Impedance Electrochemical Spectroscopy (EIS) measurements at 0.4 V_{RHE} at high frequency were performed to determine the ohmic resistance. The overall ohmic resistance value reads 0.063 Ω, which is higher than the resistance obtained for the Pt/C cathode. Similar to the Pt/C electrode, we have used the same Nafion® membrane, GDE

at the anode, GDL at the cathode side. A possible explanation for this resistance increase might be the membrane's pollution by Ni cationic species or a contact resistance between CL and the microporous layer (MPL).

II.2.2 Ohmic-corrected polarization curve at different RH

Polarization curves were recorded at different RH and total pressure, in H_2/O_2 and H_2/Air at 80°C. They were corrected from the derived ohmic resistances from EIS measurements. We evaluated the effect of the relative humidity on the performance of the PtNi nanowires as shown in the *figure IV-29* below:

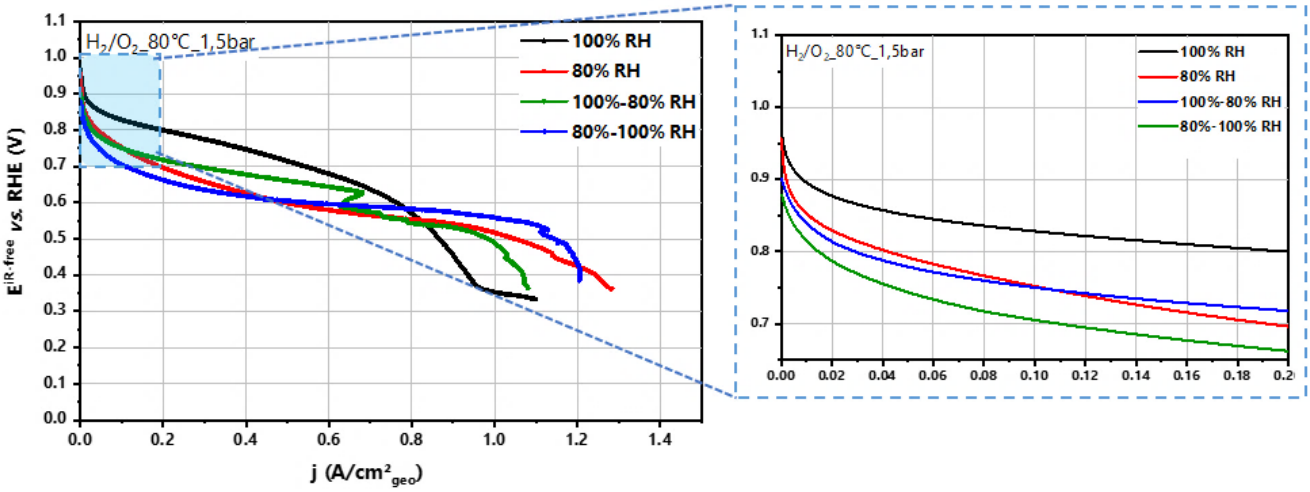

Figure IV-29: Fuel cell polarization curves (corrected from ohmic drop) of PtNiNWs cathodes for different relative humidity, keeping the same partial pressure of the gas at cell inlet: H_2/O_2, cell temperature of 80°C, at different relative humidity values (RH, same value for anode and cathode for a single number, Anode-Cathode RH otherwise) and a total pressure 1.5 bar at 100% RH, 1.38-1.5 bar (left side: at the anode-right side: the cathode) at 80%-100% RH, 1.5-1.38 bar at 100%-80% RH, and 1.38 bar at 80% RH. The total pressure was adjusted to have the same partial pressure of O_2.

The voltage at the OCV values increased while increasing relative humidity. Also, relative humidity showed significant effects on the cell's performance.

At 100 %RH and low current density (*i.e.*, high potential values [0.94 – 0.6 $V_{iR\text{-}free}$]), the nanowires have shown a higher performance comparing to the different values of %RH, maybe due to whether the higher activity of the catalyst or due to better use of Pt but the performance drops at high current densities may be due to electrode flooding in fully humidified conditions and thus the inaccessibility of oxygen to the catalytic sites.

At lower %RH, the ionic conductor resistance increases due to the membrane drying out (low hydration implies low ionomer conductivity). We can also assume lower proton access and thus the misuse of the catalyst on the nanostructure that does not include any proton conductor (absence of ionomer) at low current densities. Also, when RH decreases, the maximum current drawn from the cell increases, attesting a better accessibility of the gases to the catalytic sites.

By comparing the ohmic resistance values at different RH, we notice that 100%-80% RH gives lower resistance than 80%-100% RH (similarly at 100%-50% RH and 50%-100% RH). Thus, it would be better to hydrate the anode for the hydration of the MEA.

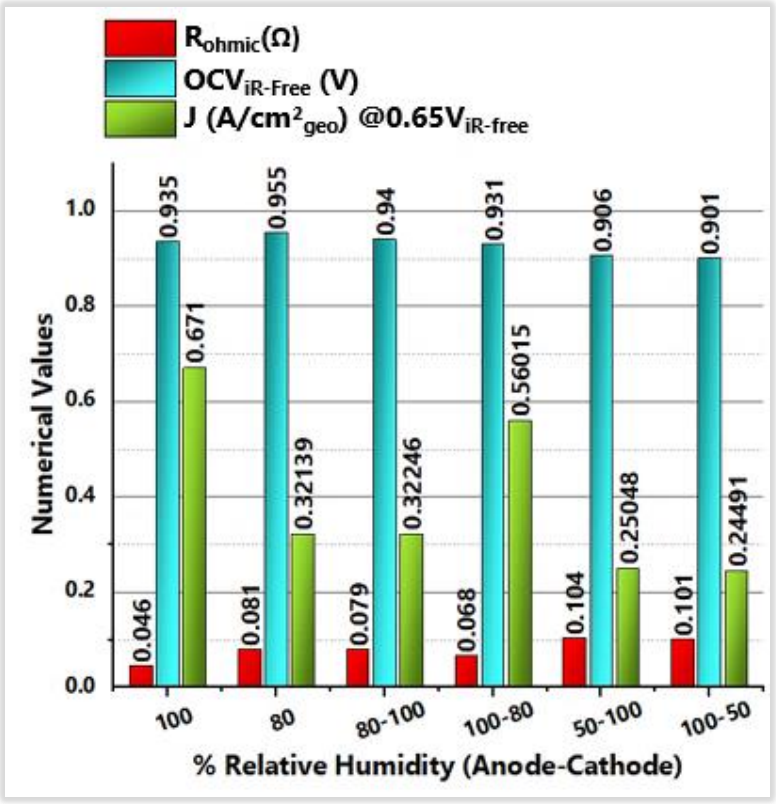

Figure IV-30: A comparative bar chart illustration of the ohmic resistance, open-circuit voltage values, and the current density at E = 0.65 $V_{iR\text{-}free}$ at different relative humidity values.

The cell performance was measured during operation in H_2/Air. Polarization curves were recorded at 80°C, with a total pressure of 1.5 bar, 1.38 bar, 1.38-1.5 bar, and 1.5-1.38 bar at 100% RH, 80% RH, 80%-100% RH, and 100%-80% RH, respectively, to keep the same partial pressure of O_2 at cell inlet whatever the RH is (*Cf., paragraph II.2*). A drastic drop of the polarization curve at 100% RH was observed as discernible from *figure IV-31*. This

could be attributed to the cell flooding, leading to lower utilization of Pt surface or the inaccessibility of oxygen to catalytic sites. At 80%-100% RH, we were able to reduce the propensity to flooding by removing the water produced at the cathode to the anode, which limits flooding by avoiding detrimental water accumulation at the cathode.

Conclusions on the RH effect slightly differ compared to operation under O_2. At 100% RH in the air, we notice very low performance even at low current density, which could probably be linked to flooding. This was observed for higher current density in O_2, where the partial pressure of the reactant is 5 times larger. For air, one must avoid fully humidified conditions on both sides. Better performance is observed at a low current density at 80%-100% RH. Performance drop at a high current density is most probably due to detrimental accumulation of water that hinders O_2 transport which effect is visible for lower partial pressure of O_2, as in Air.

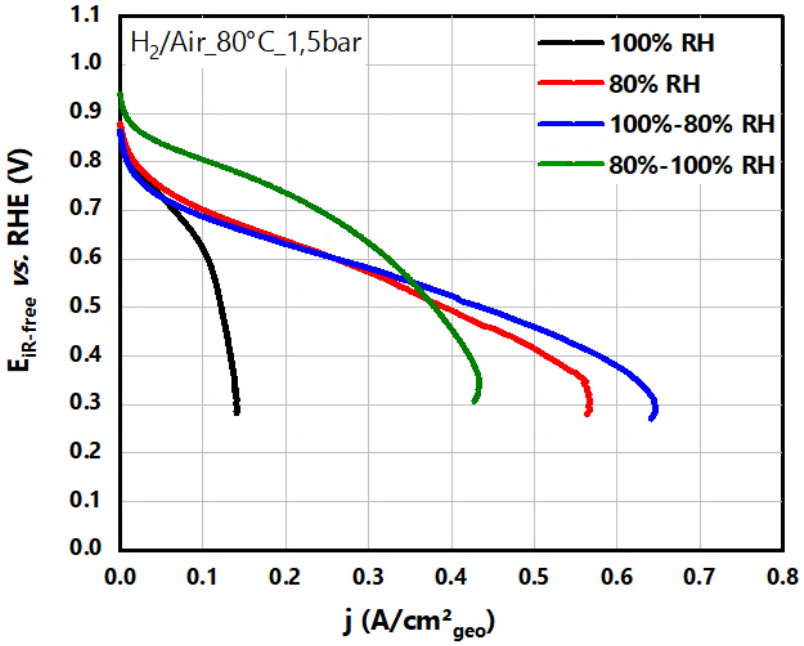

Figure IV-31: Fuel cell's polarization curves (corrected from ohmic drop) of PtNiNWs cathodes at operating conditions in the order of anode/cathode: H_2/Air, cell temperature of 80°C, at different relative humidity values and a total pressure of 1.5 bar, 1.38 bar, 1.38-1.5 bar, and 1.5-1.38 bar at 100% RH, 80% RH, 80%-100% RH, and 100%-80% RH, respectively.

II.2.3 AST protocol: PtNiNWs Degradation

The load-cycle degradation test was carried out following the same potential cycles protocol applied to the conventional Pt/C cathode mentioned in the previous paragraph

(as evidenced by DOE AST Protocol). After that, a comparison of the ECSA was performed after degradation and recorded at 80°C, a total pressure of 1 bar under H_2/N_2 gas flow (*figure IV-32*). The corresponding ECSA value is averaged from the H-adsorption and H-desorption charges between 0.1 and 0.4 V_{RHE}, reads ~11.5 cm^2_{Pt}/cm^2_{geo}, equivalent to a 40% loss. We also notice a lower shunt after degradation.

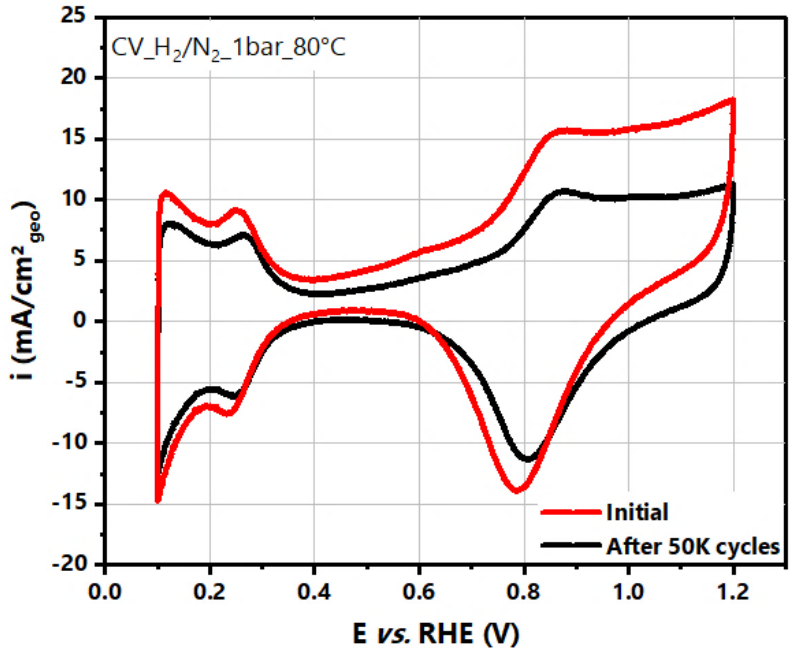

Figure IV-32: Comparison of voltammograms before degradation (red plot) and after 50K cycles (black plot) conducted in H_2/N_2 at 80°C and relative humidity of 100% and a total pressure of 1 bar, recorded at a potential sweep rate of 200 mV/s.

After degradation, the EIS measurement indicates an ohmic resistance of 0.032 Ω, which is two times lower than the ohmic resistance extracted before degradation. It might be correlated to the evacuation of cationic pollutants after cycling (enough time to leach Ni^{2+} probably). Also, we witnessed the same behavior at different RH.

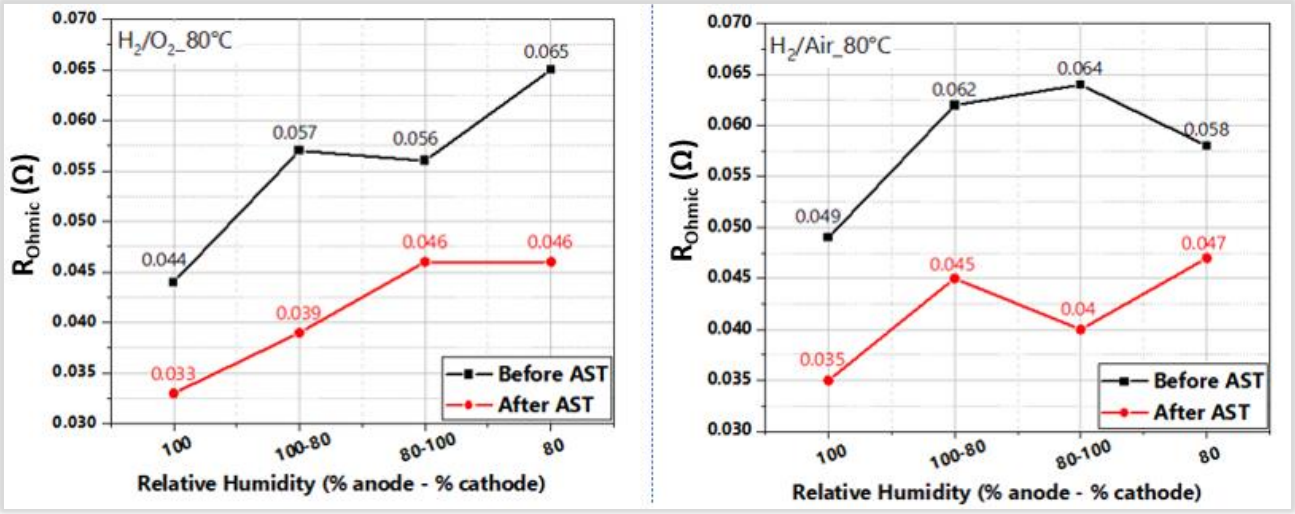

Figure IV-33: Evolution of the ohmic resistance at 0.65 $V_{iR\text{-}free}$ for different RH values in H_2/O_2 and H_2/Air at 80°C.

We compared the polarization curves obtained in H_2/O_2 at 100% RH and in H_2/Air at 80%-100% RH before and after degradation. We extracted a 58% loss in performance in H_2/O_2 and 56% in H_2/Air at E=0.65 $V_{iR\text{-}free}$, which is clearly similar at both conditions.

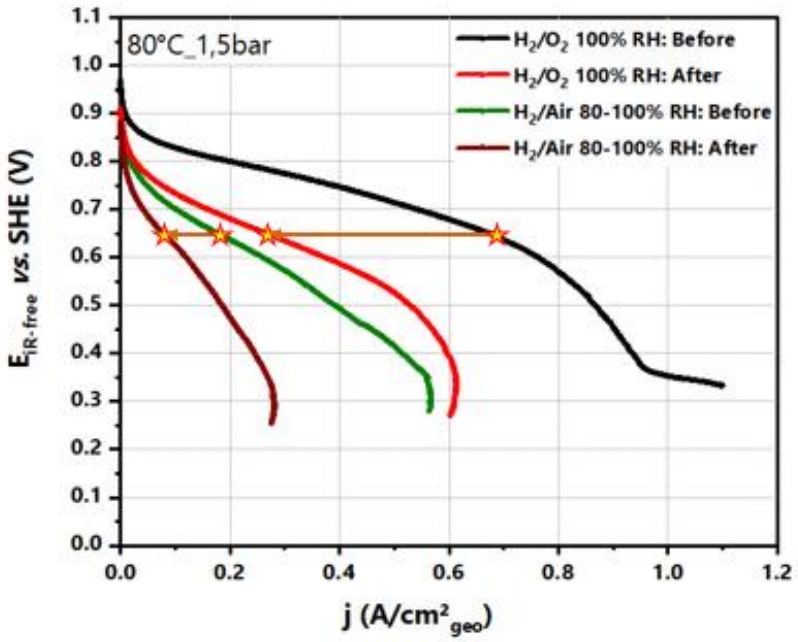

Figure IV-34: Comparison of fuel cell's polarization curves (corrected from ohmic drop) of PtNiNWs cathodes at operating conditions in the order of anode/cathode in H_2/O_2 and H_2/Air, cell temperature of 80°C, at different relative humidity values and a total pressure of 1.5 bar, 1.38 bar, 1.38-1.5 bar, and 1.5-1.38 bar at 100% RH, 80% RH, 80%-100% RH, and 100%-80% RH, respectively, before and after 50K load cycles.

II.2.4 Performance comparison

To have a better insight into the ORR activity of the PtNi nanowires, further comparisons have been carried out after degradation, as illustrated in *figure-35* below. The significant loss of the Pt surface (~40%) displayed a remarkable decrease in the ECSA, thus reducing the performance (measured at 80°C, 100% RH, and 1.5 bar). We may ascribe the drop in performance to various factors:

- Ni ion contamination of the ionomer due to its leaching from the nanowires after the AST test;
- A change in the crystal orientation of the alloy composition;
- Dissolution of Pt nanoparticles from the nanowires (diminution of the ECSA);
- PtNiNWs detachment from the membrane.

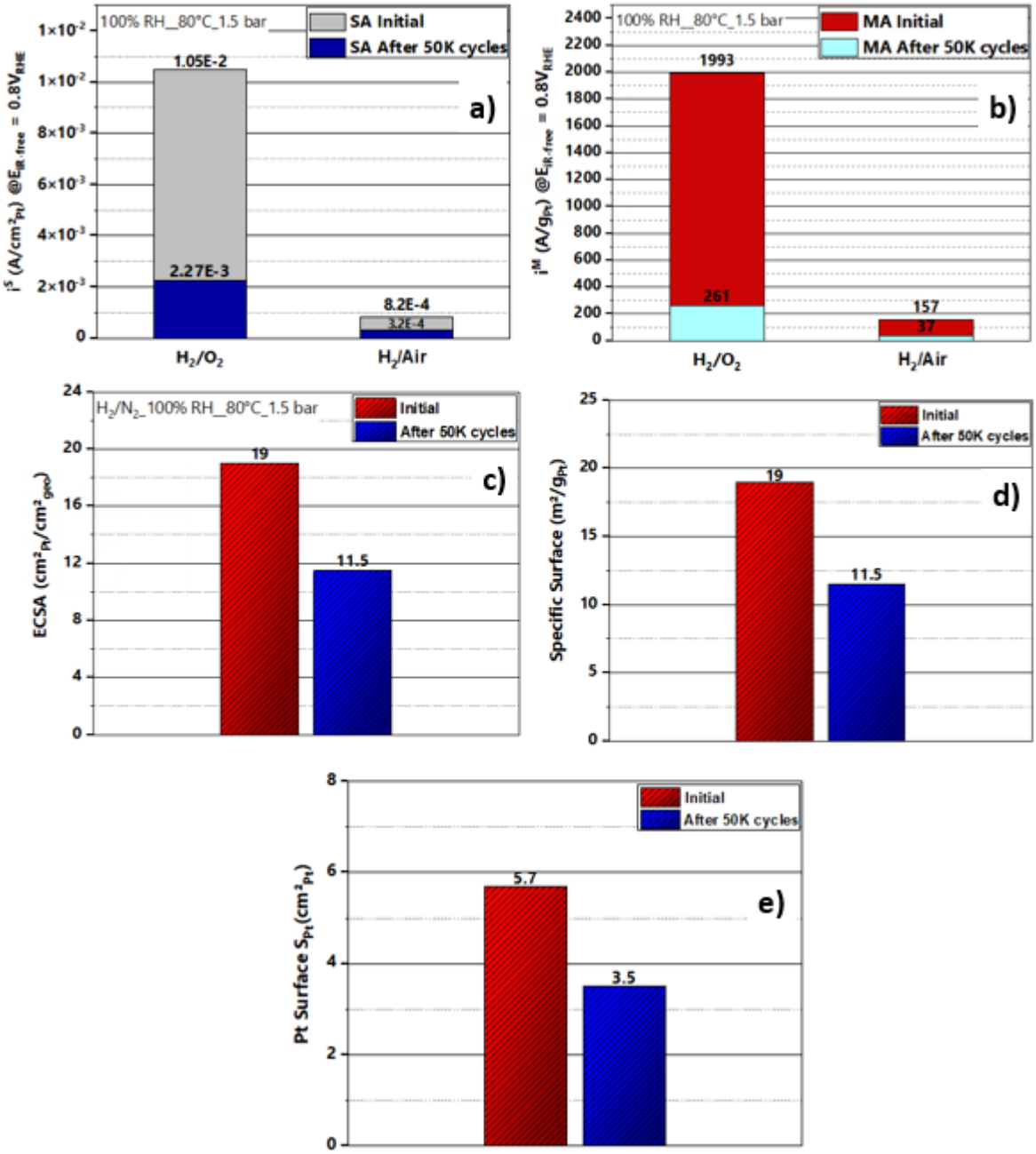

Figure IV-35: Performance comparison of the MEA with PtNiNWs at a cathode at a loading of 100 $\mu g_{Pt}/cm^2$ before degradation and after 50K potential cycles in H_2/O_2, H_2/Air, and H_2/N_2: a) and b) specific activity and mass activity data recorded at $E_{iR\text{-}free}$=0.8 V_{RHE}, c) ECSA values before and after degradation, d) Specific surface in m^2/g_{Pt}, and e) Platinum total surface before and after degradation.

As commonly known, the study of the PtNi ORR was set from very early on. In our work, PtNiNWs exhibited, after degradation, a 39% loss of the ECSA against 87% of loss in Pt/C. Nevertheless, the MA and SA drop for PtNiNWs was slightly lower than Pt/C in H_2/O_2 and H_2/Air.

	% of Mass Activity loss		% of Specific Activity loss	
	Pt/C	PtNiNWs	Pt/C	PtNiNWs
H_2/O_2	98	87	62	78
H_2/Air	97	86	72	61

Table IV-5: Comparison of the mass activity and the specific activity drop between Pt/C and PtNiNWs

The carbon-free nanowires structure with the porous surface without ionomer did not provide stability against electrochemical cycling compared to Pt/C electrode.

We can conclude from our study that the drop in the ECSA is not the only factor responsible for the activity drop after aging: the decrease in the ECSA is not necessarily related to reducing the activity. That is to say, for instance, we can imagine a reduction of activity with an increase of the ECSA if the nickel dissolved or dealloyed, or a decrease of ECSA with an increase of activity if the surface is restructured differently.

Nickel, with its low standard potential, would probably exhibit dissolution during PEMFC operation, which is well correlated with other PtNi structures reported in the literature. This issue will remain a significant concern to take into account for our following performance tests of PtNi nanotubes.

II.3 Fuel cell test of the PtNiNTs as a novel carbon-free cathode

In this last part of the performed fuel cell tests, we will assess the performance of the PtNiNTs. The MEA was assembled into the differential cell similarly to PtNiNWs (*Cf., paragraph I.1.3* earlier). The cathode Pt-loading was obtained only via UV-vis and indicated *ca.* 0.014 mg_{Pt}/cm^2.

II.3.1 The electrochemical surface area and the internal resistance of the CL

The ECSA was evaluated under fully humidified H_2/N_2 gas flow at a total pressure of 1 bar at 80°C, along with the electrochemical impedance spectroscopy to determine the protonic resistance. By integrating the H_{UPD} adsorption/desorption peak, the available

measured ECSA reads *ca.* 23 cm^2_{Pt}/cm^2_{geo}. A probable presence of Ni adatoms could be present on the surface of the catalyst.

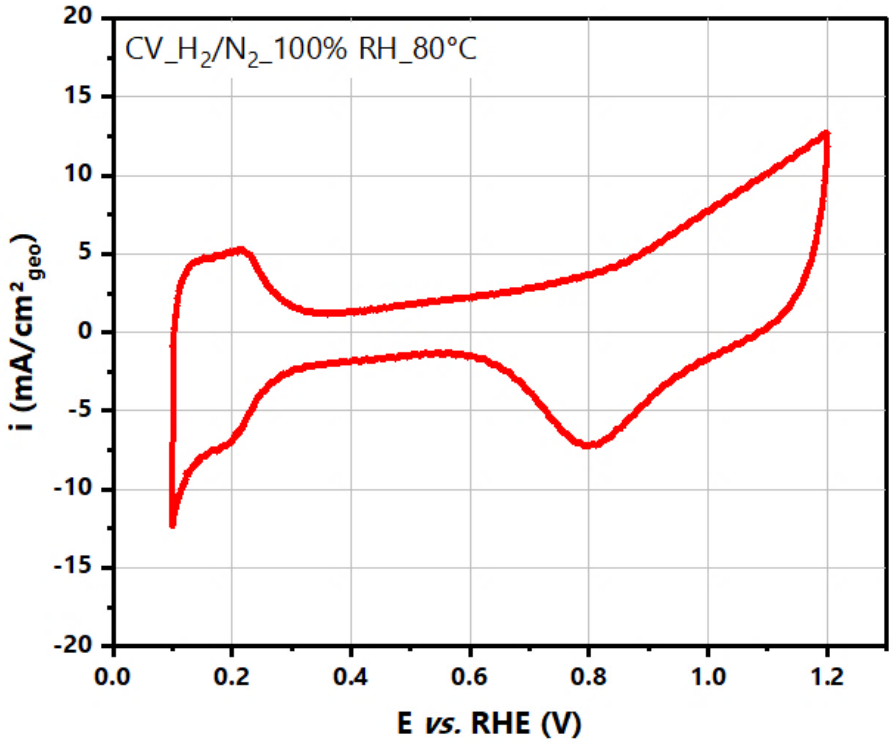

Figure IV-36: Cyclic voltammograms of PtNiNTs, recorded in fully humidified H_2/N_2 gas flow from 0.1 V_{RHE} to 1.2 V_{RHE} at 80°C with a sweep rate of 200 mV/s.

The extracted value of the overall ohmic resistance from EIS measurements in the same conditions described above amounts to 0.069 Ω, which is similar to the ohmic resistance obtained for the PtNiNWs.

II.3.2 Hydrogen-Oxygen and Hydrogen-Air polarization curves

Following the same test protocol aforementioned earlier, we assessed the experimental polarization curves at different RH values and total pressure alongside local impedance spectroscopy after the break-in process.

Optimization of the PtNiNTs fabrication and hot-pressing process:

During the fabrication process, I optimized the elaboration and the hot-pressing transfer of the PtNiNTs. *Figure IV-37-a)* displays the NTs final structure obtained after Acid leaching on the silicon substrate. The nanostructures were then transferred onto a Nafion® membrane. We observe quasi-porous PtNi nanotubes after the acid leaching

step. Also, we notice several empty zones due to the detachment of PtNiNTs during the leaching process. On the other side, *figure IV-37-b)* illustrates a self-standing PtNiNTs forest obtained after transferring the PtNiNWs onto the Nafion® membrane first, then leached via acid treatment.

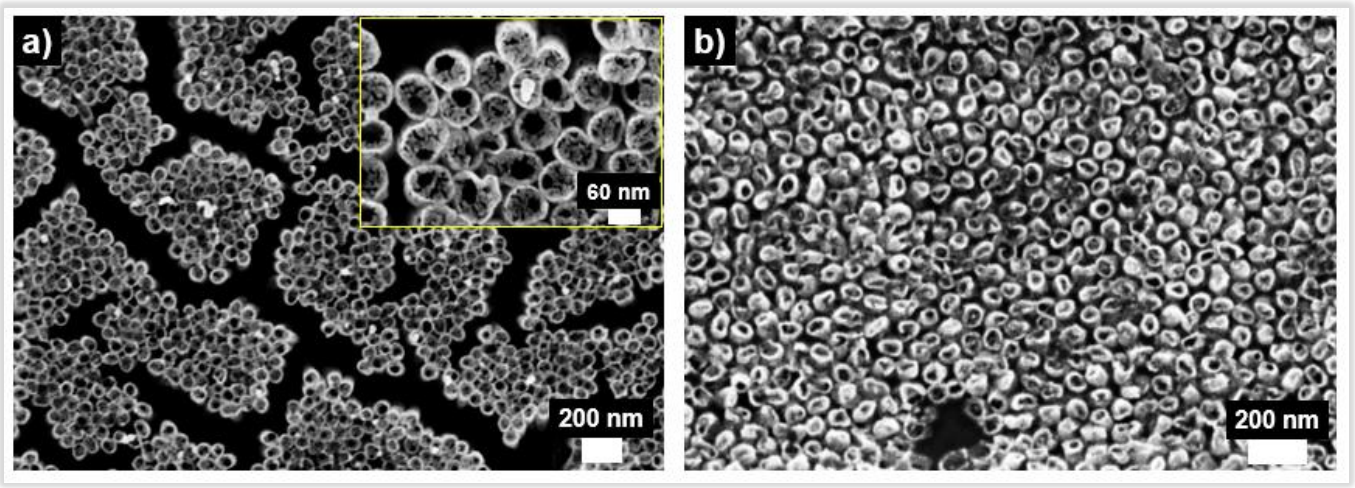

Figure IV-37: SEM top-view images of the fabricated PtNiNTs a) before optimization (acid leaching performed on PtNiNWs on a silicon substrate), and b) after optimization (acid leaching performed on PtNiNWs transferred onto Nafion® membrane).

A difference in performance between the two MEAs assessed by the polarization curve at 100% RH and 80% RH was observed. The relative humidity showed more significant effects on the polarization curve. At 100% RH, the PtNiNTs-like structure (red plot, before optimization) has shown a slight increase in performance at low current densities and tended to flood at high current densities. Lowering the RH to 80%, the flooding issue was tackled, leading to an increase in limit current at 0.4 V_{RHE} from 0.5 mA/cm^2_{geo} to ~1.5 A/cm^2_{geo}. After optimization, it is apparent that the flooding issue decreased. Also, a performance improvement was observed at high current densities at both 100% and 80% RH. To have a better insight on the effect of tubular structures (*i.e.*, less complex geometry than the Pt/C), the increase in performance might emanate from a better flow of reactants within the tubes, which exhibits a less tortuous path.

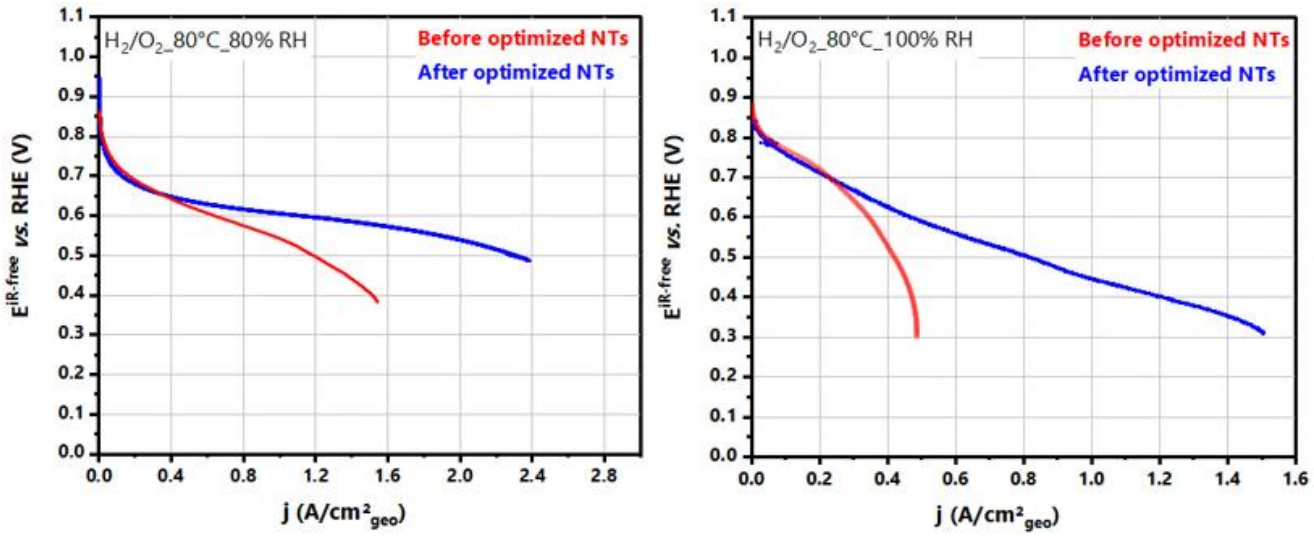

Figure IV-38: Comparison of the polarization curves of PtNiNTs before (red plot) and after optimization (blue plot) at a) 80% RH, a total pressure of 1.38 bar and 80°C, b) 100% RH, a total pressure of 1.5 bar and 80°C.

Hydrogen-Oxygen polarization curve:

Further comparisons on the effect of the RH value are shown in *figure IV-39* below. The possible improvements in the polarization curve are very significant. For 100% RH and 100%-80% RH at high current densities, the observed drop in performance might be related to **i/** flooding issues due to the inaccessibility of protons to the catalytic sites; **ii/** low use of the total Pt surface; **iii/** inhomogeneous protons transfer within the membrane and the absence of ionomer. Lowering the HR at the anode side, we tend to overcome this issue, which might be attributed to a better use/access of the catalytic surface and an easier proton transfer.

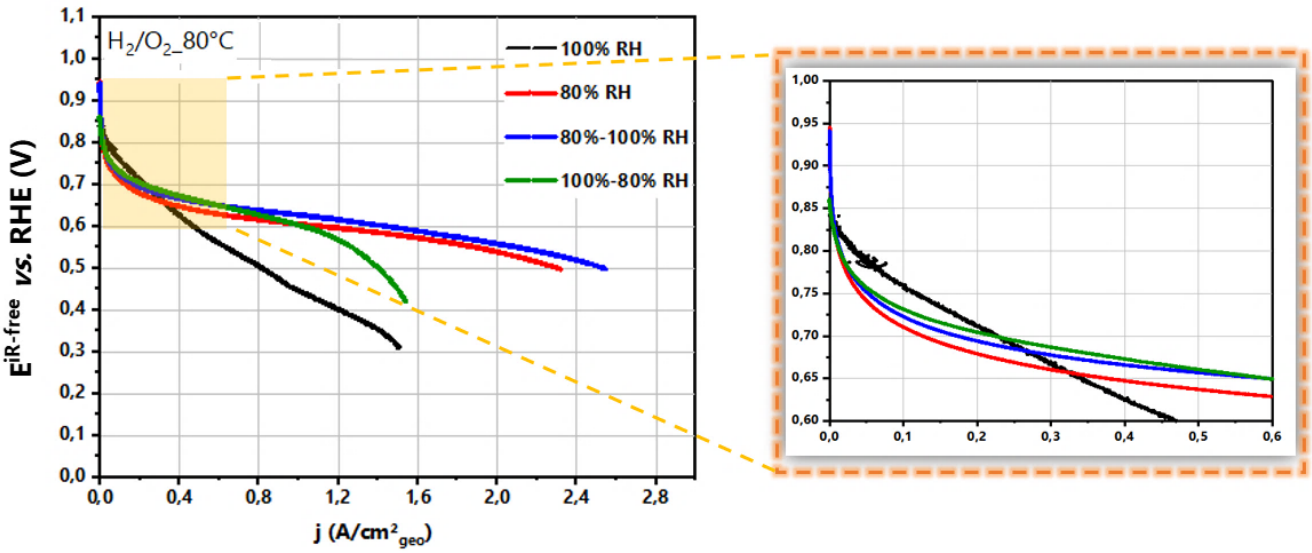

Figure IV-39: Comparison of fuel cell's ohmically-corrected polarization curves of PtNiNTs cathodes at operating conditions in the order of anode/cathode in H_2/O_2, a cell temperature of 80°C, at different relative humidity values and a total pressure of 1.5 bar, 1.38 bar, 1.38-1.5 bar, and 1.5-1.38 bar at 100% RH, 80% RH, 80%-100% RH, and 100%-80% RH, respectively.

Hydrogen-Air polarization curve:

Polarization curves were obtained during regular fuel cell operation in H_2/Air. Interestingly in H_2/Air environment, performance assessed by the polarization curve at 100%-80% HR has shown significant improvement compared to the different test conditions. It might be due to a better flow of protons in balanced hydration of the membrane at lower RH at the cathode side.

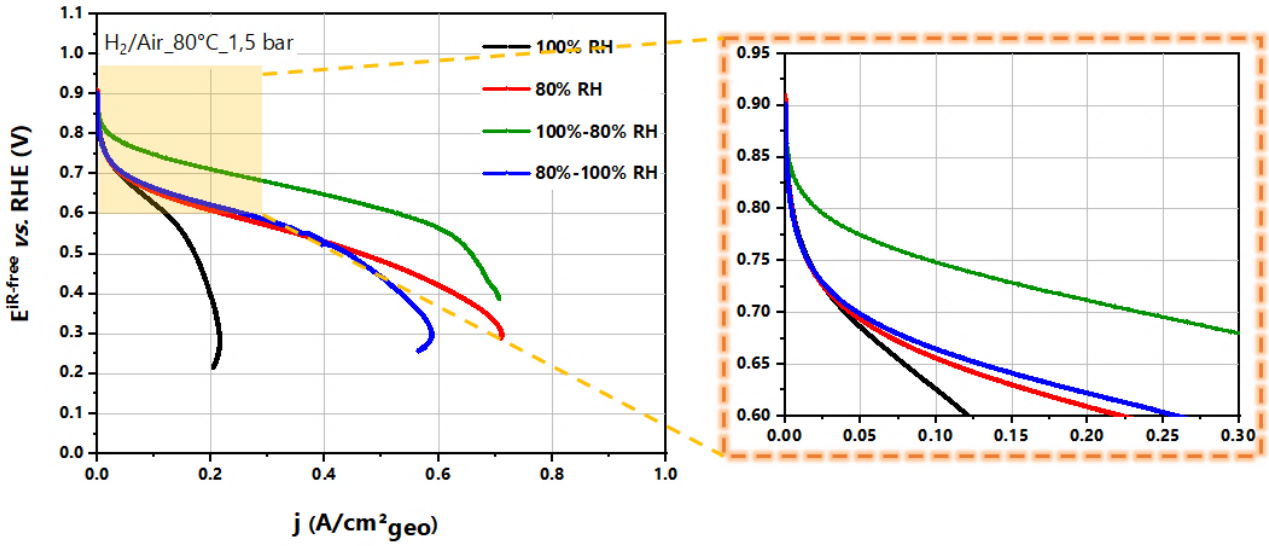

Figure IV-40: Comparison of fuel cell's ohmically-corrected polarization curves of PtNiNTs cathodes at operating conditions in the order of anode/cathode in H_2/Air, a cell temperature of 80°C, at different relative humidity values and a total pressure of 1.5 bar, 1.38 bar, 1.38-1.5 bar, and 1.5-1.38 bar at 100% RH, 80% RH, 80%-100% RH, and 100%-80% RH, respectively.

II.3.3 AST: PtNiNTs Degradation

A degradation test was carried out by applying the same voltage-cycling protocol mentioned earlier (for both Pt/C and PtNiNWs) by applying 50K load-cycles to the MEA. Then, we evaluated the evolution of the electrochemical surface area. The ECSA determination via H_{UPD} after degradation reads ~14.5 cm^2_{Pt}/cm^2_{geo}, translated to ~37% loss in the ECSA. Also, we extracted the ohmic resistance from the Nyquist, and it reads EIS 0.031 Ω, two times lower than the ohmic resistance obtained before degradation.

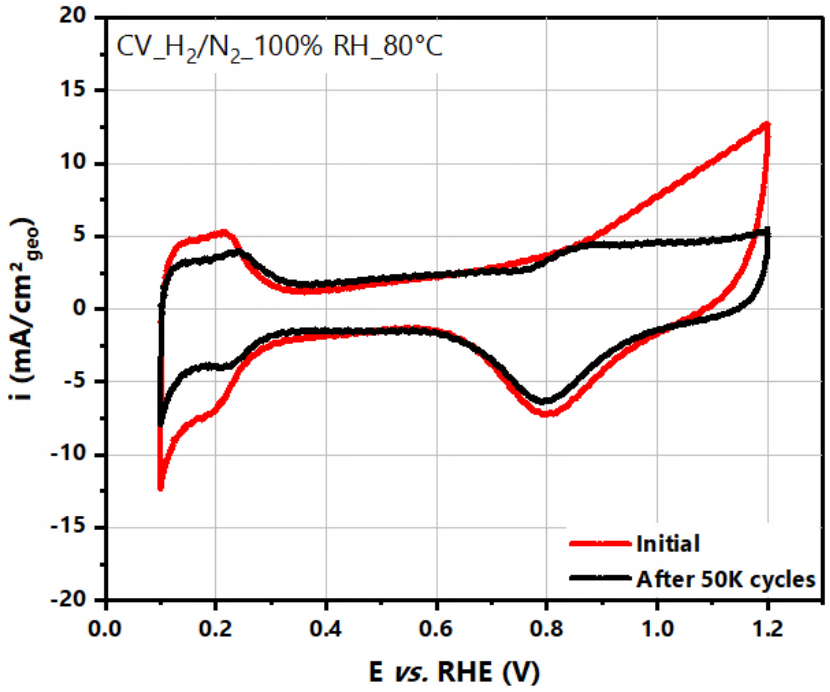

Figure IV-41: Comparison of voltammograms before degradation (red plot) and after 50K cycles (black plot) conducted in H_2/N_2 at 80°C and relative humidity of 100% and a total pressure of 1 bar, recorded at a potential sweep rate of 200 mV/s.

We compared the polarization curves at different HR (*figure IV-42).* Beforehand, they are ohmically corrected. We noticed a significant decrease in the resistance after the ASTs at all RH conditions. This similar behavior to Pt/C and PtNiNWs electrodes might be due to the CL's thinning or depolluting the membrane from cationic pollutants.

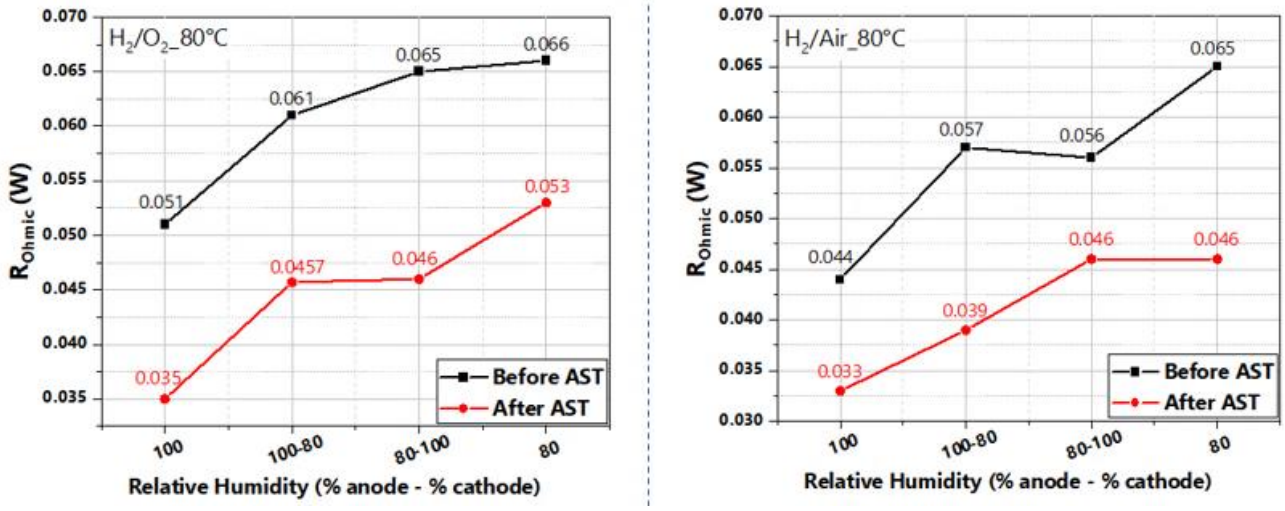

Figure IV-42: Evolution of the ohmic resistance at 0.65 $V_{iR\text{-}free}$ for different RH values in H_2/O_2 and H_2/Air at 80°C for PtNiNTs.

As evidenced in *figure IV-43* and *figure IV-44* below, a significant loss in performance was observed. At 100% RH for both H_2/O_2 and H_2/Air conditions, we extracted a loss in performance of 35% and 25%, respectively. At 0.65 $V_{iR\text{-}free}$, when the current density is increasing, we noticed a drop of ~43% in H_2/O_2 at 80%-100% RH and ~82% in H_2/Air at 100-80% RH for nanotubes (*figure IV-45*).

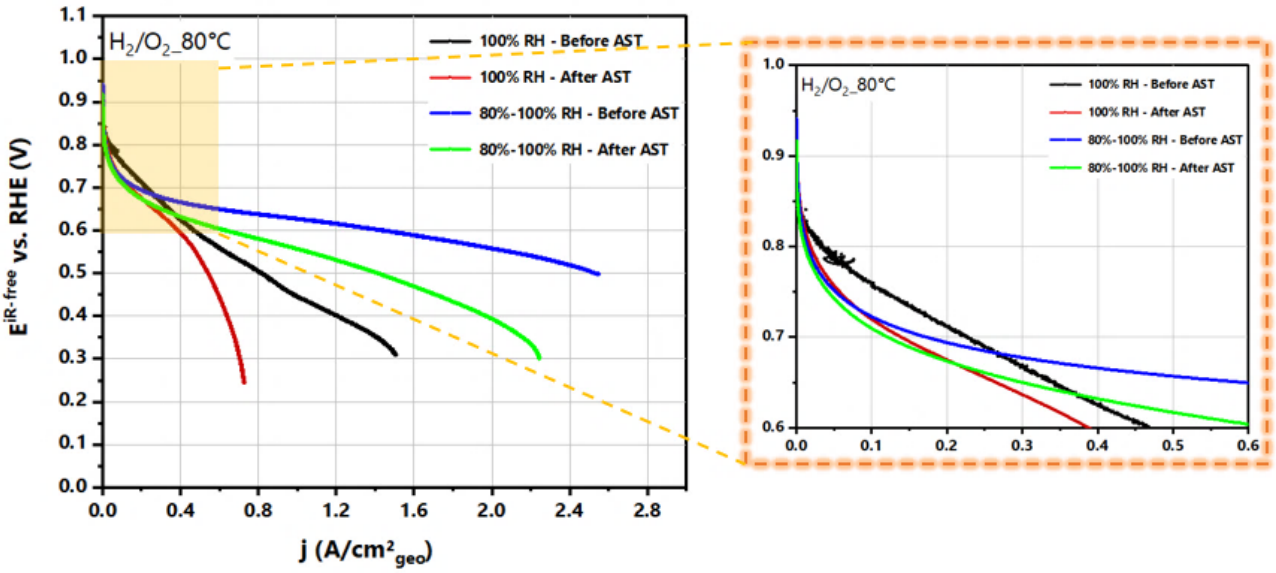

Figure IV-43: Comparison of fuel cell's polarization curves (corrected from ohmic drop) of PtNiTWs cathodes at operating conditions in H_2/O_2, cell temperature of 80°C, at different relative humidity values and total pressure (in the order of anode/cathode) of 1.5 bar and 1.38-1.5 bar, at 100% RH and 80%-100% RH, respectively, before and after 50K load cycles.

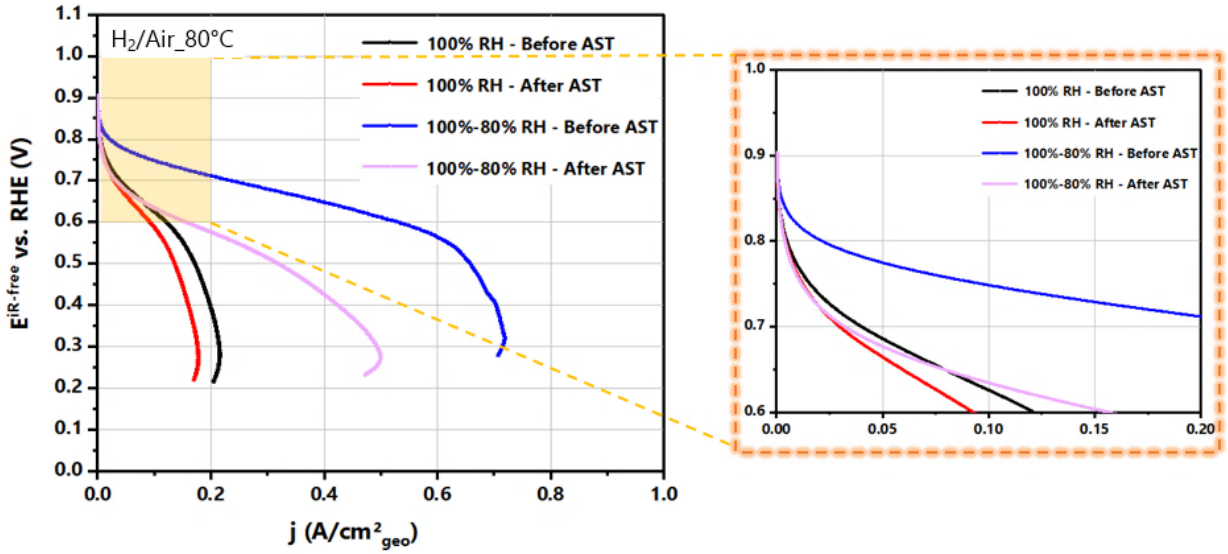

Figure IV-44: Comparison of fuel cell's polarization curves (corrected from ohmic drop) of PtNiTWs cathodes at operating conditions in H_2/Air, cell temperature of 80°C, at different relative humidity values and total pressure (in the order of anode/cathode) of 1.5 bar and 1.5-1.38 bar, at 100% RH and 100%-80% RH, respectively, before and after 50K load cycles

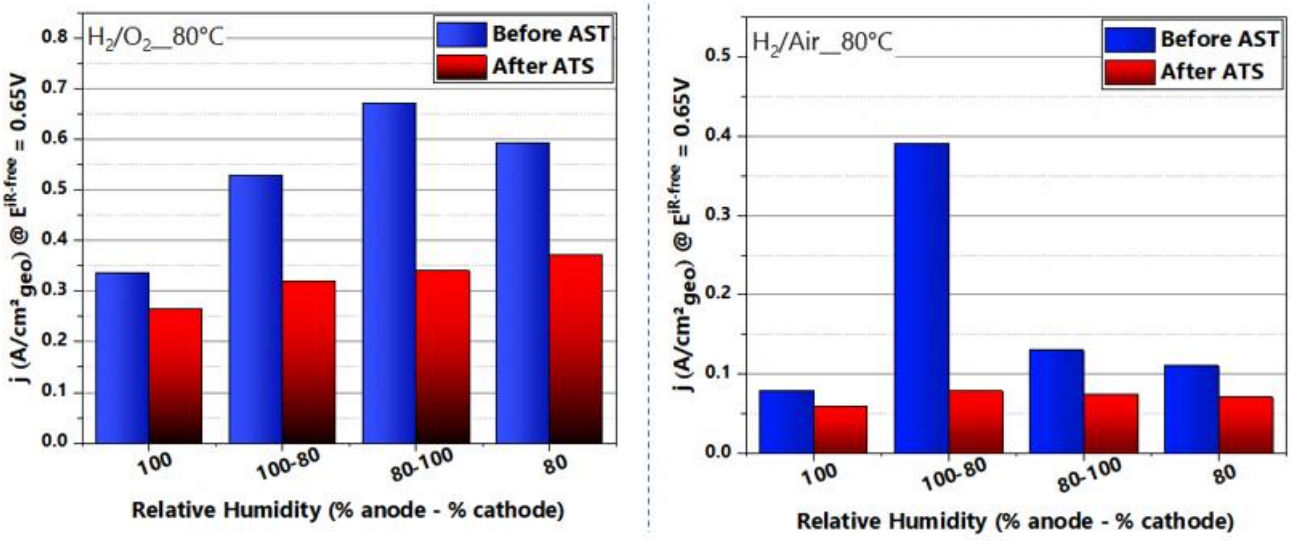

Figure IV-45: Comparison of the performance at 0.65 $V_{iR\text{-}free}$ before and after AST in H_2/O_2 and H2/Air at different relative humidity values.

II.3.4 Performance comparison

PtNiNTs showed greatly improved stability compared to Pt/C and PtNiNWs. As shown in *figure IV-46* below, we compared the activities, platinum surface, and the evolution of the ECSA after AST. The low loss of Pt surface (37% for NTs against 87.5% for Pt/C) reported that the degradation mechanisms are different in both structures.

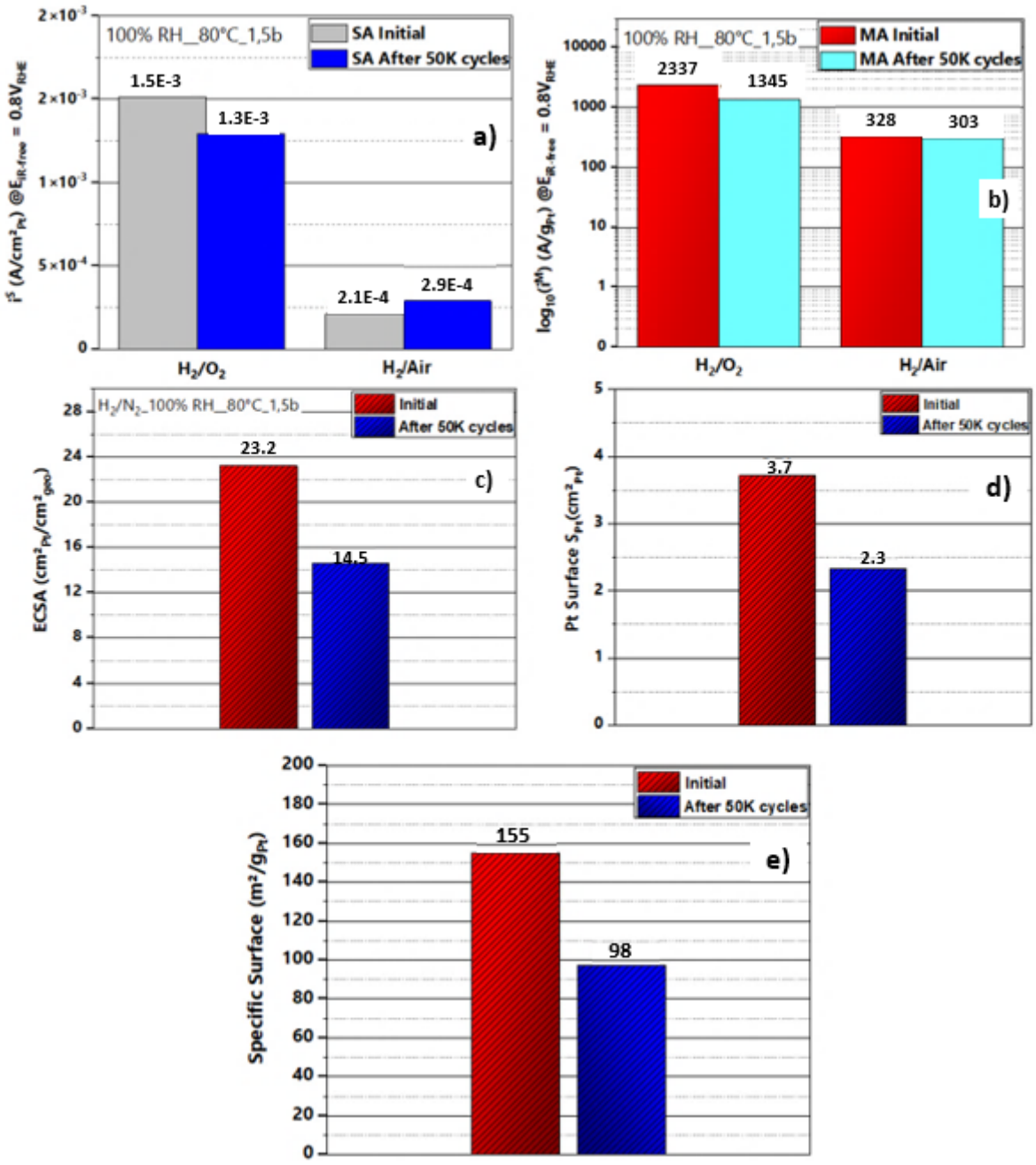

Figure IV-46: Performance comparison of the MEA with PtNiNTs at a cathode at a loading of 14 $\mu g_{Pt}/cm^2$ before degradation and after 50K potential cycles in H_2/O_2, H_2/Air, and H_2/N_2: a) and b) specific activity and mass activity data recorded at $E_{iR\text{-}free}$=0.8 V_{RHE}, c) ECSA values before and after degradation, d) Specific surface in m^2/g_{Pt}, and e) Platinum total surface before and after degradation.

PtNiNTs exhibited, after degradation, a 37% loss of the ECSA (similar to PtNiNWs) against 87% of loss in Pt/C. In fact, what is striking here, the MA and SA of NTs (obtained at 100% RH, 80°C, 1.5 bar) showed more resistance toward the AST, confirming higher durability of the NTs compared to the NWs and Pt/C. Contrary to expectations, much to our surprise, the specifiic activity in H_2/Air after degradation showed an increase of 37%. The central

hypothesis that would support this result (*i.e.*, stability) is the reorganization of the alloy's surface and better use of the catalyst's specific surface.

	% of Mass Activity loss		**% of Specific Activity loss**	
	Pt/C	PtNiNTs	Pt/C	PtNiNTs
H_2/O_2	97	42.4	63	14.5
H_2/Air	98	7	71.5	**-37**

During the load-cycle AST, we might reveal a lower loss of Ni from NTs comparing to NWs, thus the better activity of the NTs. Two explanations are likely to be the reason for this observation **i/** the effect of thermal treatment, leading to form PtNi alloy, which could exhibit a better cohesion between the two elements of the alloy, leading to an improvement in the electronic structure of the catalyst with marked changes in the catalytic properties (as reported in the literature about the PtNi alloys activity); **ii/** the acid leaching process used to remove the excessive Ni in the core in the case of NTs, causing possible less pollution of the membrane.

III. Comparison of performance and activities of the tested cathodes

Performance comparison:

We compared the performance of each MEA, before and after AST at RH values in which we got the best performances (100% RH for Pt/C, 100% RH for PtNiNWs, and 80%-100% RH for PtNiNTs), as displayed in *figure IV-47*. Relying on the polarization curves, we can notice a high sensitivity of PtNi NWs and PtNiNTs toward RH. The latter appeared to affect the electrode's performance.

Pt/C electrodes with low Pt loading faced drastic voltage and activity losses after AST. They have shown a poorly resistance toward aging with a significant loss of ECSA.

Subsequently, for PtNiNWs and PtNiNTs, at fully humidified conditions (100% RH), the PtNi nanostructures have also shown higher performance at low current densities

vis-à-vis the different values of %RH (at the anode and cathode), but the performance drops at high current densities because of the inaccessibility of O_2 due to flooding.

At lower %RH, the ionic conductor resistance increases due to the membrane drying out. We can also assume lower H^+ access and thus the misuse of the catalyst on the nanostructure that does not include any proton conductor at low current densities. After 50K cycles of AST, we assumed that the drop in performance and activity might be due to several factors:

- Drop in the ECSA;
- Ni^{2+} ion contamination of the ionomer leading to a decrease of the accessibility of H^+ into the catalyst;
- Change in the alloy's composition due to Ni dissolution;
- Possible change in preferred crystalline orientations on nanoparticles;
- PtNiNWs/NTs detachment from the membrane.

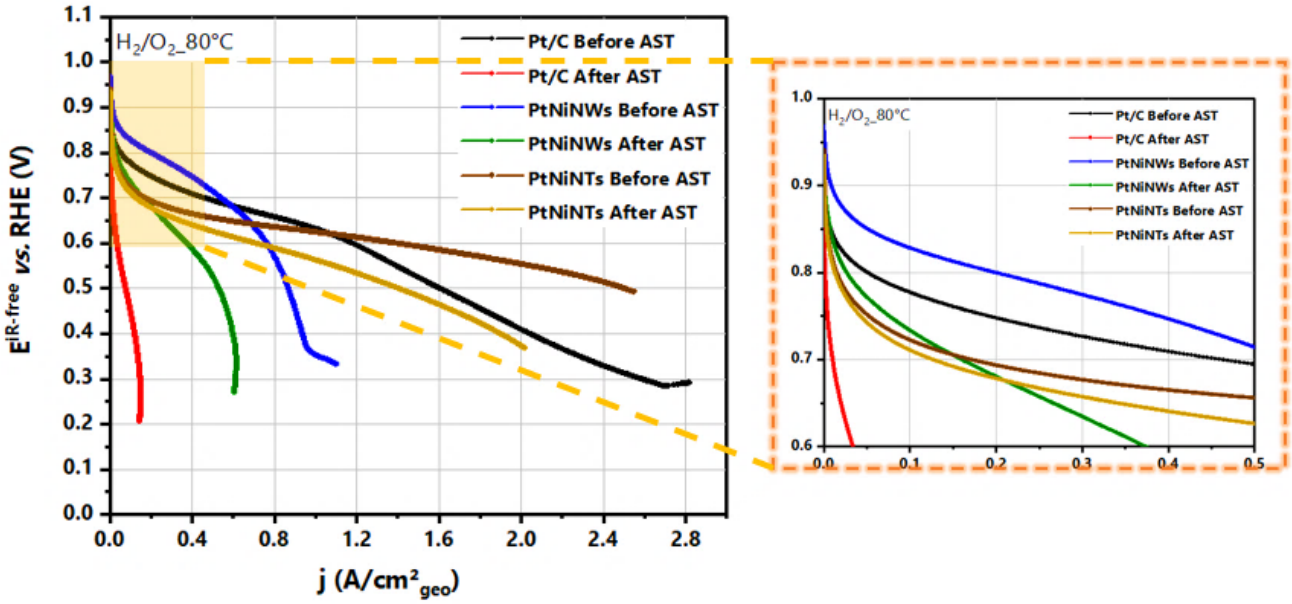

Figure IV-47: Comparison of fuel cell's polarization curves (corrected from ohmic drop) of Pt/C, PtNiNWs and PtNiNTs MEAs at operating conditions in H_2/O_2, cell temperature of 80°C, at different relative humidity values and total pressure (in the order of anode/cathode: 100% RH and 1.5 bar, 80%-100% RH and 1.38-1.5 bar), before and after 50K load cycles.

By comparing the performance of these MEAs, even if it is clear that RH affects the electrode's performance, the comparison still not significant because we used different

catalysts with different geometrical areas. It would be beneficial to compare specific and mass activities for further information.

Activity, stability, and durability comparison:

We can notice better durability of nanotubes compared to the other structures. For Pt/C, the impact of the ECSA's loss is evident in the drastic drop of performance after degradation. For PtNiNWs, the decrease of the ECSA might not be the only factor affecting the performance. Moreover, PtNiNTs behave much better than PtNiNWs most probably due to the use of both the inner and the outer surface of the tubes. *Figure IV-48* below depicts the evolution of ECSA and Pt specific surface before and after AST.

Drawing upon the RDE experiments obtained in literature, one can say that in the case of PtNi, even if the ECSA is less significant compared to Pt/C, the performance after AST was impacted. We could attribute this result to untapped Pt sites, membrane poisoning with nickel cations, or reorganization of Pt active facets, which might affect the PtNi alloy.

For PtNiNWs and PtNiNTs, however, with a lower platinum surface determined by H_{UPD}, we tended to get higher values of the ECSA, which might depend on the mechanisms related to the chemisorption of H^+ protons on the PtNi alloy.

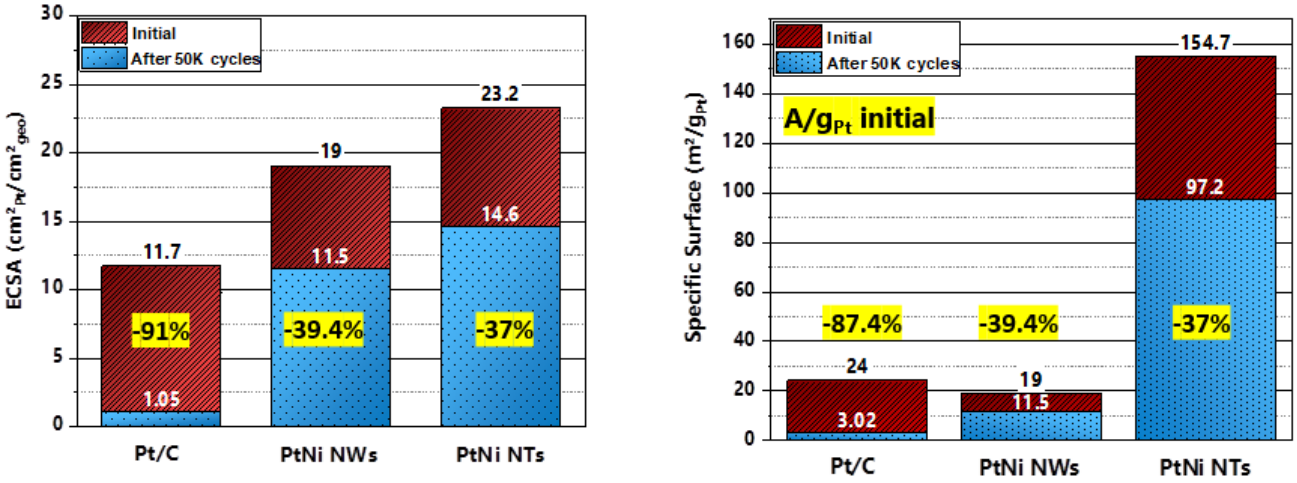

Figure IV-48: Electrochemical surface area (ECSA) and the Pt-specific surface comparison electrodes at operating conditions in H_2/O_2, cell temperature of 80°C, 100% RH and 1.5 bar, before and after 50K load cycles.

In comparing specific and mass activity, PtNiNWs have shown the best specific activity while PtNiNTs have shown the highest mass activity. The comparison of activities has demonstrated noticeable stability of PtNiNTs compared to PtNiNWs and Pt/C toward AST cycles as depicted in *figure IV-49* below.

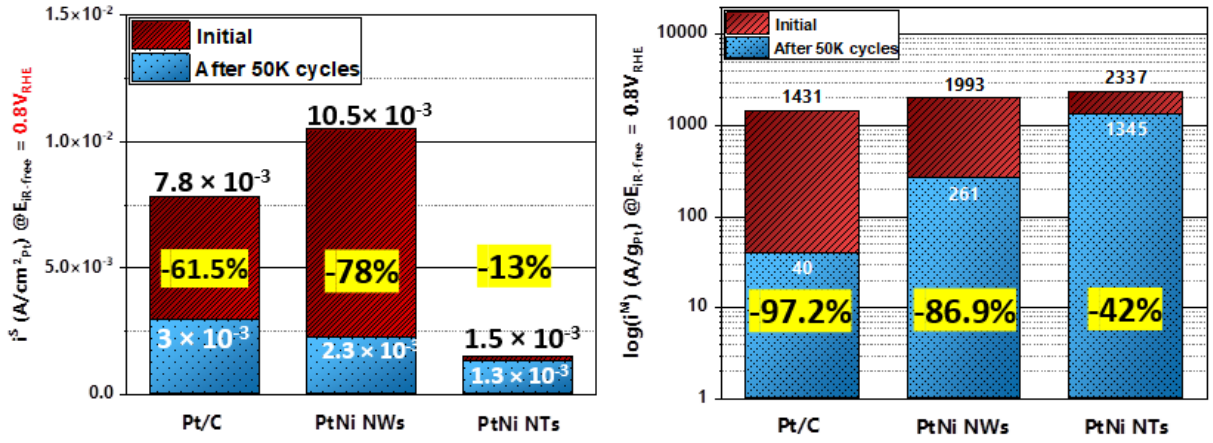

Figure IV-49: Specific and Mass activity comparison for Pt/C, PtNiNWs, and PtNiNTs electrodes at $E_{iR\text{-}free}$=0.8 V_{RHE} at operating conditions in H_2/O_2, cell temperature of 80°C, 100% RH and 1.5 bar, before and after 50K load cycles.

Conversely, the higher mass activity of the NWs (1.5 times) compared to Pt/C did not enhance the performance of the MEA (even with a higher loading of Pt for NWs). However, the performance of the Pt/C exceeded that of PtNiNWs (as referred to in *figure IV-50* and *figure IV-51* below), thus a better use of the Pt surface on Pt/C compared to other structures.

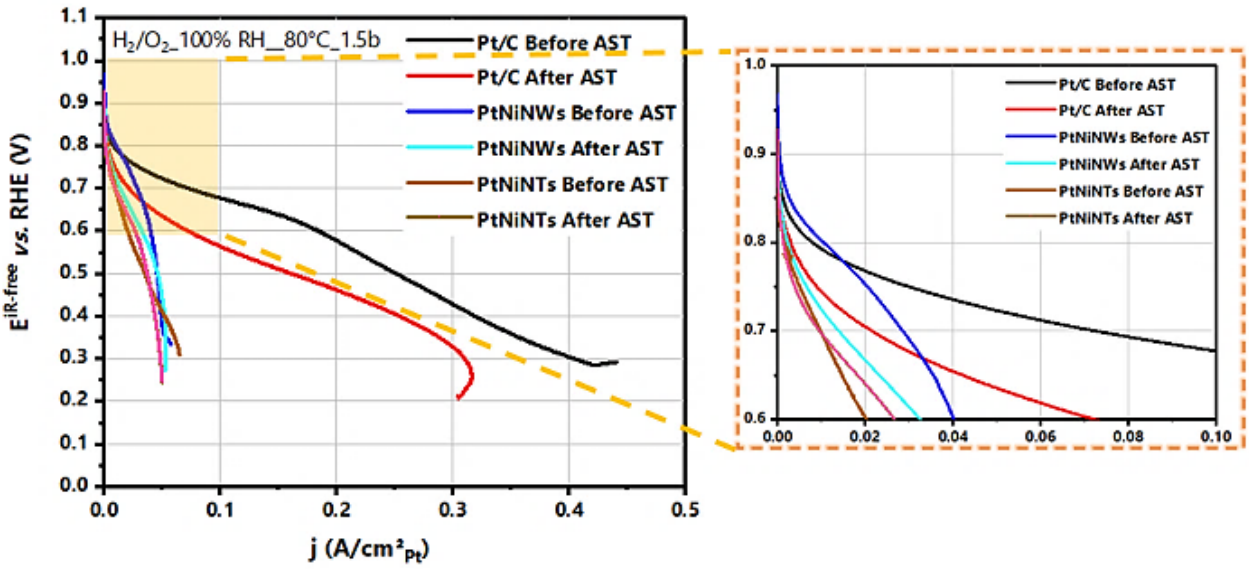

Figure IV-50: Comparison of fuel cell's polarization curves (corrected from ohmic drop) as a function of the specific surface of Pt/C, PtNiNWs, and PtNiNTs MEAs at operating conditions in H_2/O_2, cell temperature of 80°C, 100% RH and 1.5 bar, before and after 50K load cycles.

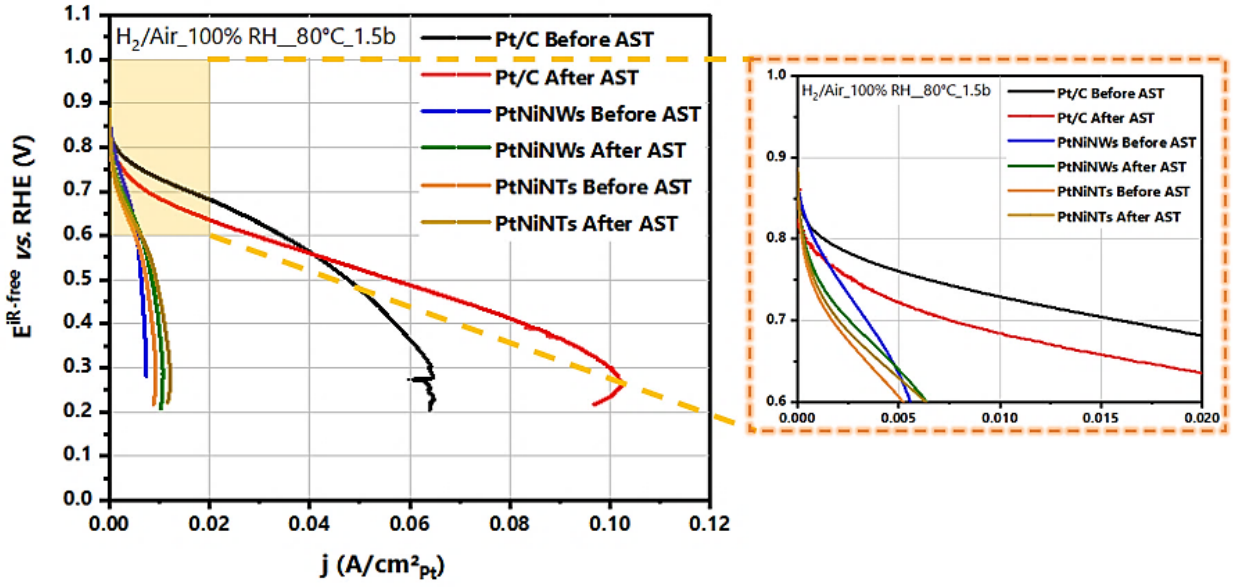

Figure IV-51: Comparison of fuel cell's polarization curves (corrected from ohmic drop) as a function of the specific surface of Pt/C, PtNiNWs, and PtNiNTs MEAs at operating conditions in H_2/Air, cell temperature of 80°C, 100% RH, and 1.5 bar, before and after 50K load cycles.

The main result covered in this comparison is the sharp increase of mass activity obtained for the nanotubes at a very low Pt loading. On comparing the polarization curves as a function of the specific mass (*figure IV-52* and *figure IV-53*), we can clearly observe the best mass activity of the PtNi, thus a better use of the Pt quantity during operation.

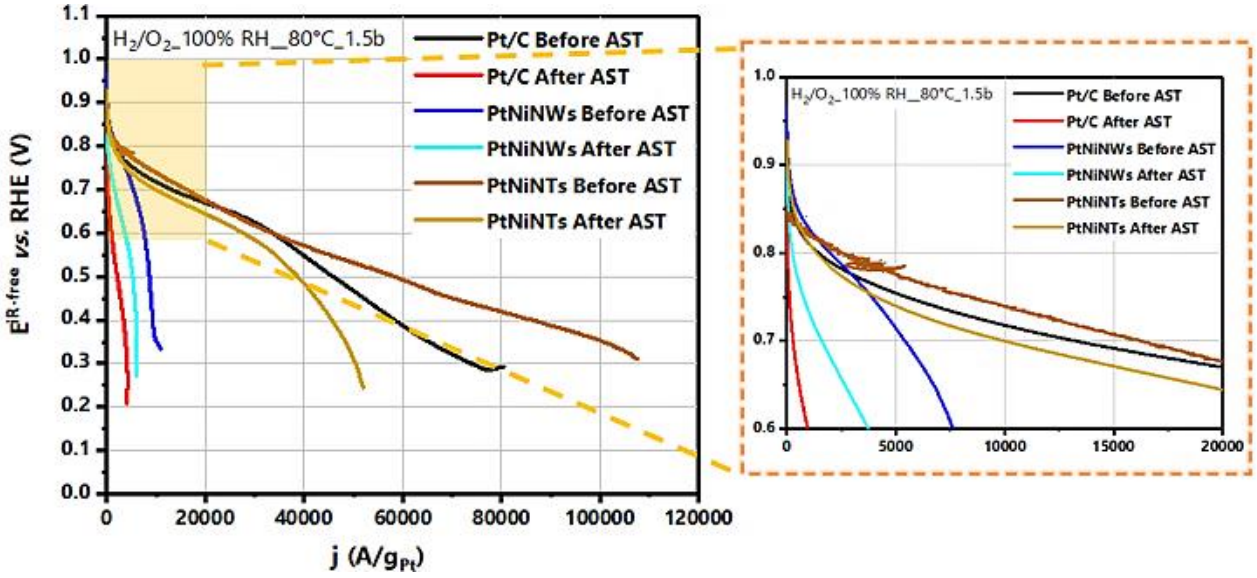

Figure IV-52: Comparison of fuel cell's polarization curves (corrected from ohmic drop) as a function of the specific mass of Pt/C, PtNiNWs, and PtNiNTs MEAs at operating conditions in H_2/O_2, cell temperature of 80°C, 100% RH and 1.5 bar, before and after 50K load cycles.

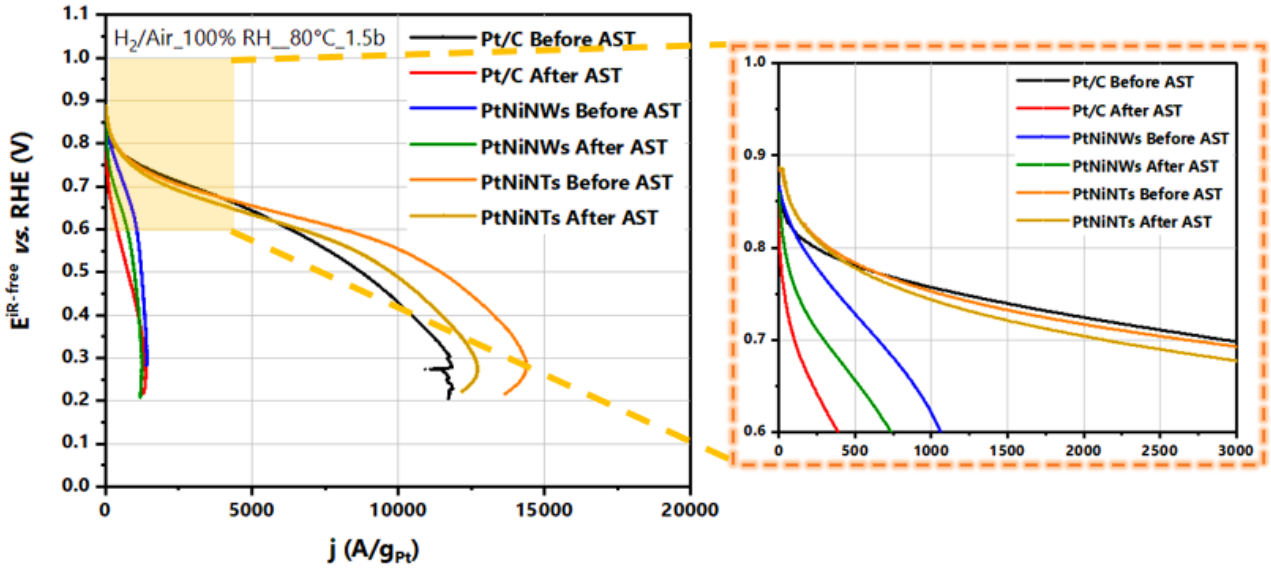

Figure IV-53: Comparison of fuel cell's polarization curves (corrected from ohmic drop) as a function of the specific mass of Pt/C, PtNiNWs, and PtNiNTs MEAs at operating conditions in H_2/Air, cell temperature of 80°C, 100% RH and 1.5 bar, before and after 50K load cycles.

Tafel Plot: Activity Comparison

To guide synthetic work and determine activities in a more detailed way, it was difficult to extract kinetic parameters from the Tafel plot (*figure IV-54*) because of the huge impact on OCV (Open Circuit Voltage) of H_2 cross-over from the anode side through the membrane due to the low ECSA. There are mixed potentials that made the analysis

difficult. There is large uncertainty on the Tafel slope, on the equilibrium voltage, and thus on the exchange current density.

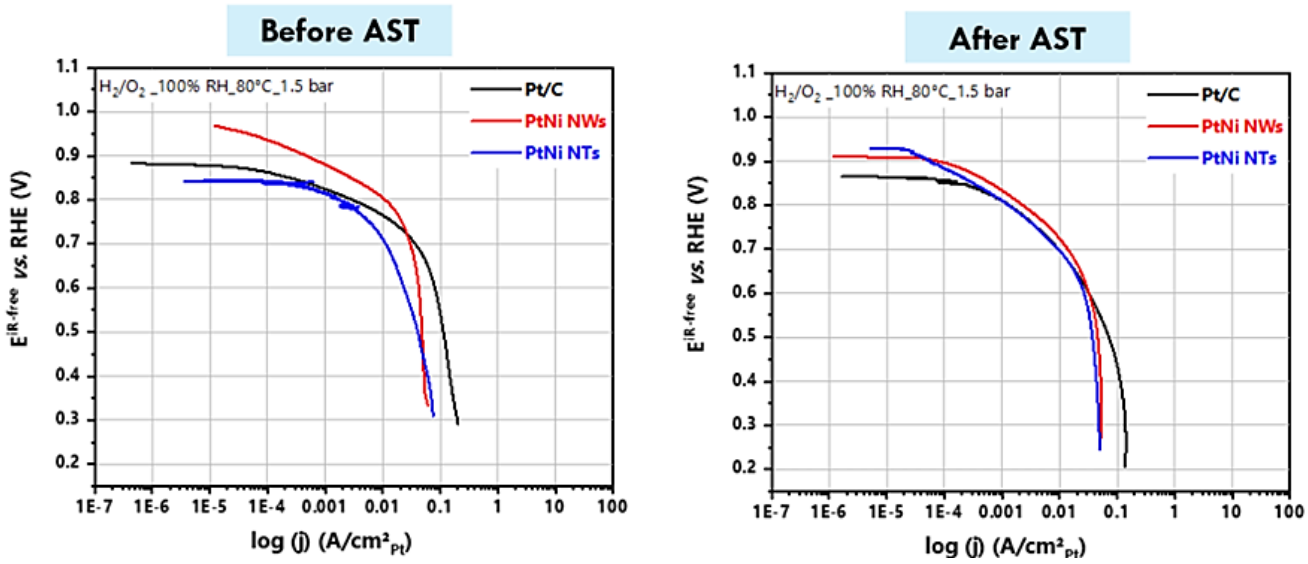

Figure IV-54: Specific Tafel plot for oxygen reduction reaction under fully humidified H_2/O_2 atmosphere at 80°C and 1.5 bar, before and after AST.

Transport losses from EIS?

let it be emphasized here that it is extremely difficult (if possible) to extract O_2 transport losses from EIS, even on the conventional electrode. This is currently a subject of research. Regarding the proton resistance in the electrode, I tried to fit spectra with the model classically described in the literature but, due to the thinness of the electrode, the values are too small to be measured. For instance, for Pt/C, we have tested thin electrodes, so the separation of transport losses of thin electrodes might be hard due to problems of discontinuities in the conductive carbon phase or in the proton-conducting ionomer.

Summary of comparisons:

This study set out to determine that higher durability and stability were observed for the PtNiNTs. Further analysis should be carried out to fathom the ORR kinetics and transport deeply. Also, to analyze the quantity of the dissolved Ni in the membrane, which is believed to be far less than PtNiNWs. *Table IV-6* below contextualizes a brief review of the properties of each MEA tested in this work before and after aging.

	$I_s^{0.8V\ iR\text{-}free}$ (A/cm^2_{Pt})	$I_m^{0.8V\ iR\text{-}free}$ (A/g_{Pt})	ECSA (cm^2_{Pt}/cm^2_{geo})	S_{Pt} (cm^2_{Pt})	Specific Surface (m^2/g_{Pt})	Loading ($\mu g_{Pt}/cm^2$)
Pt/C Before	7.8×10^{-3}	1431	12	15.2	24	35
Pt/C After	2.9×10^{-3}	39	1.05	2	3	
PtNiNWs Before	10.4×10^{-3}	1993	19	5.7	19	100
PtNiNWs After	2.3×10^{-3}	261	11.5	3.45	11.5	
PtNiNTs Before	1.5×10^{-3}	2337	23.3	4	155	14-15
PtNiNTs After	1.3×10^{-3}	1344	14.5	2.3	97.3	

Table IV-6: Summary of activities, ECSA, platinum surface, and Pt-loading of each tested cathode: Pt/C, PtNiNWs, and PtNiNTs.

List of figures and tables

References

[1]. P. Oberholzer, P. Boillat, Local Characterization of PEFCs by Differential Cells: Systematic Variations of Current and Asymmetric Relative Humidity, J. Electrochem. Soc. 161 (2014) F139–F152.

[2]. S. Prass, J. St-Pierre, M. Klingele, K.A. Friedrich, N. Zamel, Hydrogen Oxidation Artifact During Platinum Oxide Reduction in Cyclic Voltammetry Analysis of Low-Loaded PEMFC Electrodes, Electrocatalysis. 12 (2021) 45–55.

[3]. J. Zhang, H. Zhang, J. Wu, J. Zhang, Chapter 1 - PEM Fuel Cell Fundamentals, in: J. Zhang, H. Zhang, J. Wu, J. Zhang (Eds.), Pem Fuel Cell Testing and Diagnosis, Elsevier, Amsterdam, 2013: pp. 1–42.

[4]. H. A. Gasteiger, S. S. Kocha, B. Sompalli, F. T. Wagner, Activity benchmarks and requirements for Pt, Pt-alloy, and non-Pt oxygen reduction catalysts for PEMFCs, Applied Catalysis B: Environmental 56 (2005) 9–35.

[5]. T. Shinagawa, A.T. Garcia-Esparza, K. Takanabe, Insight on Tafel slopes from a microkinetic analysis of aqueous electrocatalysis for energy conversion, Sci Rep. 5 (2015) 13801.

[6]. A. Kuzume, E. Herrero, and J. M. Feliu, Oxygen reduction on stepped platinum surfaces in acidic media, J. Electroanal. Chem. (2007), vol. 599, pp. 333–343.

[7]. M. Zhiani, S. Majidi, Effect of MEA conditioning on PEMFC performance and EIS response under steady state condition, International Journal of Hydrogen Energy. 38 (2013) 9819–9825.

[8]. L. Dubau, L. Castanheira, F. Maillard, M. Chatenet, O. Lottin, G. Maranzana, J. Dillet, A. Lamibrac, J.-C. Perrin, E. Moukheiber, A. ElKaddouri, G.D. Moor, C. Bas, L. Flandin, N. Caqué, A review of PEM fuel cell durability: materials degradation, local heterogeneities of aging and possible mitigation strategies, WIREs Energy and Environment. 3 (2014) 540–560.

[9]. A. Kusoglu, A.Z. Weber, New Insights into Perfluorinated Sulfonic-Acid Ionomers, Chem. Rev. 117 (2017) 987–1104.

General Conclusion

Electricity is the lifeblood of many aspects of our world. Facing this unprecedented stare of pollution, we tend to react in a strict way, mainly in decarbonizing the existing energy sources and developing renewable energies. Questions abound about *HOW can we do it effectively*? Globalization is causing increasingly severe energy challenges unless we build new technologies. Hydrogen has shown great potential as a viable energy vector.

PEMFC has been promoted as one solution for clean, sustainable transportation. One of its major limitations is, alongside the cost, the durability of the MEA. Durability is a critical criterion for judging the practical viability of a new catalyst. The sluggish ORR kinetics at the cathode side opened vast areas of developing new nanomaterials as alterative electrocatalysts to the conventional Pt/C.

In summary, we have presented a new multi-step route for elaborating oriented PtNi nanowires and nanotubes devoted to the PEMFC cathode:

- Optimization of the fabrication process of the anodic aluminum oxide. Tuning its geometry enabled us to use it as a flexible mold for the growth of Ni nanowires. The latter was developed and optimized during this Ph.D. thesis, allowing a great control of the NWs' length.
- The structural analysis of the NiNWs covered the presence of an outer oxide layer that led to uncontrolled galvanic displacement.
- Reproducible PtNiNWs were obtained in a non-confined system (etching aluminum oxide after the growth of NiNWs) while performing a galvanic displacement process in K_2PtCl_4 diluted in a 0.05 ml HCl solution (combined GD and AL), heated up to 35°C for 7-8 minutes. HCl has shown an influence on the kinetic rate of the GD reaction. The PtNiNWs arrays are then transferred into a Nafion® membrane via an optimized hot-pressing process and tested in a real fuel cell.
- Reproducible PtNiNTs were achieved via galvanic displacement in 1mmol K_2PtCl_4 solution heated up to 80°C for 1.5 hours. A thermal treatment (at 250°C) follows this

step in a reducing environment (H_2/Ar 5%) for 2 hours. The intermediate PtNiNWs were then transferred into a Nafion® membrane. After that, the AL process is performed in a 0.5 M H_2SO_4 solution heated to 30°C. The PtNiTs on Nafion® were mounted in an MEA for fuel cell tests.

- Fuel cell tests of PtNiNWs (0.08-0.1 mg_{Pt}/cm^2) and PtNiNTs (0.014 mg_{Pt}/cm^2) were performed and compared to a low Pt-loading conventional catalyst (Pt/C, 35 μg_{Pt}/cm at the cathode, 0.1 mg_{Pt}/cm^2 at the anode). The latter exhibits a closer ECSA value to NWs and NTs. Relative humidity showed more significant effects on the performance of NWs and NTs due to water content in the membrane. In fully humidified conditions, the flooding phenomenon was more likely to occur. For the NWs, better performance was obtained at low current densities at 100% RH but dropped at higher current densities. Lowering the RH to 80%, the performance at low current densities decreased while the limit current at 0.4 V_{RHE} reached 1.2 A/cm^2_{geo} (against 0.9 A/cm^2_{geo} in 100%RH).

On the other hand, NTs exhibited better performance at 80%-100% RH. At 0.4 V_{RHE}, the value of the limit current reached ~2.4 A/cm^2_{geo}. Also, Low ECSA seemed to limit the performance of the MEAs. Greater durability was attributed to PtNiNTs after the AST degradation protocol, which might be attributed to a different degradation mechanism of Pt alloyed to Ni, the higher activity of the PtNi alloy, the well-optimized structure of the cathode.

- In a nutshell, PtNiNWs offered the best specific activity while PtNiNTs exhibited the best mass activity and stability. In this context, this study offered a fresh and broader perspective for NTs (with post-processing optimization) as a promising route to be more investigated.

The experiments held during this Ph.D. enabled me to increase my curiosity about the performance of the PtNi alloy as an electrocatalyst for the PEMFC. When I started my first fuel cell tests during the last nine months, many questions and hypotheses have arisen to the surface, as we shall see in the next section dedicated to a variety of perspectives.

Perspectives

For a better understanding of the PtNiNTs and PtNiNWs, a pretty extended list of broader perspectives for continuing investigations on these structures is expressed below:

Further morphological and structural analysis:

1) Deeper structural analysis (TEM-HAADF coupled EDX) of the MEA after the nanowires/nanotubes transfer into the membrane to have better insight into their incorporation into the Nafion® membrane, before and after degradation. Also, to have a clear idea about their degradation mechanism.
2) XPS analysis of the samples to ascertain the nature of the Pt and Ni in each nanostructure, supported with XRD measurements.
3) MEA ICP-MS measurements after degradation to verify the amount of Ni dissolution into the membrane.

Further elaboration processes:

4) To figure out a chemical process to eliminate Ni Oxide from the nickel nanowire's surface before galvanic displacement. The process might include a pre-acid leaching process of the wires in an appropriate etching solution without affecting the nickel's quality, combined with a thermal treatment in a reducing environment (H_2/Ar, for instance).
5) Ionomer thin film coating onto PtNiNWs/NTs via electrospinning or spray, as depicted in the illustration below:

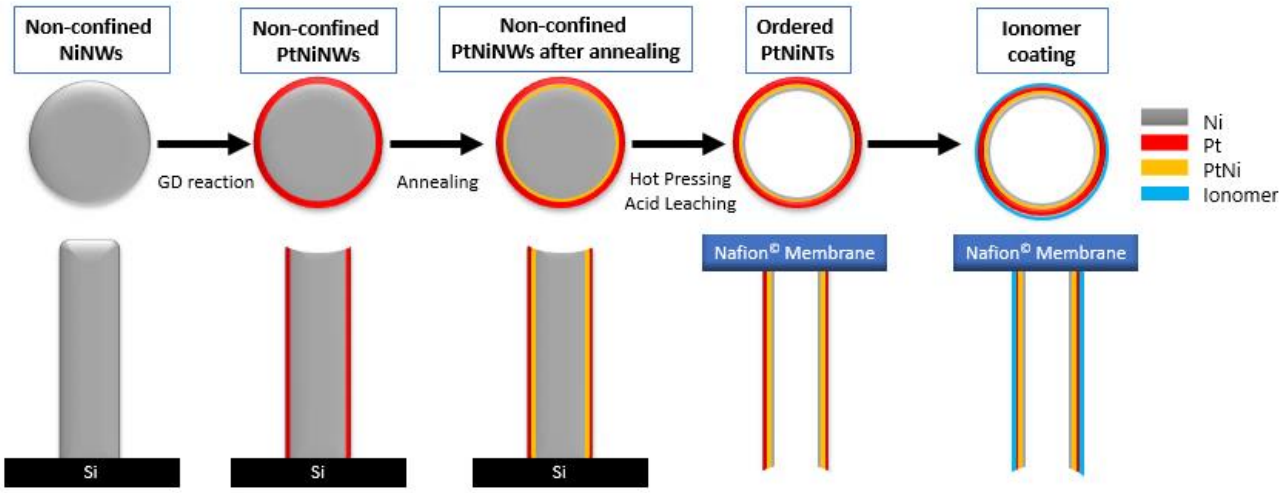

6) To extend our understating on the effect of the annealing on the PtNiNWs before acid leaching to strengthen the Pt-rich layer.
7) A profound electrochemical study of the ORR activity and transport limitation for both the NWs and the NTs.

Further MEA tests:

8) Test a large batch of the NTs and NWs in an operating fuel cell (*i.e.,* larger geometrical surface area).
9) Use a novel GDL architecture made of nanocarbon fibers (developed by Dr. Marie Fontana at CEA) alongside PtNiNTs. This combination might tackle the flooding issue at high RH and better water management.
10) Extend the fuel cell tests to assess the effect of the cell's temperature on the performance. Also, to elaborate larger nanotubes array (based on the large nanopores obtained via aluminum oxide anodization: 100nm in diameter and 800nm in thickness).
11) The development of more sophisticated NTs arrays, combining a physical vapor deposition of Platinum according to the following process highlighted below:

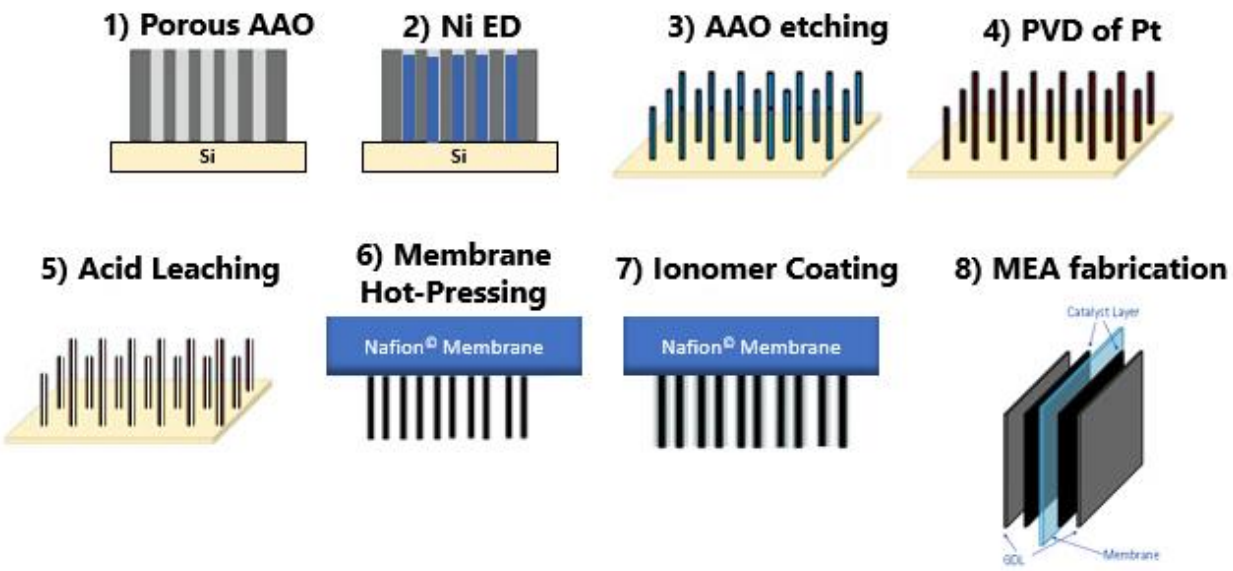

"We often talk of saving the planet, but the truth is that we must do these things to save ourselves. With or without us, the wild will return."

-David Attenborough

Appendices

Appendix A: Basic platinum-based heterogeneous electrocatalyst approaches. The four PEM fuel-cell electrocatalyst approaches (developed or under investigation) for the performance-limiting cathode ORR are shown, with Pt and Pt-alloy electrocatalysts listed according to the basic geometric structure of the catalyst particles and their supports. The main subcategories are highlighted in yellow. Catalyst approaches with the highest demonstrated activities are highlighted in blue [21].

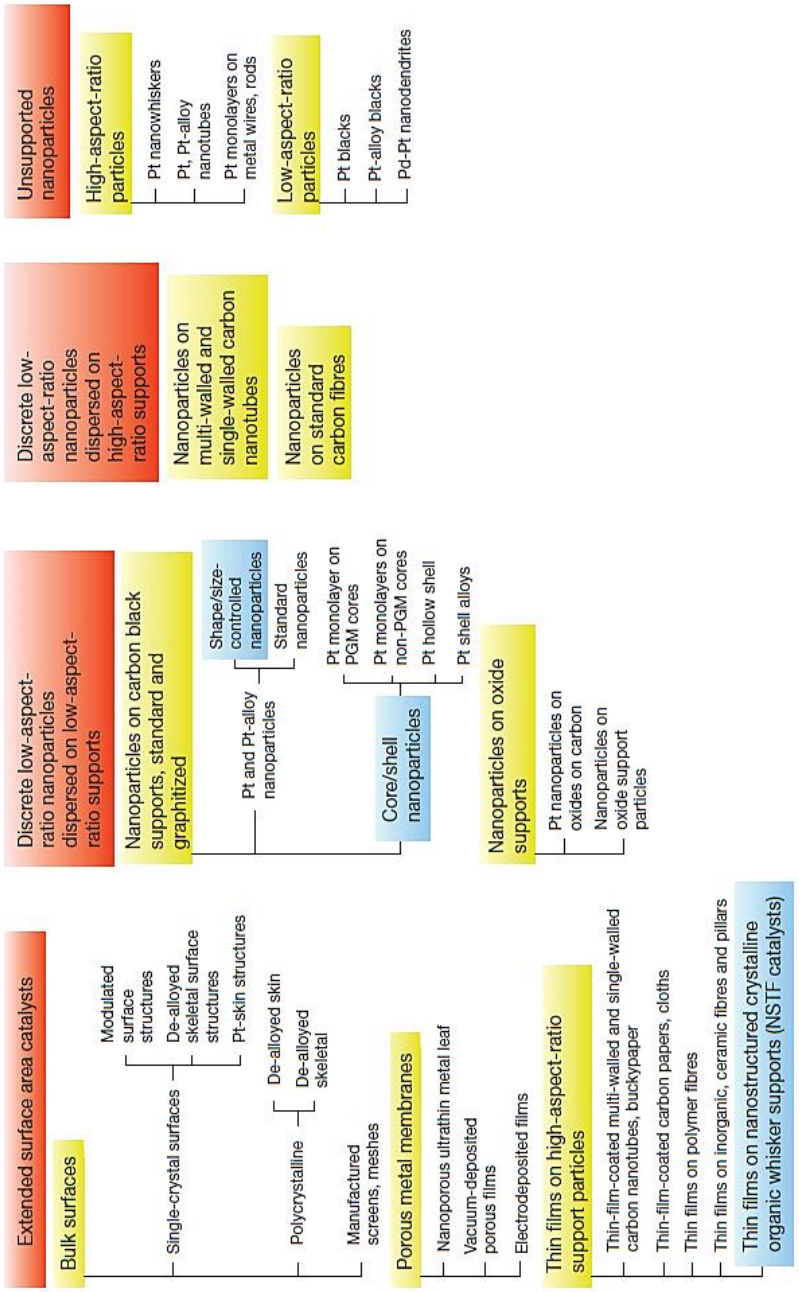

[21] Mark K. Debe, 4 | NATURE | VOL 486 | 7 JUNE 2012

Appendix B: Protocols for Testing PEM Fuel Cells and Fuel Cell Components:

Testing protocols for fuel cells and fuel cell components, developed in partnership with the U.S. DRIVE Fuel Cell Technical Team, are delineated in the Multi-Year Research, Development, and Demonstration Plan document provided by the DOE Fuel Cell Technologies Office.

The electrocatalyst protocol in Table P.1 is designed to assess cathode electrocatalyst durability through the use of a voltage square wave, in which successive cycles of surface oxidation and reduction cause accelerated catalyst degradation. The protocol uses a voltage range similar to that which is expected for an automotive drive cycle, and it seeks to maximize catalyst degradation while minimizing support corrosion. The protocol was designed to test PGM-based catalysts on carbon-based supports, and it may need to be modified to test different classes of materials.

Table P.1 Electrocatalyst Cycle and Metrics		
Cycle	Square wave cycle: steps between 0.6 V (3 s) and 0.95 V (3 s) with rise time of ~0.5 s or less; run polarization curve and ECSA at specified intervals. Single cell 25–50 cm^2	
Number	50.000 cycles	
Cycle time	6 s	
Temperature	80°C	
Relative humidity	Anode/cathode 100/100%	
Fuel/oxidant	H_2/N_2 (H_2 at 200 sccm and N_2 at 75 sccm for a 50-cm^2 cell)	
Pressure	Atmospheric pressure	
Metric [a]	**Frequency**	**Target**
Catalytic mass activity [b]	At beginning and end of test, minimum	<40% loss of initial catalytic activity
Polarization curve from 0 to >1.5 A/cm^2 [c]	After 0, 1k, 5k, 10k, and 30k cycles	<30 mV loss at 0.8 A/cm^2
ECSA/cyclic voltammetry	After 10, 100, 1k, 3k, 10k, 20k, and 30k cycles	<40% loss of initial area

[a] A protocol such as the one shown in Table P.9 should be used to recover reversible losses prior to measuring each metric.

[b] Mass activity in A/mg @ 150 kPa abs back pressure at 900 $mV_{iR\text{-}corrected}$ on H_2/O_2, 100% RH, 80°C, anode stoichiometry 2; cathode stoichiometry 9.5. A minimum hold time of 15 min is recommended, with the mass activity calculated based on the average

current during the last 1 min. Multiple points should be measured at low current, and the 0.9 $V_{iR\text{-}free}$ potential should be determined based on these measurements. Measured ORR current may be corrected for H_2 crossover. Based on the protocol published by Gasteiger et al., Applied Catalysis B: Environmental, 56 (2005): 9–35.

[c] Polarization curve per protocol in Table P.6. in the document.

Type: Attachment
URL: https://www.energy.gov/sites/prod/files/2017/05/f34/fcto_myrdd_fuel_cells.pdf
Accessed: 09/03/2021, 10:45:10 AM

“Even with all our technology and the inventions that make modern life so much easier than it once was, it takes just one big natural disaster to wipe all that away and remind us that, here on Earth, we're still at the mercy of nature. “

-Neil deGrasse Tyson

There are no endings, only new beginnings. . .

Summary

The PEM Fuel cell technology has attracted great attention for future energy conversion and storage applications. Its commercialization is still a matter of challenge due to the durability and cost limitations of the catalyst. In order to enhance their achievement on the market, it is mandatory to optimize the high costly catalyst and improve its durability and stability or to innovate a new structure of electrodes. Commercial Pt/C catalyst (nanoparticles 3–5 nm) supported carbon black is considered as the current standard catalyst offering high surface areas and high specific activity. Unfortunately, they are limited by various degradation barriers: the cost; the corrosion of the carbon support, and the Pt dissolution/agglomeration through electrochemical Ostwald ripening mechanism, which is reflected by a fast and significant loss of electrochemical surface area overtime during fuel cell operation.

This thesis focuses on reducing the amount of platinum and improving the performance and durability of membrane electrode assemblies MEAs, aiming to reduce their cost and encourage the development of PEMFCs. Previous studies have demonstrated that Pt-based catalysts such as PtCo, PtCu, and PtNi, etc., have shown to exhibit higher oxygen reduction reaction ORR activity than platinum for PEMFC and very promising enhancement in performance and stability for low Pt loading.

We aspired in this work to develop and control a new carbon-free architecture of the cathode, made only with vertically aligned PtNi nanowires and nanotubes supported onto a Nafion® membrane to improve performance and durability of the PEMFC at low Pt loading.

The fabrication process is based on a multistep process of fabrication: Elaboration and geometry tuning of the nanoporous anodic aluminum oxide used as a sacrificial template by the double-anodization technique; The pulsed electrodeposition process as an electrochemical route of Ni nanowires growth inside the aluminum oxide template; Controlled galvanic displacement process, which is an electrochemical process involving the oxidation of the transition metal by the ions of a platinum salt at different concentrations of hydrochloric acid at different concentrations and temperatures: the process also involves a thermal treatment and acid leaching leading to the formation of nanowires and nanotubes (~50 nm in diameter and ~400 nm in length); The latter are transferred onto a Nafion® membrane using an optimized hot-pressing process. Electrodes were integrated into a complete Membrane Electrode Assembly (MEA) to characterize their electrochemical and transport limitations in real operating conditions. Ultraviolet spectrophotometric determination of platinum content showed a loading of ~0.1 mg_{Pt}/cm^2 for the nanowires and ~15 $\mu g_{Pt}/cm^2$ for the nanotubes. For comparison, we have elaborated a homemade Pt/C conventional with low Pt loading (~35 $\mu g_{Pt}/cm^2$), which exhibits a close catalyst surface area to the PtNi nanostructures. The performance of the MEA was quantified by recording the polarization curves and electrochemical impedance spectroscopy measurements. Accelerated durability tests gave an insight into the interest, stability, and limitations of these nanostructures compared to conventional electrodes.

Résumé :

La technologie des piles à combustible PEM a attiré beaucoup d'attention pour les applications futures de conversion et de stockage de l'énergie. Sa commercialisation demeure un défi en raison de la durabilité et des limites de coût du catalyseur. Afin d'améliorer sa performance sur le marché, il est obligatoire d'optimiser le catalyseur coûteux et d'améliorer sa durabilité et sa stabilité ou d'innover une nouvelle structure d'électrodes. Le catalyseur conventionnel utilisé est le Pt/C (nanoparticules de 3 à 5 nm supportées sur des nanoparticules de carbone de 30 à 50 nm), et considéré comme le catalyseur standard offrant des surfaces élevées et une activité spécifique élevée. En effet, cette structure n'est pas suffisamment contrôlée et limitée par divers phénomènes de dégradation : le coût ; la corrosion du support en carbone et la dissolution/agglomération de Pt par le mécanisme de maturation Ostwald qui se traduit par une perte rapide et significative de la surface électrochimique au fil du temps pendant le fonctionnement de la pile.

Cette thèse se concentre la réduction de la quantité de platine et l'amélioration des performances et de la durabilité des assemblages Membrane/Electrodes, visant à réduire leur coût et à encourager le développement des PEMFC. Des études antérieures ont démontré que les catalyseurs à base de Pt tels que PtCo, PtCu, et PtNi etc., ont montré une activité électrochimique plus élevée que celle du Pt, et une amélioration très prometteuse des performances et de la stabilité à faible chargement en Pt.

Pour atteindre ces objectifs, nous avons mis au point des procédés pour développer et contrôler une nouvelle architecture sans carbone de la cathode, réalisée uniquement avec des nanofils et des nanotubes PtNi alignés verticalement et supportés par une membrane Nafion® pour but d'améliorer les performances et la durabilité du PEMFC à faible chargement en Pt.

Le processus de fabrication repose sur un processus de fabrication en plusieurs étapes : l'élaboration et le contrôle de la géométrie de l'alumine nanoporeuse par double-anodisation, utilisée comme moule sacrificiel; Le procédé d'électrodéposition pulsée comme voie électrochimique de croissance des nanofils de Ni à l'intérieur du moule d'alumine; Procédé de déplacement galvanique contrôlé, qui repose sur l'utilisation de différents sels de Pt à différentes concentrations d'acide chlorhydrique et à différentes concentrations et températures (impliquant également un traitement thermique et une traitement acide conduisant à la formation de nanofils et de nanotubes de ~50 nm de diamètre 400 nm de longueur); Ces derniers sont transférés sur une membrane Nafion® à via pressage à chaud optimisé. Les électrodes ont été intégrées dans un ensemble d'électrodes à membrane complet afin de caractériser leurs propriétés électrochimiques et les limites de transport dans des conditions réelles de fonctionnement. La détermination du chargement en Pt par spectrophotométrie UV-vis a montré un chargement d'environ 0.1 mg_{Pt}/cm^2 pour les nanofils et de ~15 $\mu g_{Pt}/cm^2$ pour les nanotubes. À titre de comparaison, nous avons élaboré une cathode conventionnelle en Pt/C, à faible chargement en Pt (~35 $\mu g_{Pt}/cm^2$), qui présente une surface de catalyseur proche des nanostructures en PtNi. La performance du MEA a été quantifiée par l'études des courbes de polarisation et des mesures de spectroscopie d'impédance. Des tests de durabilité accélérés ont donné un aperçu de l'intérêt, de la stabilité et des limites de ces nanostructures par rapport aux électrodes classiques.